I. Statistical Mechanics of Bubbly Liquids. II. Behavior of Sheared Suspensions of Non-Brownian Particles

Thesis by

Yevgeny Yurkovetsky

In Partial Fulfillment of the Requirements

for the Degree of

Doctor of Philosophy

California Institute of Technology

Pasadena, California

1998

(Submitted July 24, 1996)

Acknowledgments

I wish to thank my graduate studies advisor, Professor John Brady, for his guidance throughout my stay at the California Institute of Technology. From among all of my teachers throughout my life, John has been the most influential and challenging. John's impact both on this work and my development as a researcher and my overall maturing as a human being has been of the utmost profundity.

Other Caltech professors who have lent their ideas and time providing advice and serving on my candidacy and final examination committees are gratefully acknowledged: Professors Zhen-Gang Wang, Julie Kornfield, Christopher Brennen, Melany Hunt, and George Gavalas.

Thanh Phung's help with the Stokesian dynamics code and various other programs and algorithms is greatly appreciated.

Thank you, Suresh Guptha, for all your very valuable advice on Unix, Latex, and multiple other computer soft- and hardware issues.

To a fair degree, my days as a member of John's group will be fondly remembered due to the friendships I enjoyed with my fellow graduate and postdoctoral students: Thanh Phung, Phil Lovalenti, Jeff Morris, Prabhu Nott, Yvette Baxter-Drayton, Paul Rider, Mike Vicic, Mehrzad Tabatabaian, Douglas Varela, and Dave Foss who kindly helped me with the logistics of finishing up.

Finally, I would have never been able to pull this off had it not been for my friends and family in Pasadena, Los Angeles, Orange County, San Francisco, Chicago, New York City, Boston, Pennsylvania, Delaware, Zuerich, Odessa, and Moscow. I look forward to many wonderful vacations spent with my loved ones in all of those—and many more other—exciting towns, states, and countries.

Abstract

I. Statistical mechanics of bubbly liquids. The dynamics of bubbles at high Reynolds numbers is studied from the viewpoint of statistical mechanics. Individual bubbles are treated as dipoles in potential flow. A virtual mass matrix of the system of bubbles is introduced, which depends on the instantaneous positions of the bubbles, and is used to calculate the energy of the bubbly flow as a quadratic form of the bubbles' velocities. The energy is shown to be the system's Hamiltonian and is used to construct a canonical ensemble partition function, which explicitly includes the total impulse of the suspension along with its energy. The Hamiltonian is decomposed into an effective potential due to the bubbles' collective motion and a kinetic term due to the random motion about the mean. An effective bubble temperature—a measure of the relative importance of the bubbles' relative to collective motion—is derived with the help of the impulse-dependent partition function. Two effective potentials are shown to operate: one, due to the mean motion of the bubbles, dominates at low bubble temperatures where it leads to their grouping in flat clusters normal to the direction of the collective motion, while the other, temperature invariant, is due to the bubbles' position-dependent virtual mass and results in their mutual repulsion. Numerical evidence is presented for the existence of the effective potentials, the condensed and dispersed phases and a phase transition.

II. Behavior of sheared suspensions of non-Brownian particles. Suspensions of non-Brownian particles in simple shear flow of a Newtonian solvent in the range of particle phase concentration, ϕ, from 0.05 to 0.52, are studied numerically by Stokesian Dynamics. The simulations are a function of ϕ and the dimensionless shear rate, $\dot{\gamma}^*$, which measures the relative importance of the shear and short-ranged interparticle forces. The pair-distribution functions, shear viscosity, normal stress differences, suspension pressure, long-time self-diffusion coefficients, and mean square of the particle velocity fluctuations in the velocity-gradient and vorticity directions are computed,

tabulated and plotted. In concentrated suspensions ($\phi > 0.45$), two distinct microstructural patterns are shown to exist at the highest and lowest shear rates. At $\dot{\gamma}^* = 0.1$ the particles form hexagonally packed strings in the flow direction. As $\dot{\gamma}^*$ increases, the strings are gradually being replaced by non-compact clusters of particles kept together by strong lubrication forces while the particle pair-distribution displays a broken fore-aft symmetry. These changes in the microstructure are accompanied by increases in the shear viscosity, normal stress differences, suspension pressure, long-time self-diffusion coefficients, and fluctuational motion. Agreement is found between the simulation results and the theoretical predictions of Brady & Morris (1997).

Contents

List of Figures

List of Tables

Part I

Statistical Mechanics of Bubbly Liquids

Chapter 1 Introduction

The dynamics of bubbly liquids—a Newtonian liquid filled with a dispersed gas phase in the form of bubbles—is of interest in a variety of engineering problems. Bubbly flows are common in the energy-conversion, oil and chemical industries, in natural gas distribution networks, and in any flow in which rapid pressure variations can lead to phase change, e.g., cavitation, or where sound waves can be strongly modified by bubble clouds. A major theoretical and technical problem associated with bubbly flows is predicting, and thus controlling, the flow regime, and then within the flow regime understanding the transport of heat, mass, momentum, and sound.

Continuum modeling of gas/liquid flows in the region of dispersed bubbly flow is an active area of research and has been approached through a variety of different methods. One of these has been developed by Batchelor (1976), Delhaye & Achard (1976), Hinch (1977), Voinov & Petrov (1977), Banerjee & Chan (1980), Drew (1983), Biesheuvel & van Wijngaarden (1984), and Pauchon & Banerjee (1986) among others. These authors have applied averaging—in time, space, in time and space, over an ensemble, etc.—to the continuum-mechanical equations describing the exact motion of each phase at each point. The system of resulting averaged equations is closed with the help of constitutive relations determined from a list of variables that are supposed to influence the phase interactions. The resulting equations have several unknown coefficients that have to be determined in some way, e.g., from experiments. The models that different investigators have proposed usually differ in the choice of closure relationships.

Another, variational, approach has been developed by Geurst (1985, 1986) and Pauchon & Smereka (1992). These authors have chosen to volume average the energy of a two-phase flow and then treat the volume averaged energy as the Lagrangian by applying to it a generalized form of Hamilton's variational principle. Pauchon & Smereka (1992) have shown the variational and averaging approach to be comple-

mentary: the variational approach is capable of providing explicit analytical forms for the constitutive equations of the averaging approach. However, as Smereka (1993) has pointed out, although Geurst's model seems to have a sound theoretical basis, it turns out to be ill-posed in the dilute limit; Geurst and other authors argued that the ill-posedness is associated with the assumption of an isotropic arrangement of bubbles. As a result, much effort has been devoted to studying the related issues of clustering of bubbles and voidage wave propagation in bubbly liquids. Sangani & Didwania (1993*a*, *b*) and Smereka (1993) carried out computer simulations of bubbles in an ideal fluid. In both studies, it has been found that, if initially given similar velocities, the bubbles would tend to form clusters positioned broadside to the direction of motion; Smereka found that the clustering would be inhibited, however, if the variance of the initial velocities of bubbles was sufficiently large.

A kinetic theory-like approach to the problem of bubbly liquids has been investigated by Biesheuvel & Gorissen (1990) and van Wijngaarden & Kapteyn (1990). These workers have obtained effective equations by taking moments of an N-particle probability density function for bubble positions and velocities and focused their attention on the propagation of void fraction disturbances in bubble flows.

In this thesis, we present a formulation of the problem of bubbly flows from a statistical mechanics point of view. This idea was hinted at in the work of Smereka (1993), but not developed nor explored. Indeed, it is an interesting and open question as to whether this continuum problem of bubble motion has a statistical description of the same form as atoms or molecules. On the one hand, classical statistical mechanics is a powerful means of studying macroscopic bodies. It provides the molecular basis of macroscopic properties by explaining the connection between the observed values of a thermodynamic function and the properties of the molecules making up the system. On the other hand, bubbles, as considered in this thesis (of constant spherical shape and size, monodisperse, inviscid and described as dipoles in potential flow) are fundamentally different from molecules as "elementary particles" of statistical mechanics in one important aspect, namely, they do not have mass; rather, their motion results in flow of the underlying liquid of nonzero density. Thus, "virtual,"

or "added," mass of the flow is critical to the behavior of the bubbles as a statistical system. Like a molecular system, the total energy and momentum of the flow are shown to be integrals of the bubbles' motion. The interactions among the bubbles occur through the velocity field in the fluid generated by the bubbles' motion, and will be seen to be of the form similar to repulsive r^{-6} interactions in molecular systems.

By formulating and examining a bubbly flow as a statistical ensemble we can predict, discuss and quantify patterns of collective behavior of a macroscopically large number of bubbles as consequences of the distinctive features of bubbles treated as individual particles. We are able to discern factors influencing the flow's structure and properties, and describe them in thermodynamic terms, such as interaction potentials, temperature, phase transition, etc. Finally, in a fashion similar to classical atomic systems, the validity of our predictions and calculations will be tested by simulating the bubbly flow numerically and by analyzing the results of the simulations.

In Chapter 2, we approximate a bubbly flow at high Reynolds numbers as potential flow and derive its total energy. We apply Lagrange's formalism to the energy in order to derive the equations of motion for the bubbles. In Chapter 3, we show that the bubbly flow is a Hamiltonian system and define the canonical ensemble partition function, along with the "temperature" for such a flow in much the same way as is done for atomic systems. Unlike atomic systems, however, the virtual mass for the bubbly flow is dependent on the positions of all the bubbles, and as a result the partition function for an ensemble of bubbles explicitly depends on the total impulse of the flow determined in a frame of reference in which the liquid would be motionless were it not for the presence of the moving bubbles. As the relative position of the bubbles changes, so does the "mass" of the system, and therefore the center-of-mass or collective motion is coupled to the internal degrees of freedom. These two distinctive features—the coordinate-dependent mass and the momentum-dependent partition function—together give rise to a number of unusual effects not found in atomic systems. In particular, the coordinate-dependent mass results in the clustering of bubbles in the direction normal to that of their mean motion, and also in an effective repulsive potential that can prohibit the clustering at sufficiently

high values of the bubble temperature (defined as a measure of the bubbles' chaotic motion). Also in Chapter 3, we predict the value of the temperature at which a phase transition occurs between the clustered and dispersed states. In Chapter 4, we develop a molecular-dynamics-like method for simulating bubbly flows and present and discuss numerical results: snapshots of representative bubble configurations for 27 and 64 bubbles at different volume fractions and at different bubble temperatures; the influence of viscous dissipation and gravity; evidence of the effective repulsive potential and the phase transition between the clustered and random phases. These results are shown to support the statistical mechanical description.

Chapter 2 Equation of Motion for a Dispersion of Bubbles

2.1 Kinetic Energy of a Bubbly Flow

We shall make use of Lagrange's formalism in order to derive an equation of motion for bubbles in a dispersed flow. In this framework, the first step is to obtain an expression for the Lagrangian $\mathcal{L}$. In this problem, the kinetic energy of the fluid $\mathcal{T}$ will be found to be quadratic in the vector of the bubbles' velocities $\mathbf{U}$, and thus the Lagrangian is the kinetic energy $\mathcal{T}$ minus the potential energy $\mathcal{E}$. We shall set the potential energy to zero; this restriction, of course, can be relaxed if so desired. Thus, $\mathcal{L} = \mathcal{T}$, and we determine the kinetic energy as a function of the bubbles' positions and velocities. In order to do so, we model the bubbly flow as a dispersion of a finite number, N, of monodisperse spherical bubbles (maintained spherical by a presumed large interfacial tension), characterized by a constant internal pressure moving in an unbounded fluid at high Reynolds number ($Re = Ua/\nu \gg 1$) subject to gravitational, external or fluctuating pressure forces. Because the Reynolds number is large and the bubble surface is a free surface, the flow outside the bubbles is approximately inviscid and irrotational. Hence, the fluid velocity can be written as the gradient of a velocity potential, ϕ, satisfying Laplace's equation

$$\nabla^2\phi = 0, \tag{2.1}$$

everywhere in the fluid, with no flux boundary conditions on the bubble surfaces

$$\mathbf{n} \cdot \nabla\phi = \mathbf{n} \cdot \mathbf{U}^{\nu},$$

where $\mathbf{n}$ is the unit outward normal from the surface $\partial\Omega^\nu$ of bubble ν and $\mathbf{U}^\nu$ is that bubble's velocity. This is, of course, an approximation, but it is known from the work of Moore (1963, 1965) that the flow outside a moving bubble is to a very good approximation irrotational, with the vorticity confined to a thin $O(Re^{-1/2})$ boundary layer at the bubble surface and to a narrow $O(Re^{-1/4})$ wake. Furthermore, Kok (1993*a*, *b*) has shown both theoretically and experimentally that the motion of two interacting bubbles can also be predicted by the appropriate two bubble solution of Laplace's equation.

The total kinetic energy of the fluid is (cf. §§2.7–2.10, 6.2, 6.4 of Batchelor 1967)

$$\mathcal{T} = \frac{1}{2}\rho \int_{\partial\Omega^\infty} \phi \mathbf{U}^\infty \cdot \mathbf{n}^\infty dS - \frac{1}{2}\rho \sum_\nu \mathbf{U}^\nu \cdot \int_{\partial\Omega^\nu} \phi \mathbf{n}^\nu dS, \tag{2.2}$$

where $\mathbf{U}^\infty$ denotes the fluid velocity at infinity and ρ, the density of the fluid. The first integral in (2.2) is taken over a closed boundary at infinity and is, therefore, equal to zero as long as we assume that the fluid's motion is entirely due to the bubbles; indeed, we treat the bubbles as dipoles in this study (cf. Appendix), i.e., the potential ϕ falls off as r^{-2} and the liquid velocity $\mathbf{U}^\infty$ falls off as r^{-3} at large r and thus the first integral in (2.2) vanishes. The solution of (2.1) is linear in the bubbles' velocities $\mathbf{U}$ and therefore the kinetic energy can be recast, with the help of the virtual mass matrix $\mathbf{M}$, into a quadratic form:

$$\mathcal{T} = \frac{1}{2}\rho\tau \mathbf{U} \cdot \mathbf{M} \cdot \mathbf{U}, \tag{2.3}$$

where $\tau = (4/3)\pi a^3$ is the volume of a spherical bubble of radius a and $\mathbf{U}$ is a vector of the individual bubble velocities $\mathbf{U}^\nu$. The derivation of the mass matrix is given in detail in the Appendix.

We also find it convenient to write the total energy of the flow as

$$\mathcal{T} = \frac{1}{2}\rho\tau \mathbf{U}^\mu \cdot \mathbf{M}^{\mu\nu} \cdot \mathbf{U}^\nu, \tag{2.4}$$

where the Greek indices denote the individual bubbles and, if repeated, imply a

summation; $\mathbf{M}^{\mu\nu}$ are the coupling submatrices of the mass matrix $\mathbf{M}$ (cf. Appendix). Finally, the individual bubbles' momenta are defined as

$$\mathbf{P}^{\mu} = \rho\tau\mathbf{M}^{\mu\nu} \cdot \mathbf{U}^{\nu}, \tag{2.5}$$

and the total impulse of the suspension (i.e., the linear momentum that needs to be imparted to the fluid in order to generate from rest the flow due to motion of the bubbles with translational velocities $\mathbf{U}^{\mu}$) is

$$\mathbf{P}_t = \sum_{\mu=1}^{N} \mathbf{P}^{\mu}. \tag{2.6}$$

The total impulse $\mathbf{P}_t$ is an integral of the motion (cf. Art. 119 of Lamb 1932), as is the total energy $\mathcal{T}$.

2.2 Lagrangian Formulation of the Problem

From expression (2.3) for the total kinetic energy, we can derive the equation of motion for the bubbles. Let $\mathbf{R}$ denote the vector of the bubbles' centers, $\mathbf{F}^g$ the external forces such as gravity, and $\mathbf{F}^v$ the viscous forces. Then, recalling Lagrange's equation, the equation of motion of the bubbly suspension is:

$$\frac{d}{dt}\left(\frac{\partial \mathcal{L}}{\partial \dot{\mathbf{R}}}\right) = \frac{\partial \mathcal{L}}{\partial \mathbf{R}} + \mathbf{F}^g + \mathbf{F}^v. \tag{2.7}$$

Lamb (1932) and, more recently, Hinch & Nitsche (1993) have shown that the Lagrangian generalized force,

$$\mathbf{F}^L = \frac{d}{dt}\left(\frac{\partial \mathcal{L}}{\partial \dot{\mathbf{R}}}\right) - \frac{\partial \mathcal{L}}{\partial \mathbf{R}},$$

is the same as the pressure force exerted by the fluid on the bubbles $\mathbf{F}^p$. Thus, the equation of motion (2.7) is equivalent to the force balance on the massless bubbles[1]

$$\mathbf{F}^p + \mathbf{F}^g + \mathbf{F}^v = 0. \tag{2.8}$$

From (2.3) together with the fact that $\mathcal{L} = \mathcal{T}$, we compute the necessary quantities:

$$\frac{\partial \mathcal{L}}{\partial \mathbf{R}} = \frac{\partial \mathcal{T}}{\partial R_k} = \frac{\partial}{\partial R_k}\left(\frac{1}{2}\rho\tau U_i M_{ij}(R_k) U_j\right) = \frac{1}{2}\rho\tau U_i \frac{\partial M_{ij}}{\partial R_k} U_j,$$

and

$$\frac{\partial \mathcal{L}}{\partial \dot{\mathbf{R}}} = \frac{\partial \mathcal{T}}{\partial U_k} = \frac{1}{2}\rho\tau(U_i M_{ik} + M_{kj} U_j) = \rho\tau M_{kj} U_j,$$

due to the fact that the mass matrix is symmetric. Furthermore,

$$\frac{d}{dt}\left(\frac{\partial \mathcal{T}}{\partial U_k}\right) = \rho\tau(\dot{M}_{kj} U_j + M_{kj}\dot{U}_j),$$

with

$$\dot{M}_{kj} = \frac{\partial M_{kj}}{\partial R_l}\dot{R}_l = \frac{\partial M_{kj}}{\partial R_l} U_l.$$

Hence,

$$\frac{d}{dt}\left(\frac{\partial \mathcal{T}}{\partial U_k}\right) = \rho\tau\left(\frac{\partial M_{kj}}{\partial R_l} U_l U_j + M_{kj}\dot{U}_j\right),$$

and the equation of motion (2.7) becomes

$$\rho\tau M_{kj}\dot{U}_j = \rho\tau\left(\frac{1}{2} U_i \frac{\partial M_{ij}}{\partial R_k} U_j - \frac{\partial M_{kj}}{\partial R_l} U_l U_j\right) + F_k{}^g + F_k{}^v. \tag{2.9}$$

Equation (2.9) is the governing equation for determining the bubbles' motion. We see clearly that the virtual mass matrix does indeed act as the mass of the system.

Equation (2.9) defines the dynamics of the bubbles and is sufficient to follow their motion for given initial conditions under the action of prescribed forces. Before doing so, we turn to a consideration of the bubbles as a statistical ensemble and investigate

[1]Bubble mass could be added to (2.8) or (2.7) without difficulty. The conclusions of the work would not be affected for small bubble mass. Similarly, angular momentum could be added for nonspherical particles.

whether this dynamical system has thermodynamics akin to a molecular system.

Chapter 3 Bubbly Flow as a Statistical Ensemble

Consider the bubbly flow of Chapter 2 in the absence of gravity and fluid viscosity. It proves possible then to treat the total energy of the bubbly flow

$$\frac{1}{2\rho\tau}\mathbf{P}\cdot\mathbf{M}^{-1}\cdot\mathbf{P}$$

as the system's Hamiltonian, $\mathcal{H}(\mathbf{P},\mathbf{R})$, with $\mathbf{P}$ and $\mathbf{R}$ as the corresponding generalized momenta and coordinates. Indeed, $\mathcal{H}$ satisfies Hamilton's equations,

$$\dot{\mathbf{R}} = \frac{\partial\mathcal{H}}{\partial\mathbf{P}}, \tag{3.1}$$

$$\dot{\mathbf{P}} = -\frac{\partial\mathcal{H}}{\partial\mathbf{R}}, \tag{3.2}$$

which are equivalent to the equation of motion (2.9) with $\mathbf{F}^g = \mathbf{F}^v = 0$, and thus the inviscid, neutrally buoyant bubbly flow is a Hamiltonian system (with $6N$ degrees of freedom) to which the standard methods of statistical mechanics can be applied.

3.1 Effective Energies

We begin by decomposing the full energy of the bubbly flow into effective potential and kinetic energies. First, we write each bubble's individual impulse, defined by (2.5), as follows:

$$\mathbf{P}^\mu = \mathbf{p}^\mu + \frac{1}{N}\mathbf{P}_t,$$

where the deviation from the mean, $\mathbf{p}^\mu$, can be regarded as the "chaotic" impulse of bubble μ. The total energy of the flow is then

$$\mathcal{T} = \frac{1}{2\rho\tau}\left(\frac{1}{N^2}\mathbf{P}_t \cdot \sum_{\mu,\nu}\left(\mathbf{M}^{-1}\right)^{\mu\nu} \cdot \mathbf{P}_t + \mathbf{p}\cdot\mathbf{M}^{-1}\cdot\mathbf{p} + \frac{2}{N}\mathbf{P}_t \cdot \left(\sum_{\mu}\left(\mathbf{M}^{-1}\right)^{\mu\nu}\cdot\mathbf{p}^\nu\right)\right), \tag{3.3}$$

where $\mathbf{p}$ denotes the full vector of the bubbles' chaotic impulses. The first term on the right-hand side of (3.3) is due to the collective motion of the bubbles with the same velocity $\mathbf{u}_0 = (\rho\tau N)^{-1}\mathbf{P}_t \cdot \sum_{\mu,\nu}\left(\mathbf{M}^{-1}\right)^{\mu\nu}$; it depends only on the positions of the bubbles' centers, $\mathbf{R}$, and thus can be thought of as an "effective potential energy." The sum of the second and third terms in (3.3) we shall call the effective kinetic energy; it accounts for the individual, or chaotic, portion of the bubbles' motion. It is easy to see that the chaotic impulses $\mathbf{p}$ along with the positions of the bubbles' centers $\mathbf{R}$ can play the role of the generalized coordinates that satisfy Hamilton's equations of motion.

Smereka (1993) has defined effective energies by decomposing the bubble's velocity, rather than its impulse, as follows:

$$\mathbf{U}^\mu = \mathbf{u}_0 + \mathbf{u}^\mu,$$

such that

$$\mathbf{M}^{\mu\nu}\cdot\mathbf{u}^\nu = 0,$$
$$\rho\tau\mathcal{M}\cdot\mathbf{u}_0 = \mathbf{P}_t,$$

where

$$\mathcal{M} = \sum_{\mu,\nu}\mathbf{M}^{\mu\nu}.$$

Then, recalling (2.4), the total energy of the flow is

$$\mathcal{T} = \frac{1}{2\rho\tau}\mathbf{P}_t\cdot\mathcal{M}^{-1}\cdot\mathbf{P}_t + \frac{\rho\tau}{2}\mathbf{u}^\mu\cdot\mathbf{M}^{\mu\nu}\cdot\mathbf{u}^\nu. \tag{3.4}$$

Again, the first term on the right-hand side of (3.4) is due to the collective motion of the bubbles with the same velocity $\mathbf{u}_0$; it depends only on the position of the bubbles' centers $\mathbf{R}$, and thus Smereka has termed it the effective potential energy; the second term is the corresponding effective kinetic energy.

Smereka used the decomposition (3.4) to show that the effective potential energy $(2\rho\tau)^{-1}\mathbf{P}_t \cdot \mathcal{M}^{-1} \cdot \mathbf{P}_t$ approaches a minimum when the bubbles arrange themselves in flat clusters positioned broadside to the direction of the collective motion. For the purposes of the present study, we shall use the "Hamiltonian" decomposition (3.3), rather than (3.4). As given by (3.3), the total energy of the flow satisfies Hamilton's equations (3.1) and (3.2), if $\mathbf{p}$ is used as the generalized momentum instead of $\mathbf{P}$, and thus equation (3.3) can and will be used to construct the canonical ensemble partition function. The decomposition of Smereka in (3.4) is not in the standard form for statistical mechanics and cannot be used to construct the partition function.

Another result of Smereka (1993) is that the variational principle of minimal potential energy is equivalent to the principle of maximal virtual mass. To show that bubbles in collective motion with no random velocities will indeed tend to increase their virtual mass, we consider the following situation.

Suppose that initially the bubbles are randomly positioned in space but all have the same velocity, e.g., $(0, 0, 1)$. They are then released and we are interested in the change in the added-mass coefficient C_M defined as the following norm on the mass matrix:

$$C_M \equiv \frac{\mathbf{U} \cdot \mathbf{M} \cdot \mathbf{U}}{\mathbf{U} \cdot \mathbf{U}}.$$

If we write the Lagrangian of the system as $\mathcal{L} = 1/2\rho\tau C_M U^2$, then Lagrange's equation (2.7) can be transformed to

$$\dot{C}_M = \frac{1}{2}\left(\frac{\partial C_M}{\partial R_i}\right) U_i - C_M \frac{\dot{U}_i U_i}{U^2}. \tag{3.5}$$

Initially, when $\mathbf{U} = [0, 0, 1; 0, 0, 1; \ldots; 0, 0, 1]$, the first term on the right-hand side of (3.5) is proportional to the change in C_M corresponding to a rigid translation of the whole suspension along the z-axis and therefore is zero. The randomly distributed

bubbles will begin to develop velocities in the two other orthogonal directions, x and y. In order to do so, energy will have to be extracted from the bubbles' collective motion, the bubbles will slow down in the z-direction, to conserve the total energy and impulse, and thus $\dot{U}_i$ and U_i will be anti-parrallel, i.e., $\dot{U}_i U_i$ will be negative and $\dot{C}_M$ positive, which means that C_M will initially tend to increase. In other words, since the bubbles have to decelerate in the z-direction while their total impulse in that direction must be conserved, their virtual mass must increase. Smereka (1993) recognized the analogy between potential flow outside the bubbles and the effective conductivity of a material where the liquid has a unit conductivity and the spherical bubbles are insulators (cf. Appendix). He was able to show that the only way for the bubbles to increase their virtual mass would be to organize themselves in clusters positioned broadside to the direction of the collective motion; this situation corresponds to the minimal effective conductivity of the matrix in the direction of the mean flow. Thus, following Smereka, we also conclude that the bubbles' collective motion will lead to their clustering. In the next section we investigate how this clustering manifests itself when the bubbles are viewed as a thermodynamic system.

3.2 Canonical Ensemble Partition Function for Bubbly Flow

We now apply the apparatus of equilibrium statistical mechanics by treating the suspension of N bubbles as a canonical ensemble. Denoting the Hamiltonian of the ensemble by $\mathcal{H}$, the partition function, within a constant factor, is given by

$$Q = \int \exp[-\beta \mathcal{H}(\mathbf{R}, \mathbf{P}) - \boldsymbol{\gamma} \cdot \mathbf{P}_t(\mathbf{R}, \mathbf{P})] d\mathbf{R} d\mathbf{P}. \tag{3.6}$$

The integration in (3.6) is performed over the entire phase space. The form (3.6) follows from the fact that there are only seven additive integrals of motion of a classical system: the energy, linear momentum, and angular momentum. Since we have no angular momentum for spherical bubbles, only two constants β and $\boldsymbol{\gamma}$ are

needed (cf. §4 of Landau & Lifshitz 1969). β will be seen to play the role of the inverse temperature, and γ/β will be the average velocity of the bubbles.

The necessity of including the total impulse of the bubbly flow, $\mathbf{P}_t$, in the expression for the canonical ensemble partition function, is dictated by the fact that the "center-of-mass" motion is coupled to the internal degrees of freedom. As the relative coordinates change so too does the mass, leading to the coupling with the total impulse.

Let us denote for convenience the effective potential energy as $\mathcal{U}$ and the effective kinetic energy as $\mathcal{K}$, such that

$$\mathcal{U} = \frac{1}{2\rho\tau N^2}\mathbf{P}_t \cdot \sum_{\mu,\nu}\left(\mathbf{M}^{-1}\right)^{\mu\nu} \cdot \mathbf{P}_t, \tag{3.7}$$

and

$$\mathcal{K} = \frac{1}{2\rho\tau}\left(\mathbf{p}\cdot\mathbf{M}^{-1}\cdot\mathbf{p} + \frac{2}{N}\mathbf{P}_t \cdot \left(\sum_{\mu}\left(\mathbf{M}^{-1}\right)^{\mu\nu}\cdot\mathbf{p}^{\nu}\right)\right)$$

The potential energy $\mathcal{U}$ is purely $\mathbf{R}$-dependent, just as in the classical case of a gas of particles interacting via a potential. However, due to the fact that the virtual mass of the bubbly suspension is position-dependent, the kinetic energy $\mathcal{K}$ is both $\mathbf{R}$- and $\mathbf{p}$-dependent and differs from that of a classical statistical mechanical system.

Depending on the choice of the momentum generalized coordinates—one can choose either the bubbles' full impulses $\mathbf{P}$ or their chaotic impulses $\mathbf{p}$—the following two alternative expressions for the partition function are possible:

$$Q = \int \exp\left[-\frac{\beta}{2\rho\tau}\mathbf{P}\cdot\mathbf{M}^{-1}\cdot\mathbf{P} - \gamma\cdot\sum_{\mu}\mathbf{P}^{\mu}\right] d\mathbf{R}d\mathbf{P}, \tag{3.8}$$

or

$$Q = \int \exp[-\beta\mathcal{U} - \gamma\cdot\mathbf{P}_t]\left(\int \exp\left[-\beta\mathcal{K} - \gamma\cdot\sum_{\mu}\mathbf{p}^{\mu}\right] d\mathbf{p}\right) d\mathbf{R}. \tag{3.9}$$

Upon integrating (3.8) and (3.9) by parts with respect to an arbitrary component of the vector $\mathbf{P}$ or $\mathbf{p}$ and denoting by angle brackets averaging over the ensemble, we

obtain

$$\frac{\beta}{\rho\tau}\langle \mathbf{P}\cdot\mathbf{M}^{-1}\cdot\mathbf{P}\rangle - \boldsymbol{\gamma}\cdot\left\langle\sum_{\mu}\mathbf{P}^{\mu}\right\rangle = 3N, \tag{3.10}$$

and

$$\frac{\beta}{\rho\tau}\left\langle \mathbf{p}\cdot\mathbf{M}^{-1}\cdot\mathbf{p} + \frac{1}{N}\mathbf{P}_t\cdot\left(\sum_{\mu}\left(\mathbf{M}^{-1}\right)^{\mu\nu}\cdot\mathbf{p}^{\nu}\right)\right\rangle - \boldsymbol{\gamma}\cdot\left\langle\sum_{\mu}\mathbf{p}^{\mu}\right\rangle = 3N. \tag{3.11}$$

At thermal and mechanical equilibrium of the ensemble with its surroundings

$$\left\langle\sum_{\mu}\mathbf{p}^{\mu}\right\rangle = 0,$$

$$\left\langle\sum_{\mu}\mathbf{P}^{\mu}\right\rangle = \mathbf{P}_t,$$

and it follows from (3.10) and (3.11) that

$$\beta^{-1} = \frac{1}{3\rho\tau N}\left\langle \mathbf{p}\cdot\mathbf{M}^{-1}\cdot\mathbf{p} + \frac{1}{N}\mathbf{P}_t\cdot\left(\sum_{\mu}\left(\mathbf{M}^{-1}\right)^{\mu\nu}\cdot\mathbf{p}^{\nu}\right)\right\rangle, \tag{3.12}$$

and

$$\begin{aligned}\frac{\boldsymbol{\gamma}}{\beta} &= -\frac{1}{\rho\tau N}\left\langle\frac{1}{N}\sum_{\mu,\nu}\left(\mathbf{M}^{-1}\right)^{\mu\nu}\cdot\mathbf{P}_t + \left(\sum_{\mu}\left(\mathbf{M}^{-1}\right)^{\mu\nu}\cdot\mathbf{p}^{\nu}\right)\right\rangle \\ &= -\frac{1}{\rho\tau N}\left\langle\sum_{\mu}(\mathbf{M}^{-1})^{\mu\nu}\cdot\mathbf{P}^{\nu}\right\rangle = -\frac{1}{N}\left\langle\sum_{\mu}\mathbf{U}^{\mu}\right\rangle.\end{aligned} \tag{3.13}$$

Thus $\boldsymbol{\gamma}/\beta$ is equal to minus the average velocity of all the bubbles in the flow, showing that $-\boldsymbol{\gamma}\cdot\mathbf{P}_t/\beta$ is the energy of the collective motion.

That $\boldsymbol{\gamma}/\beta$ must be proportional to the average velocity of the bubbles in the ensemble could also be deduced from the following argument, adapted from §14 of Hill (1956). We consider here a generalized ensemble which can, with probabilities p_k, be found in a number of states with energies E_k; this formulation can be generalized to account for continuous states. We associate the thermodynamic internal energy E

with the ensemble average $\bar{E}$ (the averaging denoted by the overbar):

$$E \leftrightarrow \bar{E},$$

where

$$\begin{aligned} \bar{E} &= \sum_{k,\mathbf{P}_t} p_k E_k, \\ p_k &= \frac{\exp(-\beta E_k - \boldsymbol{\gamma}\cdot\mathbf{P}_t)}{Q}, \\ Q &= \sum_{k,\mathbf{P}_t} \exp(-\beta E_k - \boldsymbol{\gamma}\cdot\mathbf{P}_t). \end{aligned} \tag{3.14}$$

In differential form,

$$d\bar{E} = \sum_{k,\mathbf{P}_t} dp_k E_k, \tag{3.15}$$

where the E_k are constants. We now use (3.14) to eliminate E_k in (3.15),

$$d\bar{E} = -\frac{1}{\beta}\sum_{k,\mathbf{P}_t}(\boldsymbol{\gamma}\cdot\mathbf{P}_t + \ln p_k + \ln Q)dp_k. \tag{3.16}$$

Since

$$\bar{\mathbf{P}}_t = \sum_{k,\mathbf{P}_t} p_k \mathbf{P}_t,$$

(3.16) becomes

$$\begin{aligned} d\bar{E} &= -\frac{1}{\beta}\sum_{k,\mathbf{P}_t}(\ln p_k dp_k) - \frac{1}{\beta}\boldsymbol{\gamma}\cdot d\bar{\mathbf{P}}_t \\ &= -\frac{1}{\beta}d\left(\sum_{k,\mathbf{P}_t}(p_k \ln p_k)\right) - \frac{1}{\beta}\boldsymbol{\gamma}\cdot d\bar{\mathbf{P}}_t, \end{aligned} \tag{3.17}$$

where we have employed $\sum dp_k = 0$. With the further association $\mathbf{P}_t \leftrightarrow \bar{\mathbf{P}}_t$, (3.17) is seen to be just the statistical version of the thermodynamic equation

$$dE = TdS - \boldsymbol{\Pi}\cdot d\mathbf{P}_t, \tag{3.18}$$

where E, T and S are, as usual, the internal energy, temperature, and entropy of

the system, whereas $\mathbf{\Pi}$ is the generalized force appropriate to $\mathbf{P}_t$ (treated here as a generalized coordinate). By comparing (3.17) and (3.18) we have

$$\mathbf{\Pi} \leftrightarrow \frac{\gamma}{\beta}.$$

It can further be seen that $\mathbf{\Pi}$, along with γ/β, must have units of velocity. In our problem, there is only one characteristic velocity, namely the average velocity of the bubbles. Thus, it is reasonable, in agreement with (3.13), to assume γ/β proportional to $\bar{\mathbf{U}} \equiv N^{-1}\left\langle \sum_\mu \mathbf{U}^\mu \right\rangle$.

Now, given an ensemble at specified values of β and γ, we can always rotate the coordinate system, simultaneously rescaling the time, such that in the transformed frame of reference, $\bar{\mathbf{U}} = \mathbf{e}_c$, where $\mathbf{e}_c$ is a unit velocity vector pointing in the direction of the collective motion, this direction being the same in all appropriately rotated ensembles. In other words,

$$\gamma = \beta \mathbf{e}_c, \tag{3.19}$$

and the partition function (3.6) can be rewritten as

$$Q = \int \exp\left(-\beta[\mathcal{H}(\mathbf{R},\mathbf{P}) + \mathbf{e}_c \cdot \mathbf{P}_t(\mathbf{R},\mathbf{P})]\right) d\mathbf{R} d\mathbf{P}.$$

Finally, we define the temperature T of the system as the inverse of β, as given by (3.12):

$$T \equiv \frac{1}{\beta}.$$

The bubble temperature T can take on values from zero to infinity; it provides a measure of the relative importance of the chaotic to collective motion of the bubbles in the flow.

3.3 Effective Potentials

We shall now show that the coordinate-dependent virtual mass matrix of the bubbly flow, along with the bubbles' collective motion, give rise to two effective inter-bubble

potentials. Recalling (3.19), we begin by evaluating the integral in (3.8) over the **P**-subspace of the phase space:

$$Q = \left(\frac{2\pi\rho\tau}{\beta}\right)^{\frac{3N}{2}} \int (\det \mathbf{M})^{\frac{1}{2}} \exp\left(\frac{\beta\rho\tau \mathbf{e}_c \cdot \mathcal{M} \cdot \mathbf{e}_c}{2}\right) d\mathbf{R}, \tag{3.20}$$

where we recognize the factor

$$\left(\frac{2\pi\rho\tau}{\beta}\right)^{\frac{3N}{2}}$$

as the partition function Q^{id} of an ideal gas of N particles of mass $\rho\tau$ each, normalized by the volume occupied by the suspension V_c raised to the Nth power. Recall that $\mathcal{M}$ is the sum of the coupling submatrices $\mathbf{M}^{\mu\nu}$ of the mass matrix.

The integral in (3.20), also called the excess part Q^{ex} of the partition function, can be rewritten as

$$Q^{ex} = {V_c}^{-N} \int \exp[-\beta(\mathcal{U}_1 + \mathcal{U}_2)] d\mathbf{R}, \tag{3.21}$$

where the two effective potentials $\mathcal{U}_1$ and $\mathcal{U}_2$ are defined as

$$\beta\mathcal{U}_1 = -\frac{1}{2}\ln(\det \mathbf{M}), \tag{3.22}$$

and

$$\mathcal{U}_2 = -\frac{\rho\tau}{2}\mathbf{e}_c \cdot \mathcal{M} \cdot \mathbf{e}_c. \tag{3.23}$$

To understand the behavior of the effective potential $\mathcal{U}_1$, it will be useful to consider a dilute suspension in which only two of the N bubbles, μ and ν, are appreciably close to each other, while the remainder are sufficiently distant—from μ, ν, and each other. Then, in the matrices $\mathbf{M}_1$ and $\mathbf{M}_2$ (from (6.12) and (6.13) in the Appendix), $\nabla\nabla r_{\mu\nu}^{-1}$ and $\nabla\nabla r_{\nu\mu}^{-1}$ will contain all the significant interactions. Furthermore, if we normalize the distance between μ and ν by the bubble radius a and choose a coordinate system such that in it $\mathbf{r}_{\mu\nu} = (r, 0, 0)$, then it is straightforward to compute the

determinant of the full mass matrix of the system:

$$\det \mathbf{M} = \frac{\det \mathbf{M}_2}{\det(\mathbf{M}_1 - \mathbf{I})} = \frac{1}{2^6}\left(1 - \frac{9}{2}\left(\frac{1}{r}\right)^6 + O\left(\left(\frac{1}{r}\right)^{12}\right)\right),$$

$$\ln(\det \mathbf{M}) \sim \text{const} - \frac{9}{2}\left(\frac{1}{r}\right)^6 \text{ for large values of } r, \tag{3.24}$$

and thus:

$$\beta \mathcal{U}_1 \sim \frac{9}{4}\left(\frac{1}{r_{\mu\nu}}\right)^6 \text{ for large } r_{\mu\nu}. \tag{3.25}$$

The coordinate dependence of the virtual mass matrix acts as a repulsive, r^{-6}, potential.

The other effective potential, $\mathcal{U}_2$, bears a very close resemblance to the effective potential energy of the bubbly flow as defined in (3.7) or by Smereka (1993); the absolute value of $\mathcal{U}_2$ increases as the bubbles form clusters positioned normal to the direction of their collective motion. However, the role played by $\mathcal{U}_1$ in the partition function Q differs fundamentally from that played by $\mathcal{U}_2$ in that it is insensitive to changes in the inverse temperature β. Thus, the influence of $\mathcal{U}_2$, unlike that of $\mathcal{U}_1$, is expected to diminish with increasing temperature.

3.4 Phase Transition

The results of the previous section suggest that the spatial arrangement of bubbles in a suspension will strongly depend on the relative importance of the two effective potentials: the one due to the collective motion acts to make the bubbles cluster, while the effective potential due to the coordinate-dependent virtual mass is repulsive. Because $\beta\mathcal{U}_1$ is independent of temperature, while $\beta\mathcal{U}_2$ is proportional to $1/T$, the repulsive potential dominates at high temperature, while the collective dominates at low temperatures. Thus, one expects a "phase transition" to occur. A clustered bubbly flow ("condensed," or "frozen" phase) started at a low temperature will become more and more random as the temperature increases until at a certain value of T it becomes completely random ("gaseous," or "melted" phase).

We shall now attempt to predict the temperature of the phase transition (or, at least, an upper bound on it) for the bubbly suspension. We treat the suspension as a rarefied gas, in which not more than one pair of bubbles may be assumed to be interacting significantly at any one time, and obtain an expression for the second virial coefficient, B, as a function of the inverse temperature β for this gas. Recall the corresponding equation of state (Landau & Lifshitz 1969):

$$P = \frac{N}{\beta V}\left(1 + \frac{NB(\beta)}{V}\right), \tag{3.26}$$

where the gas has been assumed to consist of N particles, P is the pressure, and V is the volume occupied by the gas. The second virial coefficient can be evaluated as (Landau & Lifshitz 1969)

$$B(\beta) = \frac{1}{2}\int \left(1 - e^{-\beta U^{12}}\right) dV, \tag{3.27}$$

where U^{12} is the energy of interaction of the two particles and the integration is performed over the entire volume V. One can expect the phase transition to occur in the vicinity of the point where the isotherm exhibits singular behavior, i.e., where the derivative of the pressure with respect to the volume, obtained from the equation of state (3.26), vanishes. Differentiating (3.26) with respect to V yields for the value of the second virial coefficient corresponding to the phase transition temperature

$$B(\beta_{pt}) = -\frac{V}{4}. \tag{3.28}$$

The interaction energy U^{12} can be written as the sum of the potentials $\mathcal{U}_1$ and $\mathcal{U}_2$ from (3.22) and (3.23):

$$U^{12} = -\frac{1}{2\beta}\ln(\det \mathbf{M}) - \frac{\rho\tau}{2}\mathbf{e}_c \cdot \mathcal{M} \cdot \mathbf{e}_c.$$

Assume now that the collective motion of the bubbles takes place in the z-direction, i.e., that $\mathbf{e}_c = (0, 0, e_c)$. The evaluation of $\mathbf{e}_c \cdot \mathcal{M} \cdot \mathbf{e}_c$ together with the result (3.24)

for $\ln(\det \mathbf{M})$ yield (to the leading order in the small quantity a/r):

$$U^{12} = \frac{1}{\beta}\left(\ln 8 + \frac{9}{4}\left(\frac{a}{r}\right)^6\right) - \frac{\pi\rho {e_c}^2 a^3}{24}\left(2 - \frac{3}{2}\pi\left(\frac{a}{r}\right)^3\right).$$

The evaluation of the integral in (3.27) produces (again, we retain the leading order terms only),

$$B(\beta) = V\left(8\ln 8 - \frac{2}{3}\pi\beta\rho {e_c}^2 a^3\right),$$

and, from (3.28) we have the following estimate of the phase transition temperature,

$$\beta_{pt} = \frac{3(8\ln 8 + 1/4)}{2\pi\rho {e_c}^2 a^3}.$$

For the dimensionless phase transition temperature we thus obtain

$$\frac{T_{pt}}{\rho {e_c}^2 a^3} \approx 0.124. \tag{3.29}$$

In the next chapter, we shall test the validity of the above arguments by analyzing the results of numerical simulations of bubbles in a potential flow.

Chapter 4 Numerical Method and Results

To simulate the motion of bubbles in a suspension, we place at the origin a cell containing N bubbles, and periodiclly replicate the cell to fill all space (cf. Appendix). At the beginning of a simulation run, the bubbles are assigned initial positions and velocities. The equation of motion (2.9) is numerically integrated to produce the bubbles' trajectories, along with data on their velocities, accelerations, etc., so that we will be able to follow the total energy and impulse of the system—these quantities must be conserved at all times. As the simulation evolves in time, we expect the influence of the initial coordinates and velocities to diminish so that the resulting distribution will be determined solely by the nature of external and internal forces acting on the bubbles. In the course of a run, the bubbles' trajectories along with the effective kinetic and potential energies and other quantities of interest are computed. The stabilization of the effective energies signals equilibration, and all necessary statistics can then be computed.

4.1 Dynamics of a Collision of a Pair of Bubbles

We have already covered the derivation of the equation of motion. As far as its numerical integration is concerned, there are numerous codes and packages available, and we shall not discuss this aspect in detail. However, one issue still needs be resolved—that of a possible collision of a pair of bubbles. Here we follow Sangani & Didwania (1993*b*). In an inviscid flow bubbles can come arbitrarily close to each other. The viscous forces are small at large Reynolds numbers and therefore cannot prevent the bubbles from touching one another. Thus the bubbles can come in contact and the following two possibilities arise: they will either coalesce if the surface tension forces

are large compared to the inertia forces, *in the absence of surface-active impurities*, or, if the latter condition is not satisfied, as numerous experiments indicate, the bubbles will bounce away almost instantaneously. As reported by Kok (1993*b*), if the concentration of the impurities is not too high, the observed trajectories of the bubbles are in a very good agreement with those obtained theoretically using the potential flow approximation for the fluid velocity. On the other hand, if the concentration of impurities is moderate or high, wake formation affects the dynamics of the pair of bubbles, and the potential flow approximation will have to be modified to include wake effects.

When a pair of bubbles—labeled for convenience 1 and 2—undergoes a collision, the total impulse and kinetic energy of the liquid remain unchanged. Suppose that a very short range force comes into play when these two bubbles approach each other and that this force is directed along the separation vector $\mathbf{d}$ given by

$$\mathbf{d} = \frac{1}{2a}(\mathbf{r}_1 - \mathbf{r}_2).$$

We then may think that an equal and opposite impulse is applied to the two bubbles,

$$\frac{d\mathcal{I}}{dt} = F_c \delta(t - t_c)\mathbf{d},$$

for time t close to the collision time t_c. Here, F_c is the magnitude of the impulse. Integrating with respect to time in the immediate vicinity of t_c leads to a change in the impulse of bubble 1 during the collision process $\triangle\mathcal{I} = F_c\mathbf{d}$. The change in the impulse of bubble 2 is equal in magnitude and opposite in the direction to that of bubble 1, and the impulse change of all the other bubbles in the cell is zero. Thus the total impulse of the system is conserved and we need only calculate the change in the kinetic energy of the system.

The impulse due to the motion of bubble μ is

$$\mathbf{P}^{\mu} = \mathbf{M}^{\mu\nu} \cdot \mathbf{U}^{\nu},$$

and the total energy of the system can be written as

$$\mathcal{T} = \sum_{\mu} \mathcal{T}^{\mu} = \frac{1}{2}\rho\tau \sum_{\mu} \mathbf{U}^{\mu} \cdot \mathbf{P}^{\mu}.$$

We therefore require that the sum of $\mathcal{T}^{\mu}$ over all the bubbles does not change during the collision, i.e.,

$$\sum_{\mu} \triangle \mathcal{T}^{\mu} = 0. \tag{4.1}$$

During the collision, the velocities of the bubbles change linearly with the magnitude of the impulse F_c; thus,

$$\frac{2}{\rho\tau} \triangle \mathcal{T}^{\mu} = \triangle(\mathbf{U}^{\mu} \cdot \mathbf{P}^{\mu}) = F_c(\mathbf{U}^{\mu} \cdot \hat{\mathbf{P}}^{\mu} + \hat{\mathbf{U}}^{\mu} \cdot \mathbf{P}^{\mu}) + F_c^2(\hat{\mathbf{U}}^{\mu} \cdot \hat{\mathbf{P}}^{\mu}), \tag{4.2}$$

where $\hat{\mathbf{U}}^{\mu}$ is the change in the velocity of the bubble μ, and $\mathbf{U}^{\mu}$ is the velocity before the collision. The same convention applies to $\mathbf{P}^{\mu}$ and in particular we have

$$\hat{\mathbf{P}}^1 = -\hat{\mathbf{P}}^2 = \mathbf{d},$$

whereas for all $\mu > 2$, $\hat{\mathbf{P}}^{\mu} = 0$. Now, substituting (4.2) into (4.1) yields two values of F_c, one of which equals zero and corresponds to no collision, and the other corresponds to the magnitude of the total impulse during the collision

$$F_c = -\frac{\sum_{\mu}(\mathbf{U}^{\mu} \cdot \hat{\mathbf{P}}^{\mu} + \hat{\mathbf{U}}^{\mu} \cdot \mathbf{P}^{\mu})}{\sum_{\mu} \hat{\mathbf{U}}^{\mu} \cdot \hat{\mathbf{P}}^{\mu}}. \tag{4.3}$$

Thus, in dynamic simulations we first move the bubbles to the point where they collide and determine $\hat{\mathbf{U}}^{\mu}$ by solving for the velocity potential $\hat{\phi}$ given the impulses $\hat{\mathbf{P}}^{\mu}$ associated with each bubble. Substituting for $\hat{\mathbf{U}}^{\mu}$ in (4.3) allows us to determine F_c and hence the values of $\mathbf{P}^{\mu}$ and $\mathbf{U}^{\mu}$ for all the bubbles immediately after the collision.

The fact that generally the velocities of all the bubbles will change in the aftermath of the collision of just two bubbles can be explained as follows. The fluid and

the bubbles are assumed to be incompressible and thus the information about the collision is instantaneously transmitted to all the bubbles in the flow. (Physically, it is transmitted at the sound speed, which is infinite for the incompressible media.) Thus all bubbles will change their velocities in such a manner so that both the total impulse and the kinetic energy of the suspension will be conserved.

4.2 Bubbly Flow in the Absence of External Forces

To study configurations of inviscid, neutrally buoyant bubbles ($\mathbf{F}^g = \mathbf{F}^v = 0$) at different values of the bubble temperature, we conducted numerical experiments with 27 and 64 bubbles placed in a cubic unit cell at different values of the void fraction. The initial positions of the bubbles varied from closely packed clusters oriented normally to the z-direction (close to a minimum of the effective potential energy, as the collective motion in all experiments was also directed along the z-axis) to bubbles randomly distributed throughout the cell; the initial velocities—from purely collective motion, all with the same velocity, to completely random motion, with negligible resultant collective motion. As a result, the equilibrium temperatures in these experiments varied greatly. Figure 1 presents typical equilibrium configurations corresponding to different temperatures of 27 and 64 bubbles. At low temperatures the bubbles have very little kinetic energy and remain clustered as their configuration corresponds to a minimum of the effective potential energy (cf. Smereka 1993). The individual bubbles' motions are highly correlated and the added-mass coefficient is relatively large. As the temperature increases, the bubbles develop more chaotic motion until, at a certain point, the clusters disappear completely, the bubbles become randomly dispersed and, appropriately, the added-mass coefficient takes on values close to 1/2; after this point, there are no changes in the spatial arrangement of the bubbles. This point can be described as one where the transition between the clustered and random phases becomes complete.

In Figure 2 and Figure 3, we have plotted the added-mass coefficient C_M and the value of the pair-distribution function at 1.1 bubble diameters, $g(1.1)$, versus

the bubble temperature T for two different void fractions, $f = 0.014$ and $f = 0.11$. Both C_M and $g(1.1)$ can serve as measures of the relative degree of clustering of the bubbles: they increase as the bubbles collect themselves in clusters. The results in Figures 2 and 3 suggest that the transition between the clustered and random phases takes place in a temperature interval near $T \approx 5 \times 10^{-5}$ for $f = 0.014$ and near $T \approx 5 \times 10^{-4}$ for $f = 0.11$. Because we use a microcanonical ensemble in our simulations, coexistence of the two phases is observed in this temperature interval; it would thus be appropriately called a "two-phase" region. Also, because of the relatively small number of bubbles in the ensemble, we observe that the values of C_M and $g(1.1)$ are not unique when plotted against the temperature (cf. §11.3 of Allen & Tildesley 1987). Nevertheless, at very low values of the temperature, e.g., less than 10^{-6}, the bubbles are always close-packed in a flat cluster, while at high enough temperatures, $T > 10^{-2}$ say, they are always randomly distributed throughout space. These results are evidence for the existence of the two potentials (3.25) and (3.23). At low temperatures, the influence of the r^{-6} repulsive potential (3.25) is negligible and the bubbles form flat clusters due to the action of their collective potential given by (3.23). As the temperature grows, however, the repulsive potential gains more prominence and finally prohibits clustering of the bubbles (even though there is still significant collective motion).

It is interesting to see how well our earlier calculation of the transition temperature (3.29) compares with the results in Figures 2 and 3. In both cases, (3.29) seems substantially to overpredict the phase transition temperature, by a three (for $f = 0.11$) to four ($f = 0.014$) orders of magnitude. On the other hand, one has to keep in mind that (3.29) should be viewed as an estimate of the upper bound on the phase transition temperature since we only considered the second virial coefficient.

In another series of runs, conducted at three different values of the void fraction, the bubbles were initially randomly distributed in space and assigned random velocities so that the total momentum of the flow in the unit cell was small compared to the characteristic value of momentum associated with the motion of one bubble. This ensured that the bubbles did not have any appreciable collective motion during the

simulation; thus, their motion could be termed purely chaotic and it was hoped that there would be evidence of the r^{-6} repulsive potential that we discussed earlier.

We compare pair-distribution functions of bubbles without collective motion against those of hard spheres at three different void fractions: 0.014, 0.11, and 0.38 in Figure 4. At all values of the void fraction the hard-sphere pair-distribution function has a noticeable peak at contact. On the other hand, the bubble distribution either completely lacks such a peak, or, at the largest void fraction where the bubbles have little freedom of movement, the peak is lower in magnitude. These results confirm our earlier predictions that an effective repulsive potential governs the bubbles' behavior when there is little collective motion.

We conclude this section by commenting on the results of our attempt to apply a Monte Carlo procedure to compute the partition function (3.21) for our bubbly flow as a canonical ensemble. Unfortunately, these experiments proved prohibitively computer-expensive since we needed on the order of a million of bubble configurations, and the inversion of a $3N \times 3N$ matrix was required in order to compute the mass matrix for each configuration. When we gave the Monte Carlo routine the several thousand configurations that had been obtained from the molecular dynamics simulation, all but very few of these configurations were found suitable for a Monte Carlo calculation of Q, thus providing an indirect confirmation that the bubbly flow behaves as a thermodynamic system.

4.3 Bubbly Flow with Gravity and Viscous Drag

To study the influence of gravity (or, equivalently, buoyancy) as well as viscous dissipation on the structure and dynamics of a bubbly flow at high Re numbers, we used the following expressions for the forces on a single bubble μ:

$$\mathbf{F}^g = \rho\tau\mathbf{g}, \tag{4.4}$$

$$\mathbf{F}^v = 12\pi\eta a\mathbf{U}^\mu, \tag{4.5}$$

where η is the viscosity of the liquid. The viscous drag, as given by (4.5), is valid only as a leading order approximation (Smereka 1993). This approximation, however, will be sufficient for the purposes of the present discussion.[1]

First, we discuss the influence of buoyancy, in the absence of viscous dissipation. In our numerical simulations, we have always found the bubbles, regardless of their initial positions and velocities, to aggregate in flat clusters normal to the direction of gravity. Why this should be the case can be explained by examining the following situation. Consider two bubbles separated by a certain distance rising in a liquid under the influence of gravity. Such bubbles will be subjected to a force of mutual attraction; this force will grow in magnitude as the bubbles approach each other. Simultaneously, the velocity of the bubbles' rise will grow and this too will result in a larger value of the force of attraction. If the bubbles collide, they will not come as far apart as their initial separation, while their velocities collinear to the direction of gravity will grow larger, which in turn will result in an increasing attractive force, and so forth. Eventually the two bubbles will form a cluster with the line joining their centers directed normally to gravity. We can add here that Kok (1993*a*) has shown that a pair of bubbles rising under buoyancy will always rotate to be oriented in the cross-stream direction, regardless of the pair's initial orientation. This point further strengthens the applicability of the above argument to our problem.

Bubbles under the action of gravity can also be characterized in thermodynamic terms given in Chapter 3 of this thesis. As the bubbles accelerate in the direction of gravity, their collective velocity in this direction grows faster than the magnitude of their random motion and thus the temperature of the suspension decreases resulting in a phase transition from randomness to flat clusters of bubbles normal to gravity.

Finally, the combined effect of buoyancy and viscous dissipation will also be that of eventual clustering of the bubbles, regardless of their initial spatial arrangement and velocity distribution. Due to viscous dissipation, the initial velocities whose direction

[1]In general, viscous forces are obtainable from the Rayleigh dissipation function, $\mathbf{F}^v = -\partial F/\partial \dot{\mathbf{R}}$, where $F = \frac{1}{2}\dot{E}_v$, and $\dot{E}_v = 2\eta \int |\nabla\nabla\phi|^2 dV$ is the rate of energy dissipation for the inviscid flow. Equation (4.5) is the result for an isolated bubble.

will not coincide with that of gravity will decrease in magnitude until they become negligible. From that point on, all the bubbles will be moving in the direction of gravity with the same velocity that can be determined from the balance of viscous drag (4.5) and buoyancy (4.4). This motion will lead to the creation of flat clusters of bubbles normal to the direction of gravity. The corresponding numerical results have been found in agreement with the above discussion.

Thus, it can be concluded that buoyancy, acting on its own or in combination with viscous dissipation, leads to the formation of clusters of bubbles positioned broadside to the direction of gravity.

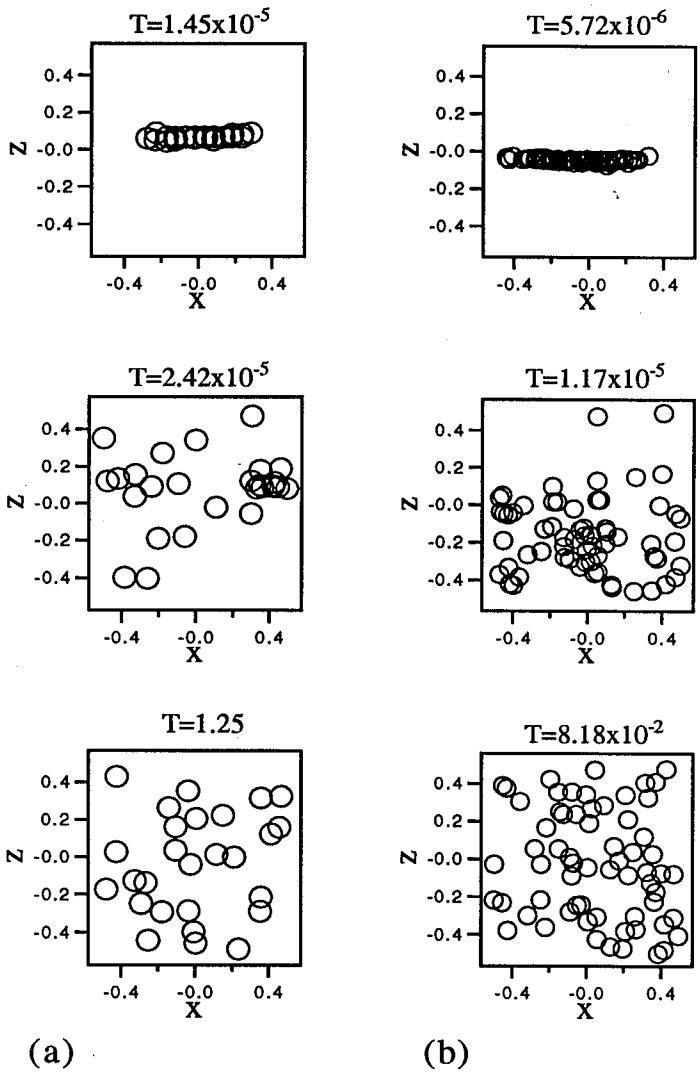

Figure 4.1: Representative configurations of 27 (a) and 64 (b) bubbles, at a void fraction of 0.014, projected onto the (x, z)-plane. As the temperature increases, the bubbles become less clustered.

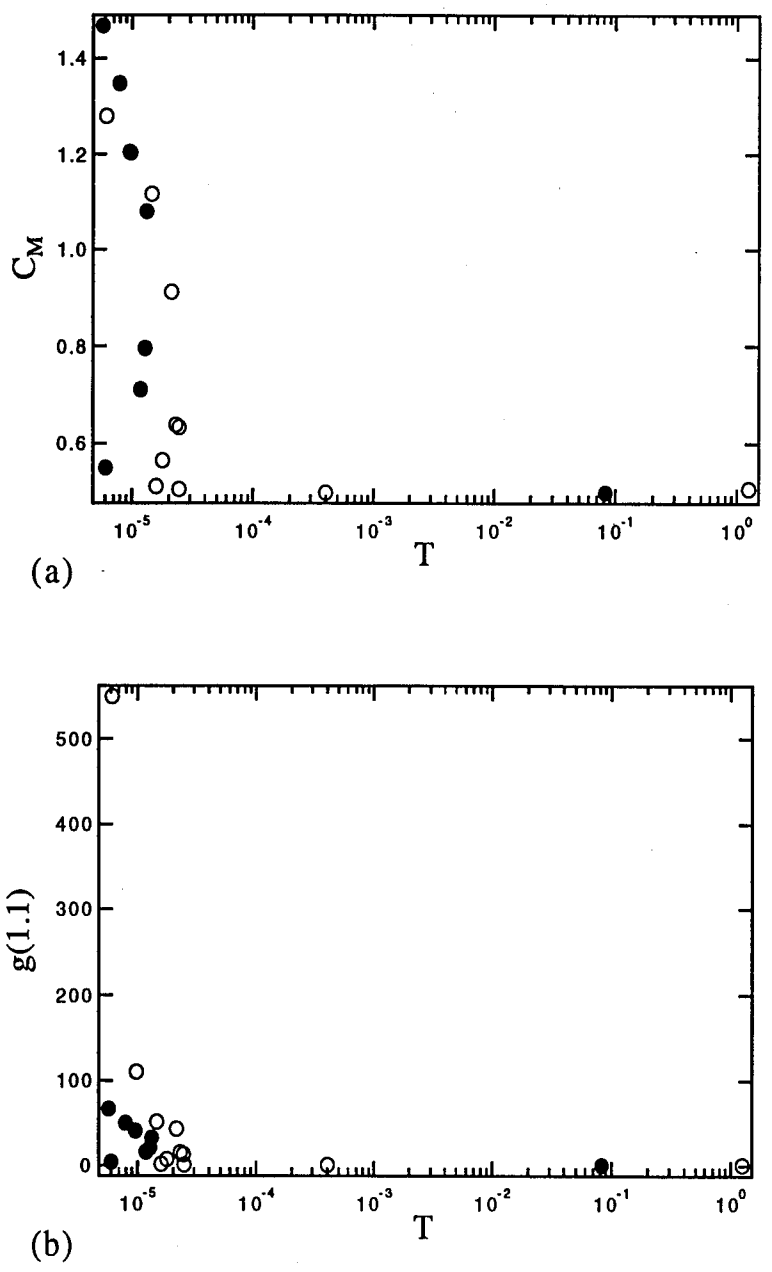

Figure 4.2: Added-mass coefficient (a) and $g(1.1)$ (b) vs. the bubble temperature as obtained in numerical runs with 27 (empty circles) and 64 bubbles (filled circles) at a void fraction of 0.014.

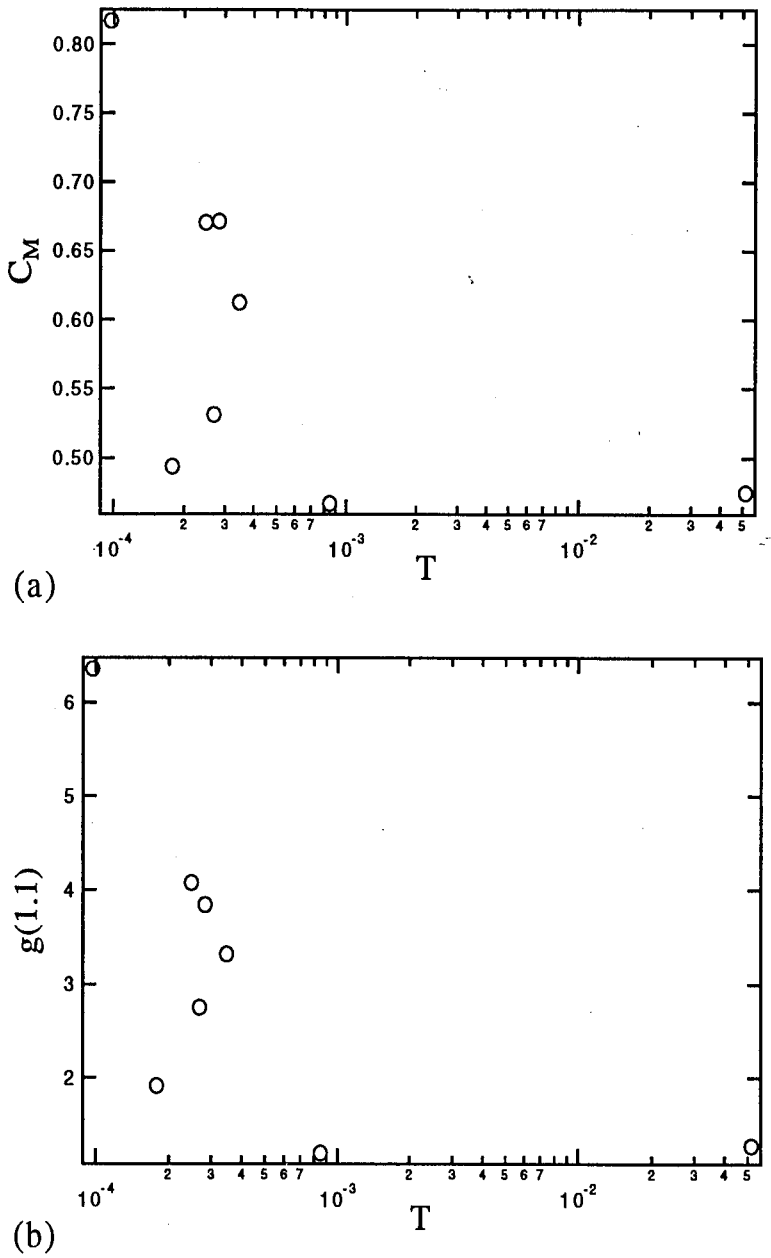

Figure 4.3: Added-mass coefficient (a) and $g(1.1)$ (b) vs. the bubble temperature for 27 bubbles at a void fraction of 0.11.

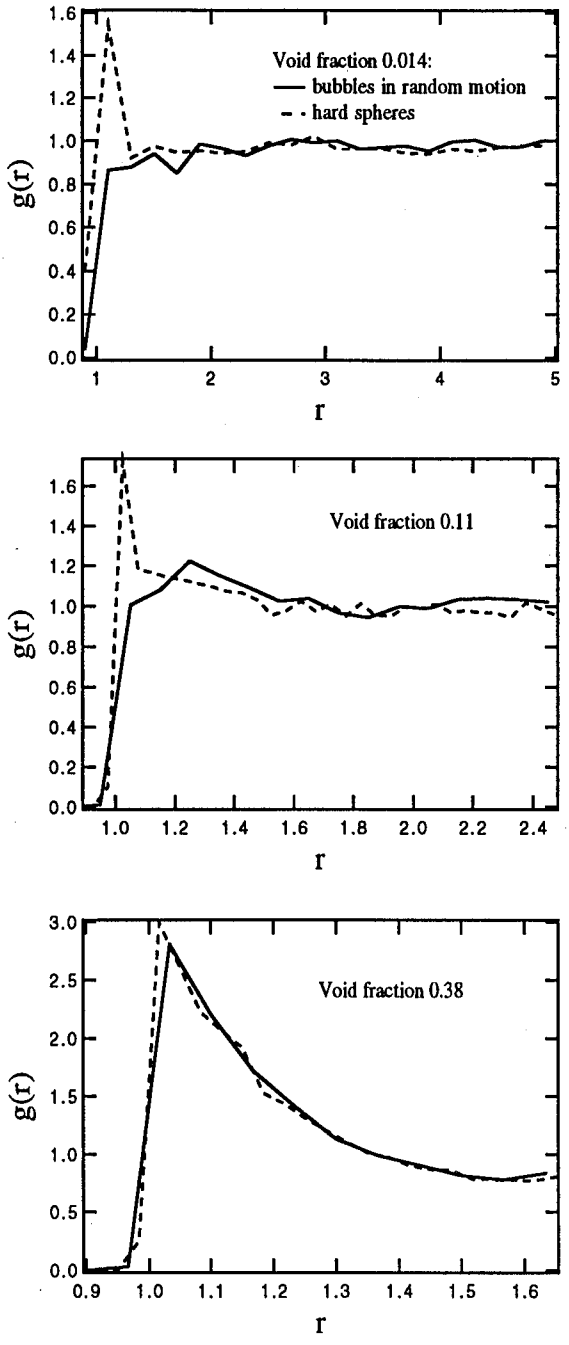

Figure 4.4: Pair-distribution functions: random bubbles vs. hard spheres. The bubbles exhibit repulsion resulting in the absence of a peak at contact.

Chapter 5 Conclusions

In this thesis, we have shown that bubbly liquids at high Reynolds numbers can be modeled as a gas of particles obeying the laws of statistical mechanics. The inviscid, massless, neutrally buoyant bubbles are approximated as dipoles in potential flow of an ideal fluid. The integrals of the bubbles' motion—the kinetic energy and the linear momentum of the flow—are derived. The second-rank tensor that arises in the derivation plays the role of an added, or virtual, mass of the flow; it accounts for the dynamical role of the fluid brought into motion by the bubbles. The expressions for the integrals of motion are similar to those of "classical" systems of material particles in that the energy is a quadratic (and Hamiltonian) and the impulse a linear form of the vector of the bubbles' velocities.

These similarities are useful in that they let us conduct further analysis along the lines of such traditional methods as statistical mechanics and molecular dynamics. Moreover, they provide a background for highlighting and analyzing the important physical features that distinguish a collection of bubbles in potential flow from material particles in vacuum. These features are:

(i) The virtual mass of the bubbly suspension depends on the bubbles' relative spatial arrangement.

(ii) The collective motion of the bubbles relatively to the otherwise undisturbed underlying liquid is coupled to the internal degrees of freedom.

Treating a collection of dipoles in potential flow as a canonical ensemble, we account for the above features by including in the partition function not only the system's Hamiltonian, but also its total impulse in the frame of reference in which the fluid would stay motionless were it not for the presence of the bubbles. Similarly, for non-spherical bubbles or particles in potential flow, one would need to explicitly include the total angular momentum in the integral for the partition function, thus

accounting for the influence of the total angular momentum on the internal degrees of freedom of the particles.

Having constructed the partition function, we proceed to treat the bubbly dispersion as an ensemble of particles interacting by means of additional effective thermodynamic potentials capturing the dynamics that distinguishes the bubbles from material particles in vacuum. In principle, the partition function is all that is needed to characterize fully the thermodynamic state of the ensemble. Though unable to compute the partition function for the bubbles with position-dependent mass, we can manipulate and analyze it such that conclusions can be made about the collective effects in the suspension.

In a fashion similar to that used in studying atomic systems, we define the temperature of the bubbly suspension as a measure of the bubbles' random motion. However, unlike classical systems, due to the position-dependent added mass of the bubbles, their random motion also results in a repulsive r^{-6} potential.

On the other hand, the collective motion of the bubbles, resulting in a non-zero total impulse of the suspension, also influences the bubbles' spatial arrangement because of its coupling to the internal degrees of freedom of the bubbles. By including the total impulse in the integral for the partition function, we are able to describe the action of the collective motion as that of another effective potential. The action of this potential results in the formation of flat clusters of bubbles oriented normally to the vector of the total impulse of the suspension.

Finally, in our thermodynamic treatment, by computing the second virial coefficient for the ensemble of bubbles, we estimate the temperature of the phase transition between the clustered and random phases.

The above theoretical results were verified by conducting molecular-dynamics-like simulations of bubbles as dipoles in potential flow.

This is the first instance we know of that has shown that a system of hydrodynamically interacting particles behaves as a thermodynamic system, obeying the same laws of classical statistical mechanics. This statistical mechanical approach may find use in modeling other hydrodynamic systems for which a Hamiltonian can be found.

Chapter 6 Appendix: Mass Matrix for a Bubbly Flow at High Reynolds Numbers

6.1 Derivation for a Finite Number of Bubbles

Following the method for solving Laplace's equation by Bonnecaze & Brady (1990, 1991) we write Laplace's equation (2.1) in its integral form,

$$\phi(\mathbf{x}) - \phi^E(\mathbf{x}) = \frac{1}{4\pi}\sum_{\nu}\int_{\partial\Omega^\nu}\left(\mathbf{F}\frac{1}{\lambda r} + \phi\nabla_y\frac{1}{r}\right)\cdot\mathbf{n}dS, \tag{6.1}$$

where $\phi(\mathbf{x})$ is the potential field at $\mathbf{x}$, $\phi^E(\mathbf{x})$ is the imposed or external potential field at $\mathbf{x}$ in the absence of any bubbles, $\mathbf{F}$ is the flux, defined as $\mathbf{F} = -\lambda\nabla_y\phi$, λ being the conductivity of the medium (equal to 1 in the fluid and 0 inside a bubble), and the integral is over the surface of the ν bubble. The distance $r = |\mathbf{x}-\mathbf{y}|$ and $\nabla_y = \partial/\partial(\mathbf{y}-\mathbf{x})$. The bubble moments are defined by

$$q^\nu \equiv \int_{\partial\Omega^\nu}\mathbf{F}\cdot\mathbf{n}dS, \tag{6.2}$$

$$\mathbf{S}^\nu \equiv \int_{\partial\Omega^\nu}(\mathbf{x}\mathbf{F} + \lambda\phi\mathbf{I})\cdot\mathbf{n}dS, \tag{6.3}$$

which are the charge (monopole) and dipole respectively, and where the position $\mathbf{x}$ in the moment definitions is defined relative to the center of the spherical bubble. Here and throughout, $\mathbf{I}$ is the usual notation for the identity matrix. Expanding the integral in (6.1) in terms of bubble moments yields,

$$\phi(\mathbf{x}) - \phi^E(\mathbf{x}) = \frac{1}{4\pi\lambda}\sum_{\nu}\left(q^\nu\frac{1}{r} + \mathbf{S}^\nu\cdot\nabla_y\frac{1}{r} + \ldots\right),$$

where the expansion has been truncated at the dipole level and the moment propagators $(1/r, \nabla_y 1/r, \ldots)$ are evaluated at $\mathbf{x} - \mathbf{R}^\nu$, where $\mathbf{R}^\nu$ is the center of bubble ν.

We can also act on the integral form of Laplace's equation (6.1) with $\nabla = \nabla_x$ to obtain

$$\nabla\phi(\mathbf{x}) - \nabla\phi^E(\mathbf{x}) = -\frac{1}{4\pi\lambda}\sum_\nu \left(q^\nu \nabla_y \frac{1}{r} + \mathbf{S}^\nu \cdot \nabla_y \nabla_y \frac{1}{r} + \ldots \right). \tag{6.4}$$

In our problem, $\mathbf{F} = -\mathbf{v}$, where $\mathbf{v}$ is the fluid velocity. The evaluation of the integrals in (6.2) and (6.3) yields

$$q^\nu = 0, \tag{6.5}$$

$$\mathbf{S}^\nu = \int_{\partial\Omega^\nu} \phi \mathbf{n} dS - \tau \mathbf{U}^\nu \tag{6.6}$$

Before going further, we need to address the issue of including multipoles of order higher than two. Accounting for the quadrupoles, octupoles, etc., will surely enhance the precision of the bubble dynamics simulations. However, as such a modification will inevitably result in a manifold slowing down of the speed of computer calculations, one must carefully consider whether the inclusion of higher order moments will affect the results significantly. The bubble problem is analogous to the effective conductivity problem with the bubbles having zero conductivity, and for this reason, as Bonnecaze & Brady (1990) have shown, the inclusion of multipoles of order higher than the dipole will lead to insignificant changes in the final results. In earlier work, we have considered the two-bubble problem, and arrived at the same conclusion. Having said that, we shall now truncate the expansion (6.4) at the dipole level, thus obtaining, with the help of (6.5) and (6.6),

$$\nabla\phi(\mathbf{x}) - \nabla\phi^E(\mathbf{x}) = -\frac{1}{4\pi}\sum_\nu \left(\int_{\partial\Omega^\nu} \phi \mathbf{n} dS - \tau \mathbf{U}^\nu \right) \cdot \nabla_y \nabla_y \frac{1}{r}. \tag{6.7}$$

Recalling equation (2.2) for the kinetic energy, we see that in order to calculate the kinetic energy of the bubbly flow, we shall need the integrals $\int_{\partial\Omega^\nu} \phi \mathbf{n} dS$. Applying

[1] The zero "charge" arises because we have assumed the bubbles to be of constant size. Non-zero charges would be obtained for bubbles of variable size (e.g., oscillating bubbles).

the divergence theorem and placing the origin at the center of the bubble, we find

$$\frac{1}{a}\int_{\partial\Omega^\nu}\phi\mathbf{x}dS=\int_{\partial\Omega^\nu}\phi\mathbf{n}dS=\int_{V_f}\nabla\phi dV.$$

To determine the above quantity, we derive a Faxén-type law, which relates the integral $\int_{\partial\Omega^\nu}\phi\mathbf{n}dS$ to the analogous integral $\int_{\partial\Omega^\nu}\phi'\mathbf{n}dS$ in the ν bubble's absence (the fact being denoted by the prime), known from the potential theory to be equal to $\tau\nabla_y\phi'(\mathbf{R}^\nu)$ (cf. Kellogg 1953), and the dipole of that bubble. As a first step, we rewrite (6.1) in the form appropriate for a point on the surface of the bubble,

$$\phi(\mathbf{x})-2\phi'(\mathbf{x})=\frac{1}{2\pi a}\int_{\partial\Omega^{\nu_y}}\left(\mathbf{F}\frac{1}{r}+\phi\frac{(\mathbf{x}-\mathbf{y})}{r^3}\right)\cdot\mathbf{y}dS_y.$$

Now multiply both sides of the above expression by $\mathbf{x}$ and integrate the product over the surface of the sphere with respect to the variable $\mathbf{x}$ to give

$$\int_{\partial\Omega^{\nu_x}}\mathbf{x}[\phi(\mathbf{x})-2\phi'(\mathbf{x})]dS_x=\frac{1}{2\pi a}\int_{\partial\Omega^{\nu_x}}\int_{\partial\Omega^{\nu_y}}\mathbf{x}\left[\left(\mathbf{F}\frac{1}{r}+\phi\frac{(\mathbf{x}-\mathbf{y})}{r^3}\right)\cdot\mathbf{y}\right]dS_ydS_x. \quad (6.8)$$

The evaluation of the right-hand side of (6.8) yields

$$\int_{\partial\Omega^{\nu_x}}\mathbf{x}[\phi(\mathbf{x})-2\phi'(\mathbf{x})]dS_x=-\frac{8}{9}\pi a^4\mathbf{U}-\frac{1}{3}\int_{\partial\Omega^{\nu_y}}\mathbf{y}\phi(\mathbf{y})dS_y,$$

or just

$$\frac{2}{3}\overline{\mathbf{x}\phi(\mathbf{x})}-\overline{\mathbf{x}\phi'(\mathbf{x})}=-\frac{a^2}{9}\mathbf{U}, \quad (6.9)$$

where

$$\overline{\mathbf{x}\phi(\mathbf{x})}=\frac{1}{4\pi a^2}\int_{\partial\Omega^{\nu_x}}\mathbf{x}\phi(\mathbf{x})dS_x.$$

We can now introduce the following quantity:

$$\overline{\nabla\phi(\mathbf{x})}=\frac{1}{\tau}\int_{V_f}\nabla\phi(\mathbf{x})dV,$$

and, by virtue of the divergence theorem,

$$\overline{\mathbf{x}\phi(\mathbf{x})} = \frac{a^2}{3}\overline{\nabla\phi(\mathbf{x})}.$$

Now (6.9) can be put in the form

$$\frac{2}{3}\overline{\nabla\phi(\mathbf{x})} - \overline{\nabla\phi'(\mathbf{x})} = -\frac{\mathbf{U}}{3}. \tag{6.10}$$

We remark here briefly that a Faxén-type relation, analogous to (6.10), holds for the quantity

$$\overline{\phi(\mathbf{x})} = \frac{1}{4\pi a^2}\int_{\partial\Omega^{\nu_x}} \phi(\mathbf{x})dS_x,$$

and it reads

$$\overline{\phi(\mathbf{x})} - \overline{\phi'(\mathbf{x})} = \frac{q}{4\pi a},$$

which, upon recalling the expression for the charge (6.5), reduces to the simple form

$$\overline{\phi(\mathbf{x})} - \overline{\phi'(\mathbf{x})} = 0.$$

For bubble μ, in the absence of the gradient of any external potential, i.e., when the fluid's motion is wholly due to the motion of the bubbles, using (6.7), we obtain

$$\nabla\phi'(\mathbf{R}^\mu) = -\frac{a^3}{3}\sum_{\nu\neq\mu}(\overline{\nabla\phi(\mathbf{R}^\nu)} - \mathbf{U}^\nu)\cdot\nabla_y\nabla_y\frac{1}{r_{\mu\nu}},$$

where $r_{\mu\nu} = |\mathbf{R}^\mu - \mathbf{R}^\nu|$. Combining the above result with the Faxén law (6.9) and recalling that $\overline{\nabla\phi'(\mathbf{x})} = \nabla\phi'(\mathbf{x})$ (cf. Kellog 1953), we have

$$\overline{\nabla\phi(\mathbf{R}^\mu)} = -\frac{\mathbf{U}^\mu}{2} - \frac{a^3}{2}\sum_{\nu\neq\mu}(\overline{\nabla\phi(\mathbf{R}^\nu)} - \mathbf{U}^\nu)\cdot\nabla_y\nabla_y\frac{1}{r_{\mu\nu}}. \tag{6.11}$$

Now we find it convenient to put (6.11) in matrix form,

$$\overline{\nabla\phi(\mathbf{R})} = \mathbf{M}_1\cdot\overline{\nabla\phi(\mathbf{R})} + \mathbf{M}_2\cdot\mathbf{U},$$

where $\overline{\nabla\phi(\mathbf{R})}$ and $\mathbf{U}$ are vectors defined as

$$\overline{\nabla\phi(\mathbf{R})} = [\overline{\nabla\phi(\mathbf{R}^1)}, \overline{\nabla\phi(\mathbf{R}^2)}, \ldots, \overline{\nabla\phi(\mathbf{R}^N)}]^T$$

and

$$\mathbf{U} = [\mathbf{U}^1, \mathbf{U}^2, \ldots, \mathbf{U}^N]^T,$$

whereas $\mathbf{M}_1$ and $\mathbf{M}_2$ are matrices of the following form,

$$\mathbf{M}_1 = -\frac{a^3}{2}\begin{pmatrix} 0 & \nabla_y\nabla_y r_{12}^{-1} & \nabla_y\nabla_y r_{13}^{-1} & \ldots & \nabla_y\nabla_y r_{1N}^{-1} \\ \nabla_y\nabla_y r_{21}^{-1} & 0 & \nabla_y\nabla_y r_{23}^{-1} & \ldots & \nabla_y\nabla_y r_{2N}^{-1} \\ \ldots & \ldots & \ldots & \ldots & \ldots \\ \nabla_y\nabla_y r_{N1}^{-1} & \nabla_y\nabla_y r_{N2}^{-1} & \nabla_y\nabla_y r_{N3}^{-1} & \ldots & 0 \end{pmatrix}, \quad (6.12)$$

$$\mathbf{M}_2 = -\frac{a^3}{2}\begin{pmatrix} a^{-3}\mathbf{I} & -\nabla_y\nabla_y r_{12}^{-1} & -\nabla_y\nabla_y r_{13}^{-1} & \ldots & -\nabla_y\nabla_y r_{1N}^{-1} \\ -\nabla_y\nabla_y r_{21}^{-1} & a^{-3}\mathbf{I} & -\nabla_y\nabla_y r_{23}^{-1} & \ldots & -\nabla_y\nabla_y r_{2N}^{-1} \\ \ldots & \ldots & \ldots & \ldots & \ldots \\ -\nabla_y\nabla_y r_{N1}^{-1} & -\nabla_y\nabla_y r_{N2}^{-1} & -\nabla_y\nabla_y r_{N3}^{-1} & \ldots & a^{-3}\mathbf{I} \end{pmatrix} \quad (6.13)$$

We are now in a position to deduce a formula that will establish a direct relation between the vectors $\overline{\nabla\phi(\mathbf{R})}$ and $\mathbf{U}$,

$$\overline{\nabla\phi(\mathbf{R})} = (\mathbf{I} - \mathbf{M}_1)^{-1} \cdot \mathbf{M}_2 \cdot \mathbf{U}.$$

We shall define as the *mass matrix* the following matrix of tensors,

$$\mathbf{M} \equiv -(\mathbf{I} - \mathbf{M}_1)^{-1} \cdot \mathbf{M}_2.$$

The reason why it is appropriate for the matrix $\mathbf{M}$ to be called mass matrix will become clear in the course of the following argument. Once again, recall the expression (2.2) for the total kinetic energy of the fluid in our problem together with the relation

$$\sum_\nu \mathbf{U}^\nu \cdot \int_{\partial\Omega^\nu} \phi \mathbf{n}^\nu dS = \tau \mathbf{U} \cdot \overline{\nabla\phi} = -\tau \mathbf{U} \cdot \mathbf{M} \cdot \mathbf{U}.$$

Then the expression for the total kinetic energy can be rewritten as

$$\mathcal{T} = \frac{1}{2}\rho\tau \mathbf{U} \cdot \mathbf{M} \cdot \mathbf{U}, \tag{6.14}$$

and it is now obvious that, indeed, the matrix $\mathbf{M}$ plays here the role of virtual, or added mass of the entire system, normalized by a factor of $\rho\tau$.

6.2 Extension to Infinite Systems

To model the infinite medium, we apply periodic boundary conditions to a cell of volume V_c containing N particles. We are no longer in a position to argue that the velocity at infinity is zero. Rather, the whole medium is now set into motion, i.e., there is a bulk flow; the kinetic energy (per unit cell) of this flow is

$$\mathcal{T}_{bf} = \frac{\mathbf{P}_t \cdot \mathbf{P}_t}{2\rho V_c(1-f)},$$

and there is a corresponding velocity,

$$\mathbf{U}_{bf} = \frac{\mathbf{P}_t}{\rho V_c(1-f)},$$

where f is the void fraction.

Returning to the potential flow problem, the bulk flow corresponds to a continuous

dipole distribution throughout the medium. We must account for this distribution in our derivation of an expression for the gradient of the potential. Bonnecaze & Brady (1990) have addressed this problem; proceeding along the lines of §§4 and 5 of their paper, we rewrite the equation for the potential gradient in a form similar to (6.4), recalling the expression for the charge (6.5) and accounting for an infinite number of bubbles (cf. equation (35), Bonnecaze & Brady 1990),

$$\nabla\phi(\mathbf{x}) - \nabla\phi^E(\mathbf{x}) = -\frac{n\langle\mathbf{S}\rangle}{3} - \frac{1}{4\pi}\sum_{\nu}\mathbf{S}^{\nu}\cdot\nabla_y\nabla_y\frac{1}{r} + \frac{1}{4\pi}\int_{V-V_\epsilon} n\langle\mathbf{S}\rangle\cdot\nabla_y\nabla_y\frac{1}{r}dV,$$

where $n\langle\mathbf{S}\rangle$ is the average particle dipole density, related to the motion of the entire liquid as a whole, V is the volume enclosed by S^∞, a distant boundary surface, which surrounds $\mathbf{x}$, and V_ϵ is the volume of a sphere of radius ϵ surrounding $\mathbf{x}$.

The cell is periodically replicated to fill all space; the sums over the infinite particles are replaced by double sums over the N particles in the lth cell of the system and over all the replicated cells. To make the resulting double sums converge rapidly, we use the Ewald summation expression (A 2.4) from Bonnecaze & Brady (1990),

$$\begin{aligned}\frac{n\langle\mathbf{S}\rangle}{3} &+ \frac{1}{4\pi}\sum_{\nu}\mathbf{S}^{\nu}\cdot\nabla_y\nabla_y\frac{1}{r} - \frac{1}{4\pi}\int_{V-V_\epsilon} n\langle\mathbf{S}\rangle\cdot\nabla_y\nabla_y\frac{1}{r}dV \\ &= \frac{\mathbf{S}^{\mu_0}}{4\pi}\frac{40}{3}\xi^3\pi^{-\frac{1}{2}} + \frac{1}{4\pi}\sum_{l}\sum_{\substack{\nu \\ \nu_l\neq\mu_0}}\mathbf{S}^{\nu_l}\cdot\boldsymbol{\Delta}^{(r)} \\ &+ \frac{1}{4\pi}\frac{1}{V_c}\sum_{\substack{k \\ k\neq 0}}\sum_{\nu}\mathbf{S}^{\nu_l}\cdot\boldsymbol{\Delta}^{(k)},\end{aligned}$$

where

$$\begin{aligned}\boldsymbol{\Delta}^{(r)} &= \left[\left(8\xi^7r^4 - 36\xi^5r^2 + 16\xi^3 + 4\xi r^{-2}\right)\frac{e^{-\xi^2r^2}}{\sqrt{\pi}} + \frac{2\mathrm{erfc}(\xi r)}{r^3}\right] \\ &\times \frac{(\mathbf{R}^{\mu_0} - \mathbf{R}^{\nu_l})(\mathbf{R}^{\mu_0} - \mathbf{R}^{\nu_l})}{r^2} \\ &+ \left[\left(4\xi^5r^3 - 12\xi^3r + 2\xi r^{-1}\right)\frac{e^{-\xi^2r^2}}{\sqrt{\pi}} + \frac{\mathrm{erfc}(\xi r)}{r^2}\right]\end{aligned}$$

$$\times \left[\frac{(\mathbf{R}^{\mu_0} - \mathbf{R}^{\nu_l})(\mathbf{R}^{\mu_0} - \mathbf{R}^{\nu_l})}{r^3} - \frac{\mathbf{I}}{r}\right],$$

$$\boldsymbol{\Delta}^{(k)} = \frac{4\pi}{k^2}\left[1 + \frac{1}{4}\left(\frac{k}{\xi}\right)^2 + \frac{1}{8}\left(\frac{k}{\xi}\right)^4\right] e^{-k^2/4\xi^2} \cos[\mathbf{k}\cdot(\mathbf{R}^{\mu} - \mathbf{R}^{\nu})]\mathbf{kk}.$$

In the expressions above, l is the cell index number, ν is the particle index number, $\mathbf{R}^{\mu_0}$ is the position of the particle μ in the zeroth cell, $\mathbf{R}^{\nu_l}$ is the position of the particle ν in the lth cell, $\mathbf{k}$ is the periodic cell reciprocal or wave vector, k is its magnitude, $r = |\mathbf{R}^{\mu_0} - \mathbf{R}^{\nu_l}|$, and $\mathbf{R}^{\mu} - \mathbf{R}^{\nu}$ is the position vector difference between bubbles μ and ν within a cell. The arbitrary number ξ regulates the speed of convergence for the sums and is typically chosen to be $1/V_c^{\frac{1}{3}}$. Each sum converges exponentially fast.

It is now straightforward to rewrite matrices $\mathbf{M}_1$ and $\mathbf{M}_2$ of (6.12) and (6.13) in terms of the Ewald sums. All of the analysis of the previous subsection will apply to the case of an infinite number of bubbles, except the total kinetic energy as given by (6.14) should now be thought of as that of an elementary cell rather than all fluid (the same obviously applies to the total momentum as given by (2.6)).

References

Allen, M. P. and Tildesley, D.J. 1987 *Computer Simulation of Liquids.* Clarendon.

Banerjee, S. and Chan, A. M. C. 1980 Separated flow model I. Analysis of the averaged and local instantaneous formulations. *Int. J. Multiphase Flow* **6**, 1.

Batchelor, G. K. 1967 *An Introduction to Fluid Dynamics.* Cambridge University Press.

Batchelor, G. K. 1976 Developments in microhydrodynamics. In *Theoretical and Applied Mechanics* (ed. W. Koiter), p. 33. North Holland.

Biesheuvel, A. and Gorissen, W. C. M. 1990 Void fraction disturbances in a uniform bubbly liquid. *Int. J. Multiphase Flow* **16**, 211.

Biesheuvel, A. and Wijngaarden, L. van 1984 Two-phase flow equations for a dilute dispersion of gas bubbles in liquid. *J. Fluid Mech.* **148**, 301.

Bonnecaze, R. T. and Brady, J. F. 1990 A method for determining the effective conductivity of dispersions of particles. *Proc. R. Soc. Lond.* A **430**, 285.

Bonnecaze, R. T. and Brady, J. F. 1991 The effective conductivity of random suspensions of spherical particles. *Proc. R. Soc. Lond.* A **432**, 445.

Delhaye, J. M. and Achard J. L. 1976 On the averaging operators introduced in two-phase flow modeling. In *Proc. 1st OECD/NEA Specialist Mtg on Transient Two-Phase Flow*, vol. 1, p. 5. Toronto.

Drew, D. A. 1983 Mathematical modeling of two-phase flow. *Ann. Rev. Fluid Mech.* **15**, 261.

Geurst, J. A. 1985 Virtual mass in two-phase bubbly flow. *Physica* A **129**, 233.

Geurst, J. A. 1986 Variational principles and two-fluid hydrodynamics of bubbly liquid/gas mixtures. *Physica* A **135**, 455.

Hill, T. L. 1956 *Statistical Mechanics.* McGraw–Hill (Dover edition 1987).

Hinch, E. J. 1977 An averaged-equation approach to particle interactions in a fluid suspension. *J. Fluid Mech.* **83**, 695.

Hinch, E. J. and Nitsche, L. C. 1993 Nonlinear drift interactions between fluctuating colloidal particles: oscillatory and stochastic motions. *J. Fluid Mech.* **256**, 343.

Kellogg, O. D. 1953 *Foundations of Potential Theory.* Dover.

Kok, J. B. W. 1993*a* Dynamics of gas bubbles moving through liquid. Part I. Theory. *Eur. J. Mech. B Fluids* **12**, No. 4, 515.

Kok, J. B. W. 1993*b* Dynamics of gas bubbles moving through liquid. Part II. Experiment. *Eur. J. Mech. B Fluids* **12**, No. 4, 541.

Lamb, H. 1932 *Hydrodynamics*, 6th edn. Cambridge University Press (Dover edition 1945).

Landau, L. D. and Lifshitz, E. M. 1969 *Statistical Physics.* Pergamon.

Moore, D. W. 1963 The boundary layer on a spherical gas bubble. *J. Fluid Mech.* **16**, 161.

Moore, D. W. 1965 The velocity of rise of distorted gas bubbles in a liquid of small viscosity. *J. Fluid Mech.* **23**, 749.

Pauchon, C. and Banerjee, S. 1986 Interphase momentum interaction effects in the averaged multifield model. Part I: Void propagation in bubbly flows. *Int. J. Multiphase Flow* **12**, 559.

Pauchon, C. and Smereka, P. 1992 Momentum interactions in dispersed flow: an averaging and a variational approach. *Int. J. Multiphase Flow* **18(1)**, 65.

Sangani, A. S. and Didwania, A. K. 1993*a* Dispersed phase stress tensor in flows of bubbly liquids at large Reynolds numbers. *J. Fluid Mech.* **248**, 27.

Sangani, A. S. and Didwania, A. K. 1993*b* Dynamic simulations of flows of bubbly liquids at large Reynolds numbers. *J. Fluid Mech.* **250**, 307.

Smereka, P. 1993 On the motion of bubbles in a periodic box. *J. Fluid Mech.* **254**, 79.

Voinov, A. V. and Petrov, A. G. 1977 On the stress tensor in a fluid containing dispersed particles. *J. Appl. Math. Mech.* **41**, 368.

Wijngaarden, L. van and Kapteyn, C. 1990 Concentration waves in dilute bubble/liquid mixtures. *J. Fluid Mech.* **212**, 111.

Part II

Behavior of Sheared Suspensions of Non-Brownian Particles

Chapter 7 Introduction

Suspensions of non-Brownian particles (usually, 10 μm and larger in size, with negligible Brownian motion) in a Newtonian fluid undergoing Stokes flow are very common in nature and in many important industrial processes; clays, coal and cement slurries, and drilling muds are some of the more immediate examples. The detailed knowledge of the patterns of macroscopic behavior of such suspensions is necessary for the improvement of the existing technologies, as well as for the development of new processes and applications.

Non-Brownian particles suspended in fluid flow interact through hydrodynamic and interparticle forces; it is the relative importance of these forces that determines the structure and properties of the flow. Over the last years significant research effort has focused on the non-Newtonian rheological behavior (finite normal stress differences and a particle phase contribution to the isotropic stress) that these systems are known to exhibit. Gadala-Maria (1979) reported normal stress differences scaling roughly as $\eta\dot{\gamma}$, where η is the viscosity of the solvent and $\dot{\gamma}$ the shear rate, for a suspension of polystyrene spheres in water undergoing simple shear motion at vanishing Reynolds number. Phung (1993) calculated finite normal stress differences scaling as $\eta\dot{\gamma}$ in his Stokesian Dynamics simulations of sheared colloidal suspensions at high (10^6) values of the Péclet number, defined as the ratio of shear to Brownian forces, $Pe = \dot{\gamma}a^2/2D$, where a is the particle radius and D is the diffusivity of an isolated particle.

Net migration of particles in inhomogeneous stress or shear fields (e.g., those occuring in flows in tubes or channels) along with its influence on the suspension rheology have been observed in experimental studies. Among such studies, Leighton & Acrivos (1987) and Abbott *et al.* (1991) observed the movement of particles away from regions of high to low shear in Couette devices, while Gadala-Maria & Acrivos (1980) observed the steady decrease of the viscosity of a concentrated suspension due

to the migration. Nott & Brady (1994) carried out Stokesian Dynamics simulations of the pressure-driven flow of a non-Brownian suspension in a channel and reported the migration of particles towards the center of the channel, where the shear rate is lower. Theoretical models for this migration phenomenon have been put forward by Leighton & Acrivos (1987b) and Nott & Brady (1994). The former authors proposed a diffusion equation for particles, to be solved in conjunction with the continuity and momentum equations for the entire suspension. Nott & Brady developed a model in which macroscopic mass, momentum, and energy balances are constructed and solved simultaneously, for the particle phase and for the entire suspension. They showed how the diffusive flux model of Leighton & Acrivos is contained within their model; moreover, by introducing the notions of the suspension pressure and temperature as measure of the particle fluctuational motion (thus making the description of the suspension nonlocal), the suspension balance model of Nott & Brady was proven successful where the diffusive flux model failed, viz. in explaining the lack of migration in torsional flow, observed in the experiments of Chow *et al.* (1994), and the absence of close-packing of particles in the regions of zero shear rate. The results of the suspension balance model for channel flow have been found in good agreement with Stokesian Dynamics simulations.

Investigating hydrodynamic diffusion of non-Brownian particles is another active area of research (cf. Davis (1996) and references therein). Hydrodynamic diffusion refers to the fluctuating motion of particles in a dispersion, which occurs due to particle interactions. Eckstein, Bailey & Shapiro (1977), Leighton & Acrivos (1987), and Phan & Leighton (1996) have experimentally obtained long-time self-diffusion coefficients for sheared suspensions of non-Brownian particles. Phung (1993) computed finite long-time self-diffusivities for suspensions of hard spheres at $Pe \gg 1$.

Phung's findings of finite normal stress differences and long-time self-diffusivities were initially considered surprising in that at high Pe there did not appear signs of a transition to the pure hydrodynamic limit, $Pe^{-1} = 0$, when the normal stress differences and particle pressure must vanish owing to the reversibility of Stokes flow.

Brady & Morris (1997) have demonstrated how the non-Newtonian rheology of

strongly-sheared suspensions is related to the fore-aft microstructural asymmetry (determined analytically in their paper and observed by Parsi & Gadala-Maria (1987) experimentally and by Phung (1993) in simulations) due to weak Brownian motion combined with an interparticle force of hard-sphere type maintaining particles at a minimum separation of $2b$, with $b > a$. Brady & Morris have investigated the thin $O(aPe^{-1})$ boundary layer at particle contact in which the effects of Brownian diffusion and advection balance while the interparticle force results in an asymmetric pair-distribution function with an $O(Pe)$ contact value. Normal stress differences of $O(\eta\dot{\gamma}\phi^2)$ and a shear-induced self-diffusivity of $O(\dot{\gamma}a^2\phi)$ as $Pe \to \infty$ thus result. Brady & Morris expect the conclusions of their work to apply to suspensions of particles interacting via a force of an extended (but short) range even in the absence of Brownian motion.

It is the purpose of this work to report on a study of the structure, rheology, diffusion, and the fluctuational (i.e., relative to the bulk) particle motion of sheared monodisperse suspensions of non-Brownian particles interacting by means of a pairwise short-ranged repulsive interparticle force. For a given type of particle interaction, the system is described by two parameters, the particle phase volume fraction ϕ and the ratio of the shear to the interparticle force, denoted $\dot{\gamma}^*$.

At low values of the volume fraction ($0 < \phi < 0.25$), suspended particles stay well-separated for most of the time of a simulation, encountering their neighbors only infrequently. The interparticle force does not influence the structure nor the macroscopic properties to any significant extent as we see little variation with $\dot{\gamma}^*$ of the shear viscosity, normal stress differences, etc. Nor, to any appreciable extent, is the motion of the particles observed to display a diffusive; the particles simply follow the streamlines of the bulk shear motion, with little random walk present, due of the rarity of important collisions of pairs of particless. Accordingly, the values of the long-time self-diffusion coefficients remain very low and difficult to determine in a molecular-dynamics-like simulation. At higher volume fractions, however, particle collisions become much more common. The values of the macroscopic properties rapidly increase; in the absence of interparticle force, at high values of ϕ, particles

captured by strong lubrication forces would eventually form cell-spanning clusters leading to an infinitely large shear viscosity. The repulsive interparticle force, however, works to limit the growth of clusters. Moreover, as ϕ continues to increase, the interparticle force eventually leads to the particles' ordering in flowing strings accompanied by a decrease in the shear viscosity, self-diffusivites, and other properties. The particle volume fraction at which this transition occurs, the extent of the transition, and the influence it exerts on the properties all depend on $\dot{\gamma}^*$. For a higher value of $\dot{\gamma}^*$, the transition to hexagonally packed strings occurs at a higher value of ϕ. In a pattern reminiscent of Phung's simulations, we calculate finite non-Newtonian rheological properties and long-time self-diffusivities even at the highest simulated shear rate, $\dot{\gamma}^* = 10^4$.

The microstructure of the simulated suspensions is investigated with the help of the pair-distribution function, $g(\mathbf{r})$. An examination of the radial and angular dependence of $g(\mathbf{r})$ establishes the connection between changes in microstructure and macroscopic suspension properties, such as rheology and self-diffusivity.

An important aspect of this work is that it presents for the first time, in addition to the other rheological quantities such as the shear viscosity and normal stress differences, the results of a calculation of the osmotic, or suspension, pressure defined as negative one-third of the trace of the suspension bulk stress tensor. The significance of the suspension pressure has been demonstrated only recently by Nott & Brady (1994). Together with the normal stress differences, the pressure is used in their suspension balance model in the momentum balance in the directions perpendicular to the mean motion, to explain net migration of particles, or lack thereof. A calculation of the suspension pressure as part of a dynamic simulation became possible only recently, after Jeffrey, Morris & Brady (1993) determined the hydrodynamic functions necessary for the computation of the elements of the trace of the bulk stress tensor. For the osmotic pressure as well as for the other rheological quantities, we tabulate and plot its total value as well as the separate contributions to it from hydrodynamic interactions and the interparticle force, for the entire range of simulated values of $\dot{\gamma}^*$ and ϕ.

Chapter 8 Outline of the Simulation Method

8.1 Stokesian Dynamics of Non-Brownian Suspensions

In this section we follow the relevant discussions in Phung, Brady & Bossis (1996) and Phung (1993) and present only a brief description of the Stokesian Dynamics method used in our simulations. A more detailed treatment is available elsewhere in the literature (Brady & Bossis 1985, 1988; Bossis & Brady 1984, 1987, 1989). We will be investigating a suspension of N rigid spherical particles, all of the same radius a, in an incompressible Newtonian fluid of viscosity η and density ρ. The motion of the fluid is governed by the Navier-Stokes equation, while the particle motion is described by the N-body Langevin equation:

$$\mathbf{m} \cdot \frac{d\mathbf{U}}{dt} = \mathbf{F}^H + \mathbf{F}^P + \mathbf{F}^B, \tag{8.1}$$

where $\mathbf{m}$ is the generalized mass/moment-of-inertia matrix of dimension $6N \times 6N$, $\mathbf{U}$ is the the vector of the particles' translational/rotational velocity of dimension $6N$, and $\mathbf{F}^H$, $\mathbf{F}^P$, and $\mathbf{F}^B$ are the force/torque vectors, all of dimension $6N$. $\mathbf{F}^H$ is the hydrodynamic force/torque exerted by the fluid on the particles, $\mathbf{F}^P$ represents the deterministic non-hydrodynamic forces, interparticle and external, and $\mathbf{F}^B$ is the stochastic force that gives rise to Brownian motion.

In this work, we will be concerned with suspensions of non-Brownian particles in Stokes flow; this means that both the inertia term and the Brownian force term in the Langevin equation (8.1) can be set equal to zero. Thus, appropriately simplified,

(8.1) becomes

$$\mathbf{F}^H + \mathbf{F}^P = 0. \tag{8.2}$$

The hydrodynamic force on the particles in a suspension undergoing bulk linear shear flow is

$$\mathbf{F}^H = -\mathbf{R}_{FU} \cdot (\mathbf{U} - \langle \mathbf{U} \rangle) + \mathbf{R}_{FE} : \langle \mathbf{E} \rangle, \tag{8.3}$$

where $\langle \mathbf{U} \rangle$ is the velocity of the bulk shear flow (imposed at infinity) evaluated at the particle center, $\langle \mathbf{E} \rangle$ is the symmetric part of the gradient of the imposed shear flow (the bulk shear rate is given by $\dot{\gamma} = |\langle \mathbf{E} \rangle|$), and $\mathbf{R}_{FU}(\mathbf{x})$ and $\mathbf{R}_{FE}(\mathbf{x})$ are the configuration-dependent resistance tensors, independent of the flow field. The generalized configuration vector $\mathbf{x}$ specifies the location and orientation of all the particles.

In general, the non-hydrodynamic force $\mathbf{F}^P$ may be of any form, interparticle or external. In this work we will exclusively study the effects of the pairwise-repulsive, along the line of centers, force of the following form:

$$\mathbf{F}^P_{\alpha\beta} = \mathbf{F}^P_0 \frac{\tau e^{-\tau s}}{1 - e^{-\tau s}}, \tag{8.4}$$

where α and β denote the particles in a pair, $s = (|\mathbf{x}_\alpha - \mathbf{x}_\beta| - 2a)/a$ is the dimensionless separation between particle surfaces, $|\mathbf{F}^P_0|$ is the force magnitude, and τ is a variable parameter setting the range of the force. This form of the interparticle force corresponds to charged particles interacting in an ionic salt solution through Derjaguin-Landau-Verwey-Overbeek-type forces at constant surface charge. As given by (8.4), the interparticle force varies as $1/s$ as $s \to 0$ and decays to $O(10^{-2}|\mathbf{F}^P_0|\tau)$ when $s \sim O(4.5\tau^{-1})$. All of the simulation runs presented in this study were conducted using $\tau = 1000$; this value of τ roughly corresponds to polystyrene spherical particles of $O(10\ \mu\text{m})$ in size suspended in 50 percent glycerol-water mixture containing 10^{-3} M KCl. However, for our purposes, these specific details are unimportant as we expect the conclusions of our work to apply to all suspensions of particles interacting by means of a short-range repulsive force.

The evolution equation for the particles is obtained by integrating (8.2) over a time

step Δt that is small compared with the time over which the configuration changes. A second integration in time produces the evolution equation for the particle positions with error of $O(\Delta t^2)$:

$$\Delta \mathbf{x} = \{\langle \mathbf{U} \rangle + \mathbf{R}_{FU}^{-1} \cdot [\mathbf{R}_{FE} : \langle \mathbf{E} \rangle + \mathbf{F}^P]\} \Delta t, \tag{8.5}$$

where $\Delta \mathbf{x}$ is the change in particle position during the time step Δt.

Non-dimensionalizing $\mathbf{x}$ by the characteristic particle size a; the time by the convective time scale given by $\dot{\gamma}^{-1}$; the shear force by $6\pi\eta a^2\dot{\gamma}$; the interparticle forces by their magnitude $|\mathbf{F}_0^P|$; the hydrodynamic resistance tensors $\mathbf{R}_{FU}$ by $6\pi\eta a$ and $\mathbf{R}_{FE}$ by $6\pi\eta a^2$, the evolution equation (8.5) becomes:

$$\Delta \mathbf{x} = \{\langle \mathbf{U} \rangle + \mathbf{R}_{FU}^{-1} \cdot [\mathbf{R}_{FE} : \langle \mathbf{E} \rangle + \dot{\gamma}^{*-1}\mathbf{F}^P]\} \Delta t, \tag{8.6}$$

where $\dot{\gamma}^* \equiv 6\pi\eta a^2\dot{\gamma}/|\mathbf{F}_0^P|$ is the nondimensional shear rate, defined as the ratio of the shear and interparticle forces.

The resistance tensors $\mathbf{R}_{FU}$ and $\mathbf{R}_{FE}$ can be written as part of a grand resistance tensor $\mathcal{R}$ that relates the force/torque ($\mathbf{F}$) and stresslet ($\mathbf{S}$) exerted by the fluid on the particles to the particle velocities and the rate of strain. The corresponding inverse is called the grand mobility tensor, $\mathcal{M} = \mathcal{R}^{-1}$. The method to construct the tensor $\mathcal{R}$ proceeds by obtaining an approximation to $\mathcal{M}$ by combining Faxén laws for particle velocities with a truncated multipole moment representation of the particles. This approximation to the grand mobility tensor, denoted $\mathcal{M}^\infty$, is then inverted to yield a far-field approximation to the grand resistance tensor. This many-body approximation to the resistance tensor lacks, however, the important near-field lubrication effects. Lubrication would only be reproduced upon inversion of the mobility tensor if all multipole moments were included. Because of their short-range nature, lubrication forces are two-body interactions and are introduced in a pairwise-additive fashion in the resistance tensor. Thus, the approximate grand resistance

tensor that includes near-field lubrication and far-field many-body interactions is

$$\mathcal{R} = (\mathcal{M}^{\infty})^{-1} + \mathcal{R}_{lub}, \tag{8.7}$$

where $\mathcal{R}_{lub}$ stands for the near-field lubrication interactions. Thus constructed, the grand resistance tensor is then partitioned and used in the evolution equation (8.6) and in the calculation of macroscopic properties. This procedure captures both the near- and far-field physics and has given excellent results for all situations in which a comparison has been possible (Durlofsky, Brady & Bossis 1987; Brady *et al.* 1988; Phillips, Brady & Bossis 1988).

It should also be noted that the long-range $(1/r)$ nature of the hydrodynamic interactions requires care in simulating infinite suspensions, i.e., letting $N \to \infty$, $V \to \infty$, keeping $n = N/V$ fixed. To avoid badly divergent summation expressions, O'Brien's (1979) method is employed in dynamic simulation. Used with periodic boundary conditions, this method renormalizes all divergent and conditionally convergent hydrodynamic interactions and accelerates the convergence of the interactions with the help of the Ewald summation technique (Beenakker 1986).

From the evolution equation (8.6) we conclude that, for a given form of the interparticle force, the behavior of the suspension depends on the dimensionless parameters $\dot{\gamma}^*$ and ϕ, the volume fraction of particles. In our computer simulations, given an initial configuration of N particles at time $t = 0$, we integrate (8.6) in time to follow the dynamic evolution of the suspension microstructure and calculate and store quantities of interest, e.g., the velocities of the particles, the components of the bulk stress tensor, etc. We employ a fourth order Adams-Bashforth scheme for the integration. A small amount $(-10^{-2} < s < 0)$ of particle overlap may occur because of the finite time step. When overlap occurs we set the interactions at a nondimensional surface-surface separation $s = 10^{-8}$ and proceed with the integration. This method preserves the symmetry of particle trajectories in the pure hydrodynamic limit (Brady & Bossis 1988) and produces the correct equilibrium structure in the pure Brownian limit (Phung *et al.* 1996). A multiple time-stepping scheme is also

used since the mobility interactions vary on the scale of the particle size, while the lubrication interactions vary on the scale of the particle surface separation. The time step is governed by accurately resolving the close particle encounters and the mobility interactions are computed less frequently so that the computer time required in the two sections is roughly the same.

Appropriately averaged over particle configurations and time, the results of a simulation yield the macroscopic properties of the suspension. We will mainly concentrate on the diffusion coefficients and rheological properties, such as the bulk viscosity, the normal stress differences, etc. The long-time self-diffusivity $\mathbf{D}^s_\infty$ measures a particle's ability to move far from its initial position. It is defined as

$$\mathbf{D}^s_\infty = \lim_{t\to\infty} \frac{1}{2}\frac{d}{dt}\langle(\mathbf{x} - \langle\mathbf{x}\rangle)^2\rangle, \tag{8.8}$$

where the angle brackets denote averaging over the N particles.

For rheology, the bulk stress $\langle\boldsymbol{\Sigma}\rangle$ is needed. This is defined as an average over the volume V containing the N particles and is given by

$$\langle\boldsymbol{\Sigma}\rangle = -\langle p\rangle_f \mathbf{I} + 2\eta\langle\mathbf{E}\rangle + \langle\boldsymbol{\Sigma}_p\rangle, \tag{8.9}$$

where $\langle p\rangle_f$ is the constant pressure in the fluid phase, $\mathbf{I}$ is the isotropic tensor, and $2\eta\langle\mathbf{E}\rangle$ is the deviatoric stress contribution from the fluid. The particle contribution to the stress $\langle\boldsymbol{\Sigma}_p\rangle$ is given by

$$\langle\boldsymbol{\Sigma}_p\rangle = n\{\langle\mathbf{S}^H\rangle + \langle\mathbf{S}^F\rangle\}, \tag{8.10}$$

where n is the number density of particles. The particles make two contributions to the bulk stress: (a) a mechanical stress transmitted by the fluid due to the shear flow, $\langle\mathbf{S}^H\rangle$; and (b) a stress due to the interparticle forces, $\langle\mathbf{S}^F\rangle$. These contributions are given by

$$\langle\mathbf{S}^H\rangle \;=\; -\langle\mathbf{R}_{SU}\cdot\mathbf{R}^{-1}_{FU}\cdot\mathbf{R}_{FE} - \mathbf{R}_{SE}\rangle : \langle\mathbf{E}\rangle, \tag{8.11}$$

$$\langle \mathbf{S}^F \rangle = -\langle (\mathbf{R}_{SU} \cdot \mathbf{R}_{FU}^{-1} + \mathbf{xI}) \cdot \mathbf{F}^P \rangle. \tag{8.12}$$

The configuration-dependent resistance tensors $\mathbf{R}_{SU}(\mathbf{x})$ and $\mathbf{R}_{SE}(\mathbf{x})$ are similar to $\mathbf{R}_{FU}$ and $\mathbf{R}_{FE}$ and relate the particle stresslet $\mathbf{S}$ to the particle velocities and to the imposed rate of strain, respectively. In the absence of external torques and because the interparticle force is along the line of particle centers, the stresslet is the symmetric (but not traceless) first moment of the force distribution integrated over the particle surface.

From this point on, for labeling purposes, we shall assume that the imposed shear flow in a dynamic simulation takes place along the x-axis while the velocity gradient is in the y-direction, so that $\langle \mathbf{u}_x \rangle = \dot{\gamma} y$; the vorticity of the bulk flow will point in the direction of the z-axis. For simple shear flow, the relative viscosity of the suspension is defined by the ratio of the xy component of the bulk stress $\langle \mathbf{\Sigma}_{xy} \rangle$ to the xy component of the rate of strain $\langle \mathbf{E}_{xy} \rangle$. In the dimensionless form, the relative viscosity becomes:

$$\eta_r = \frac{\langle \mathbf{\Sigma}_{xy} \rangle}{2\eta \langle \mathbf{E}_{xy} \rangle} = 1 + \eta_r^H + \eta_r^F, \tag{8.13}$$

with

$$\eta_r^H = \frac{9}{2}\phi \frac{1}{N} \overline{\sum_{\alpha=1}^{N} (\mathbf{S}_\alpha^H)_{xy}}, \tag{8.14}$$

$$\eta_r^F = \frac{9}{2}\phi \frac{1}{N} \overline{\sum_{\alpha=1}^{N} (\mathbf{S}_\alpha^F)_{xy}}, \tag{8.15}$$

where α denotes individual particles and the overbar time-averaging over the course of a dynamic simulation run. The factor of $9/2$ arises in equations (8.14) and (8.15) as a result of non-dimensionalization.

The non-Newtonian rheology of a suspension is characterized by the first and second normal stress differences defined as follows,

$$N_1 = \langle \mathbf{\Sigma}_{xx} \rangle - \langle \mathbf{\Sigma}_{yy} \rangle,$$

$$N_2 = \langle \mathbf{\Sigma}_{yy} \rangle - \langle \mathbf{\Sigma}_{zz} \rangle,$$

and by a contribution to the isotropic stress, called suspension (or particle, or osmotic) pressure. Nott & Brady (1995) have shown that the requirement that the suspension pressure be constant in directions perpendicular to the mean motion leads to particle migration and concentration variations in inhomogeneous flow. In the next section we describe in detail the procedure employed to calculate the suspension pressure.

8.2 Calculation of the Suspension Pressure

The osmotic or suspension pressure Π of a suspension of particles is defined as minus one-third the trace of the bulk stress tensor. Recalling (8.9), we write

$$\Pi = -\frac{1}{3}n\{\langle S^H \rangle + \langle S^F \rangle\}, \tag{8.16}$$

where $S^H \equiv \mathbf{I} : \mathbf{S}^H$ and $S^F \equiv \mathbf{I} : \mathbf{S}^F$ have been used to denote the contributions to the osmotic pressure due to the hydrodynamic and interparticle forces. Using the expressions (8.11) and (8.12) and introducing the notation $\mathbf{P} \equiv \mathbf{I} : \mathbf{R}_{SU}$ and $\mathbf{Q} \equiv \mathbf{I} : \mathbf{R}_{SE}$, we obtain

$$\begin{aligned} \langle S^H \rangle &= -\langle \mathbf{P} \cdot \mathbf{R}_{FU}^{-1} \cdot \mathbf{R}_{FE} - \mathbf{Q} \rangle : \langle \mathbf{E} \rangle, \\ \langle S^F \rangle &= -\langle (\mathbf{P} \cdot \mathbf{R}_{FU}^{-1} + \mathbf{x}) \cdot \mathbf{F}^P \rangle. \end{aligned}$$

The procedure used to calculate the osmotic pressure follows closely the algorithm employed in Stokesian Dynamics to compute the rheological quantities (Brady *et al.* 1988). First, we calculate the far-field, many-body approximation to the pressure. The Faxén law for the pressure moment integrated over the surface of a given particle α is (Jeffrey *et al.* 1993):

$$S_\alpha = 4\pi a^3 p^\infty(\mathbf{x}_\alpha), \tag{8.17}$$

where $p^\infty(\mathbf{x}_\alpha)$ is the "ambient" pressure that would exist at the location $\mathbf{x}_\alpha$ of the center of the particle in its absence. Using the Green function for the pressure field of Stokes' flow (Ladyzhenskaya 1963), the ambient pressure $p^\infty(\mathbf{x}_\alpha)$ can be written in terms of integrals of the force distribution on the surfaces of all the other particles and an integral over a mathematical surface Γ' of large radius lying entirely within fluid:

$$p^{\infty}(\mathbf{x}_\alpha) = -\frac{1}{4\pi}\sum_{\substack{\beta \\ \beta\neq\alpha}}\int \frac{\mathbf{x}-\mathbf{y}}{|\mathbf{x}-\mathbf{y}|^3}\cdot\sigma\cdot\mathbf{n}dS_y + \frac{1}{4\pi}\int_{S_{\Gamma'}}\left[\frac{\mathbf{x}-\mathbf{y}}{|\mathbf{x}-\mathbf{y}|^3}\cdot\sigma - 6\eta\mathbf{u}\cdot\frac{(\mathbf{x}-\mathbf{y})(\mathbf{x}-\mathbf{y})}{|\mathbf{x}-\mathbf{y}|^3}\right]\cdot\mathbf{n}dS_y. \quad (8.18)$$

For the particles in the periodically replicated unit cell of a dynamic simulation, we follow Brady *et al.* (1988) and expand the integrals over the individual particle surfaces in (8.18) in terms of the force distribution moments, truncating the expansion at the stresslet level. We then apply the renormalization procedure of O'Brien (1979) together with Ewald's summation technique and obtain the following rapidly convergent expressions:

$$p^{\infty}(\mathbf{x}_\alpha) = -\frac{1}{4\pi}\sum_{l}\sum_{\substack{\beta \\ \beta_l\neq\alpha_0}}(\mathbf{M}_{pF}^{(r)}\cdot\mathbf{F}_{\beta_l}+\mathbf{M}_{pS}^{(r)}:\mathbf{S}_{\beta_l}) - \frac{1}{4\pi V_c}\sum_{\substack{k \\ k\neq 0}}\sum_{\beta}(\mathbf{M}_{pF}^{(k)}\cdot\mathbf{F}_{\beta_l}+\mathbf{M}_{pS}^{(k)}:\mathbf{S}_{\beta_l}), \quad (8.19)$$

where (Bonnecaze & Brady 1990)

$$\begin{aligned}
\mathbf{M}_{pF}^{(r)} &= \left[\left(4\xi^5r^3-12\xi^3r+2\xi r^{-1}\right)\frac{e^{-\xi^2r^2}}{\sqrt{\pi}}+\frac{\mathrm{erfc}(\xi r)}{r^2}\right]\frac{(\mathbf{R}^{\alpha_0}-\mathbf{R}^{\beta_l})}{r},\\
\mathbf{M}_{pF}^{(k)} &= \frac{4\pi}{k^2}\left[1+\frac{1}{4}\left(\frac{k}{\xi}\right)^2+\frac{1}{8}\left(\frac{k}{\xi}\right)^4\right]e^{-k^2/4\xi^2}\sin[\mathbf{k}\cdot(\mathbf{R}^{\alpha}-\mathbf{R}^{\beta})]\mathbf{k},\\
\mathbf{M}_{pS}^{(r)} &= \left[\left(8\xi^7r^4-36\xi^5r^2+16\xi^3+4\xi r^{-2}\right)\frac{e^{-\xi^2r^2}}{\sqrt{\pi}}+\frac{2\mathrm{erfc}(\xi r)}{r^3}\right]\\
&\times \frac{(\mathbf{R}^{\alpha_0}-\mathbf{R}^{\beta_l})(\mathbf{R}^{\alpha_0}-\mathbf{R}^{\beta_l})}{r^2}\\
&+ \left[\left(4\xi^5r^3-12\xi^3r+2\xi r^{-1}\right)\frac{e^{-\xi^2r^2}}{\sqrt{\pi}}+\frac{\mathrm{erfc}(\xi r)}{r^2}\right]\\
&\times \left[\frac{(\mathbf{R}^{\alpha_0}-\mathbf{R}^{\beta_l})(\mathbf{R}^{\alpha_0}-\mathbf{R}^{\beta_l})}{r^3}-\frac{\mathbf{I}}{r}\right],\\
\mathbf{M}_{pS}^{(k)} &= \frac{4\pi}{k^2}\left[1+\frac{1}{4}\left(\frac{k}{\xi}\right)^2+\frac{1}{8}\left(\frac{k}{\xi}\right)^4\right]e^{-k^2/4\xi^2}\cos[\mathbf{k}\cdot(\mathbf{R}^{\alpha}-\mathbf{R}^{\beta})]\mathbf{kk}.
\end{aligned}$$

In the above expressions, l is the cell index number, V_c is the volume of the cell, β is the particle index number, $\mathbf{R}^{\alpha 0}$ is the position of the particle α in the zeroth cell, $\mathbf{R}^{\beta l}$ is the position of the particle β in the lth cell, $\mathbf{k}$ is the periodic cell reciprocal or wave vector, k is its magnitude, $r = |\mathbf{R}^{\alpha 0} - \mathbf{R}^{\beta l}|$, and $\mathbf{R}^{\alpha} - \mathbf{R}^{\beta}$ is the position vector difference between bubbles α and β within a cell. The arbitrary number ξ regulates the speed of convergence for the sums and is typically chosen to be $\sqrt{\pi}/V_c^{\frac{1}{3}}$. Each sum converges exponentially fast.

For pairs of nearly touching particles, the use of the exact values for the particle forces and stresslets in (8.19) leads to aphysically large values of the suspension pressure. This happens because the force distribution moments higher than the stresslet, not included in (8.19), become large for lubricating particles subjected to highly non-localized hydrodynamic forces. Recall that, in Stokesian Dynamics, higher moments and screening effects are accounted for by inverting the far-field mobility matrix and adding to the invert the exact near-fild resistance matrix. For the purposes of calculating the suspension pressure, however, no similar mobility-to-resistance inversion procedure is possible, since the pressure does not appear in the equations of motion of individual particles. To overcome this difficulty without having to account for the higher moments explicitly, and in the hopes of capturing important screening effects, we propose to use in (8.19) "effective" forces and stresslets obtained in the following manner:

$$\begin{pmatrix} \mathbf{F} \\ \mathbf{S} \end{pmatrix} = (\mathcal{M}^{\infty})^{-1} \cdot \begin{pmatrix} \mathbf{U} - \mathbf{U}^{\infty} \\ -\mathbf{E}^{\infty} \end{pmatrix}. \tag{8.20}$$

The physical meaning of the effective forces and stresslets as given by (8.20) can be interpreted as follows. For the purposes of the far-field approximation, we treat the particles as if they were subject to only two non-zero force distribution moments, viz. forces and stresslets, exerted by the fluid, with all the higher moments assumed equal to zero. In order to create the actual flow field, as represented by the velocity/rate-of-strain vector, the forces and stresslets on such particles must assume the values given by (8.20).

Next, we add to the far-field approximation of the suspension pressure the near-

field or lubrication contribution from close pairs of particles. Following Jeffrey *et al.* (1993), we calculate the contributions to the pressure at the reference particle α by all its neighbors within a dimensionless distance of four (an arbitrary choice that allows for computational efficiency and is physically sensible since at so large a distance near-filed pairwise interactions safely can be neglected):

$$\begin{pmatrix} S_\alpha \\ S_\beta \end{pmatrix} = \eta \begin{pmatrix} \mathbf{P}_{\alpha\alpha} & \mathbf{P}_{\alpha\beta} & \mathbf{Q}_{\alpha\alpha} & \mathbf{Q}_{\alpha\beta} \\ \mathbf{P}_{\beta\alpha} & \mathbf{P}_{\beta\beta} & \mathbf{Q}_{\beta\alpha} & \mathbf{Q}_{\beta\beta} \end{pmatrix} \cdot \begin{pmatrix} \mathbf{U}_\alpha - \mathbf{U}_\alpha^\infty \\ \mathbf{U}_\beta - \mathbf{U}_\beta^\infty \\ -\mathbf{E}^\infty \\ -\mathbf{E}^\infty \end{pmatrix}, \tag{8.21}$$

where the quantities $\mathbf{P}$ and $\mathbf{Q}$ are computed according to the procedure outlined in Jeffrey *et al.* (1993). To avoid double counting the portion of the near-field interaction which has been captured by the mobility approximation (8.20), we have followed Jeffrey *et al.* by subtracting from the sum the terms in the resistance formulation of $O(s^{-7})$ and larger, where s is the separation distance, noting that the leading error in the moment expansion is due to neglect of the change to the pressure environment of a reference sphere by the induced quadrupole upon a neighboring sphere, which behaves as s^{-8}.

This concludes the description of the numerical method employed in this study. In the next sections we shall describe the results of our investigation of non-Brownian suspensions as a function of the particle volume fraction ϕ and nondimensional shear rate $\dot{\gamma}^*$.

Chapter 9 Simulation Results

In this chapter we present the results of Stokesian Dynamics simulations of unit cells of 27 and 64 monodisperse particles, subject to hydrodynamic and repulsive pairwise interparticle forces. The specifications of the simulations and details of the sampling and averaging procedures are summarized in Tables 9.1–9.3 for runs with 27 particles in the unit cell. In these tables we report the number of runs for each studied point in the $\dot{\gamma}^*$-ϕ parameter space; the simulation time step, $\triangle t$; the total duration of each run, T; the length t_{diff} and the number of the simulation intervals used for the computation of the long-time self-diffusivity coefficients. In the beginning of each run particles were assigned random positions; the first 5,000 to 10,000 time steps were not used in the calculation of the rheological and other properties. To avoid severe particle overlap, shorter time steps were employed in the runs of concentrated suspensions at $\dot{\gamma}^* = 0.1$.

The runs with 64 particles in the unit cell, conducted at ϕ =0.30, 0.40, 0.45, 0.50, and 0.52 and $\dot{\gamma}^*$ =10, 100, and 1000, were all 50 strains long, with the time step $\triangle t = 10^{-3}$. Because the 64-particle runs were not long nor numerous enough, no long-time self-diffusivity was computed.

The outline of the presentation of the results will be as follows: first, we will discuss the suspension microstructure (the angularly averaged pair-distribution function $g(r)$ and the probability density functions $g(x,y)$, $g(x,z)$, and $g(z,y)$); second, the suspension rheology (the shear viscosity, the normal stress differences, and the suspension pressure); third, the short-time self-diffusivity (or particle mobility) and the long-time self-diffusivity in the velocity-gradient and vorticity directions, $D^s_{\infty,yy}$ and $D^s_{\infty,zz}$; finally, the suspension temperature defined as a measure of the translational and rotational velocity fluctuation, $\langle \mathbf{U}'\mathbf{U}' \rangle$ and $\langle \mathbf{\Omega}'\mathbf{\Omega}' \rangle$.

We conclude these general remarks by noting that, unless indicated otherwise in the table or figure caption, the results presented in this chapter are those obtained in

simulation runs with 27 particles in the unit cell.

9.1 Suspension Microstructure

In this section we investigate how suspensions sheared at different shear rates display different patterns of microstructural particle arrangement. We will see later how these different microstructural patterns profoundly affect the macroscopic suspension properties.

We study the suspension microstructure by determining the angularly-averaged pair-distribution function $g(r)$ together with the probability density functions $g(x,y)$, $g(x,z)$, and $g(z,y)$. Given a particle at the origin, the pair-distribution function $g(\mathbf{r})$ describes the probability of finding a second particle at the location $\mathbf{r}$ normalized by the particle density in the suspension. The angularly-averaged pair-distribution function $g(r)$ contains only information on the relative separation of the particles. It is obtained by dividing the central portion of the unit cell into thin spherical shells (we employed the radial thickness of 0.001 in our simulations). We then compute the particle density in each shell and weight it with the overall particle density of the suspension.

The angular dependence of $g(\mathbf{r})$ can be concluded from the projections of $g(\mathbf{r})$ on the (x,y), (x,z), and (z,y) planes, i.e., from the probability density functions $g(x,y)$, $g(x,z)$, and $g(z,y)$. In simulations, these functions are obtained by dividing the faces of the unit cell into small squares of a $(0.1, 0.1)$ dimension each. The particle positions are then projected onto these squares and the probability density function is computed of finding a particle at a position in a particular square relative to the particle at the origin. A density plot of the plane projection distribution function can then be created.

In the next sections we present the functions $g(r)$, $g(x,y)$, $g(x,z)$, and $g(z,y)$ focusing mainly on the region of high ϕ, where changes in $\dot{\gamma}^*$ have pronounced effect on the microscopic structure and macroscopic properties of suspensions.

9.1.1 Angularly-Averaged Pair-Distribution Function

The results of the calculation of $g(r)$ are presented in Tables 9.4–9.8 and plotted in Figures 9.1–9.8.

The pair-distribution functions $g(r)$ for simulation runs with 64 particles in the unit cell are plotted in Figure 9.1; the unit cell dimensions in these runs allow us to investigate $g(r)$ until the center-center separation $r = 4$. We observe two peaks of pair-distribution, one at $r = 2$, the other at slightly less than $r = 4$. At high shear rates the first peak corresponds to pairs of particles kept together by lubrication forces; the second, much less strongly pronounced peak suggests that, to some extent, particles form chains (or clusters) consisting of more than two particles. In Tables 9.4–9.5 and 9.8 and in Figure 9.2 we have compiled and plotted the values $g(2)$ of the angularly-averaged pair-distribution function at the particle-particle separation corresponding to particle contact, $r = 2$, as a function of the particle phase volume fraction ϕ and dimensionless shear rate $\dot{\gamma}^*$. For the runs at the highest $\dot{\gamma}^*$, 1000 and 10^4, based on our simulations, it would appear as if $r = 2$ were the location of the maximum of the pair-distribution function. In reality, however, $g(r)$ must peak at an $r > 2$ for all finite shear rates; the peak is located where particle advection due to the imposed shear flow is balanced by the flux due to the repulsive interparticle force.

In Figures 9.6–9.8 we have plotted $g(r)$ for the runs at the highest concentrations, $\phi = 0.45$, 0.50, and 0.52. As $\dot{\gamma}^*$ and ϕ increase, so does the magnitude of $g(2)$. As $\dot{\gamma}^* \to \infty$, in the pure hydrodynamic limit, $g(2)$ becomes singularly large, of $O((r-2)^{-0.781}(\ln(r-2)^{-1})^{-0.29})$ (Batchelor & Green 1972). However, as $\dot{\gamma}^*$ decreases, we see the peak of the $g(r)$ shift away from $r = 2$ and that signals the appearance of a fluid-filled gap separating particles in close pairs. In Tables 9.6–9.7 we have compiled the data on the magnitude and location of the peak of $g(r)$.

The above observations lead us to the conclusion that particles in concentrated, strongly-sheared suspensions form clusters, bound by strong lubrication forces, that later will be found responsible for the shear-thickening behavior at high ϕ. This behavior is similar to that of Brownian suspensions at high Pe numbers observed by

Phung (1993) and Phung *et al.* (1996) in their Stokesian dynamics simulations.

9.1.2 Probability Density Functions

The plots of the probability density functions $g(x,y)$, $g(x,z)$, and $g(z,y)$, shown in Figures 9.9–9.20, help visualize the striking differences in the structural arrangement of suspended particles as we go from low to high shear rates. At the lowest value of the shear rate, $\dot{\gamma}^* = 0.1$, the particles form strings oriented in the flow direction (the x-axis), hexagonally-packed in the velocity-gradient–vorticity plane (the (z,y)-plane). As $\dot{\gamma}^*$ increases, the string pattern gradually disappears until eventually, at the highest $\dot{\gamma}^* = 10^4$, we no longer observe strings even in runs at the highest particle density simulated, $\phi = 0.52$.

The plots of $g(x,y)$ are very useful in analyzing the boundary layer in the compressive quadrants ($xy < 0$), where particle surfaces come in contact, in contrast to the extensional quadrants ($xy > 0$), where we observe fewer (or none at all) close pairs. Again, the degree to which this phenomenon is pronounced depends on the value of $\dot{\gamma}^*$. When the latter is low, there is only small distortion of the fore-aft symmetry; as $\dot{\gamma}^*$ increases, the distortion and the difference between the compressive and extensional quadrants become more obvious.

Brady & Morris (1997) have investigated the connection between the broken fore-aft symmetry and the non-Newtonian rheology (normal stress differences and suspension pressure) and hydrodynamic diffusion in a suspension. In the next section we discuss the results of our simulations and test their agreement with the predictions of Brady & Morris.

9.2 Suspension Rheology

9.2.1 Shear Viscosity

The results for the steady shear viscosities of suspensions in the range of ϕ from 0.05 to 0.52 as a function of $\dot{\gamma}^*$ are summarized in Tables 9.9–9.14 for 27 particles and in Table 9.33 for 64 particles and plotted in Figures 9.21–9.23 together with experimental measurements of Rutgers (1962), Gadala-Maria (1979), and Pätzold (1980) and Phung's (1993) Stokesian Dynamics simulation results for a Brownian hard-sphere suspension sheared at $Pe = 10^4$.

For simple shear flow in the (x, y)-plane, the relative viscosity η_r, the viscosity of the suspension normalized by the fluid viscosity, is the relation between the xy component of the bulk stress tensor $\langle\Sigma\rangle$ and the xy component of the bulk rate of strain $\langle\mathbf{E}\rangle$. The viscosity of a suspension along with the contributions to it due to the hydrodynamic and intrparticle forces are defined with the aid of the equations (8.13)–(8.15).

An examination of the plots in Figures 9.21–9.23 reveals little variation with $\dot{\gamma}^*$ in either the total viscosity η_r or the hydrodynamic contribution η^H to the total for the runs at low particle fraction, $\phi \leq 0.3$. When the suspension becomes concentrated, at high values of $\dot{\gamma}^*$, i.e., with little repulsive force present, the particles form clusters bound together by strong lubrication forces and that results in an increase in the hydrodynamic contribution η^H to the viscosity. In this range of $\dot{\gamma}^*$ the magnitude of the interparticle force contribution η^F to the total shear viscosity is lower than that of the hydrodynamic contribution by several orders of magnitude. As $\dot{\gamma}^*$ decreases, the interparticle force becomes more effective in breaking the clusters of lubricating particles and that results in an overall decrease of the total shear viscosity, even though the interparticle force contribution increases dramatically (by two decades going from $\dot{\gamma}^* = 0.1$ to 10^4).

We observe good agreement between our results and other researchers' experimental findings shown in Figure 9.21. The results obtained by Phung (1993) for the shear viscosity of a hard-sphere suspension at $Pe = 10^4$ agree most closely with our

results for the highest value of $\dot{\gamma}^* = 10^4$; this means that, as far as the suspension viscosity is concerned, the actions of weak Brownian motion and of weak interparticle repulsion are similar in that they manage to keep particles in the suspension from forming large, unit-cell-spanning clusters.

9.2.2 Normal Stress Differences

The normal stress differences help characterize the non-Newtonian behavior of suspensions due to the anisotropic deformation of the microstucture. Tables 9.15–9.26 and 9.34–9.35 and Figures 9.24–9.29 present the simulation results for the first and second normal stress differences and the contributions due to the hydrodynamic and interparticle forces for runs with 27 and 64 particles. Unfortunately, the poor quality of the results of the normal stress differences limits us to making only qualitative generalizations.

Whenever possible, we have compared our results with those obtained by Phung (1993) for hard spheres at $Pe = 10^4$.

First Normal Stress Difference

The results of the first normal stress difference are detailed in Tables 9.15–9.20 and 9.34 and in Figures 9.24–9.26. From these we conclude that the dominant contribution to the total comes from the hydrodynamic forces. The total first normal stress difference N_1 is negative and grows in magnitude with $\dot{\gamma}^*$. The contribution from the interparticle force N_1^F is positive (except in runs with 64 particles at $\dot{\gamma}^* = 10$) and decreases in its magnitude as $\dot{\gamma}^*$ grows (behavior similar to that of η^F).

Second Normal Stress Difference

The results of the second normal stress difference (the total N_2, together with the hydrodynamic and interparticle force contributions, N_2^H and N_2^F) can be found in Tables 9.21–9.26 and 9.35 and in Figures 9.27–9.29. All three quantities have been found negative. We note reasonable agreement between our data for N_2^H at $\dot{\gamma}^* = 10^4$

and Phung's (1993) results for N_2^H at $Pe = 10^4$. The hydrodynamic contribution N_2^H displays behavior similar to that of N_1^H and η^H, namely that at high enough values of ϕ, the hydrodynamic contributions increase with increasing $\dot{\gamma}^*$. Of all the normal stress quantities, N_2^F has proven the most difficult to estimate reliably; the available data do not allow us to make any conclusions as to the influence of changes in $\dot{\gamma}^*$ on N_2^F; it is also doubtful that, unlike N_1^F, the interparticle force contribution N_2^F should appear to dominate the hydrodynamic contribution N_2^H, even in runs at the highest values of $\dot{\gamma}^*$ (it should be noted that the scatter of the results is significant).

Comparison with the Normal Stress Data of Gadala-Maria (1979)

Using a parallel-plate Couette device, Gadala-Maria (1979) measured the difference between the first and second normal stress differences, $N_1 - N_2$, for a concentrated sheared suspension of polystyrene spheres (40 to 50 μm in diameter) in oil. $N_1 - N_2$ was found roughly to scale with the shear rate. In Figure 9.30 we have plotted Gadala-Maria's data together with $N_1 - N_2$ obtained in our simulations.

We observe reasonable agreement between the results of our simulations at high shear rates ($\dot{\gamma}^* = 10^4, 1000$, and 100) and Gadala-Maria's experiments.

Interpretaion of the Signs of the Normal Stress Differences

To explain why we have obtained positive values for N_1^F and negative for N_2^F, we note that for close pairs of particles the behavior of the interparticle-force contribution to the stress is given by

$$\langle \mathbf{\Sigma}^F \rangle \sim - \int \mathbf{r}\mathbf{r} g(\mathbf{r}) d\mathbf{r}, \tag{9.1}$$

where $\mathbf{r}$ is the vector separating the centers of the two particles and $g(\mathbf{r})$ is the pair-distribution function. A positive N_1^F results from the resultant negative yy interparticle-force stress generated along the extensional axis of the flow. The interparticle force acts to repel two particles that are pushed together by shear, and the component of this repulsion along the y-axis is a positive yy pressure or a negative stress. A similar component exists along the x-axis and, owing to the symmetry

along the compressive axis,(cf. the (x, y) plots in Figures 9.17 and 9.20) the corresponding contribution to the first normal stress difference is zero. The symmetry is broken along the extensional axis, however, and the absence of close pairs in the far-aft region results in a relatively larger magnitude of the yy stress and a positive N_1^F. The interparticle-force contribution to the second normal stress difference, N_2^F is negative because, owing to the compression of the shear flow, the yy stress is larger in magnitude than the zz stress.

We now address the issue of the sign of the hydrodynamic contribution to the normal stresses. For a suspension that is subject to bulk steady simple shearing motion, by considering pairs of particles, Batchelor & Green (1972) derived the components of the particle contribution to the bulk suspension stress. Using expressions from §6 of their paper, we conclude that the hydrodynamic contributions to the first and second normal stress differences should be proportional to the following integrals:

$$N_1 \sim \int \frac{\mathbf{r}_1\mathbf{r}_2(\mathbf{r}_1^2 - \mathbf{r}_2^2)}{r^4} M p(\mathbf{r}, t) d\mathbf{r}, \tag{9.2}$$

$$N_2 \sim \int \frac{\mathbf{r}_1\mathbf{r}_2}{r^2}\left(L + \frac{\mathbf{r}_2^2 - \mathbf{r}_3^2}{r^2} M\right) p(\mathbf{r}, t) d\mathbf{r}, \tag{9.3}$$

where $p(\mathbf{r}, t)$ is the time-dependent probability density for the vector $\mathbf{r}$, and the non-dimensional scalar functions M and L depend on the non-dimensional distance between the particles, r/a; their asymptotic behavior is as follows:

$$M \sim \frac{25a^3}{2r^3}, \tag{9.4}$$

$$L \sim -\frac{5a^3}{2r^3}, \tag{9.5}$$

as $r/a \to \infty$.

The examination of the xy-projections of steady state pair distribution at high shear rates, in Figures 9.17 and 9.20, taking into account the lack of close pairs along the extensional axis, lets one conclude that (9.2) predicts a negative N_1^H which is in agreement with our simulation results. This type of analysis fails, however, to predict the sign of N_2^H.

9.2.3 Suspension Pressure

The suspension pressure is defined by equation (8.16) as minus one-third the trace of the bulk stress tensor. We have summarized in Tables 9.27–9.32 and 9.36 and plotted in Figures 9.31–9.33 the simulation results for the total suspension pressure as well as for the separate contributions to it by the hydrodynamic and interparticle forces.

By examining the plots we conclude that the behavior of all three quantities, the total and the two contributions, is similar to that of the shear viscosity. At high particle phase concentrations, there is significant dependence of the suspension pressure Π on the shear rate: as $\dot{\gamma}^*$ increases so too does the total pressure and the hydrodynamic-force pressure while the interparticle-force contribution vanishes.

9.2.4 Normal Stresses and Net Migration of Particles

In order to explain the absence of particle net migration in torsional flow (observed in the experiments of Chow *et al.* 1994), Nott & Brady (1995) proposed the following argument. In cylindrical coordinates (r, θ, z) the velocity of torsional flow is in the θ-direction, grows linearly with the radius r and has a gradient in the z-direction: $\langle \mathbf{u} \rangle = rh(z)\hat{\theta}$. The radial momentum balance is given by

$$-\frac{\partial \langle \Sigma_{rr} \rangle_p}{\partial r} = \frac{\langle \Sigma_{rr} \rangle_p - \langle \Sigma_{\theta\theta} \rangle_p}{r}. \tag{9.6}$$

Because of the linear dependence of $\langle \mathbf{\Sigma} \rangle$ on r, the radial momentum balance (9.6) implies the following relation among the pressure and the first and second normal stress differences to prevent migration,

$$\Pi + \frac{1}{3}(4N_1 + 5N_2) = 0. \tag{9.7}$$

In Figure 9.34 we have plotted the quantity on the left-hand side of (9.7), based on results of our simulations, to determine whether there is cancellation. We conclude from the plot that the cancellation is rather poor. This, at least in part, may be due to the poor quality of the data on the interparticle-force contribution to the second

normal stress difference, N_2^F, as obtained in our simulations. Excluding N_2^F from 9.7 (based on the assumption that in reality N_2^F should be small in comparison to N_2^H, as indeed is the case with N_1^F and N_1^H), we observe a much better cancellation of normal stresses, in Figure 9.35, up to the particle phase fraction of 0.45.

9.2.5 Comparison with Scaling Predictions of Brady & Morris (1997)

In this section we check the agreement between our simulation results and the relevant scaling predictions made by Brady & Morris (1997). These authors have analytically calculated the viscosity and second normal stress difference for a suspension of particles of radius a that are prevented from approaching one another at distances smaller than $b > a$ by a hard-sphere-type pairwise interparticle force. This force breaks the fore-aft symmetry for close pairs of particles and thus leads to a finite viscosity correction and second normal stress difference. Below are the scalings obtained by Brady & Morris for the hydrodynamic and interparticle-force contributions to the shear viscosity and normal stresses of a dilute suspension:

$$\eta^H \sim \eta\phi^2(b/a-1)^{0.22}, \tag{9.8}$$

$$\eta^F \sim \eta\phi^2(b/a-1)^{1.22}, \tag{9.9}$$

$$N^H \sim \eta\dot{\gamma}\phi^2(b/a-1)^{0.22}, \tag{9.10}$$

$$N^F \sim \eta\dot{\gamma}\phi^2(b/a-1)^{1.22}, \tag{9.11}$$

where the hydrodynamic contribution to the viscosity (9.8) is over and above the relative high-frequency dynamic viscosity η_r^∞, corresponding to the equilibrium, hard sphere distribution. This quantity has been calculated by Phillips *et al.* (1988), Phung (1993) (as the hydrodynamic contribution to the viscosity of a Brownian sheared suspension in the limit of low Pe number), and determined experimentally by van der Werff *et al.* (1989), among others. In this work, we have used the results obtained by Phillips *et al.*

For concentrated suspensions the right-hand sides of (9.8)–(9.11) should be multiplied by a factor of $g^{\infty}(2b;\phi)/\hat{D}_0^s(\phi)$, where $g^{\infty}(2b;\phi)$ is the pair-distribution function at infinite Péclet number evaluated at the location of its peak, $2b$, and $\hat{D}_0^s(\phi)$ is the short-time self-diffusivity at the volume fraction and flow conditions of interest, nondimensionalized by the short-time self-diffusivity at infinite dilution.

To compare our results with the scalings (9.8)–(9.11), we have plotted the hydrodynamic and interparticle-force viscosities, normal stress differences, and suspension pressures against both ϕ^2 and $\phi^2 g^{\infty}(2b;\phi)/\hat{D}_0^s(\phi)$, thus testing the entire range of simulated values of ϕ. For $g^{\infty}(2b;\phi)$ we used the maximum value of the pair-distribution function determined at ϕ and $\dot{\gamma}^*$ of interest; for $\hat{D}_0^s(\phi)$, the short-time self-diffusivities obtained in our simulations. We did not account for the factors of $(b/a-1)^{0.22}$ and $(b/a-1)^{1.22}$ in our scaling checks because we could determine a finite $(b/a-1)$ only for the simulation runs at low $\dot{\gamma}^*$ (cf. Tables 9.6–9.7) and even in those runs the variation in $(b/a-1)^{0.22}$ and $(b/a-1)^{1.22}$ was not large enough to let us make a definite conclusion as to the specific influence of those factors on the rheological functions.

The double logarithmic plots of $\eta^H - \eta_r{}^{\infty}$, η^F, N_1^H, N_1^F, N_2^H, N_2^F, Π^H, and Π^F against ϕ^2 and $\phi^2 g^{\infty}(2b;\phi)/\hat{D}_0^s(\phi)$ are presented in Figures 9.36–9.51. By examining the plots we conclude that the agreement of η^H, η^F, Π^H, and Π^F with the scaling predictions is quite good at both low and high ϕ. The normal stress differences scale as ϕ^2 at low ϕ; the high ϕ scaling with $\phi^2 g^{\infty}(2b;\phi)/\hat{D}_0^s(\phi)$ is not as well-pronounced, due to the high degree of scatter in our results.

9.2.6 Relation between the Suspension Microstructure and the Interparticle-Force Contributions to the Shear Viscosity, Normal Stress Differences, and Suspension Pressure

From the original non-dimensionalization employed to derive the evolution equation (8.6) it follows that the interparticle contributions to the stress tensor scale as $\dot{\gamma}^{*-1}$. To clarify the dependence of these contributions on the suspension microstructure as

the shear rate changes over five decades, we have plotted the products of $\dot{\gamma}^*$ with η_r^F, N_1^F, N_2^F, and Π^F as a function of $\dot{\gamma}^*$ at fixed ϕ.

The interparticle-force contributions to the shear viscosity and suspension pressure in concentrated suspensions at high shear rates scale linearly with the contact value of the angularly-averaged pair-distribution function, as evidenced in the plots shown in Figures 9.53 and 9.57.

9.3 Self-Diffusion of Suspended Particles

9.3.1 Short-Time Self-Diffusion

In this section we present the results of calculation of the short-time self-diffusion coefficient as average of the elements of the trace of the diffusion tensor

$$D_0^s = \langle tr\mathbf{D} \rangle, \tag{9.12}$$

where the translational and rotational diffusion tensors, $\mathbf{D}_0$ and $\mathbf{D}_r$ respectively, are defined according to the Stokes-Einstein relations:

$$\begin{aligned} \mathbf{D}_0 &= kT\mathbf{R}_{FU}^{-1}, \\ \mathbf{D}_r &= kT\mathbf{R}_{L\Omega}^{-1}. \end{aligned}$$

Even though the motion of non-Brownian particles on short time-scales is not diffusive, D_0^s and D_r^s are still useful as measures of the instantaneous particle mobility.

Tables 9.37–9.47 and Figures 9.58 and 9.59 present the short-time self-diffusion coefficients $D_{0_{xx}}^s$, $D_{0_{yy}}^s$, $D_{0_{zz}}^s$, $D_{r_{xx}}^s$, $D_{r_{yy}}^s$, $D_{r_{zz}}^s$, together with the averages

$$\begin{aligned} \langle D_0^s \rangle &= \frac{1}{3}(D_{0_{xx}}^s + D_{0_{yy}}^s + D_{0_{zz}}^s), \\ \langle D_r^s \rangle &= \frac{1}{3}(D_{r_{xx}}^s + D_{r_{yy}}^s + D_{r_{zz}}^s). \end{aligned}$$

In the tables and plots the translational and rotational self-diffusion coefficients are normalized by the corresponding infinite dilution coefficients, $kT/(6\pi\eta a)$ and $kT/(8\pi\eta a^3)$, respectively. Going from dilute to concentrated suspensions, the self-diffusion coefficients decrease dramatically. At the highest concentrations there is a pronounced dependence of both D_0^s and D_r^s on $\dot{\gamma}^*$: particle in the suspensions undergoing motion at higher shear rates have less of a mobility, both translational and rotational. This is not surprising considering that particles in strongly-sheared suspensions spend more time in close pairs and clusters (cf. data on the pair-distribution

function $g(r)$ in Section 9.1); accordingly, the mobility of particles in close contact with other particles is expected to be lower than that of particles in weakly-sheared suspensions, where the repulsive force succeeds in preventing close encounters of particles.

Examining the plots in Figure 9.58, we observe that the mobility does not asymptote to unity as $\phi \to 0$ and that at $\phi = 0.30$ and 0.40 simulations with 64 particles in the unit cell yield higher values of D_0^s. Following Phillips, Brady & Bossis (1988), we attribute these findings to the periodic replication of the unit cell employed in our simulations. Indeed, due to periodic boundary conditions imposed on the unit cell of N particles in our simulations, we have the motion of each individual particle in superposition with the "drifting," or "sedimenting," motion of a simple cubic lattice of volume fraction ϕ/N. Insofar as the translational short-time self-diffusivity is concerned, this "sedimenting" effect scales as $N^{-\frac{1}{3}}$. In order to correct for this effect and thus obtain the "true" short-time translational self-diffusivities, for those data points in the $(\phi, \dot{\gamma})$ space for which we have D_0^s values for both N=27 and 64, we have extrapolated to infinite N using the scaling from Phillips *et al.* (1988):

$$D^s_{0,N} = D^s_{0,\infty} + \alpha(\phi) N^{-\frac{1}{3}}, \tag{9.13}$$

where $\alpha(\phi)$ is a function used to describe the decay of the effects of periodicity. Thus obtained extrapolated mobilities can also be found in Figure 9.58.

Phillips *et al.* also analyzed the finite size effects for the rotational mobility and found them to be much weaker, scaling at most as N^{-1}. Our results of D_r^s, plotted in Figure 9.59, agree with these findings.

9.3.2 Long-Time Self-Diffusion

The long-time self-diffusion coefficients are obtained by differentiating the mean square displacement of the particles with respect to time. Such differentiation is performed on a number of sample intervals in each run and then the mean values of the coefficients along with their standard deviations are obtained by averaging

over all the sample intervals. In Tables 9.48–9.51 we have reported the long-time self-diffusion coefficients in the velocity-gradient and vorticity direction, $D^s_{\infty,yy}$ and $D^s_{\infty,zz}$, respectively, and their standard deviations. The results in these tables are for simulation runs with 27 particles only; our runs with 64 particles in the unit cell were not long nor numerous enough for the calculation of the diffusion coefficients. We have plotted the coefficients in Figures 9.60 and 9.61. Although the standard deviations are high, due to the relatively short simulation runs, we can nevertheless draw important conclusions about patterns of self-diffusion of particles in the studied flow. When the particle volume fraction is low, $\phi < 0.3$, there is little diffusive motion, as the particles are following streamlines most of the time; interparticle collisions, necessary for random walk, occur only rarely.

However, as ϕ increases, collisions become more frequent, and the particles' self-diffusion becomes much more evident; accordingly, the self-diffusion coefficients increase by an order of magnitude until, at around $\phi = 0.4 - 0.45$, depending on the relative magnitude of the interparticle repulsive force, the suspension begins to order itself in a string-flowing pattern, and the self-diffusion coefficients drop dramatically. This phenomenon is best pronounced at the lowest values of $\dot{\gamma}^*$, 0.1 and 1. At the highest shear rate, $\dot{\gamma}^* = 10^4$, we do not see a decrease in self-diffusion, as the suspension does not show signs of ordering even at the highest value of the particle volume fraction.

Another feature of the plots in Figures 9.60 and 9.61 is that $D^s_{\infty,yy}$ is generally larger than $D^s_{\infty,zz}$. Also, $D^s_{\infty,zz}$ peaks at a higher value of ϕ.

For comparison we have plotted the self-diffusion coefficients obtained by Phung (1993) for a hard-sphere suspension at $Pe = 10^4$ as well as the results of experiments of Eckstein *et al.* (1977), Leighton & Acrivos (1987), and Phan & Leighton (1993). These researchers' and our results agree reasonably well. Also, our finding that $D^s_{\infty,yy} > D^s_{\infty,zz}$ is in qualitative agreement with the coresponding results of Da Cunha & Hinch (1996) who studied irreversible pairwise collisions in a dilute suspension of non-Brownian particles with small surface roughness, modeled as a normal force between the surfaces of the spheres which stops the particles becoming closer

than a non-zero minimum separation but no force is exerted when the particles separate. Da Cunha & Hinch predicted very anisotropic diffusion, with the diffusivity in the direction of the velocity gradient being more than an order of magnitude larger than the diffusivity in the direction of the vorticity.

Comparison with Scaling Predictions of Brady & Morris (1997)

Brady & Morris (1997) have determined the self-diffusivity of a sheared suspension for $Pe \gg 1$ from the temporal evolution of the spatial correlation of particle position. At high particle concentrations, they predict the following scaling for the long-time self-diffusion coefficient:

$$D^s_\infty \sim \dot{\gamma} a^2 (b/a - 1)^{0.22} \phi g^\infty(2b; \phi), \tag{9.14}$$

where $g^\infty(2b; \phi)$ is the pair-distribution function evaluated at the location of its peak, $2b$, at the volume fraction and flow conditions of interest. In a fashion similar to that employed in Section 9.2.5, we have plotted in Figures 9.62 and 9.63 the long-time self-diffusion coeffeicients $D^s_{yy,\infty}$ and $D^s_{zz,\infty}$ obtained in our simulations against $\phi g^\infty(2b; \phi)$. For $g^\infty(2b; \phi)$ we used the maximum value of the pair-distribution function determined at ϕ and $\dot{\gamma}^*$ of interest. We did not include the factor of $(b/a - 1)^{0.22}$ in our scaling checks due to the insufficient resolution of the pair-distribution function $g(r)$ (cf. Section 9.2.5). Upon the inspection of the plots in Figures 9.62 and 9.63 we conclude that there is reasonable agreement of our results with the scaling prediction (9.14) of Brady & Morris (1997).

9.4 Suspension Temperature

In Tables 9.52–9.65 and Figures 9.64–9.69 we report the results of our calculations of the translational and rotational suspension temperature defined as the mean square of the translational and rotational velocity fluctuation, i.e.:

$$\mathbf{T}^{tr} = \langle \mathbf{U}'\mathbf{U}' \rangle,$$
$$\mathbf{T}^{rot} = \langle \mathbf{\Omega}'\mathbf{\Omega}' \rangle.$$

Nott & Brady (1994) introduced the suspension temperature as a fundamental variable determining the particle pressure to enable a nonlocal description, accounting for the finite size of the particles, in their suspension balance model. Based on the fact that the hydrodynamic pressure has a contribution from the motion of the particles relative to the average motion, Nott & Brady argued that the pressure should be related to the fluctuational motion of the particles. More specifically, it should be proportional to the square root of the temperature, rather than being proportional to the local value of the shear rate. In a homogeneous shear flow, these alternative approaches are equivalent, as the temperature is proportional to the shear rate squared, $\dot{\gamma}^2$; in *inhomogeneous* flow, however, the temperature need not be proportional to $\dot{\gamma}^2$ nor be zero where the shear rate is zero.

We have separately calculated the three components of each temperature, in the x-, y-, and z-directions. All the temperatures remain low at low values of ϕ (zero when $\phi = 0$) due to the little fluctuational translational and rotational motion in all directions.

For higher particle phase concentrations, the temperatures display behavior similar to that of the self-diffusion coefficients: interparticle collisions and random walk become more common, the fluctuational motion and the temperatures grow until, in cases of stronger interparticle repulsion, at low shear rates $\dot{\gamma}^*$ and high enough values of ϕ, the suspended particles order themselves in flowing strings and this leads to a decrease in fluctuational motion. At high shear rates, noncompact clusters rotating

en masse in the xy plane lead to an increase in the fluctuational motion. Appropriately, T_x^{tr} and T_y^{tr} are found to be larger than T_z^{tr}, while T_z^{rot} is larger than both T_x^{rot} and T_y^{rot}.

An examination of the plots of T_x^{tr} and T_y^{tr} also reveals a discrepancy between the results for 27 particles in the unit cell and those for 64 particles, at $\phi = 0.30$: the temperature is higher in the cell with 64 particles. As ϕ increases, the discrepancy disappears. We propose the following explanation of this phenomenon. The particle concentration $\phi = 0.30$ corresponds to the early stage of particle cluster formation in the unit cell, when not all particles are involved in this process yet. The noncompact clusters that do form, however, grow to a larger size in a cell with more particles. This results in a higher value of the temperature for $N = 64$ than that for $N = 27$. As ϕ increases, eventually all particles in the unit cell participate in cluster formation and thus the difference between the results for 27 and 64 particles disappears.

Table 9.1: The specifications of the Stokesian Dynamics simulation runs with 27 particles in the unit cell at $\dot{\gamma}^* = 0.1$.

ϕ	$\#runs$	$\triangle t$	T	t_{diff}	$\#int$
0.05	2	0.001	100.0	50.0	12
0.10	2	0.001	100.0	50.0	12
0.15	2	0.001	80.0	40.0	10
0.20	2	0.001	80.0	40.0	10
0.25	2	0.001	60.0	30.0	8
0.30	2	0.0005	60.0	30.0	8
0.35	2	0.0005	60.0	30.0	8
0.40	2	0.0005	60.0	30.0	8
0.45	1	0.0002	100.0	30.0	8
0.50	1	0.0002	100.0	30.0	8
0.52	1	0.0001	100.0	30.0	8

Table 9.2: The specifications of the Stokesian Dynamics simulation runs with 27 particles in the unit cell at $\dot{\gamma}^* = 1$.

ϕ	$\#runs$	$\triangle t$	T	t_{diff}	$\#int$
0.05	2	0.001	100.0	50.0	12
0.10	2	0.001	100.0	50.0	12
0.15	2	0.001	80.0	40.0	10
0.20	2	0.001	80.0	40.0	10
0.25	2	0.001	60.0	30.0	8
0.30	2	0.001	60.0	30.0	8
0.35	2	0.001	60.0	30.0	8
0.40	2	0.001	60.0	30.0	8
0.45	2	0.0005	100.0	30.0	16
0.50	2	0.0005	100.0	30.0	16
0.52	2	0.0005	100.0	30.0	16

Table 9.3: The specifications of the Stokesian Dynamics simulation runs with 27 particles in the unit cell at $\dot{\gamma}^* = 10$, 100, 1000, and 10^4.

ϕ	$\#runs$	$\triangle t$	T	t_{diff}	$\#int$
0.05	2	0.001	100.0	50.0	12
0.10	2	0.001	100.0	50.0	12
0.15	2	0.001	80.0	40.0	10
0.20	2	0.001	80.0	40.0	10
0.25	2	0.001	60.0	30.0	8
0.30	2	0.001	60.0	30.0	8
0.35	2	0.001	60.0	30.0	8
0.40	2	0.001	60.0	30.0	8
0.45	3	0.001	100.0	30.0	24
0.50	3	0.001	100.0	30.0	24
0.52	3	0.001	100.0	30.0	24

Table 9.4: The mean ($g(2)$) and the standard deviation (σ) of the angularly-averaged pair-distribution function at particle contact for $\dot{\gamma}^* = 0.1$, 1, and 10.

	$\dot{\gamma}^* = 0.1$		$\dot{\gamma}^* = 1$		$\dot{\gamma}^* = 10$	
ϕ	$g(2)$	σ	$g(2)$	σ	$g(2)$	σ
0.05	0.000	0.000	0.000	0.000	0.58	0.49
0.10	0.000	0.000	0.000	0.000	0.145	0.041
0.15	0.000	0.000	0.000	0.000	0.16	0.16
0.20	0.000	0.000	0.000	0.000	0.102	0.062
0.25	0.000	0.000	0.000	0.000	0.058	0.082
0.30	0.010	0.014	0.010	0.014	0.378	0.014
0.35	0.000	0.000	0.000	0.000	0.57	0.27
0.40	0.000	0.000	0.015	0.021	0.66	0.14
0.45	0.000		0.013	0.018	0.62	0.15
0.50	0.000		0.064	0.008	0.79	0.22
0.52	0.000		0.129	0.040	0.772	0.047

Table 9.5: The mean ($g(2)$) and the standard deviation (σ) of the angularly-averaged pair-distribution function at particle contact for $\dot{\gamma}^* = 100$, 1000, and 10^4.

	$\dot{\gamma}^* = 100$		$\dot{\gamma}^* = 1000$		$\dot{\gamma}^* = 10^4$	
ϕ	$g(2)$	σ	$g(2)$	σ	$g(2)$	σ
0.05	2.2	1.2	9.2	6.7	48	29
0.10	1.60	0.29	6.58	0.25	18.2	3.1
0.15	0.99	0.90	11.12	0.30	38.5	1.9
0.20	0.946	0.021	12.5	6.3	41	16
0.25	1.15	0.28	21.8	2.2	57.9	5.2
0.30	2.37	0.71	41.6	2.8	101.5	0.2
0.35	4.25	0.08	87.7	1.6	173.9	2.2
0.40	12.63	0.89	158.4	7.2	281	31
0.45	17.0	1.2	181.4	2.7	306.0	7.2
0.50	45.2	2.6	262.7	7.6	400	15
0.52	47.2	2.7	256	16	409	15

Table 9.6: The magnitude ($g^{max}(r)$) and location (r^{max}) of the peak of the angularly-averaged pair-distribution function for $\dot{\gamma}^* = 0.1$, 1, and 10.

	$\dot{\gamma}^* = 0.1$		$\dot{\gamma}^* = 1$		$\dot{\gamma}^* = 10$	
ϕ	$g^{max}(r)$	r^{max}	$g^{max}(r)$	r^{max}	$g^{max}(r)$	r^{max}
0.05	26.0	2.010	28.2	2.008	26.3	2.006
0.10	18.1	2.010	19.5	2.008	16.9	2.005
0.15	23.0	2.010	24.0	2.007	24.9	2.005
0.20	31.3	2.009	34.3	2.007	30.7	2.005
0.25	51.4	2.009	50.3	2.007	42.0	2.005
0.30	76.0	2.009	68.0	2.007	58.2	2.004
0.35	83.7	2.009	85.0	2.006	83.3	2.004
0.40	109.1	2.008	113.5	2.006	105.6	2.004
0.45	116.6	2.008	123.1	2.006	118.2	2.004
0.50	127.8	2.008	120.7	2.006	141.0	2.003
0.52	122.9	2.008	120.5	2.005	142.7	2.003

Table 9.7: The magnitude ($g^{max}(r)$) and location (r^{max}) of the peak of the angularly-averaged pair-distribution function for $\dot{\gamma}^* = 100$, 1000, and 10^4.

	$\dot{\gamma}^* = 100$		$\dot{\gamma}^* = 1000$		$\dot{\gamma}^* = 10^4$	
ϕ	$g^{max}(r)$	r^{max}	$g^{max}(r)$	r^{max}	$g^{max}(r)$	r^{max}
0.05	28.8	2.005	25.3	2.002	48.2	2.000
0.10	19.5	2.003	15.1	2.001	18.2	2.000
0.15	28.1	2.003	32.6	2.001	42.9	2.001
0.20	28.2	2.003	32.7	2.001	40.6	2.000
0.25	39.3	2.003	54.9	2.001	57.9	2.000
0.30	67.4	2.002	75.0	2.001	101.5	2.000
0.35	96.6	2.002	101.0	2.001	173.9	2.000
0.40	112.1	2.002	158.5	2.000	281.0	2.000
0.45	126.1	2.002	181.4	2.000	306.0	2.000
0.50	179.2	2.001	262.7	2.000	399.8	2.000
0.52	176.8	2.001	256.5	2.000	409.5	2.000

Table 9.8: The magnitudes of the angularly-averaged pair-distribution function at particle contact ($g(2)$) and of its peak ($g^{max}(r)$) and the location (r^{max}) of the peak for runs with 64 particles in the unit cell. At $\dot{\gamma}^* = 1000$ the peak is located at $r = 2.000$ at $\phi = 0.40, 0.45, 0.50$, and 0.52. At $\dot{\gamma}^* = 1000, \phi = 0.30$, the peak is located at $r^{max} = 2.001$ with $g^{max}(r) = 76.9$.

	$\dot{\gamma}^* = 10$			$\dot{\gamma}^* = 100$			$\dot{\gamma}^* = 1000$
ϕ	$g(2)$	$g^{max}(r)$	r^{max}	$g(2)$	$g^{max}(r)$	r^{max}	$g(2)$
0.30	1.54	57.8	2.004	9.64	61.5	2.002	56.2
0.40	3.44	98.8	2.004	19.25	104.1	2.002	138.1
0.45	5.02	105.2	2.003	35.5	120.7	2.001	212.1
0.50	6.04	134.1	2.003	41.3	149.0	2.001	262.1
0.52	7.44	145.8	2.003	68.2	166.2	2.001	314.9

Table 9.9: The mean and the standard deviation of the relative shear viscosity for $\dot{\gamma}^* = 0.1$, 1, and 10.

	$\dot{\gamma}^* = 0.1$		$\dot{\gamma}^* = 1$		$\dot{\gamma}^* = 10$	
ϕ	η_r	σ	η_r	σ	η_r	σ
0.05	1.151	0.001	1.154	0.003	1.153	0.003
0.10	1.350	0.005	1.350	0.007	1.349	0.002
0.15	1.589	0.018	1.597	0.011	1.601	0.020
0.20	1.892	0.011	1.910	0.019	1.908	0.021
0.25	2.336	0.003	2.360	0.006	2.333	0.001
0.30	3.005	0.026	2.999	0.012	2.995	0.029
0.35	4.049	0.057	3.966	0.031	4.015	0.055
0.40	5.550	0.056	5.694	0.057	5.77	0.11
0.45	7.622		7.82	0.22	8.41	0.12
0.50	9.511		10.54	0.76	12.72	0.37
0.52	10.470		13.13	0.94	14.3	1.2

Table 9.10: The mean and the standard deviation of the relative shear viscosity for $\dot{\gamma}^* = 100$, 1000, and 10^4.

	$\dot{\gamma}^* = 100$		$\dot{\gamma}^* = 1000$		$\dot{\gamma}^* = 10^4$	
ϕ	η_r	σ	η_r	σ	η_r	σ
0.05	1.154	0.004	1.152	0.003	1.156	0.004
0.10	1.354	0.002	1.354	0.000	1.354	0.002
0.15	1.620	0.042	1.630	0.007	1.633	0.002
0.20	1.918	0.035	1.925	0.034	1.955	0.055
0.25	2.360	0.008	2.412	0.012	2.430	0.007
0.30	3.082	0.005	3.097	0.048	3.167	0.007
0.35	4.198	0.024	4.332	0.021	4.522	0.057
0.40	6.012	0.035	6.45	0.10	7.05	0.33
0.45	9.02	0.11	9.91	0.36	11.11	0.14
0.50	13.62	0.44	16.13	0.38	19.7	1.5
0.52	15.17	0.68	18.9	1.9	25.4	1.0

Table 9.11: The mean and the standard deviation of the hydrodynamic contribution to the relative shear viscosity for $\dot{\gamma}^* = 0.1$, 1, and 10.

	$\dot{\gamma}^* = 0.1$		$\dot{\gamma}^* = 1$		$\dot{\gamma}^* = 10$	
ϕ	η_r^H	σ	η_r^H	σ	η_r^H	σ
0.05	0.151	0.001	0.154	0.003	0.153	0.003
0.10	0.349	0.005	0.350	0.006	0.348	0.002
0.15	0.588	0.017	0.596	0.011	0.601	0.020
0.20	0.888	0.011	0.908	0.018	0.907	0.020
0.25	1.323	0.003	1.35	0.01	1.334	0.001
0.30	1.97	0.02	1.98	0.01	1.98	0.03
0.35	2.93	0.04	2.90	0.03	2.97	0.05
0.40	4.27	0.04	4.47	0.04	4.64	0.10
0.45	5.99		6.32	0.19	7.05	0.11
0.50	7.46		8.49	0.53	10.8	0.3
0.52	8.22		10.3	0.6	12.0	1.0

Table 9.12: The mean and the standard deviation of the hydrodynamic contribution to the relative shear viscosity for $\dot{\gamma}^* = 100$, 1000, and 10^4.

	$\dot{\gamma}^* = 100$		$\dot{\gamma}^* = 1000$		$\dot{\gamma}^* = 10^4$	
ϕ	η_r^H	σ	η_r^H	σ	η_r^H	σ
0.05	0.154	0.004	0.152	0.003	0.156	0.004
0.10	0.354	0.002	0.3541	4×10^{-4}	0.354	0.002
0.15	0.619	0.042	0.630	0.007	0.633	0.002
0.20	0.917	0.034	0.925	0.034	0.955	0.055
0.25	1.36	0.01	1.41	0.01	1.43	0.01
0.30	2.08	0.01	2.10	0.05	2.17	0.01
0.35	3.18	0.02	3.33	0.02	3.52	0.06
0.40	4.96	0.03	5.44	0.10	6.05	0.33
0.45	7.87	0.11	8.88	0.36	10.1	0.1
0.50	12.3	0.4	15.1	0.4	18.7	1.5
0.52	13.7	0.6	17.8	1.9	24.4	1.0

Table 9.13: The mean and the standard deviation of the interparticle force contribution to the relative shear viscosity for $\dot{\gamma}^* = 0.1$, 1, and 10.

	$\dot{\gamma}^* = 0.1$		$\dot{\gamma}^* = 1$		$\dot{\gamma}^* = 10$	
ϕ	η_r^F	σ	η_r^F	σ	η_r^F	σ
0.05	7.82×10^{-5}	2.5×10^{-5}	6.8×10^{-5}	2.3×10^{-5}	3.96×10^{-5}	3.4×10^{-6}
0.10	4.26×10^{-4}	4.5×10^{-5}	2.71×10^{-4}	9.4×10^{-5}	1.34×10^{-4}	1.8×10^{-5}
0.15	8.9×10^{-4}	5.2×10^{-4}	7.2×10^{-4}	1.2×10^{-4}	5.1×10^{-4}	1.2×10^{-4}
0.20	0.00329	5.7×10^{-4}	0.00273	6.6×10^{-4}	0.00144	4.5×10^{-4}
0.25	0.0117	1×10^{-4}	0.00954	7.8×10^{-4}	0.00441	2.6×10^{-4}
0.30	0.0384	0.0030	0.0249	0.0018	0.0151	0.0019
0.35	0.116	0.012	0.0641	0.0038	0.0426	0.0058
0.40	0.282	0.018	0.221	0.013	0.134	0.010
0.45	0.632		0.494	0.029	0.359	0.013
0.50	1.05		1.05	0.23	0.971	0.097
0.52	1.25		1.83	0.29	1.32	0.23

Table 9.14: The mean and the standard deviation of the interparticle force contribution to the relative shear viscosity for $\dot{\gamma}^* = 100$, 1000, and 10^4.

	$\dot{\gamma}^* = 100$		$\dot{\gamma}^* = 1000$		$\dot{\gamma}^* = 10^4$	
ϕ	η_r^F	σ	η_r^F	σ	η_r^F	σ
0.05	1.75×10^{-5}	6.2×10^{-6}	3.3×10^{-6}	2.1×10^{-6}	8.3×10^{-7}	5.0×10^{-7}
0.10	6.78×10^{-5}	7.7×10^{-6}	1.15×10^{-5}	9×10^{-7}	1.12×10^{-6}	3.8×10^{-7}
0.15	2.7×10^{-4}	1.7×10^{-4}	7.08×10^{-5}	1.5×10^{-6}	5.70×10^{-6}	2×10^{-8}
0.20	6.5×10^{-4}	2.3×10^{-4}	1.24×10^{-4}	5.8×10^{-5}	1.31×10^{-5}	7.7×10^{-6}
0.25	0.00201	2.0×10^{-4}	4.74×10^{-4}	1.5×10^{-5}	4.0×10^{-5}	8×10^{-6}
0.30	0.00709	3.5×10^{-5}	0.00126	6×10^{-5}	1.22×10^{-4}	5×10^{-6}
0.35	0.0202	8×10^{-4}	0.00393	1×10^{-5}	3.70×10^{-4}	4×10^{-6}
0.40	0.0551	0.0010	0.0110	7×10^{-4}	0.00126	1.8×10^{-4}
0.45	0.144	0.007	0.0264	0.0021	0.00291	2.1×10^{-4}
0.50	0.356	0.023	0.0655	0.0048	0.0084	0.0011
0.52	0.446	0.039	0.091	0.018	0.0128	5×10^{-4}

Table 9.15: The mean and the standard deviation of the total first normal stress difference, normalized by $\eta\dot{\gamma}$, for $\dot{\gamma}^* = 0.1$, 1, and 10.

	$\dot{\gamma}^* = 0.1$		$\dot{\gamma}^* = 1$		$\dot{\gamma}^* = 10$	
ϕ	$-N_1$	σ	$-N_1$	σ	$-N_1$	σ
0.05	0.00175	6.3×10^{-4}	0.00234	5.0×10^{-4}	0.00227	1.9×10^{-4}
0.10	0.00834	2.4×10^{-4}	0.00732	6.4×10^{-4}	0.00735	7×10^{-5}
0.15	0.0165	0.0036	0.0174	0.0062	0.0192	0.0050
0.20	0.044	0.011	0.045	0.010	0.043	0.014
0.25	0.089	0.014	0.106	0.027	0.083	0.012
0.30	0.219	0.065	0.200	0.027	0.202	0.018
0.35	0.507	0.016	0.342	0.085	0.360	0.004
0.40	0.738	0.052	0.705	0.077	0.800	0.037
0.45	0.922		1.00	0.11	1.38	0.48
0.50	0.256		0.152	0.076	1.52	0.39
0.52	0.783		1.17	0.14	-0.4	1.8

Table 9.16: The mean and the standard deviation of the total first normal stress difference, normalized by $\eta\dot{\gamma}$, for $\dot{\gamma}^* = 100$, 1000, and 10^4.

	$\dot{\gamma}^* = 100$		$\dot{\gamma}^* = 1000$		$\dot{\gamma}^* = 10^4$	
ϕ	$-N_1$	σ	$-N_1$	σ	$-N_1$	σ
0.05	0.0022	0.0013	0.00166	7.3×10^{-4}	0.0029	0.0018
0.10	0.00809	6×10^{-5}	0.00643	6.6×10^{-4}	0.00632	1.2×10^{-4}
0.15	0.0242	0.0079	0.0227	0.0020	0.0190	7×10^{-4}
0.20	0.0377	0.0087	0.0386	0.0087	0.0352	0.0081
0.25	0.0796	1×10^{-4}	0.084	0.035	0.089	0.010
0.30	0.235	0.001	0.195	0.036	0.173	0.019
0.35	0.333	0.094	0.367	0.050	0.378	0.079
0.40	0.87	0.12	0.88	0.21	0.94	0.15
0.45	1.24	0.29	1.77	0.33	1.20	0.09
0.50	1.22	0.32	2.03	0.55	1.45	0.17
0.52	-0.11	0.29	1.0	1.3	2.2	1.3

Table 9.17: The mean and the standard deviation of the hydrodynamic contribution to the total first normal stress difference, normalized by $\eta\dot{\gamma}$, for $\dot{\gamma}^* = 0.1$, 1, and 10.

	$\dot{\gamma}^* = 0.1$		$\dot{\gamma}^* = 1$		$\dot{\gamma}^* = 10$	
ϕ	$-N_1^H$	σ	$-N_1^H$	σ	$-N_1^H$	σ
0.05	0.00186	6.4×10^{-4}	0.00245	5.2×10^{-4}	0.00234	2.1×10^{-4}
0.10	0.00886	3.2×10^{-4}	0.00776	4.4×10^{-4}	0.00759	1.0×10^{-4}
0.15	0.0175	0.0039	0.0184	0.0062	0.0200	0.0052
0.20	0.047	0.011	0.048	0.010	0.044	0.014
0.25	0.0978	0.013	0.112	0.025	0.087	0.012
0.30	0.231	0.056	0.213	0.027	0.209	0.018
0.35	0.514	0.018	0.364	0.074	0.378	0.018
0.40	0.755	0.049	0.725	0.049	0.813	0.018
0.45	1.00		1.06	0.09	1.37	0.41
0.50	0.757		0.662	0.053	1.62	0.35
0.52	0.530		1.30	0.03	0.2	1.3

Table 9.18: The mean and the standard deviation of the hydrodynamic contribution to the total first normal stress difference, normalized by $\eta\dot{\gamma}$, for $\dot{\gamma}^* = 100$, 1000, and 10^4.

	$\dot{\gamma}^* = 100$		$\dot{\gamma}^* = 1000$		$\dot{\gamma}^* = 10^4$	
ϕ	$-N_1^H$	σ	$-N_1^H$	σ	$-N_1^H$	σ
0.05	0.0023	0.0013	0.00167	7.4×10^{-4}	0.0029	0.0018
0.10	0.00825	7×10^{-5}	0.00647	6.7×10^{-4}	0.00632	1.2×10^{-4}
0.15	0.0247	0.0082	0.0229	0.0020	0.0190	6×10^{-4}
0.20	0.0386	0.0088	0.0389	0.0087	0.0353	0.0081
0.25	0.0819	1×10^{-4}	0.085	0.034	0.089	0.010
0.30	0.240	0.002	0.197	0.035	0.174	0.019
0.35	0.346	0.091	0.370	0.050	0.378	0.078
0.40	0.88	0.11	0.88	0.21	0.94	0.15
0.45	1.27	0.28	1.77	0.32	1.20	0.09
0.50	1.39	0.30	2.06	0.54	1.46	0.17
0.52	0.14	0.31	1.1	1.3	2.2	1.3

Table 9.19: The mean and the standard deviation of the interparticle force contribution to the first normal stress difference, normalized by $\eta\dot{\gamma}$, for $\dot{\gamma}^* = 0.1$, 1, and 10.

	$\dot{\gamma}^* = 0.1$		$\dot{\gamma}^* = 1$		$\dot{\gamma}^* = 10$	
ϕ	N_1^F	σ	N_1^F	σ	N_1^F	σ
0.05	1.07×10^{-4}	1.6×10^{-5}	1.09×10^{-4}	2.1×10^{-5}	6.9×10^{-5}	1.4×10^{-5}
0.10	5.18×10^{-4}	7.5×10^{-5}	4.4×10^{-4}	2.0×10^{-4}	2.34×10^{-4}	2.9×10^{-5}
0.15	0.00106	3.4×10^{-4}	0.00102	1.1×10^{-5}	7.6×10^{-4}	2.6×10^{-4}
0.20	0.00298	2.1×10^{-4}	0.00261	2.2×10^{-4}	0.00161	8×10^{-5}
0.25	0.0086	0.0015	0.0060	0.0024	0.00405	4.5×10^{-4}
0.30	0.0123	0.0088	0.0122	2.9×10^{-4}	0.00790	2.8×10^{-4}
0.35	0.00631	0.0018	0.021	0.011	0.0182	0.0018
0.40	0.0174	0.0032	0.020	0.027	0.013	0.020
0.45	0.082		0.062	0.017	-0.01	0.07
0.50	0.500		0.510	0.023	0.099	0.037
0.52	-0.253		0.13	0.11	0.61	0.45

Table 9.20: The mean and the standard deviation of the interparticle force contribution to the first normal stress difference, normalized by $\eta\dot{\gamma}$, for $\dot{\gamma}^* = 100$, 1000, and 10^4.

	$\dot{\gamma}^* = 100$		$\dot{\gamma}^* = 1000$		$\dot{\gamma}^* = 10^4$	
ϕ	N_1^F	σ	N_1^F	σ	N_1^F	σ
0.05	3.90×10^{-5}	6.4×10^{-6}	1.40×10^{-5}	6.5×10^{-6}	3.0×10^{-6}	1.1×10^{-6}
0.10	1.56×10^{-4}	4.4×10^{-5}	4.03×10^{-5}	8.3×10^{-6}	7.31×10^{-6}	9.8×10^{-7}
0.15	4.7×10^{-4}	2.7×10^{-4}	1.89×10^{-4}	2.0×10^{-5}	2.72×10^{-5}	2.3×10^{-6}
0.20	8.7×10^{-4}	1.1×10^{-4}	2.69×10^{-4}	6.0×10^{-5}	5.4×10^{-5}	1.5×10^{-5}
0.25	0.00227	4×10^{-5}	8.2×10^{-4}	2.8×10^{-4}	1.15×10^{-4}	2.2×10^{-5}
0.30	0.00420	5.43×10^{-4}	0.00161	1.2×10^{-4}	2.88×10^{-4}	8×10^{-6}
0.35	0.0128	0.0031	0.00360	2.2×10^{-4}	6.6×10^{-4}	1.4×10^{-4}
0.40	0.0094	0.0097	0.0056	0.0019	9.1×10^{-4}	4.5×10^{-4}
0.45	0.0303	0.0086	0.0049	0.0054	0.00240	1.4×10^{-4}
0.50	0.164	0.027	0.029	0.013	0.00619	3×10^{-5}
0.52	0.257	0.018	0.038	0.021	0.00620	2.0×10^{-4}

Table 9.21: The mean and the standard deviation of the total second normal stress difference, normalized by $\eta\dot{\gamma}$, for $\dot{\gamma}^* = 0.1$, 1, and 10.

	$\dot{\gamma}^* = 0.1$		$\dot{\gamma}^* = 1$		$\dot{\gamma}^* = 10$	
ϕ	$-N_2$	σ	$-N_2$	σ	$-N_2$	σ
0.05	0.00100	7×10^{-5}	0.00112	7.7×10^{-4}	0.0016	0.0012
0.10	0.0054	0.0011	0.0048	0.0038	0.0029	0.0010
0.15	0.0056	0.0070	0.0081	0.0011	0.0079	0.0043
0.20	0.0190	0.0058	0.029	0.015	0.11	0.13
0.25	0.0525	0.0042	0.0794	0.0032	0.17	0.18
0.30	0.164	0.001	0.25	0.11	0.37	0.31
0.35	0.409	0.035	0.425	0.021	0.83	0.55
0.40	0.683	0.036	0.80	0.16	2.81	0.69
0.45	1.08		1.12	0.27	5.89	0.23
0.50	0.311		1.4	1.9	12.5	3.3
0.52	0.766		21.0	0.4	14.1	1.7

Table 9.22: The mean and the standard deviation of the total second normal stress difference, normalized by $\eta\dot{\gamma}$, for $\dot{\gamma}^* = 100$, 1000, and 10^4.

	$\dot{\gamma}^* = 100$		$\dot{\gamma}^* = 1000$		$\dot{\gamma}^* = 10^4$	
ϕ	$-N_2$	σ	$-N_2$	σ	$-N_2$	σ
0.05	3.2×10^{-4}	3.8×10^{-4}	5.0×10^{-4}	5.3×10^{-4}	3.1×10^{-4}	1.0×10^{-4}
0.10	0.0031	0.0012	0.00186	1.2×10^{-4}	4.3×10^{-4}	3.1×10^{-4}
0.15	0.010	0.011	0.0083	0.0011	0.0045	0.0019
0.20	0.023	0.010	0.012	0.014	0.010	0.013
0.25	0.0468	9×10^{-4}	0.095	0.070	0.24	0.11
0.30	0.203	0.031	0.277	0.045	0.26	0.15
0.35	0.67	0.19	1.26	0.83	1.36	0.02
0.40	1.69	0.44	3.37	0.10	3.2	1.5
0.45	4.26	0.09	9.9	1.8	7.61	0.55
0.50	7.4	3.0	13.4	1.1	12.1	3.1
0.52	6.0	1.2	18	10	15.1	3.3

Table 9.23: The mean and the standard deviation of the hydrodynamic contribution to the second normal stress difference, normalized by $\eta\dot{\gamma}$, for $\dot{\gamma}^* = 0.1$, 1, and 10.

	$\dot{\gamma}^* = 0.1$		$\dot{\gamma}^* = 1$		$\dot{\gamma}^* = 10$	
ϕ	$-N_2^H$	σ	$-N_2^H$	σ	$-N_2^H$	σ
0.05	9.01×10^{-4}	5.5×10^{-5}	0.00101	7.4×10^{-4}	0.0016	0.0012
0.10	0.0048	0.0011	0.0043	0.0037	0.00270	9.9×10^{-4}
0.15	0.0047	0.0063	0.0072	0.0013	0.0071	0.0039
0.20	0.0164	0.0051	0.027	0.014	0.0229	0.0057
0.25	0.0469	0.0037	0.0721	0.0033	0.0452	0.0067
0.30	0.146	0.006	0.1582	1×10^{-4}	0.163	0.023
0.35	0.348	0.029	0.380	0.023	0.354	0.080
0.40	0.564	0.024	0.70	0.14	0.78	0.17
0.45	0.838		0.95	0.20	1.22	0.24
0.50	0.347		0.76	0.76	1.57	0.10
0.52	0.598		1.21	0.57	1.3	1.0

Table 9.24: The mean and the standard deviation of the hydrodynamic contribution to the second normal stress difference, normalized by $\eta\dot{\gamma}$, for $\dot{\gamma}^* = 100$, 1000, and 10^4.

	$\dot{\gamma}^* = 100$		$\dot{\gamma}^* = 1000$		$\dot{\gamma}^* = 10^4$	
ϕ	$-N_2^H$	σ	$-N_2^H$	σ	$-N_2^H$	σ
0.05	3.0×10^{-4}	3.8×10^{-4}	4.9×10^{-4}	5.2×10^{-4}	3.1×10^{-4}	1.0×10^{-4}
0.10	0.0029	0.0011	0.00182	1.3×10^{-4}	4.2×10^{-4}	3.1×10^{-4}
0.15	0.010	0.011	0.00803	0.0010	0.0029	0.0041
0.20	0.0173	0.0038	0.012	0.014	0.010	0.013
0.25	0.0446	0.0021	0.053	0.011	0.0271	0.0076
0.30	0.166	0.010	0.136	0.014	0.099	0.032
0.35	0.410	0.065	0.439	0.063	0.345	0.080
0.40	0.929	0.067	0.975	0.095	0.952	0.076
0.45	1.55	0.11	1.73	0.19	2.22	0.12
0.50	1.53	0.37	2.67	0.38	3.39	0.74
0.52	1.89	0.78	2.70	0.04	5.45	0.40

Table 9.25: The mean and the standard deviation of the interparticle force contribution to the second normal stress difference, normalized by $\eta\dot{\gamma}$, for $\dot{\gamma}^* = 0.1$, 1, and 10.

	$\dot{\gamma}^* = 0.1$		$\dot{\gamma}^* = 1$		$\dot{\gamma}^* = 10$	
ϕ	$-N_2^F$	σ	$-N_2^F$	σ	$-N_2^F$	σ
0.05	1.04×10^{-4}	1.5×10^{-5}	1.04×10^{-4}	2.9×10^{-5}	6.1×10^{-5}	3.2×10^{-5}
0.10	6.77×10^{-4}	6.1×10^{-5}	4.7×10^{-4}	1.5×10^{-4}	2.45×10^{-4}	2.9×10^{-5}
0.15	9.2×10^{-4}	7.0×10^{-4}	9.4×10^{-4}	1.4×10^{-4}	7.3×10^{-4}	3.6×10^{-4}
0.20	0.00264	7.7×10^{-4}	0.0026	0.0011	0.09	0.12
0.25	0.00562	5.9×10^{-4}	0.00733	1.3×10^{-4}	0.13	0.18
0.30	0.0183	0.0047	0.09	0.11	0.21	0.29
0.35	0.0611	0.0059	0.0457	0.0011	0.48	0.63
0.40	0.119	0.012	0.095	0.028	2.03	0.52
0.45	0.238		0.170	0.069	4.67	0.47
0.50	-0.0364		0.6	1.2	10.9	3.4
0.52	0.168		19.8	0.9	12.8	2.7

Table 9.26: The mean and the standard deviation of the interparticle force contribution to the second normal stress difference, normalized by $\eta\dot{\gamma}$, for $\dot{\gamma}^* = 100$, 1000, and 10^4.

	$\dot{\gamma}^* = 100$		$\dot{\gamma}^* = 1000$		$\dot{\gamma}^* = 10^4$	
ϕ	$-N_2^F$	σ	$-N_2^F$	σ	$-N_2^F$	σ
0.05	2.93×10^{-5}	1×10^{-7}	1.12×10^{-5}	4.5×10^{-6}	2.5×10^{-6}	1.0×10^{-6}
0.10	1.60×10^{-4}	2.4×10^{-5}	4.11×10^{-5}	5.1×10^{-6}	7.4×10^{-6}	1.4×10^{-6}
0.15	4.4×10^{-4}	4.2×10^{-4}	2.5×10^{-4}	1.7×10^{-4}	0.0016	0.0022
0.20	0.0054	0.0067	1.4×10^{-4}	1.2×10^{-4}	3.5×10^{-5}	1.2×10^{-5}
0.25	0.0022	0.0012	0.042	0.059	0.21	0.12
0.30	0.036	0.040	0.141	0.060	0.17	0.12
0.35	0.26	0.12	0.82	0.89	1.01	0.09
0.40	0.76	0.50	2.40	0.01	2.2	1.4
0.45	2.71	0.03	8.2	1.6	5.39	0.66
0.50	5.8	2.6	10.7	1.4	8.7	2.3
0.52	4.15	0.47	16	10	9.7	3.7

Table 9.27: The mean and the standard deviation of the total suspension pressure, normalized by $\eta\dot{\gamma}$, for $\dot{\gamma}^* = 0.1$, 1, and 10.

	$\dot{\gamma}^* = 0.1$		$\dot{\gamma}^* = 1$		$\dot{\gamma}^* = 10$	
ϕ	Π	σ	Π	σ	Π	σ
0.05	0.0043	0.0011	0.00496	9.5×10^{-4}	0.00624	2.9×10^{-4}
0.10	0.0200	0.0031	0.0193	0.0033	0.0144	0.0020
0.15	0.0379	0.0097	0.0400	0.0051	0.0397	0.0086
0.20	0.132	0.023	0.124	0.023	0.109	0.028
0.25	0.333	0.014	0.333	0.007	0.268	0.022
0.30	0.756	0.001	0.697	0.023	0.653	0.060
0.35	1.57	0.05	1.45	0.07	1.28	0.08
0.40	2.80	0.04	2.88	0.10	2.69	0.02
0.45	4.59		4.72	0.12	5.07	0.25
0.50	6.94		8.4	1.4	10.4	0.8
0.52	8.00		11.7	0.7	13.2	1.5

Table 9.28: The mean and the standard deviation of the total suspension pressure, normalized by $\eta\dot{\gamma}$, for $\dot{\gamma}^* = 100$, 1000, and 10^4.

	$\dot{\gamma}^* = 100$		$\dot{\gamma}^* = 1000$		$\dot{\gamma}^* = 10^4$	
ϕ	Π	σ	Π	σ	Π	σ
0.05	0.0050	0.0014	0.0025	0.0011	0.0043	0.0023
0.10	0.0161	3.3×10^{-4}	0.0106	0.0017	0.0080	0.0033
0.15	0.044	0.015	0.0415	0.0043	0.0277	0.0064
0.20	0.0094	0.019	0.070	0.019	0.056	0.033
0.25	0.243	0.019	0.221	0.002	0.151	0.013
0.30	0.635	0.008	0.494	0.027	0.384	0.018
0.35	1.34	0.06	0.805	0.67	0.937	0.007
0.40	2.79	0.02	2.78	0.17	2.64	0.33
0.45	5.43	0.20	5.82	0.29	5.54	0.38
0.50	11.0	0.5	12.7	0.8	14.8	2.0
0.52	13.1	0.8	15.6	1.2	22.1	0.9

Table 9.29: The mean and the standard deviation of the hydrodynamic contribution to the suspension pressure, normalized by $\eta\dot{\gamma}$, for $\dot{\gamma}^* = 0.1$, 1, and 10.

	$\dot{\gamma}^* = 0.1$		$\dot{\gamma}^* = 1$		$\dot{\gamma}^* = 10$	
ϕ	Π^H	σ	Π^H	σ	Π^H	σ
0.05	0.00409	9.7×10^{-4}	0.00476	9.0×10^{-4}	0.00612	2.9×10^{-4}
0.10	0.0190	0.0031	0.0186	0.0030	0.0141	0.0020
0.15	0.0356	0.0088	0.0381	0.0049	0.0383	0.0083
0.20	0.124	0.022	0.117	0.022	0.105	0.027
0.25	0.306	0.013	0.312	0.007	0.257	0.021
0.30	0.680	0.006	0.645	0.019	0.619	0.057
0.35	1.35	0.04	1.30	0.06	1.18	0.06
0.40	2.22	0.02	2.42	0.12	2.40	0.02
0.45	3.17		3.60	0.10	4.27	0.21
0.50	3.76		4.92	0.56	7.68	0.45
0.52	4.02		6.55	0.45	9.0	1.1

Table 9.30: The mean and the standard deviation of the hydrodynamic contribution to the suspension pressure, normalized by $\eta\dot{\gamma}$, for $\dot{\gamma}^* = 100$, 1000, and 10^4.

	$\dot{\gamma}^* = 100$		$\dot{\gamma}^* = 1000$		$\dot{\gamma}^* = 10^4$	
ϕ	Π^H	σ	Π^H	σ	Π^H	σ
0.05	0.0049	0.0013	0.0025	0.0011	0.0043	0.0023
0.10	0.0159	3×10^{-4}	0.0105	0.0017	0.0080	0.0033
0.15	0.043	0.0015	0.0412	0.0043	0.0277	0.0064
0.20	0.093	0.018	0.069	0.019	0.056	0.033
0.25	0.237	0.018	0.219	0.002	0.151	0.013
0.30	0.617	0.007	0.489	0.027	0.383	0.018
0.35	1.29	0.05	0.79	0.67	0.935	0.007
0.40	2.65	0.02	2.74	0.17	2.63	0.33
0.45	5.05	0.18	5.74	0.29	5.53	0.37
0.50	9.77	0.46	12.4	0.8	14.7	2.0
0.52	11.5	0.8	15.3	1.2	22.1	0.9

Table 9.31: The mean and the standard deviation of the interparticle force contribution to the suspension pressure, normalized by $\eta\dot{\gamma}$, for $\dot{\gamma}^* = 0.1$, 1, and 10.

	$\dot{\gamma}^* = 0.1$		$\dot{\gamma}^* = 1$		$\dot{\gamma}^* = 10$	
ϕ	Π^F	σ	Π^F	σ	Π^F	σ
0.05	2.25×10^{-4}	8.4×10^{-5}	2.00×10^{-4}	4.9×10^{-5}	1.27×10^{-4}	2×10^{-6}
0.10	9.57×10^{-4}	1.3×10^{-5}	6.8×10^{-4}	2.4×10^{-4}	3.85×10^{-4}	2.0×10^{-5}
0.15	0.00226	9.6×10^{-4}	0.00187	2.2×10^{-4}	0.00140	3.1×10^{-4}
0.20	0.0076	0.0011	0.0062	0.0011	0.0038	0.0010
0.25	0.0267	5×10^{-4}	0.0205	4×10^{-4}	0.0111	0.0010
0.30	0.0764	0.0045	0.0520	0.0047	0.0338	0.0032
0.35	0.221	0.011	0.149	0.009	0.096	0.014
0.40	0.577	0.022	0.465	0.011	0.291	8×10^{-4}
0.45	1.42		1.12	0.02	0.798	0.042
0.50	3.18		3.44	0.81	2.67	0.40
0.52	3.99		5.20	0.23	4.23	0.40

Table 9.32: The mean and the standard deviation of the interparticle force contribution to the suspension pressure, normalized by $\eta\dot{\gamma}$, for $\dot{\gamma}^* = 100$, 1000, and 10^4.

	$\dot{\gamma}^* = 100$		$\dot{\gamma}^* = 1000$		$\dot{\gamma}^* = 10^4$	
ϕ	Π^F	σ	Π^F	σ	Π^F	σ
0.05	7.4×10^{-5}	2.5×10^{-5}	2.2×10^{-5}	1.2×10^{-5}	7.5×10^{-6}	3.5×10^{-6}
0.10	2.35×10^{-4}	8×10^{-6}	6.0×10^{-5}	1.3×10^{-5}	1.10×10^{-5}	1.4×10^{-6}
0.15	8.6×10^{-4}	3.7×10^{-4}	3.23×10^{-4}	2.1×10^{-5}	5.95×10^{-5}	7×10^{-7}
0.20	0.00195	6.1×10^{-4}	5.9×10^{-4}	1.3×10^{-4}	1.07×10^{-4}	3.5×10^{-5}
0.25	0.00574	4.3×10^{-4}	0.00191	3×10^{-5}	2.99×10^{-4}	4.1×10^{-5}
0.30	0.0181	6×10^{-4}	0.00459	2.7×10^{-4}	7.76×10^{-4}	7×10^{-7}
0.35	0.0510	0.0022	0.0128	4×10^{-4}	0.00205	4×10^{-5}
0.40	0.1332	0.3×10^{-4}	0.0349	1×10^{-4}	0.00580	8.1×10^{-4}
0.45	0.380	0.018	0.0893	0.0027	0.0133	5×10^{-4}
0.50	1.19	0.06	0.263	0.016	0.0418	0.0049
0.52	1.65	0.03	0.370	0.031	0.0645	4×10^{-4}

Table 9.33: The relative shear viscosity (the total, together with the hydrodynamic and interparticle force contributions) from simulation runs with 64 particles in the unit cell.

	$\dot{\gamma}^* = 10$			$\dot{\gamma}^* = 100$			$\dot{\gamma}^* = 1000$		
ϕ	η_r	η_r^H	η_r^F	η_r	η_r^H	η_r^F	η_r	η_r^H	η_r^F
0.30	3.03	2.01	0.0155	3.11	2.10	0.00833	3.14	2.14	0.00154
0.40	5.66	4.53	0.123	5.91	4.85	0.0518	6.43	5.42	0.0107
0.45	8.37	7.03	0.339	8.86	7.72	0.132	9.84	8.82	0.0253
0.50	12.27	10.41	0.866	12.38	11.10	0.275	16.03	14.97	0.0631
0.52	15.65	13.22	1.43	13.49	12.14	0.353	20.69	19.60	0.0989

Table 9.34: The first normal stress difference (the total, together with the hydrodynamic and interparticle force contributions), normalized by $\eta\dot{\gamma}$, from simulation runs with 64 particles in the unit cell.

	$\dot{\gamma}^* = 10$			$\dot{\gamma}^* = 100$			$\dot{\gamma}^* = 1000$		
ϕ	$-N_1$	$-N_1^H$	N_1^F	$-N_1$	$-N_1^H$	N_1^F	$-N_1$	$-N_1^H$	N_1^F
0.30	0.238	0.245	0.00714	0.259	0.263	0.00411	0.276	0.277	0.00132
0.40	1.03	1.02	-0.0150	0.826	0.836	0.00977	0.875	0.880	0.00501
0.45	1.35	1.33	-0.0219	1.40	1.41	0.0109	1.91	1.91	0.000873
0.50	1.80	1.75	-0.0479	1.52	1.56	0.0405	2.32	2.33	0.0110
0.52	2.00	1.92	-0.0797	1.10	1.17	0.0730	2.66	2.67	0.0109

Table 9.35: The second normal stress difference (the total, together with the hydrodynamic and interparticle force contributions), normalized by $\eta\dot{\gamma}$, from simulation runs with 64 particles in the unit cell.

	$\dot{\gamma}^* = 10$			$\dot{\gamma}^* = 100$			$\dot{\gamma}^* = 1000$		
ϕ	$-N_2$	$-N_2^H$	$-N_2^F$	$-N_2$	$-N_2^H$	$-N_2^F$	$-N_2$	$-N_2^H$	$-N_2^F$
0.30	0.328	0.172	0.157	0.806	0.187	0.620	0.371	0.147	0.224
0.40	4.07	0.668	3.40	1.85	0.848	0.998	5.44	0.980	4.46
0.45	9.85	1.39	8.46	9.30	1.62	7.68	26.5	1.54	25.0
0.50	11.1	1.52	9.55	13.4	1.96	11.4	16.0	2.79	13.2
0.52	22.4	2.28	20.1	13.9	0.367	13.6	20.3	4.51	15.8

Table 9.36: The suspension pressure (the total, together with the hydrodynamic and interparticle force contributions), normalized by $\eta\dot{\gamma}$, from simulation runs with 64 particles in the unit cell.

	$\dot{\gamma}^* = 10$			$\dot{\gamma}^* = 100$			$\dot{\gamma}^* = 1000$		
ϕ	Π	Π^H	Π^F	Π	Π^H	Π^F	Π	Π^H	Π^F
0.30	0.747	0.712	0.0351	0.753	0.733	0.0204	0.644	0.639	0.00531
0.40	2.83	2.56	0.269	2.86	2.73	0.128	2.93	2.90	0.0340
0.45	5.38	4.55	0.828	5.50	5.15	0.355	5.91	5.82	0.0903
0.50	10.29	7.82	2.47	9.37	8.45	0.918	12.49	12.24	0.256
0.52	14.66	10.47	4.19	11.48	9.98	1.51	18.86	18.44	0.416

Table 9.37: The translational short-time self-diffusion coefficients, normalized by the diffusion coefficient of an isolated Brownian particle, $kT/6\pi\eta a$, for $\dot{\gamma}^* = 0.1$, 1, and 10.

	$\dot{\gamma}^* = 0.1$			$\dot{\gamma}^* = 1$			$\dot{\gamma}^* = 10$		
ϕ	$D^s_{0_{xx}}$	$D^s_{0_{yy}}$	$D^s_{0_{zz}}$	$D^s_{0_{xx}}$	$D^s_{0_{yy}}$	$D^s_{0_{zz}}$	$D^s_{0_{xx}}$	$D^s_{0_{yy}}$	$D^s_{0_{zz}}$
0.05	0.666	0.647	0.647	0.656	0.637	0.643	0.655	0.638	0.644
0.10	0.583	0.553	0.554	0.585	0.554	0.560	0.585	0.554	0.561
0.15	0.512	0.477	0.484	0.510	0.475	0.486	0.509	0.474	0.486
0.20	0.438	0.403	0.399	0.435	0.400	0.404	0.430	0.395	0.393
0.25	0.359	0.327	0.320	0.360	0.328	0.328	0.359	0.326	0.318
0.30	0.286	0.262	0.261	0.291	0.261	0.265	0.287	0.260	0.259
0.35	0.222	0.205	0.206	0.227	0.203	0.206	0.221	0.198	0.199
0.40	0.167	0.154	0.153	0.164	0.150	0.149	0.157	0.145	0.145
0.45	0.127	0.115	0.113	0.124	0.112	0.111	0.113	0.106	0.104
0.50	0.0981	0.0877	0.0861	0.0908	0.0781	0.0746	0.0784	0.0738	0.0699
0.52	0.0889	0.0810	0.0821	0.0762	0.0724	0.0681	0.0700	0.0624	0.0600

Table 9.38: The translational short-time self-diffusion coefficients, normalized by $kT/6\pi\eta a$, for $\dot{\gamma}^* = 100$, 1000, and 10^4.

	$\dot{\gamma}^* = 100$			$\dot{\gamma}^* = 1000$			$\dot{\gamma}^* = 10^4$		
ϕ	$D^s_{0_{xx}}$	$D^s_{0_{yy}}$	$D^s_{0_{zz}}$	$D^s_{0_{xx}}$	$D^s_{0_{yy}}$	$D^s_{0_{zz}}$	$D^s_{0_{xx}}$	$D^s_{0_{yy}}$	$D^s_{0_{zz}}$
0.05	0.649	0.631	0.637	0.650	0.637	0.642	0.636	0.624	0.626
0.10	0.583	0.551	0.566	0.582	0.551	0.565	0.578	0.550	0.555
0.15	0.497	0.464	0.480	0.490	0.460	0.471	0.479	0.451	0.466
0.20	0.430	0.395	0.394	0.426	0.394	0.395	0.423	0.393	0.407
0.25	0.358	0.323	0.321	0.347	0.318	0.318	0.347	0.316	0.316
0.30	0.276	0.252	0.253	0.279	0.249	0.252	0.267	0.242	0.238
0.35	0.212	0.189	0.190	0.204	0.182	0.183	0.196	0.172	0.177
0.40	0.149	0.137	0.137	0.140	0.127	0.126	0.126	0.115	0.114
0.45	0.104	0.0958	0.0946	0.0913	0.0854	0.0835	0.0822	0.0748	0.0749
0.50	0.0699	0.0623	0.0595	0.0580	0.0529	0.0514	0.0462	0.0425	0.0416
0.52	0.0620	0.0556	0.0537	0.0469	0.0439	0.0415	0.0364	0.0353	0.0336

Table 9.39: The rotational short-time self-diffusion coefficients, normalized by the diffusion coefficient of an isolated Brownian particle, $kT/8\pi\eta a^3$, for $\dot{\gamma}^* = 0.1$, 1, and 10.

	$\dot{\gamma}^* = 0.1$			$\dot{\gamma}^* = 1$			$\dot{\gamma}^* = 10$		
ϕ	$D^s_{r_{xx}}$	$D^s_{r_{yy}}$	$D^s_{r_{zz}}$	$D^s_{r_{xx}}$	$D^s_{r_{yy}}$	$D^s_{r_{zz}}$	$D^s_{r_{xx}}$	$D^s_{r_{yy}}$	$D^s_{r_{zz}}$
0.05	0.884	0.902	0.908	0.876	0.896	0.897	0.875	0.896	0.895
0.10	0.845	0.871	0.875	0.850	0.878	0.874	0.850	0.879	0.874
0.15	0.803	0.836	0.836	0.801	0.838	0.829	0.799	0.836	0.826
0.20	0.743	0.779	0.783	0.740	0.779	0.776	0.728	0.766	0.770
0.25	0.665	0.701	0.711	0.671	0.709	0.707	0.656	0.696	0.707
0.30	0.604	0.631	0.634	0.603	0.638	0.632	0.593	0.629	0.626
0.35	0.544	0.562	0.560	0.536	0.566	0.557	0.521	0.550	0.545
0.40	0.478	0.491	0.490	0.465	0.481	0.478	0.450	0.464	0.460
0.45	0.424	0.431	0.433	0.414	0.423	0.421	0.396	0.399	0.399
0.50	0.386	0.381	0.382	0.355	0.363	0.369	0.341	0.341	0.344
0.52	0.380	0.366	0.360	0.348	0.342	0.345	0.321	0.322	0.325

Table 9.40: The rotational short-time self-diffusion coefficients, normalized by $kT/8\pi\eta a^3$, for $\dot{\gamma}^* = 100$, 1000, and 10^4.

	$\dot{\gamma}^* = 100$			$\dot{\gamma}^* = 1000$			$\dot{\gamma}^* = 10^4$		
ϕ	$D^s_{r_{xx}}$	$D^s_{r_{yy}}$	$D^s_{r_{zz}}$	$D^s_{r_{xx}}$	$D^s_{r_{yy}}$	$D^s_{r_{zz}}$	$D^s_{r_{xx}}$	$D^s_{r_{yy}}$	$D^s_{r_{zz}}$
0.05	0.866	0.887	0.889	0.872	0.893	0.889	0.853	0.872	0.872
0.10	0.850	0.882	0.866	0.849	0.881	0.864	0.843	0.874	0.862
0.15	0.782	0.819	0.808	0.769	0.806	0.797	0.751	0.787	0.778
0.20	0.723	0.764	0.765	0.719	0.759	0.758	0.742	0.778	0.764
0.25	0.651	0.697	0.698	0.638	0.681	0.678	0.627	0.675	0.669
0.30	0.574	0.610	0.602	0.560	0.607	0.597	0.528	0.572	0.574
0.35	0.495	0.528	0.521	0.468	0.504	0.496	0.437	0.480	0.462
0.40	0.426	0.441	0.435	0.388	0.408	0.401	0.343	0.359	0.356
0.45	0.364	0.371	0.368	0.322	0.327	0.324	0.276	0.285	0.280
0.50	0.303	0.309	0.312	0.264	0.266	0.265	0.215	0.214	0.213
0.52	0.294	0.295	0.295	0.245	0.242	0.244	0.200	0.195	0.196

Table 9.41: The mean and the standard deviation of the average short-time translational self-diffusivity coefficient, normalized by $kT/6\pi\eta a$, for $\dot{\gamma}^* = 0.1$, 1, and 10.

	$\dot{\gamma}^* = 0.1$		$\dot{\gamma}^* = 1$		$\dot{\gamma}^* = 10$	
ϕ	$\langle D_0^s \rangle$	σ	$\langle D_0^s \rangle$	σ	$\langle D_0^s \rangle$	σ
0.05	0.653	0.007	0.646	0.003	0.645	0.001
0.10	0.563	0.001	0.566	0.002	0.567	0.001
0.15	0.491	0.005	0.490	0.003	0.490	0.003
0.20	0.413	0.004	0.413	0.002	0.406	0.003
0.25	0.335	0.001	0.338	0.002	0.334	0.004
0.30	0.269	0.002	0.273	0.002	0.269	0.003
0.35	0.211	0.002	0.212	0.001	0.206	0.006
0.40	0.158	0.001	0.155	0.001	0.149	0.001
0.45	0.119		0.116	0.001	0.108	0.002
0.50	0.0906		0.0812	0.0050	0.0740	0.0018
0.52	0.0840		0.0722	0.0004	0.0641	0.0001

Table 9.42: The mean and the standard deviation of the average short-time translational self-diffusivity coefficient, normalized by $kT/6\pi\eta a$, for $\dot{\gamma}^* = 100$, 1000, and 10^4.

	$\dot{\gamma}^* = 100$		$\dot{\gamma}^* = 1000$		$\dot{\gamma}^* = 10^4$	
ϕ	$\langle D_0^s \rangle$	σ	$\langle D_0^s \rangle$	σ	$\langle D_0^s \rangle$	σ
0.05	0.639	0.007	0.643	0.001	0.629	0.010
0.10	0.567	0.003	0.566	0.003	0.561	0.003
0.15	0.480	0.004	0.474	0.010	0.465	0.009
0.20	0.406	0.001	0.405	0.001	0.408	0.004
0.25	0.334	0.003	0.328	0.006	0.326	0.004
0.30	0.260	0.002	0.260	0.003	0.249	0.001
0.35	0.197	0.003	0.190	0.004	0.182	0.001
0.40	0.141	0.002	0.131	0.002	0.118	0.005
0.45	0.0981	0.0015	0.0867	0.0002	0.0773	0.0001
0.50	0.0639	0.0008	0.0541	0.0006	0.0435	0.0025
0.52	0.0571	0.0005	0.0441	0.0015	0.0351	0.0016

Table 9.43: The mean and the standard deviation of the average short-time rotational self-diffusivity coefficient, normalized by $kT/8\pi\eta a^3$, for $\dot{\gamma}^* = 0.1$, 1, and 10.

	$\dot{\gamma}^* = 0.1$		$\dot{\gamma}^* = 1$		$\dot{\gamma}^* = 10$	
ϕ	$\langle D_r^s \rangle$	σ	$\langle D_r^s \rangle$	σ	$\langle D_r^s \rangle$	σ
0.05	0.898	0.006	0.889	0.002	0.889	0.002
0.10	0.864	0.003	0.868	0.002	0.868	0.001
0.15	0.825	0.006	0.823	0.008	0.820	0.005
0.20	0.768	0.005	0.765	0.001	0.755	0.004
0.25	0.692	0.004	0.696	0.003	0.687	0.008
0.30	0.623	0.003	0.625	0.003	0.616	0.009
0.35	0.555	0.005	0.553	0.001	0.539	0.012
0.40	0.486	0.001	0.475	0.001	0.458	0.003
0.45	0.429		0.420	0.001	0.398	0.004
0.50	0.383		0.363	0.008	0.342	0.004
0.52	0.369		0.345	0.001	0.322	0.001

Table 9.44: The mean and the standard deviation of the average short-time rotational self-diffusivity coefficient, normalized by $kT/8\pi\eta a^3$, for $\dot{\gamma}^* = 100$, 1000, and 10^4.

	$\dot{\gamma}^* = 100$		$\dot{\gamma}^* = 1000$		$\dot{\gamma}^* = 10^4$	
ϕ	$\langle D_r^s \rangle$	σ	$\langle D_r^s \rangle$	σ	$\langle D_r^s \rangle$	σ
0.05	0.880	0.010	0.885	0.001	0.866	0.013
0.10	0.866	0.006	0.865	0.005	0.859	0.003
0.15	0.803	0.009	0.791	0.010	0.772	0.009
0.20	0.750	0.004	0.745	0.001	0.761	0.013
0.25	0.682	0.006	0.666	0.009	0.657	0.010
0.30	0.596	0.002	0.588	0.005	0.558	0.002
0.35	0.515	0.007	0.489	0.011	0.460	0.012
0.40	0.434	0.004	0.399	0.003	0.353	0.013
0.45	0.368	0.004	0.325	0.001	0.280	0.001
0.50	0.308	0.001	0.265	0.001	0.214	0.007
0.52	0.295	0.001	0.243	0.003	0.197	0.006

Table 9.45: The short-time translational self-diffusivity coefficients, normalized by $kt/6\pi\eta a$, obtained in simulations with 64 particles in the unit cell.

	$\dot{\gamma}^* = 10$			$\dot{\gamma}^* = 100$			$\dot{\gamma}^* = 1000$		
ϕ	$D^s_{0_{xx}}$	$D^s_{0_{yy}}$	$D^s_{0_{zz}}$	$D^s_{0_{xx}}$	$D^s_{0_{yy}}$	$D^s_{0_{zz}}$	$D^s_{0_{xx}}$	$D^s_{0_{yy}}$	$D^s_{0_{zz}}$
0.30	0.315	0.285	0.289	0.304	0.278	0.277	0.297	0.270	0.268
0.40	0.176	0.165	0.162	0.170	0.156	0.154	0.158	0.142	0.145
0.45	0.121	0.117	0.115	0.116	0.108	0.107	0.101	0.0950	0.0912
0.50	0.0845	0.0813	0.0777	0.0775	0.0741	0.0717	0.0611	0.0583	0.0560
0.52	0.0711	0.0672	0.0642	0.0686	0.0615	0.0586	0.0483	0.0480	0.0451

Table 9.46: The short-time rotational self-diffusivity coefficients, normalized by $kT/8\pi\eta a^3$, obtained in simulations with 64 particles in the unit cell.

	$\dot{\gamma}^* = 10$			$\dot{\gamma}^* = 100$			$\dot{\gamma}^* = 1000$		
ϕ	$D^s_{r_{xx}}$	$D^s_{r_{yy}}$	$D^s_{r_{zz}}$	$D^s_{r_{xx}}$	$D^s_{r_{yy}}$	$D^s_{r_{zz}}$	$D^s_{r_{xx}}$	$D^s_{r_{yy}}$	$D^s_{r_{zz}}$
0.30	0.594	0.630	0.620	0.574	0.604	0.602	0.548	0.584	0.582
0.40	0.456	0.466	0.466	0.432	0.447	0.445	0.394	0.414	0.401
0.45	0.394	0.395	0.394	0.367	0.374	0.369	0.321	0.325	0.324
0.50	0.341	0.339	0.343	0.318	0.314	0.316	0.262	0.261	0.261
0.52	0.317	0.317	0.320	0.295	0.294	0.301	0.243	0.240	0.240

Table 9.47: The average short-time translational and rotational self-diffusivity coefficients, normalized by $kT/6\pi\eta a$ and $kT/8\pi\eta a^3$, respectively, obtained in simulations with 64 particles in the unit cell.

	$\dot{\gamma}^* = 10$		$\dot{\gamma}^* = 100$		$\dot{\gamma}^* = 1000$	
ϕ	$\langle D^s_0 \rangle$	$\langle D^s_r \rangle$	$\langle D^s_0 \rangle$	$\langle D^s_r \rangle$	$\langle D^s_0 \rangle$	$\langle D^s_r \rangle$
0.30	0.296	0.614	0.286	0.593	0.278	0.571
0.40	0.167	0.463	0.160	0.441	0.148	0.403
0.45	0.118	0.395	0.110	0.370	0.0958	0.323
0.50	0.0812	0.341	0.0744	0.316	0.0585	0.262
0.52	0.0675	0.318	0.0629	0.297	0.0471	0.240

Table 9.48: The mean ($D^s_{\infty,yy}$) and the standard deviation (σ) of the long-time self-diffusivity, normalized by $\dot{\gamma}a^2$, in the velocity-gradient direction for $\dot{\gamma}^* = 0.1$, 1, and 10.

	$\dot{\gamma}^* = 0.1$		$\dot{\gamma}^* = 1$		$\dot{\gamma}^* = 10$	
ϕ	$D^s_{\infty,yy}$	σ	$D^s_{\infty,yy}$	σ	$D^s_{\infty,yy}$	σ
0.05	0.0037	0.0064	0.0036	0.0036	0.0031	0.0041
0.10	0.0018	0.0025	0.0022	0.0046	0.0031	0.0031
0.15	0.0028	0.0039	0.0022	0.0044	0.0023	0.0030
0.20	0.0023	0.0041	0.0032	0.0062	0.0053	0.0067
0.25	0.0035	0.0040	0.0103	0.0068	0.0108	0.0054
0.30	0.0149	0.0083	0.0133	0.0096	0.0220	0.0127
0.35	0.0268	0.0127	0.0221	0.0150	0.0157	0.0068
0.40	0.0262	0.0084	0.0291	0.0113	0.0371	0.0281
0.45	0.0280	0.0133	0.0234	0.0161	0.0228	0.0154
0.50	0.0046	0.0038	0.0243	0.0114	0.0204	0.0177
0.52	0.0021	0.0034	0.0017	0.0029	0.0173	0.0121

Table 9.49: The mean ($D^s_{\infty,yy}$) and the standard deviation (σ) of the long-time self-diffusivity, normalized by $\dot{\gamma}a^2$, in the velocity-gradient direction for $\dot{\gamma}^* = 100$, 1000, and 10^4.

	$\dot{\gamma}^* = 100$		$\dot{\gamma}^* = 1000$		$\dot{\gamma}^* = 10^4$	
ϕ	$D^s_{\infty,yy}$	σ	$D^s_{\infty,yy}$	σ	$D^s_{\infty,yy}$	σ
0.05	0.0013	0.0042	0.0037	0.0041	0.0046	0.0062
0.10	0.0032	0.0025	0.0019	0.0024	0.0031	0.0049
0.15	0.0025	0.0031	0.0045	0.0058	0.0057	0.0049
0.20	0.0058	0.0058	0.0025	0.0039	0.0046	0.0028
0.25	0.0079	0.0064	0.0106	0.0067	0.0058	0.0054
0.30	0.0113	0.0086	0.0231	0.0089	0.0130	0.0063
0.35	0.0243	0.0168	0.0243	0.0098	0.0171	0.0173
0.40	0.0428	0.0281	0.0290	0.0179	0.0275	0.0206
0.45	0.0309	0.0184	0.0430	0.0208	0.0391	0.0253
0.50	0.0216	0.0146	0.0315	0.0177	0.0513	0.0262
0.52	0.0183	0.0193	0.0259	0.0162	0.0561	0.0231

Table 9.50: The mean ($D^s_{\infty,zz}$) and the standard deviation (σ) of the long-time self-diffusivity, normalized by $\dot{\gamma}a^2$, in the vorticity direction for $\dot{\gamma}^* = 0.1$, 1, and 10.

	$\dot{\gamma}^* = 0.1$		$\dot{\gamma}^* = 1$		$\dot{\gamma}^* = 10$	
ϕ	$D^s_{\infty,zz}$	σ	$D^s_{\infty,zz}$	σ	$D^s_{\infty,zz}$	σ
0.05	0.0017	0.0024	0.0018	0.0020	0.0007	0.0010
0.10	0.0005	0.0008	0.0013	0.0019	0.0006	0.0008
0.15	0.0018	0.0013	0.0021	0.0018	0.0020	0.0021
0.20	0.0019	0.0010	0.0027	0.0026	0.0024	0.0022
0.25	0.0035	0.0022	0.0062	0.0041	0.0046	0.0031
0.30	0.0071	0.0044	0.0066	0.0048	0.0081	0.0044
0.35	0.0122	0.0060	0.0205	0.0118	0.0163	0.0049
0.40	0.0231	0.0121	0.0212	0.0094	0.0140	0.0108
0.45	0.0210	0.0079	0.0372	0.0177	0.0216	0.0169
0.50	0.0093	0.0096	0.0200	0.0133	0.0185	0.0195
0.52	0.0019	0.0036	0.0020	0.0020	0.0189	0.0147

Table 9.51: The mean ($D^s_{\infty,zz}$) and the standard deviation (σ) of the long-time self-diffusivity, normalized by $\dot{\gamma}a^2$, in the vorticity direction for $\dot{\gamma}^* = 100$, 1000, and 10^4.

	$\dot{\gamma}^* = 100$		$\dot{\gamma}^* = 1000$		$\dot{\gamma}^* = 10^4$	
ϕ	$D^s_{\infty,zz}$	σ	$D^s_{\infty,zz}$	σ	$D^s_{\infty,zz}$	σ
0.05	-0.0002	0.0023	0.0025	0.0052	0.0021	0.0019
0.10	0.0003	0.0012	0.0008	0.0005	0.0011	0.0014
0.15	0.0012	0.0011	0.0016	0.0011	0.0014	0.0009
0.20	0.0025	0.0024	0.0018	0.0023	0.0021	0.0019
0.25	0.0022	0.0020	0.0018	0.0014	0.0035	0.0015
0.30	0.0030	0.0032	0.0035	0.0034	0.0018	0.0032
0.35	0.0100	0.0074	0.0093	0.0081	0.0097	0.0047
0.40	0.0238	0.0085	0.0227	0.0104	0.0134	0.0093
0.45	0.0308	0.0148	0.0396	0.0231	0.0250	0.0148
0.50	0.0335	0.0207	0.0319	0.0140	0.0328	0.0150
0.52	0.0155	0.0107	0.0283	0.0142	0.0390	0.0229

Table 9.52: The mean square (T_x^{tr}) and the standard deviation (σ) of the particle translational velocity fluctuation, normalized by $(\dot{\gamma}a)^2$, in the flow direction for $\dot{\gamma}^* =$ 0.1, 1, and 10.

	$\dot{\gamma}^* = 0.1$		$\dot{\gamma}^* = 1$		$\dot{\gamma}^* = 10$	
ϕ	T_x^{tr}	σ	T_x^{tr}	σ	T_x^{tr}	σ
0.05	0.00640	0.00076	0.00631	0.00094	0.00637	0.00073
0.10	0.0165	0.0011	0.0160	0.0047	0.0144	0.0061
0.15	0.0187	0.0016	0.0219	0.0044	0.0230	0.0028
0.20	0.0256	0.0027	0.0262	0.0006	0.0244	0.0015
0.25	0.0404	0.0016	0.0435	0.0010	0.0516	0.0107
0.30	0.0616	0.0010	0.0581	0.0002	0.0614	0.0053
0.35	0.0962	0.0066	0.102	0.005	0.0898	0.0011
0.40	0.127	0.000	0.125	0.001	0.124	0.005
0.45	0.149		0.167	0.006	0.168	0.005
0.50	0.141		0.222	0.007	0.205	0.016
0.52	0.161		0.158	0.003	0.233	0.032

Table 9.53: The mean square (T_x^{tr}) and the standard deviation (σ) of the particle translational velocity fluctuation, normalized by $(\dot{\gamma}a)^2$, in the flow direction for $\dot{\gamma}^* =$ 100, 1000, and 10^4.

	$\dot{\gamma}^* = 100$		$\dot{\gamma}^* = 1000$		$\dot{\gamma}^* = 10^4$	
ϕ	T_x^{tr}	σ	T_x^{tr}	σ	T_x^{tr}	σ
0.05	0.00627	0.00088	0.00617	0.00076	0.00630	0.00021
0.10	0.0190	0.0034	0.0200	0.0043	0.0189	0.0006
0.15	0.0248	0.0042	0.0235	0.0079	0.0293	0.0086
0.20	0.0366	0.0001	0.0354	0.0023	0.0398	0.0012
0.25	0.0448	0.0039	0.0491	0.0031	0.0493	0.0053
0.30	0.0677	0.0011	0.0659	0.0026	0.0630	0.0034
0.35	0.0932	0.0069	0.0892	0.0008	0.0990	0.0031
0.40	0.135	0.001	0.138	0.001	0.158	0.005
0.45	0.183	0.012	0.195	0.005	0.214	0.007
0.50	0.231	0.028	0.270	0.021	0.324	0.017
0.52	0.237	0.009	0.303	0.015	0.393	0.024

Table 9.54: The mean square (T_y^{tr}) and the standard deviation (σ) of the particle translational velocity fluctuation, normalized by $(\dot{\gamma}a)^2$, in the velocity-gradient direction for $\dot{\gamma}^* = 0.1$, 1, and 10.

	$\dot{\gamma}^* = 0.1$		$\dot{\gamma}^* = 1$		$\dot{\gamma}^* = 10$	
ϕ	T_y^{tr}	σ	T_y^{tr}	σ	T_y^{tr}	σ
0.05	0.0136	0.0039	0.0140	0.0014	0.0142	0.0024
0.10	0.0334	0.0050	0.0342	0.0023	0.0329	0.0012
0.15	0.0525	0.0052	0.0591	0.0029	0.0615	0.0007
0.20	0.0712	0.0006	0.0793	0.0039	0.0730	0.0016
0.25	0.1040	0.0057	0.0995	0.0027	0.112	0.012
0.30	0.1245	0.0007	0.123	0.006	0.127	0.008
0.35	0.144	0.017	0.162	0.008	0.149	0.003
0.40	0.170	0.000	0.184	0.003	0.178	0.009
0.45	0.168		0.191	0.015	0.198	0.012
0.50	0.133		0.212	0.006	0.198	0.013
0.52	0.138		0.149	0.009	0.213	0.031

Table 9.55: The mean square (T_y^{tr}) and the standard deviation (σ) of the particle translational velocity fluctuation, normalized by $(\dot{\gamma}a)^2$, in the velocity-gradient direction for $\dot{\gamma}^* = 100$, 1000, and 10^4.

	$\dot{\gamma}^* = 100$		$\dot{\gamma}^* = 1000$		$\dot{\gamma}^* = 10^4$	
ϕ	T_y^{tr}	σ	T_y^{tr}	σ	T_y^{tr}	σ
0.05	0.0139	0.0024	0.0140	0.0045	0.0134	0.0030
0.10	0.0367	0.0058	0.0383	0.0025	0.0363	0.0049
0.15	0.0619	0.0016	0.0773	0.0082	0.0750	0.0007
0.20	0.0860	0.0094	0.0848	0.0013	0.0913	0.0157
0.25	0.101	0.004	0.111	0.009	0.120	0.007
0.30	0.129	0.007	0.1436	0.0001	0.144	0.003
0.35	0.160	0.001	0.172	0.011	0.208	0.006
0.40	0.204	0.007	0.194	0.025	0.237	0.004
0.45	0.210	0.009	0.242	0.002	0.272	0.015
0.50	0.217	0.018	0.268	0.028	0.327	0.020
0.52	0.216	0.007	0.282	0.006	0.361	0.021

Table 9.56: The mean square (T_z^{tr}) and the standard deviation (σ) of the particle translational velocity fluctuation, normalized by $(\dot{\gamma}a)^2$, in the vorticity direction for $\dot{\gamma}^* = 0.1$, 1, and 10.

	$\dot{\gamma}^* = 0.1$		$\dot{\gamma}^* = 1$		$\dot{\gamma}^* = 10$	
ϕ	T_z^{tr}	σ	T_z^{tr}	σ	T_z^{tr}	σ
0.05	0.00356	0.00006	0.00365	0.00128	0.00367	0.00098
0.10	0.00848	0.00078	0.00889	0.00047	0.00941	0.00034
0.15	0.0135	0.0007	0.0148	0.0012	0.0154	0.0008
0.20	0.0177	0.0005	0.0161	0.0015	0.0206	0.0009
0.25	0.0256	0.0021	0.0302	0.0026	0.0287	0.0023
0.30	0.0418	0.0016	0.0377	0.0011	0.0399	0.0051
0.35	0.0553	0.0062	0.0614	0.0011	0.0567	0.0065
0.40	0.0822	0.0012	0.0855	0.0030	0.0722	0.0063
0.45	0.0909		0.111	0.010	0.108	0.004
0.50	0.0887		0.137	0.010	0.130	0.012
0.52	0.0855		0.0944	0.0051	0.140	0.023

Table 9.57: The mean square (T_z^{tr}) and the standard deviation (σ) of the particle translational velocity fluctuation, normalized by $(\dot{\gamma}a)^2$, in the vorticity direction for $\dot{\gamma}^* = 100$, 1000, and 10^4.

	$\dot{\gamma}^* = 100$		$\dot{\gamma}^* = 1000$		$\dot{\gamma}^* = 10^4$	
ϕ	T_z^{tr}	σ	T_z^{tr}	σ	T_z^{tr}	σ
0.05	0.00368	0.00036	0.00377	0.00094	0.00371	0.00081
0.10	0.00950	0.00092	0.0109	0.0016	0.00937	0.00095
0.15	0.0149	0.0011	0.0167	0.0012	0.0193	0.0010
0.20	0.0243	0.0027	0.0214	0.0027	0.0280	0.0027
0.25	0.0298	0.0023	0.0314	0.0017	0.0309	0.0012
0.30	0.0407	0.0077	0.0452	0.0004	0.0435	0.0033
0.35	0.0597	0.0047	0.0616	0.0052	0.0633	0.0022
0.40	0.088	0.009	0.0880	0.0095	0.0928	0.0108
0.45	0.115	0.001	0.132	0.005	0.139	0.004
0.50	0.144	0.018	0.177	0.017	0.206	0.018
0.52	0.145	0.003	0.188	0.008	0.253	0.001

Table 9.58: The mean square (T_x^{rot}) and the standard deviation (σ) of the particle rotational velocity fluctuation, normalized by $\dot{\gamma}^2$, in the flow direction for $\dot{\gamma}^* = 0.1$, 1, and 10.

	$\dot{\gamma}^* = 0.1$		$\dot{\gamma}^* = 1$		$\dot{\gamma}^* = 10$	
ϕ	T_x^{rot}	σ	T_x^{rot}	σ	T_x^{rot}	σ
0.05	0.00161	0.00019	0.00200	0.00019	0.00202	0.00016
0.10	0.00224	0.00007	0.00231	0.00001	0.00263	0.00015
0.15	0.00397	0.00040	0.00403	0.00040	0.00422	0.00005
0.20	0.00541	0.00025	0.00551	0.00086	0.00583	0.00040
0.25	0.00840	0.00124	0.00867	0.00023	0.00906	0.00213
0.30	0.0119	0.0004	0.0111	0.0005	0.0116	0.0003
0.35	0.0150	0.0014	0.0165	0.0008	0.0168	0.0001
0.40	0.0194	0.0008	0.0197	0.0009	0.0200	0.0005
0.45	0.0191		0.0222	0.0019	0.0229	0.0010
0.50	0.0151		0.0244	0.0010	0.0243	0.0025
0.52	0.0150		0.0168	0.0009	0.0256	0.0038

Table 9.59: The mean square (T_x^{rot}) and the standard deviation (σ) of the particle rotational velocity fluctuation, normalized by $\dot{\gamma}^2$, in the flow direction for $\dot{\gamma}^* = 100$, 1000, and 10^4.

	$\dot{\gamma}^* = 100$		$\dot{\gamma}^* = 1000$		$\dot{\gamma}^* = 10^4$	
ϕ	T_x^{rot}	σ	T_x^{rot}	σ	T_x^{rot}	σ
0.05	0.00194	0.00001	0.00192	0.00063	0.00260	0.00056
0.10	0.00248	0.00006	0.00244	0.00020	0.00256	0.00023
0.15	0.00411	0.00019	0.00510	0.00013	0.00540	0.00017
0.20	0.00679	0.00061	0.00690	0.00124	0.00843	0.00048
0.25	0.00921	0.00017	0.00940	0.00044	0.0103	0.0019
0.30	0.0116	0.0022	0.0145	0.0012	0.0158	0.0012
0.35	0.0170	0.0013	0.0189	0.0025	0.0206	0.0012
0.40	0.0223	0.0011	0.0238	0.0004	0.0300	0.0007
0.45	0.0261	0.0004	0.0326	0.0004	0.0379	0.0014
0.50	0.0283	0.0026	0.0378	0.0033	0.0474	0.0034
0.52	0.0273	0.0011	0.0383	0.0004	0.0549	0.0028

Table 9.60: The mean square (T_y^{rot}) and the standard deviation (σ) of the particle rotational velocity fluctuation, normalized by $\dot{\gamma}^2$, in the velocity-gradient direction for $\dot{\gamma}^* = 0.1$, 1, and 10.

	$\dot{\gamma}^* = 0.1$		$\dot{\gamma}^* = 1$		$\dot{\gamma}^* = 10$	
ϕ	T_y^{rot}	σ	T_y^{rot}	σ	T_y^{rot}	σ
0.05	0.00156	0.00008	0.00207	0.00040	0.00214	0.00015
0.10	0.00184	0.00004	0.00217	0.00005	0.00300	0.00007
0.15	0.00318	0.00006	0.00330	0.00040	0.00352	0.00022
0.20	0.00369	0.00034	0.00385	0.00064	0.00500	0.00028
0.25	0.00572	0.00044	0.00742	0.00100	0.00695	0.00022
0.30	0.00926	0.00068	0.00842	0.00049	0.00976	0.00121
0.35	0.0130	0.0011	0.0138	0.0007	0.0133	0.0005
0.40	0.0161	0.0006	0.0171	0.0004	0.0170	0.0004
0.45	0.0197		0.0215	0.0013	0.0229	0.0004
0.50	0.0178		0.0264	0.0019	0.0262	0.0016
0.52	0.0138		0.0188	0.0004	0.0268	0.0032

Table 9.61: The mean square (T_y^{rot}) and the standard deviation (σ) of the particle rotational velocity fluctuation, normalized by $\dot{\gamma}^2$, in the velocity-gradient direction for $\dot{\gamma}^* = 100$, 1000, and 10^4.

	$\dot{\gamma}^* = 100$		$\dot{\gamma}^* = 1000$		$\dot{\gamma}^* = 10^4$	
ϕ	T_y^{rot}	σ	T_y^{rot}	σ	T_y^{rot}	σ
0.05	0.00223	0.00007	0.00233	0.00044	0.00306	0.00070
0.10	0.00224	0.00015	0.00305	0.00088	0.00224	0.00001
0.15	0.00350	0.00011	0.00404	0.00011	0.00510	0.00030
0.20	0.00641	0.00021	0.00522	0.00053	0.00714	0.00050
0.25	0.00729	0.00035	0.00912	0.00036	0.00814	0.00066
0.30	0.00944	0.00196	0.0121	0.0010	0.0126	0.0007
0.35	0.0148	0.0010	0.0161	0.0003	0.0182	0.0006
0.40	0.0199	0.0027	0.0230	0.0038	0.0263	0.0014
0.45	0.0253	0.0005	0.0298	0.0010	0.0357	0.0004
0.50	0.0306	0.0030	0.0390	0.0030	0.0488	0.0029
0.52	0.0291	0.0004	0.0402	0.0020	0.0560	0.0012

Table 9.62: The mean square (T_z^{rot}) and the standard deviation (σ) of the particle rotational velocity fluctuation, normalized by $\dot{\gamma}^2$, in the vorticity direction for $\dot{\gamma}^* =$ 0.1, 1, and 10.

	$\dot{\gamma}^* = 0.1$		$\dot{\gamma}^* = 1$		$\dot{\gamma}^* = 10$	
ϕ	T_z^{rot}	σ	T_z^{rot}	σ	T_z^{rot}	σ
0.05	0.00556	0.00072	0.00644	0.00061	0.00643	0.00007
0.10	0.00868	0.00050	0.0101	0.0009	0.00866	0.00004
0.15	0.0135	0.0006	0.0148	0.0013	0.0152	0.0004
0.20	0.0182	0.0001	0.0203	0.0012	0.0198	0.0005
0.25	0.0276	0.0011	0.0253	0.0023	0.0318	0.0042
0.30	0.0324	0.0031	0.0343	0.0007	0.0327	0.0008
0.35	0.0394	0.0045	0.0439	0.0042	0.0428	0.0014
0.40	0.0469	0.0009	0.0485	0.0007	0.0509	0.0024
0.45	0.0497		0.0543	0.0007	0.0568	0.0019
0.50	0.0373		0.0560	0.0013	0.0562	0.0020
0.52	0.0371		0.0393	0.0020	0.0571	0.0056

Table 9.63: The mean square (T_z^{rot}) and the standard deviation (σ) of the particle rotational velocity fluctuation, normalized by $\dot{\gamma}^2$, in the vorticity direction for $\dot{\gamma}^* =$ 100, 1000, and 10^4.

	$\dot{\gamma}^* = 100$		$\dot{\gamma}^* = 1000$		$\dot{\gamma}^* = 10^4$	
ϕ	T_z^{rot}	σ	T_z^{rot}	σ	T_z^{rot}	σ
0.05	0.00715	0.00051	0.00656	0.00111	0.00831	0.00180
0.10	0.00978	0.00027	0.01150	0.00059	0.0110	0.0012
0.15	0.0151	0.0004	0.0190	0.0014	0.0187	0.0004
0.20	0.0227	0.0006	0.0224	0.0001	0.0256	0.0030
0.25	0.0283	0.0002	0.0305	0.0004	0.0340	0.0043
0.30	0.0389	0.0003	0.0408	0.0020	0.0440	0.0017
0.35	0.0472	0.0011	0.0528	0.0047	0.0610	0.0001
0.40	0.0586	0.0048	0.0649	0.0050	0.0766	0.0018
0.45	0.0642	0.0014	0.0791	0.0007	0.0931	0.0053
0.50	0.0662	0.0052	0.0836	0.0049	0.106	0.003
0.52	0.0628	0.0024	0.0868	0.0022	0.114	0.005

Table 9.64: The mean square of the particle translational velocity fluctuation, normalized by $(\dot{\gamma}a)^2$ for simulation runs with 64 particles in the unit cell.

	$\dot{\gamma}^* = 10$			$\dot{\gamma}^* = 100$			$\dot{\gamma}^* = 1000$		
ϕ	T_x^{tr}	T_y^{tr}	T_z^{tr}	T_x^{tr}	T_y^{tr}	T_z^{tr}	T_x^{tr}	T_y^{tr}	T_z^{tr}
0.30	0.0793	0.142	0.0440	0.0879	0.156	0.0503	0.0986	0.170	0.0474
0.40	0.139	0.192	0.0911	0.148	0.203	0.0887	0.160	0.232	0.0967
0.45	0.186	0.211	0.123	0.198	0.233	0.125	0.209	0.275	0.129
0.50	0.236	0.232	0.153	0.218	0.214	0.144	0.288	0.283	0.184
0.52	0.308	0.268	0.200	0.206	0.184	0.141	0.325	0.323	0.228

Table 9.65: The mean square of the particle rotational velocity fluctuation, normalized by $\dot{\gamma}^2$, for simulation runs with 64 particles in the unit cell.

	$\dot{\gamma}^* = 10$			$\dot{\gamma}^* = 100$			$\dot{\gamma}^* = 1000$		
ϕ	T_x^{rot}	T_y^{rot}	T_z^{rot}	T_x^{rot}	T_y^{rot}	T_z^{rot}	T_x^{rot}	T_y^{rot}	T_z^{rot}
0.30	0.0113	0.00994	0.0347	0.0139	0.0114	0.0388	0.0139	0.0116	0.0445
0.40	0.0205	0.0181	0.0531	0.0222	0.0194	0.0572	0.0251	0.0234	0.0672
0.45	0.0252	0.0229	0.0554	0.0268	0.0248	0.0666	0.0325	0.0280	0.0794
0.50	0.0273	0.0279	0.0584	0.0265	0.0271	0.0617	0.0382	0.0358	0.0825
0.52	0.0326	0.0341	0.0622	0.0245	0.0263	0.0544	0.0446	0.0426	0.0845

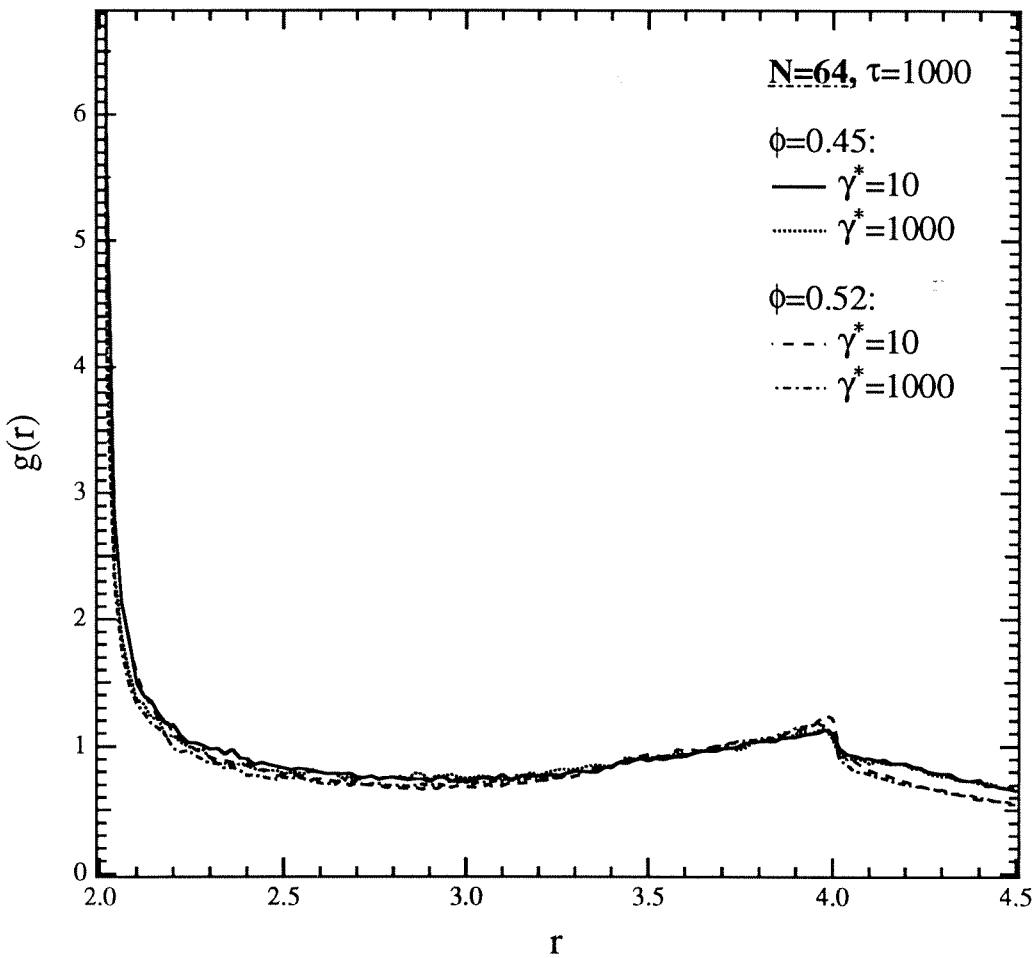

Figure 9.1: The angularly-averaged pair-distribution function for runs with 64 particles in the unit cell.

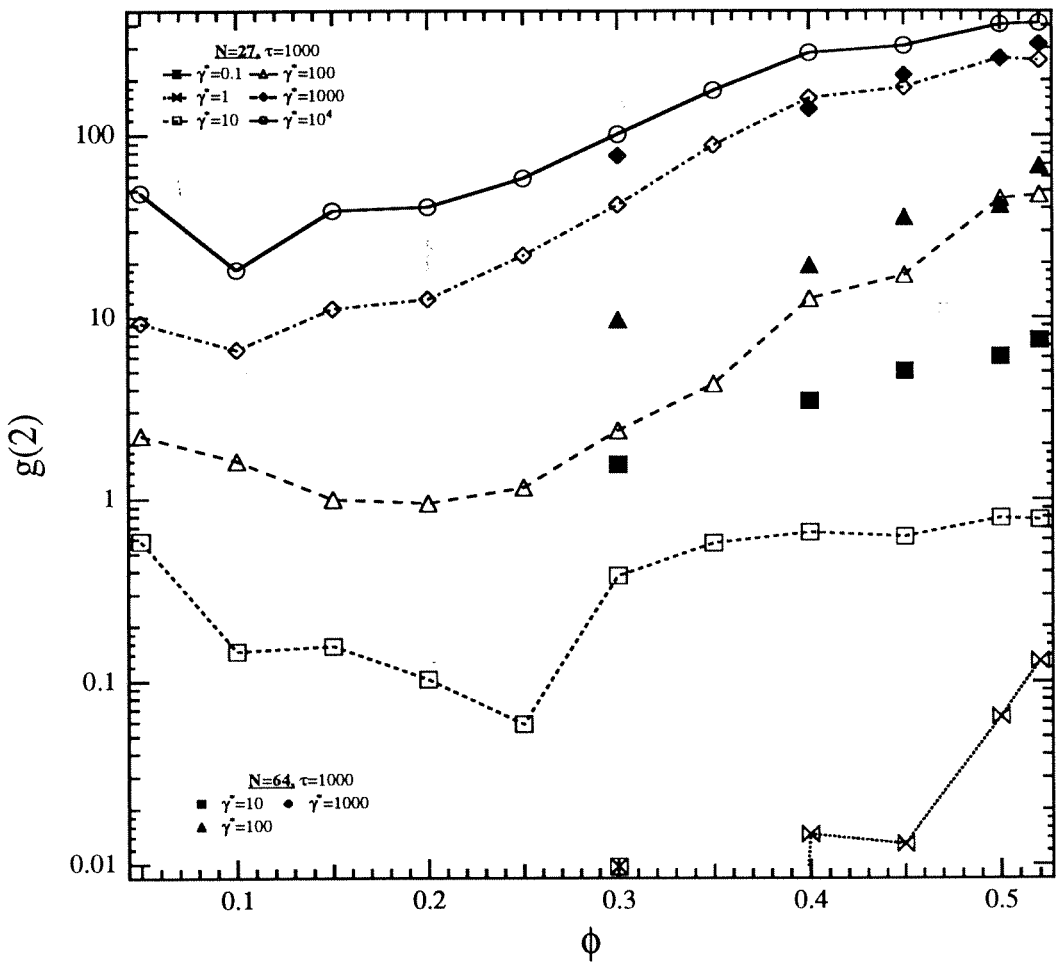

Figure 9.2: The magnitude $g(2)$ (shown on a logarithmic scale) of the angularly-averaged pair-distribution function evaluated at particle contact as a function of ϕ and $\dot{\gamma}^*$.

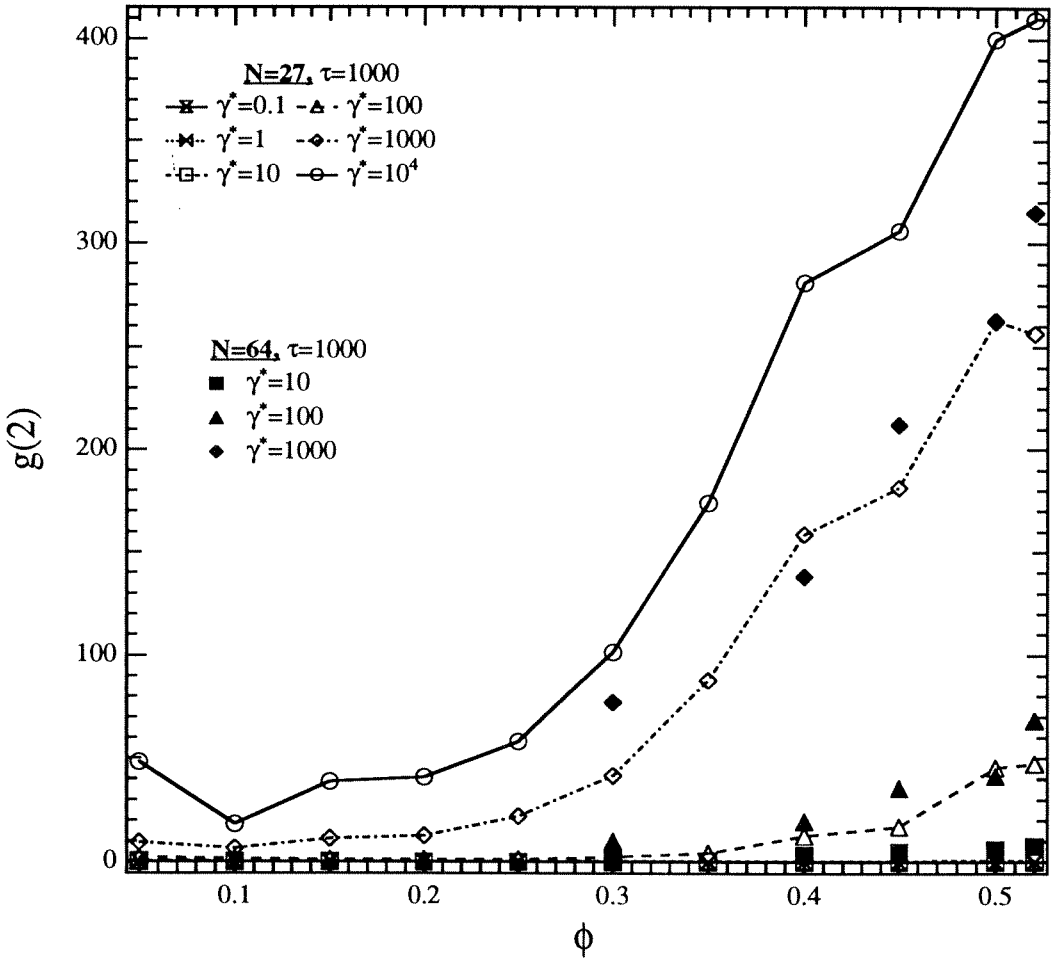

Figure 9.3: The magnitude $g(2)$ (shown on a linear scale) of the angularly-averaged pair-distribution function evaluated at particle contact as a function of ϕ and $\dot{\gamma}^*$.

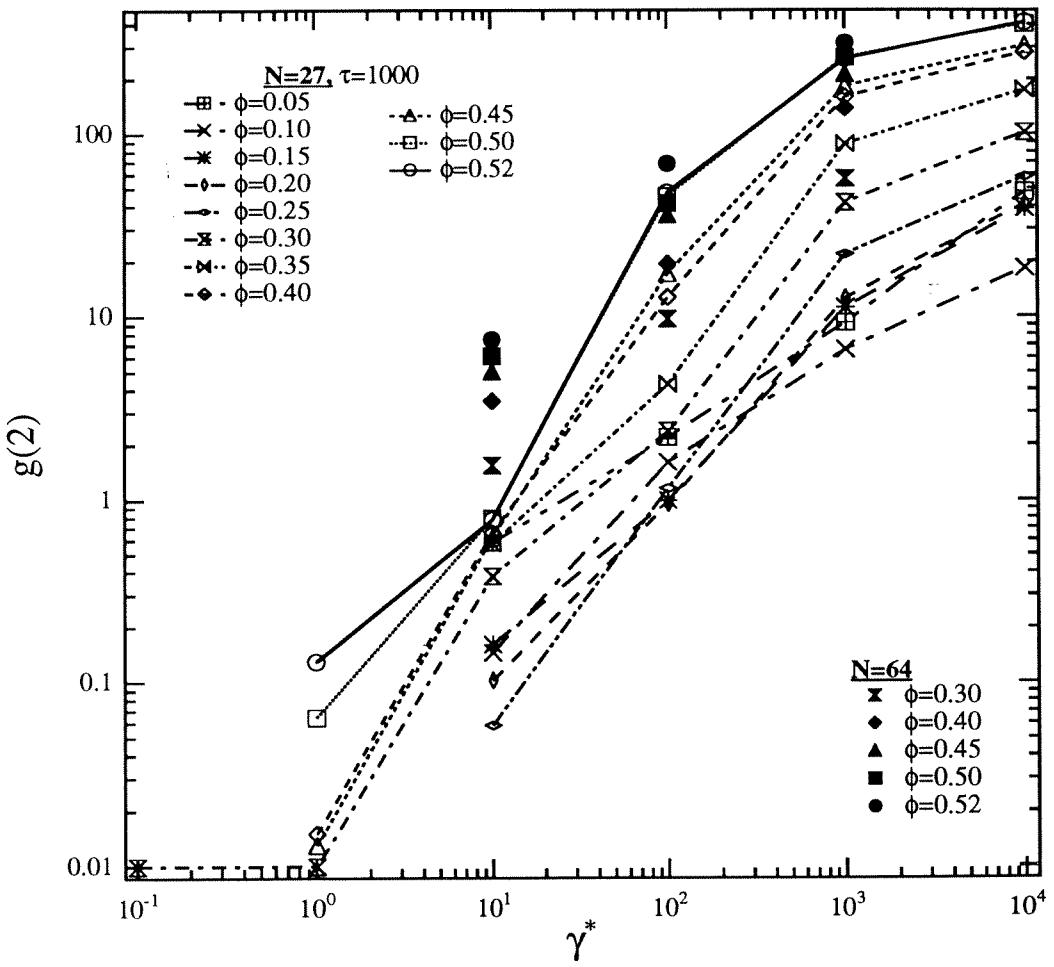

Figure 9.4: The magnitude $g(2)$ of the angularly-averaged pair-distribution function evaluated at particle contact as a function of $\dot{\gamma}^*$ and ϕ.

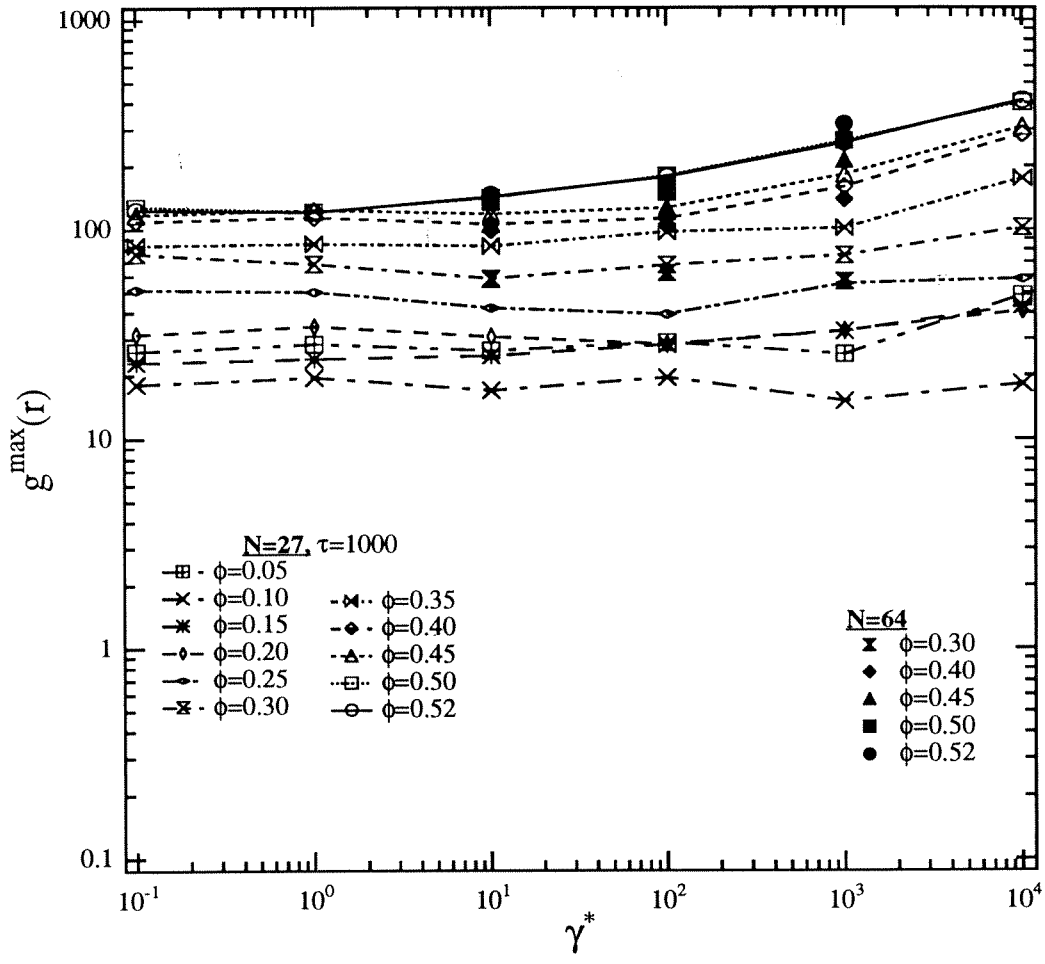

Figure 9.5: The maximum $g^{max}(r)$ of the angularly-averaged pair-distribution function as a function of $\dot{\gamma}^*$ and ϕ.

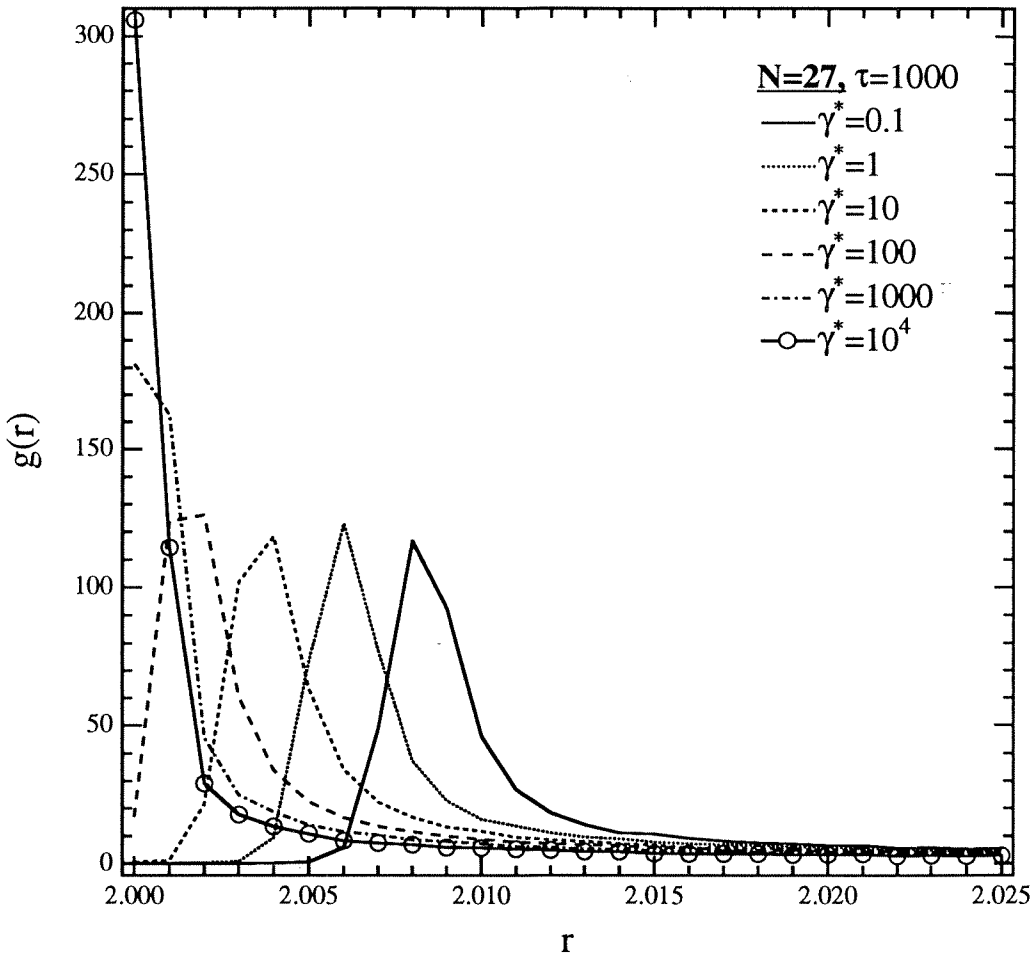

Figure 9.6: Angularly-averaged pair-distribution function for runs at the particle volume fraction of 0.45.

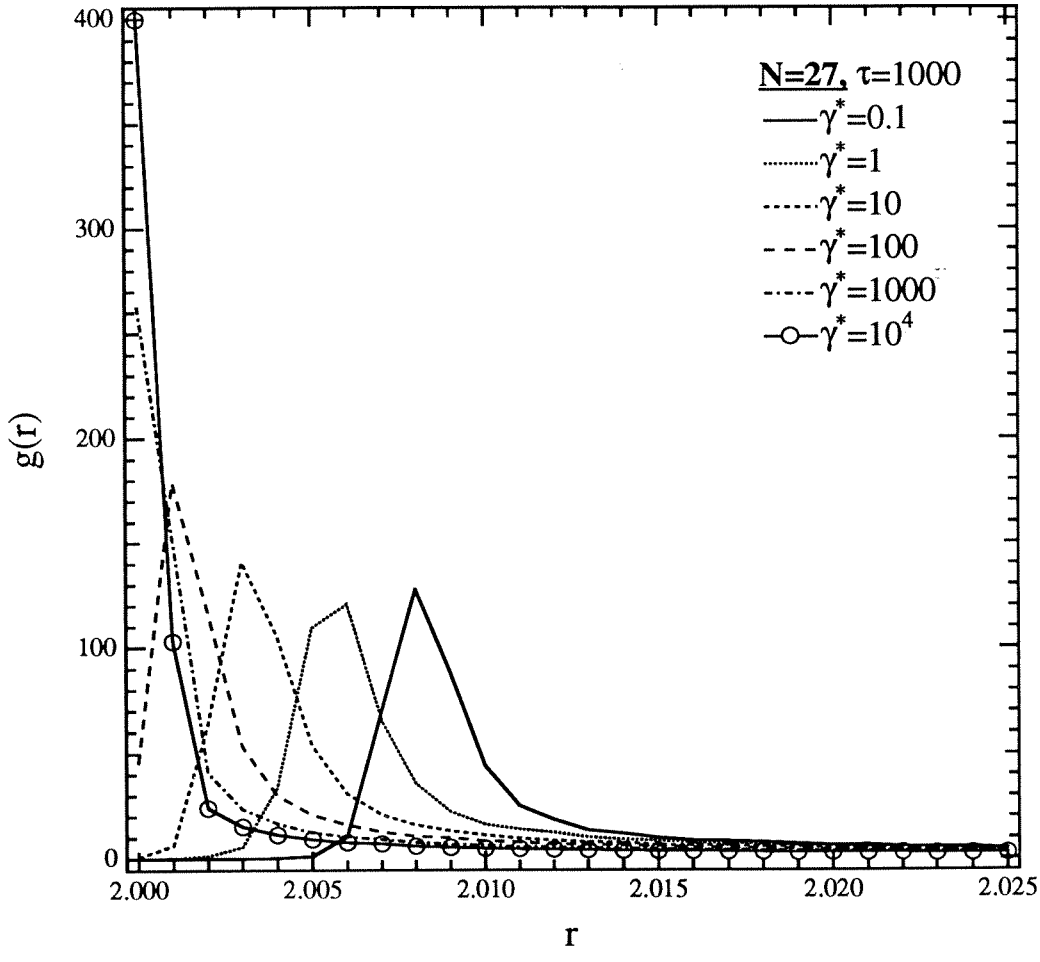

Figure 9.7: Angularly-averaged pair-distribution function for runs at the particle volume fraction of 0.50.

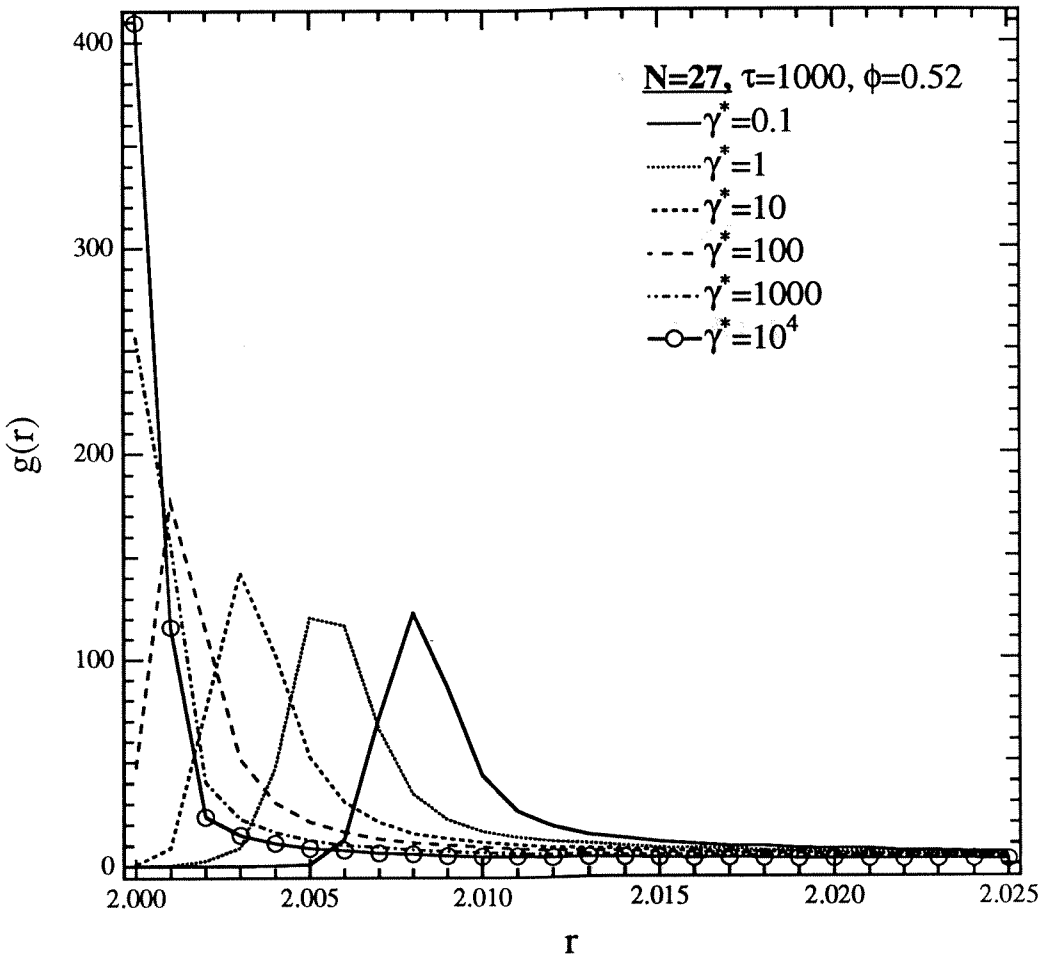

Figure 9.8: Angularly-averaged pair-distribution function for runs at the particle volume fraction of 0.52.

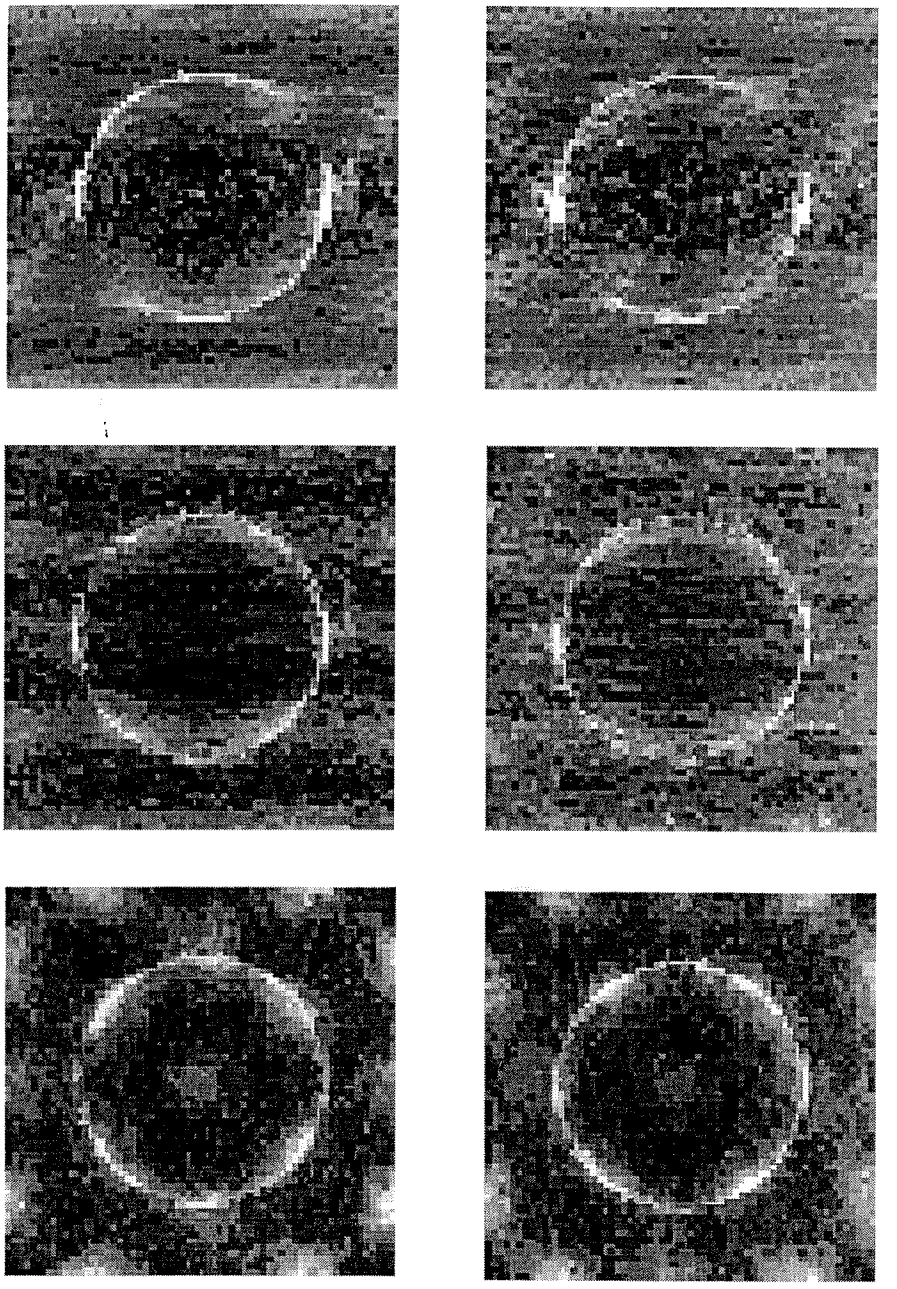

Figure 9.9: A plot of probability density for finding a particle given that there is a particle at the origin, in the (x, y)-plane (top row), (x, z)-plane (middle row), and the (z, y)-plane (bottom row) for suspensions at $\phi = 0.45$ and $\dot{\gamma}^* = 0.1$ (left column) and 1 (right column). There are 27 particles in the unit cell. Regions of light color represent high probability and dark low.

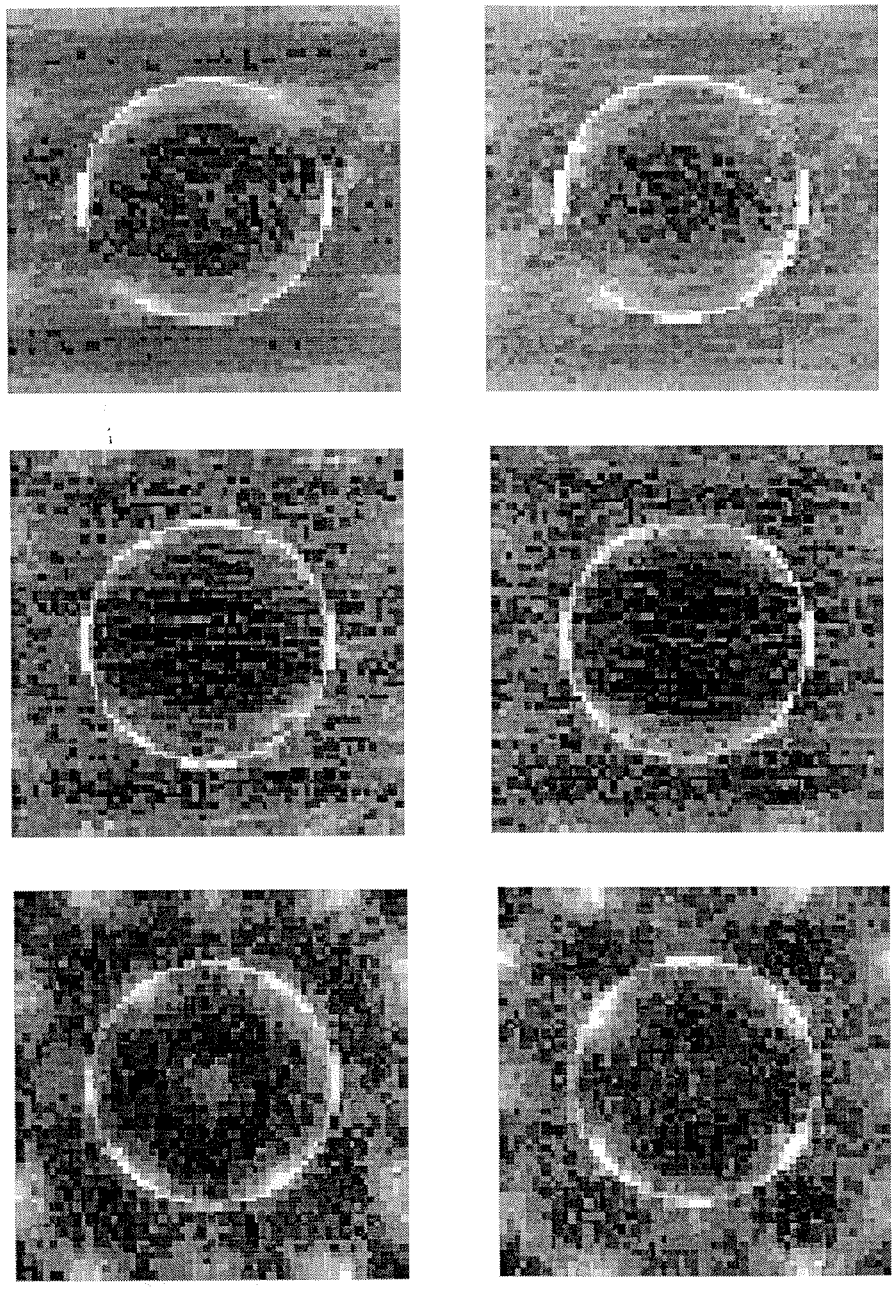

Figure 9.10: A plot of probability density for finding a particle given that there is a particle at the origin, in the (x, y)-plane (top row), (x, z)-plane (middle row), and the (z, y)-plane (bottom row) for suspensions at $\phi = 0.45$ and $\dot{\gamma}^* = 10$ (left column) and 100 (right column). There are 27 particles in the unit cell. Regions of light color represent high probability and dark low.

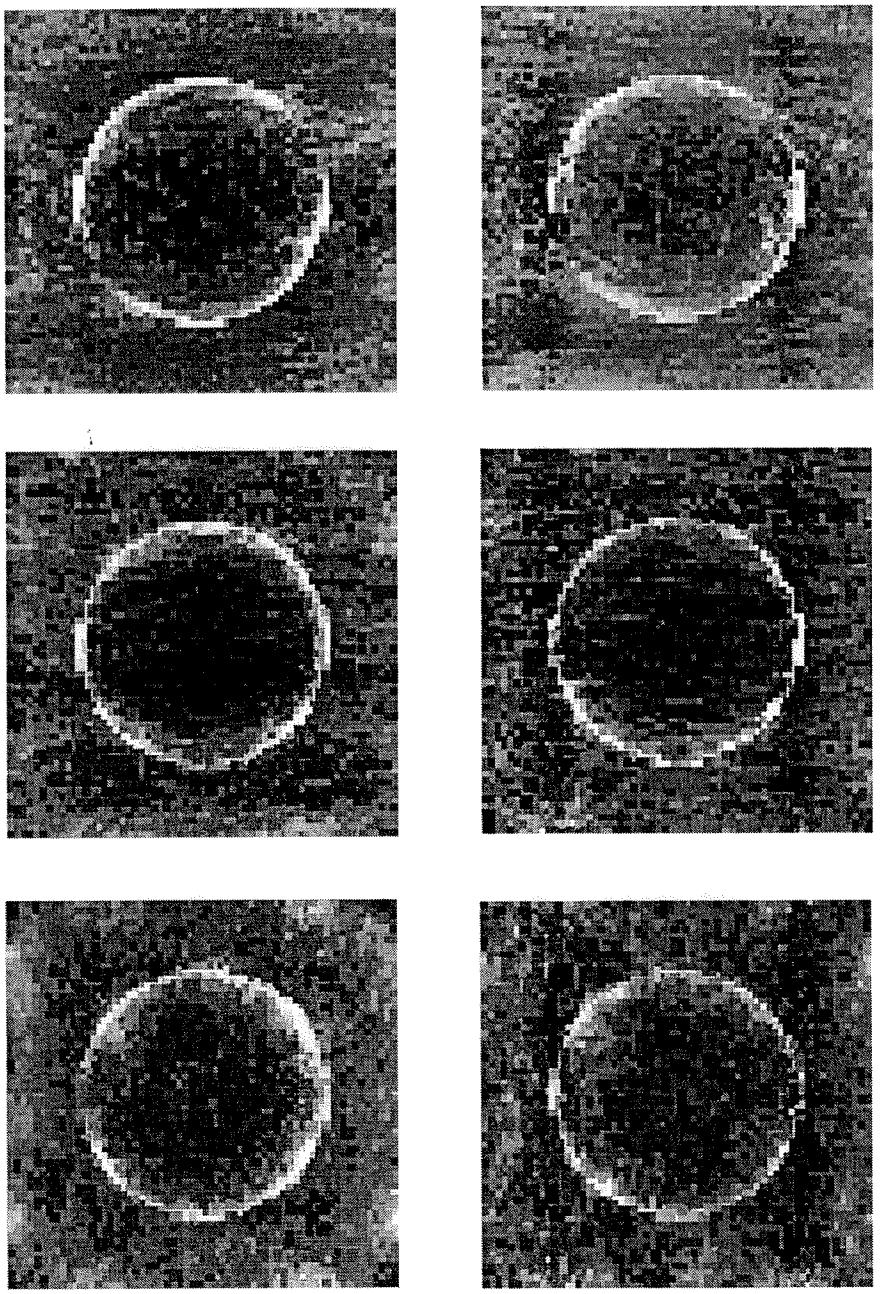

Figure 9.11: A plot of probability density for finding a particle given that there is a particle at the origin, in the (x, y)-plane (top row), (x, z)-plane (middle row), and the (z, y)-plane (bottom row) for suspensions at $\phi = 0.45$ and $\dot{\gamma}^* = 1000$ (left column) and 10^4 (right column). There are 27 particles in the unit cell. Regions of light color represent high probability and dark low.

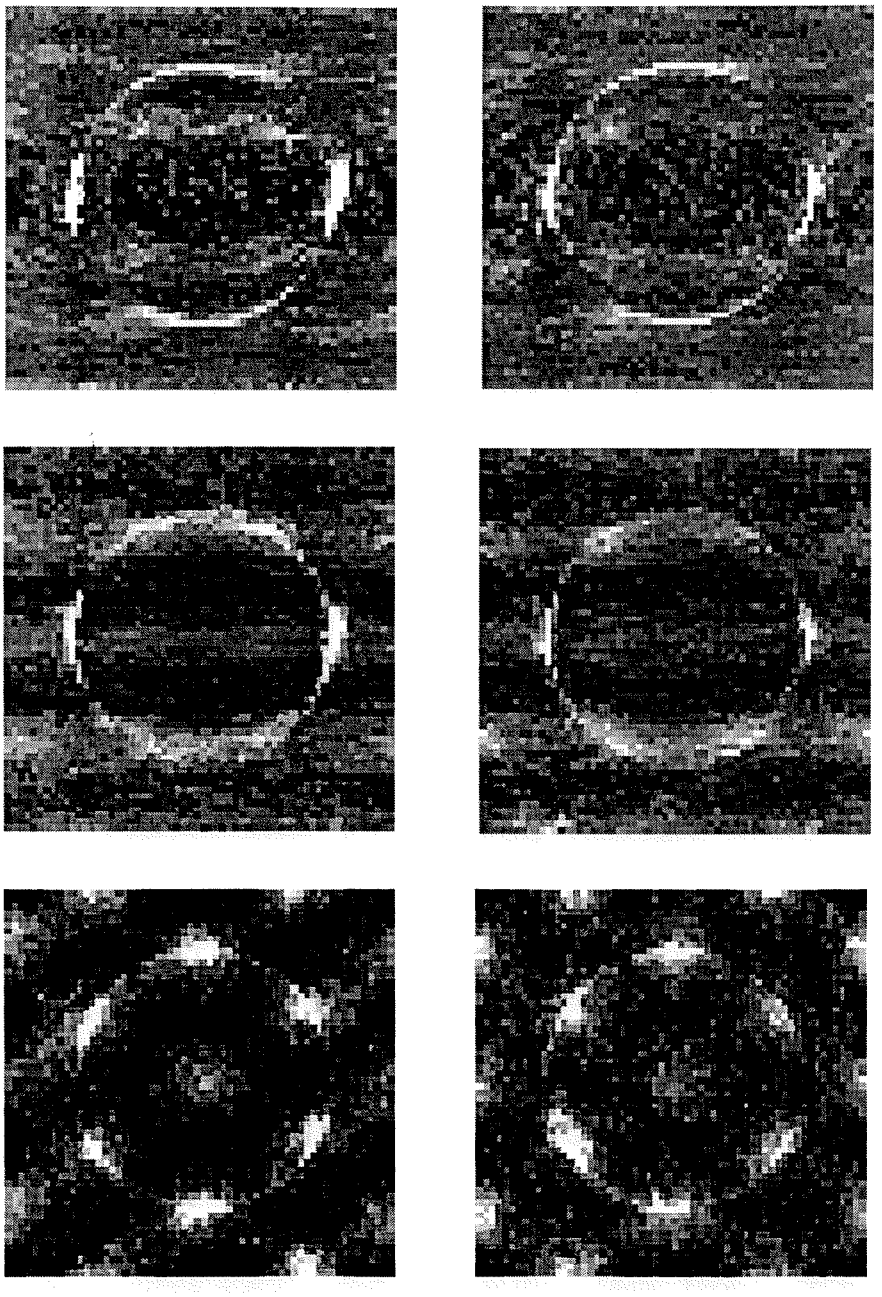

Figure 9.12: A plot of probability density for finding a particle given that there is a particle at the origin, in the (x, y)-plane (top row), (x, z)-plane (middle row), and the (z, y)-plane (bottom row) for suspensions at $\phi = 0.50$ and $\dot{\gamma}^* = 0.1$ (left column) and 1 (right column). There are 27 particles in the unit cell. Regions of light color represent high probability and dark low.

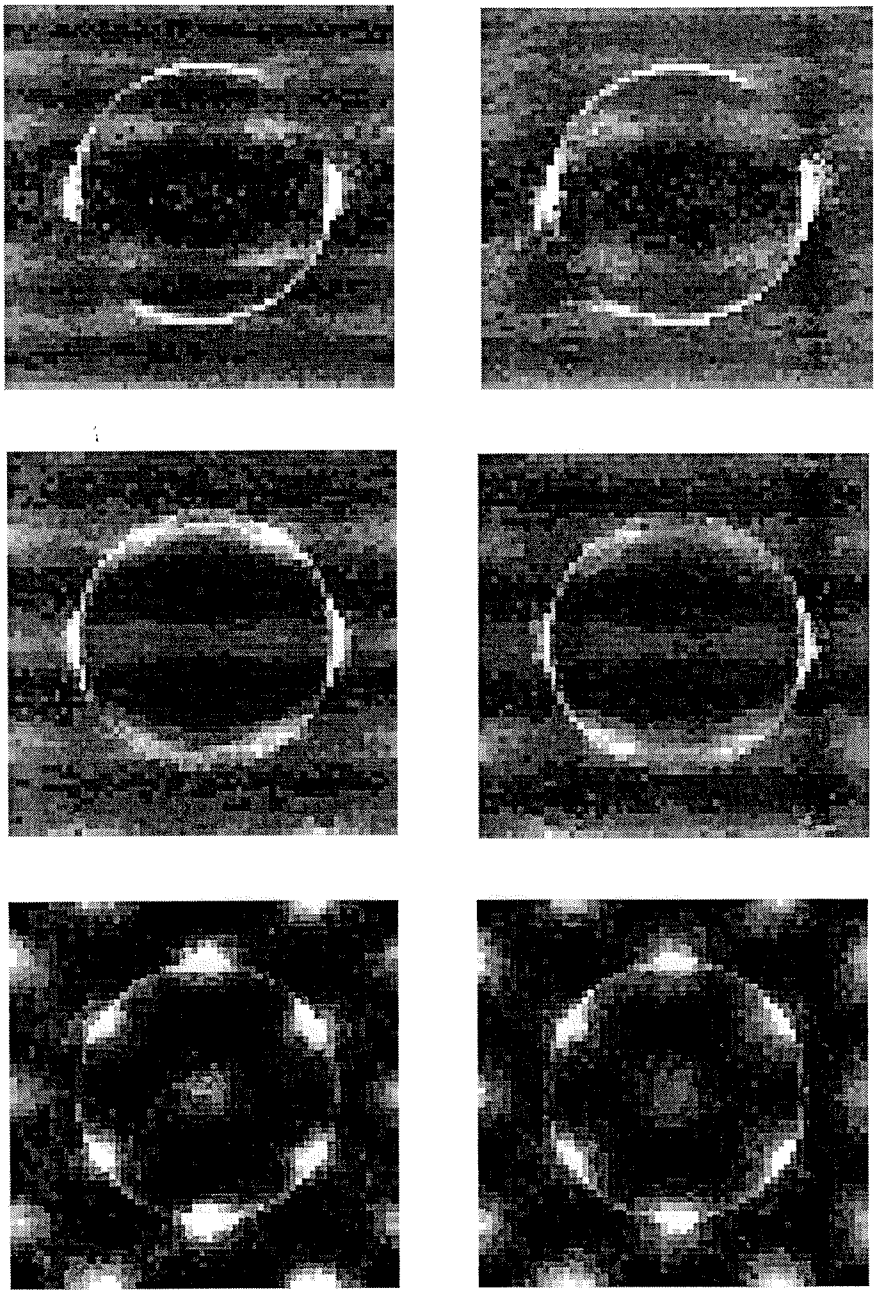

Figure 9.13: A plot of probability density for finding a particle given that there is a particle at the origin, in the (x, y)-plane (top row), (x, z)-plane (middle row), and the (z, y)-plane (bottom row) for suspensions at $\phi = 0.50$ and $\dot{\gamma}^* = 10$ (left column) and 100 (right column). There are 27 particles in the unit cell. Regions of light color represent high probability and dark low.

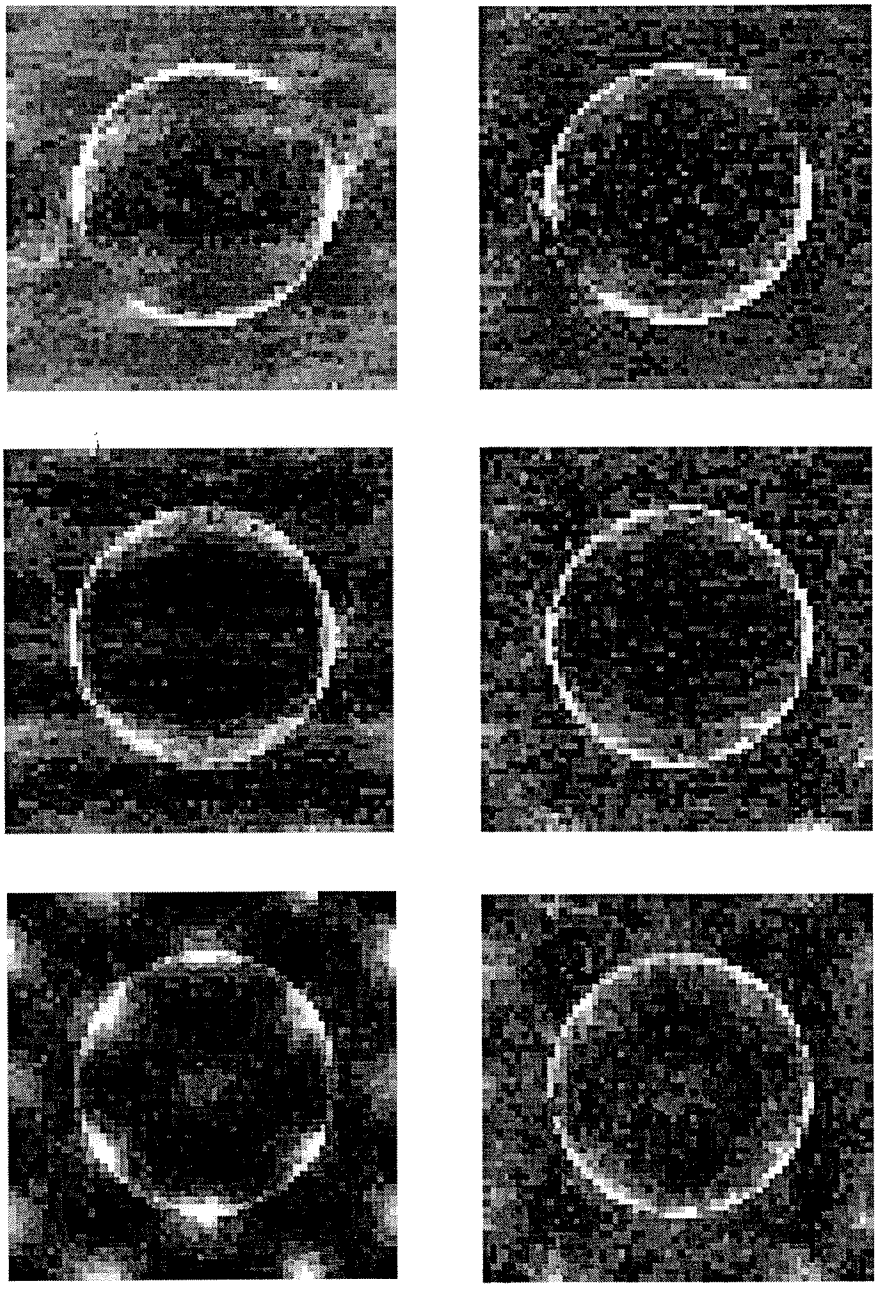

Figure 9.14: A plot of probability density for finding a particle given that there is a particle at the origin, in the (x, y)-plane (top row), (x, z)-plane (middle row), and the (z, y)-plane (bottom row) for suspensions at $\phi = 0.50$ and $\dot{\gamma}^* = 1000$ (left column) and 10^4 (right column). There are 27 particles in the unit cell. Regions of light color represent high probability and dark low.

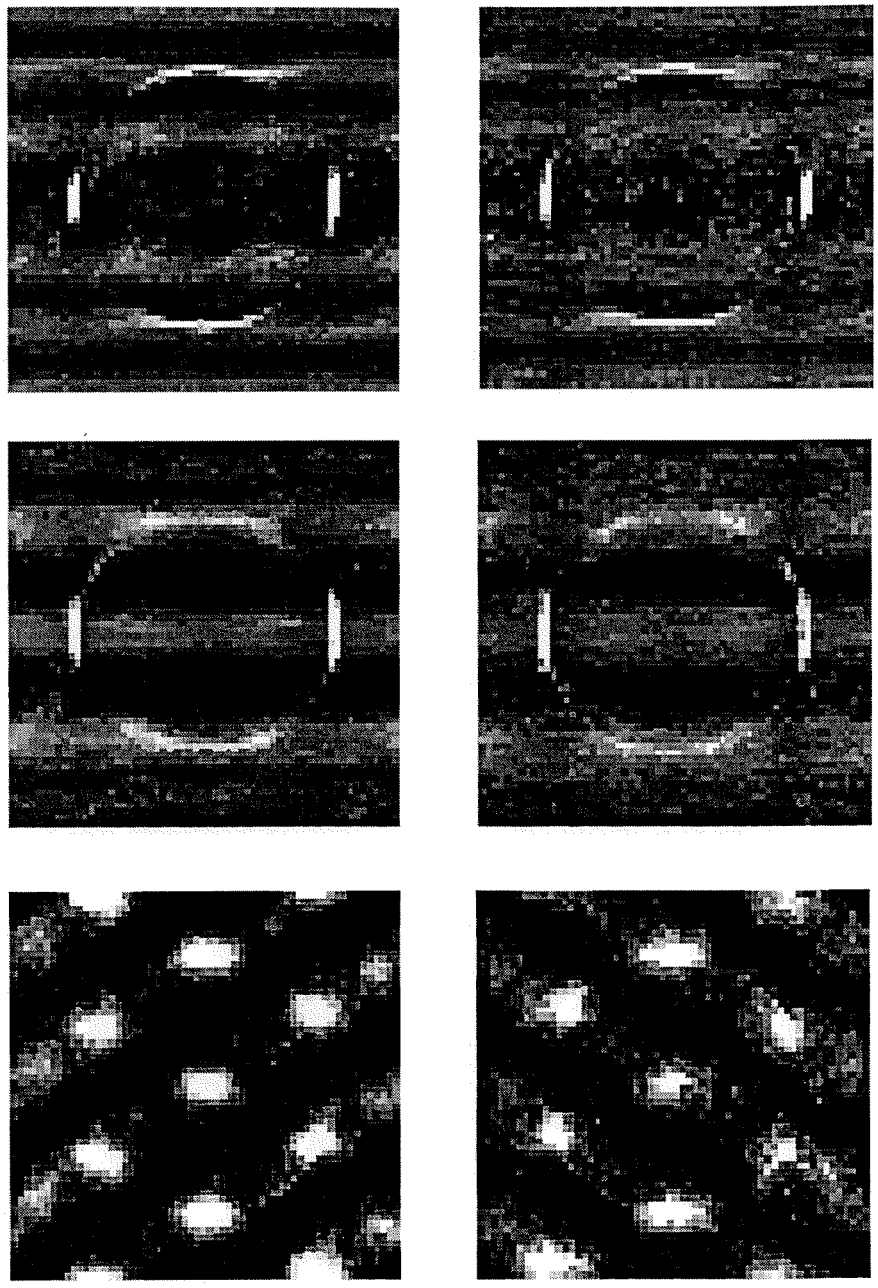

Figure 9.15: A plot of probability density for finding a particle given that there is a particle at the origin, in the (x, y)-plane (top row), (x, z)-plane (middle row), and the (z, y)-plane (bottom row) for suspensions at $\phi = 0.52$ and $\dot{\gamma}^* = 0.1$ (left column) and 1 (right column). There are 27 particles in the unit cell. Regions of light color represent high probability and dark low.

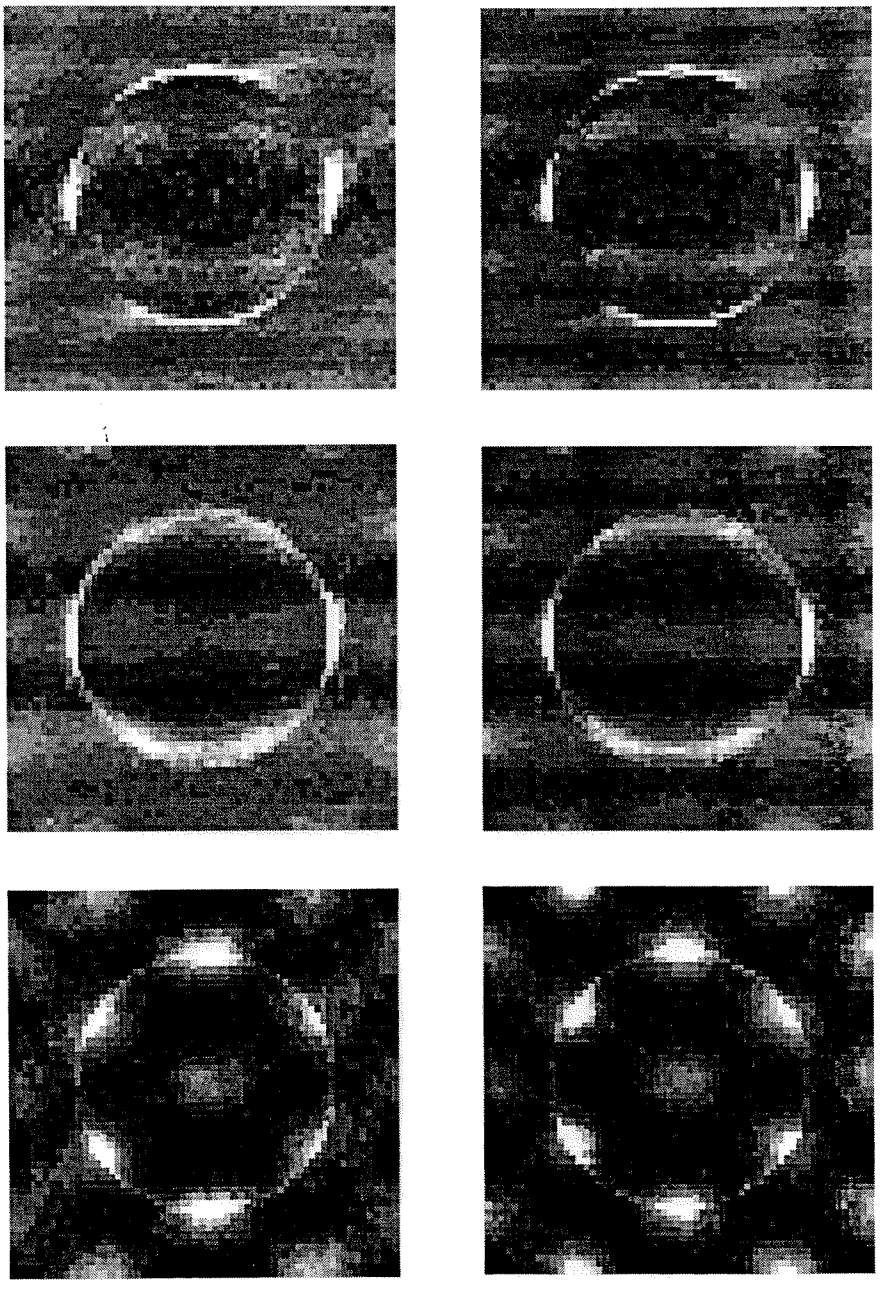

Figure 9.16: A plot of probability density for finding a particle given that there is a particle at the origin, in the (x, y)-plane (top row), (x, z)-plane (middle row), and the (z, y)-plane (bottom row) for suspensions at $\phi = 0.52$ and $\dot{\gamma}^* = 10$ (left column) and 100 (right column). There are 27 particles in the unit cell. Regions of light color represent high probability and dark low.

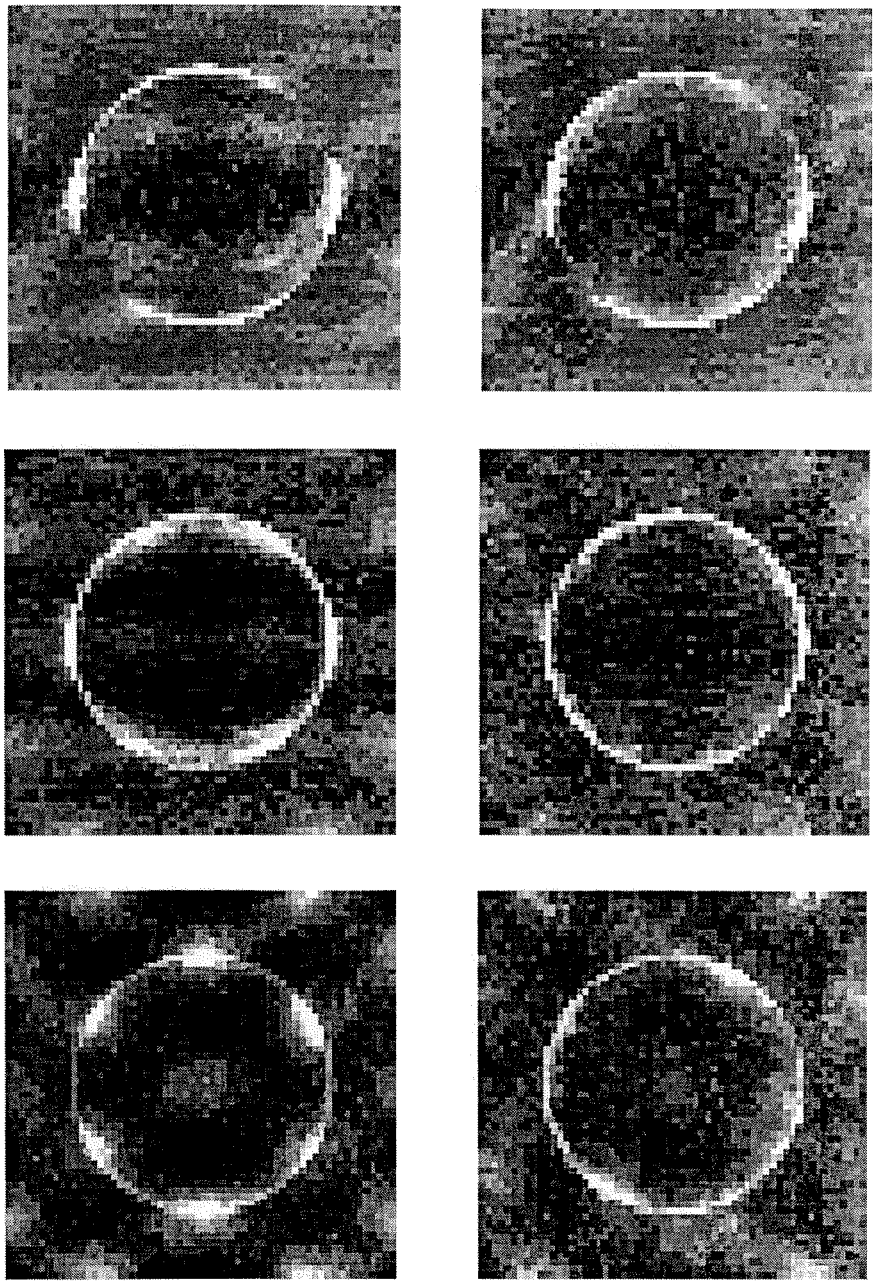

Figure 9.17: A plot of probability density for finding a particle given that there is a particle at the origin, in the (x, y)-plane (top row), (x, z)-plane (middle row), and the (z, y)-plane (bottom row) for suspensions at $\phi = 0.52$ and $\dot{\gamma}^* = 1000$ (left column) and 10^4 (right column). There are 27 particles in the unit cell. Regions of light color represent high probability and dark low.

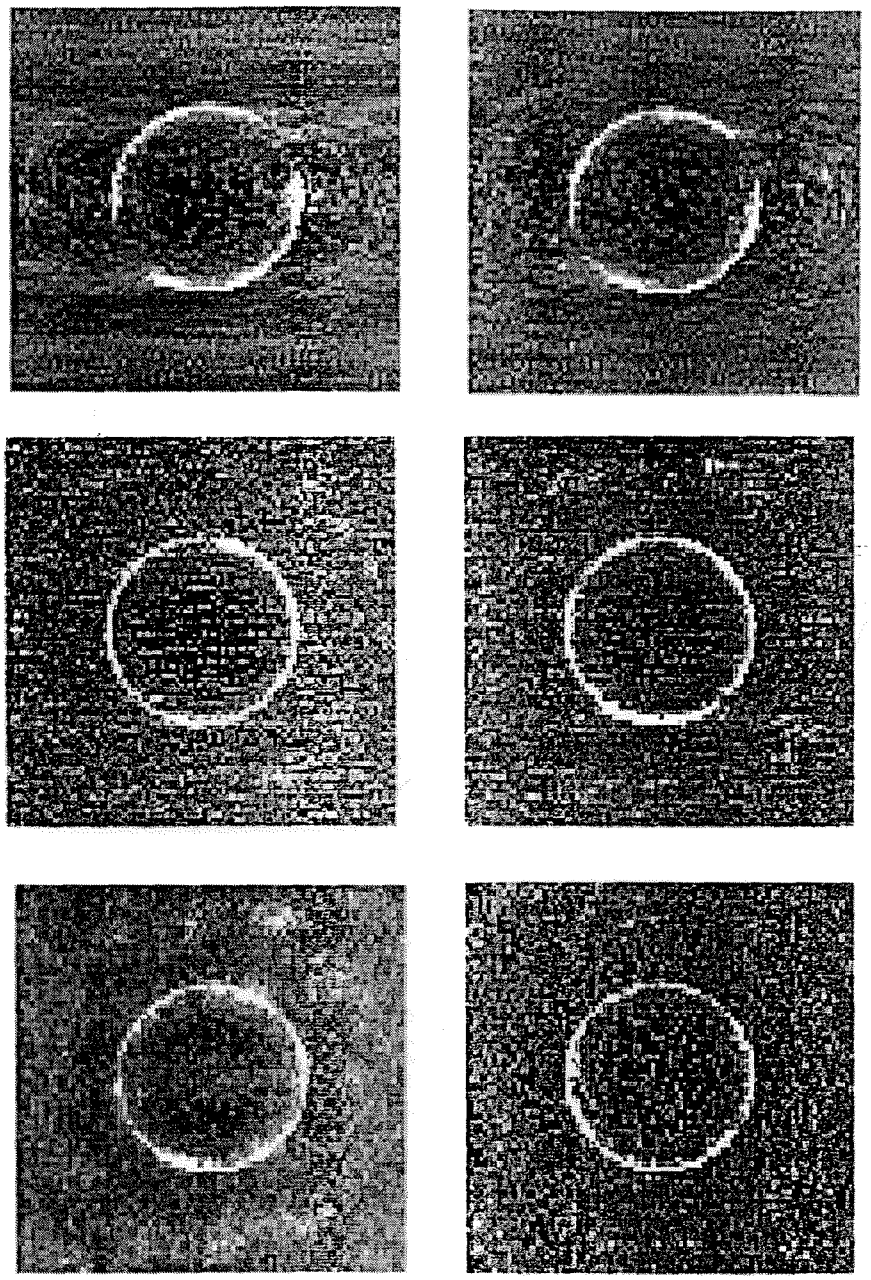

Figure 9.18: A plot of probability density for finding a particle given that there is a particle at the origin, in the (x, y)-plane (top row), (x, z)-plane (middle row), and the (z, y)-plane (bottom row) for suspensions at $\phi = 0.45$ and $\dot{\gamma}^* = 10$ (left column) and 1000 (right column). There are 64 particles in the unit cell. Regions of light color represent high probability and dark low.

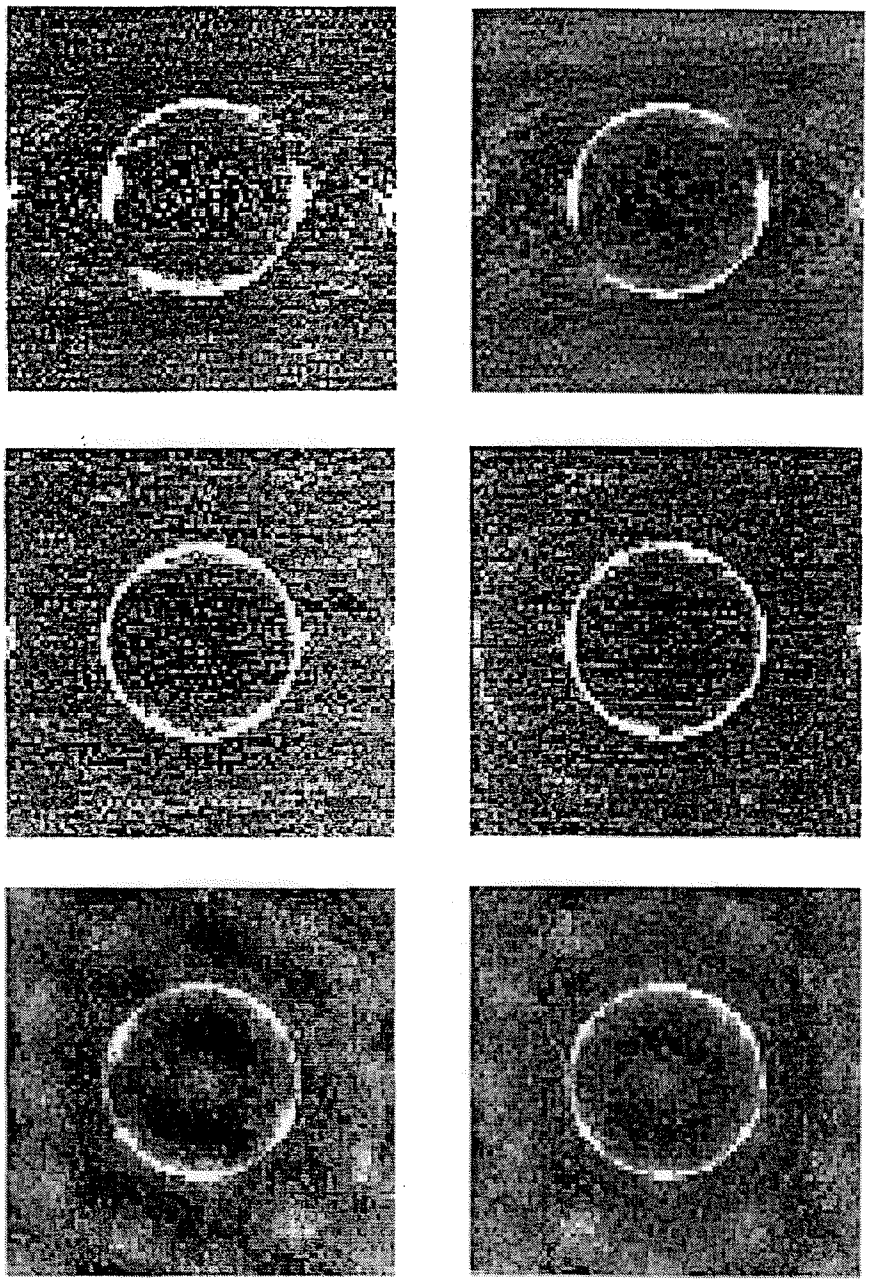

Figure 9.19: A plot of probability density for finding a particle given that there is a particle at the origin, in the (x, y)-plane (top row), (x, z)-plane (middle row), and the (z, y)-plane (bottom row) for suspensions at $\phi = 0.50$ and $\dot{\gamma}^* = 10$ (left column) and 1000 (right column). There are 64 particles in the unit cell. Regions of light color represent high probability and dark low.

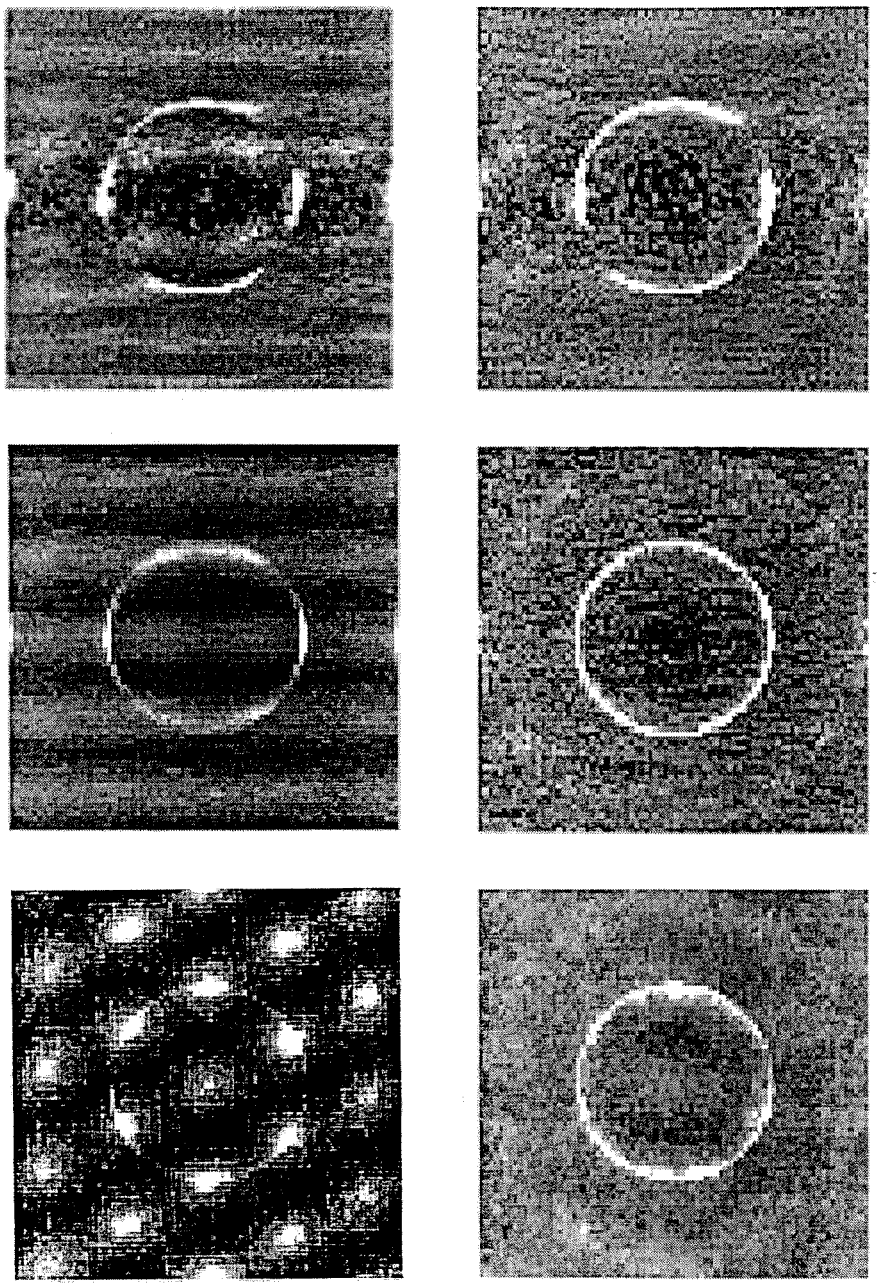

Figure 9.20: A plot of probability density for finding a particle given that there is a particle at the origin, in the (x, y)-plane (top row), (x, z)-plane (middle row), and the (z, y)-plane (bottom row) for suspensions at $\phi = 0.52$ and $\dot{\gamma}^* = 10$ (left column) and 1000 (right column). There are 64 particles in the unit cell. Regions of light color represent high probability and dark low.

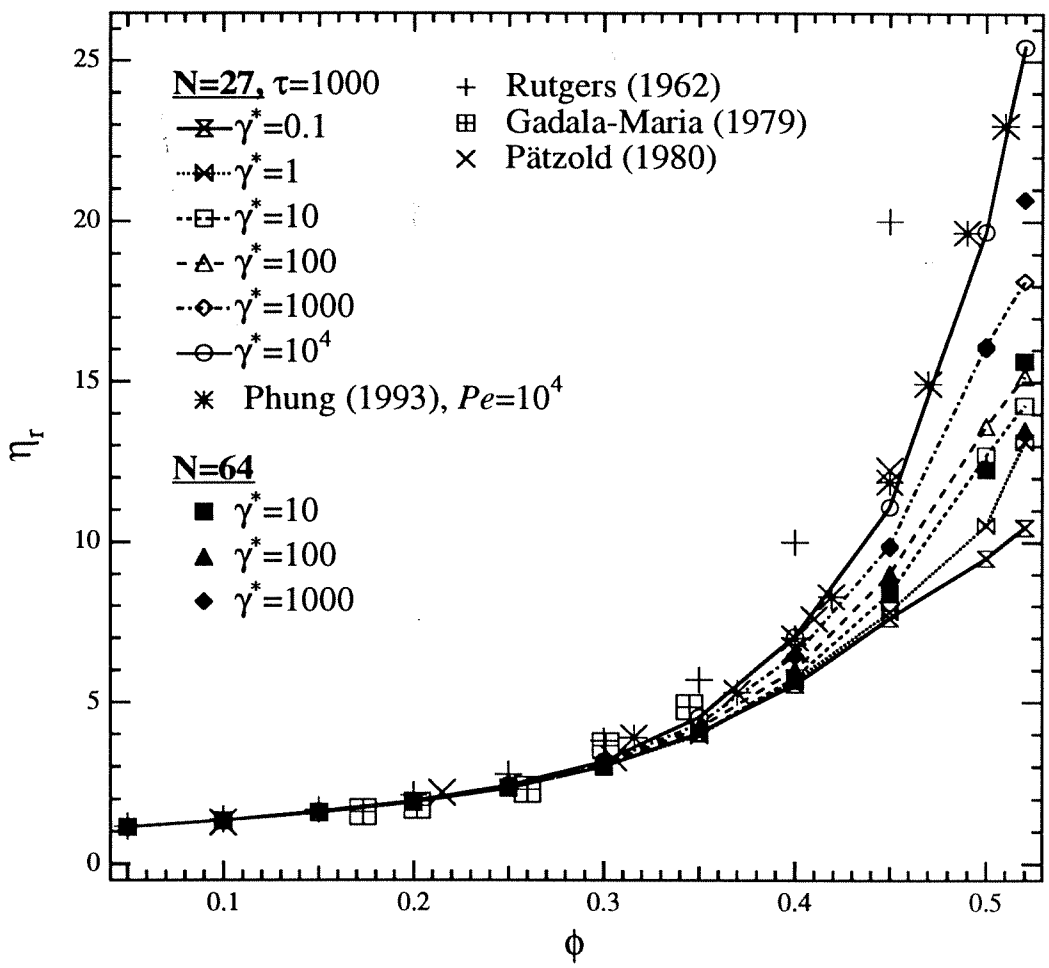

Figure 9.21: The total shear viscosity of suspensions.

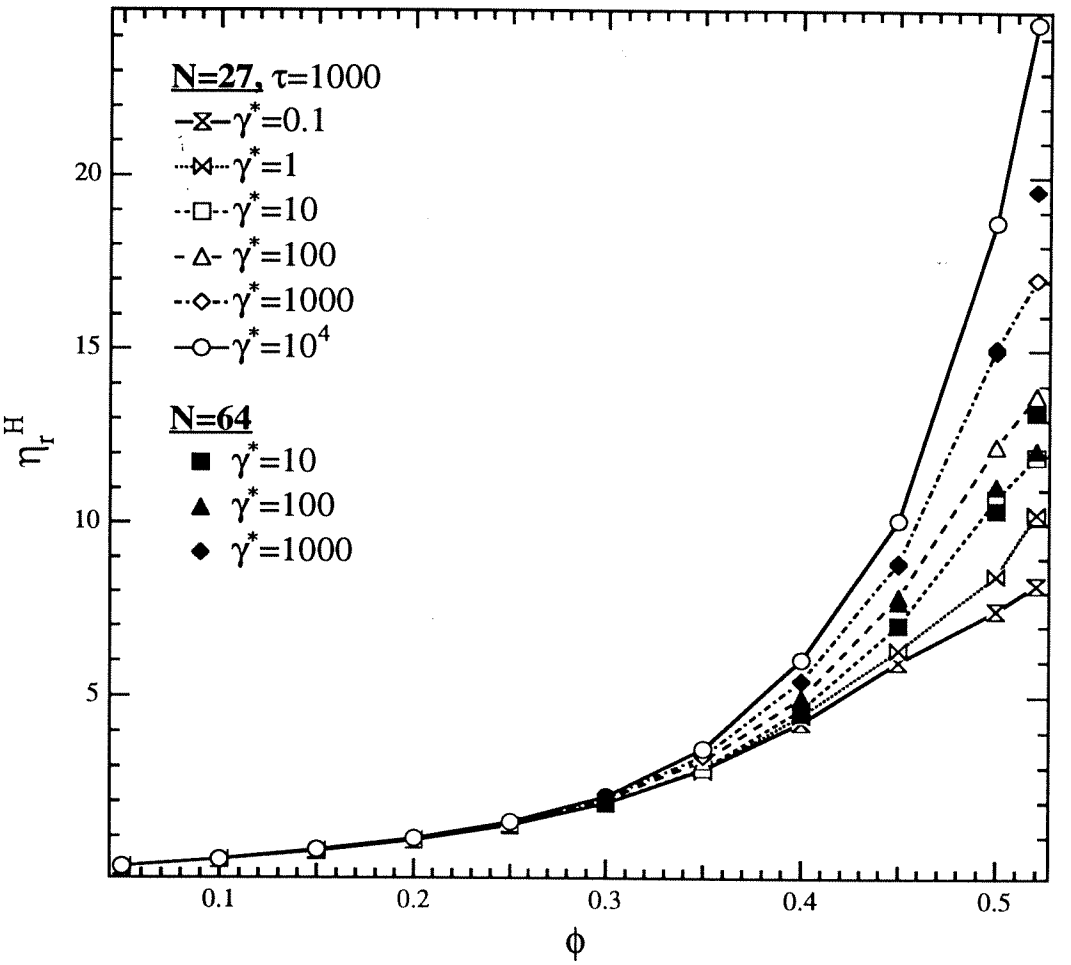

Figure 9.22: The hydrodynamic contribution to the shear viscosity of suspensions.

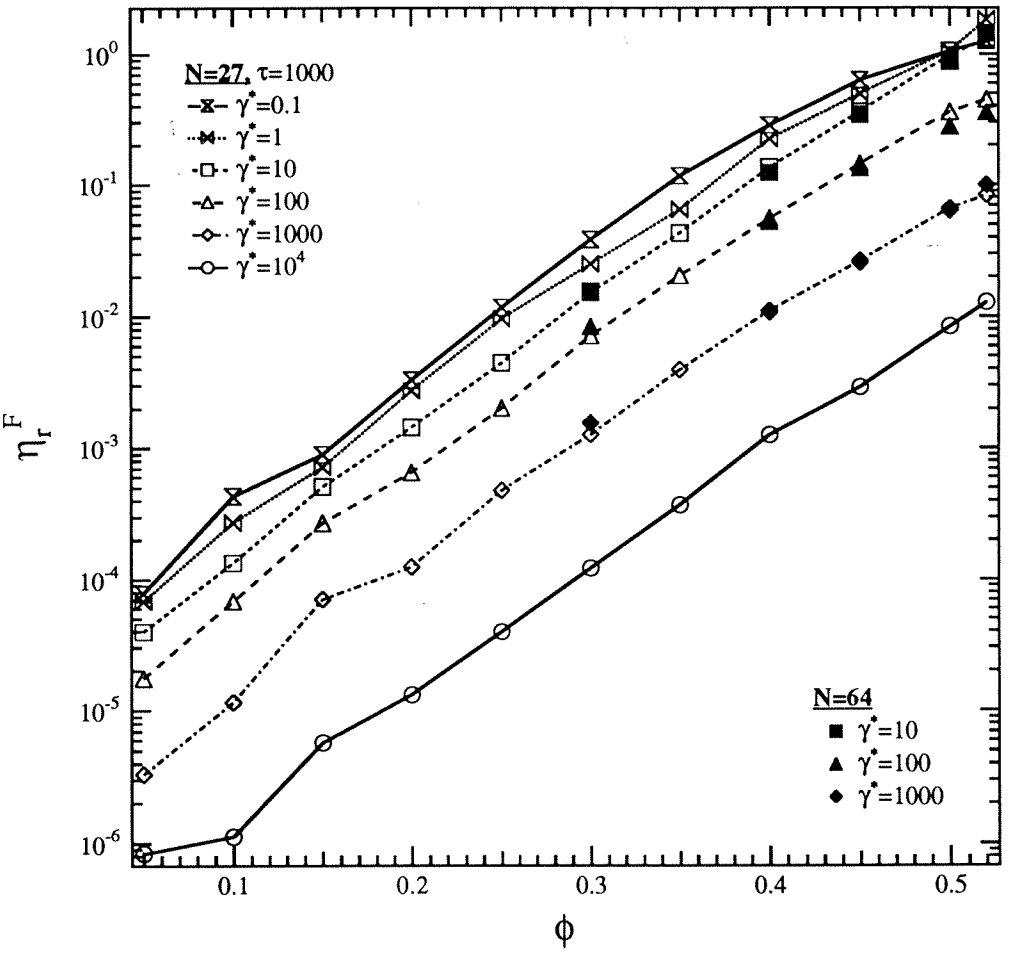

Figure 9.23: The interparticle-force contribution to the shear viscosity of suspensions.

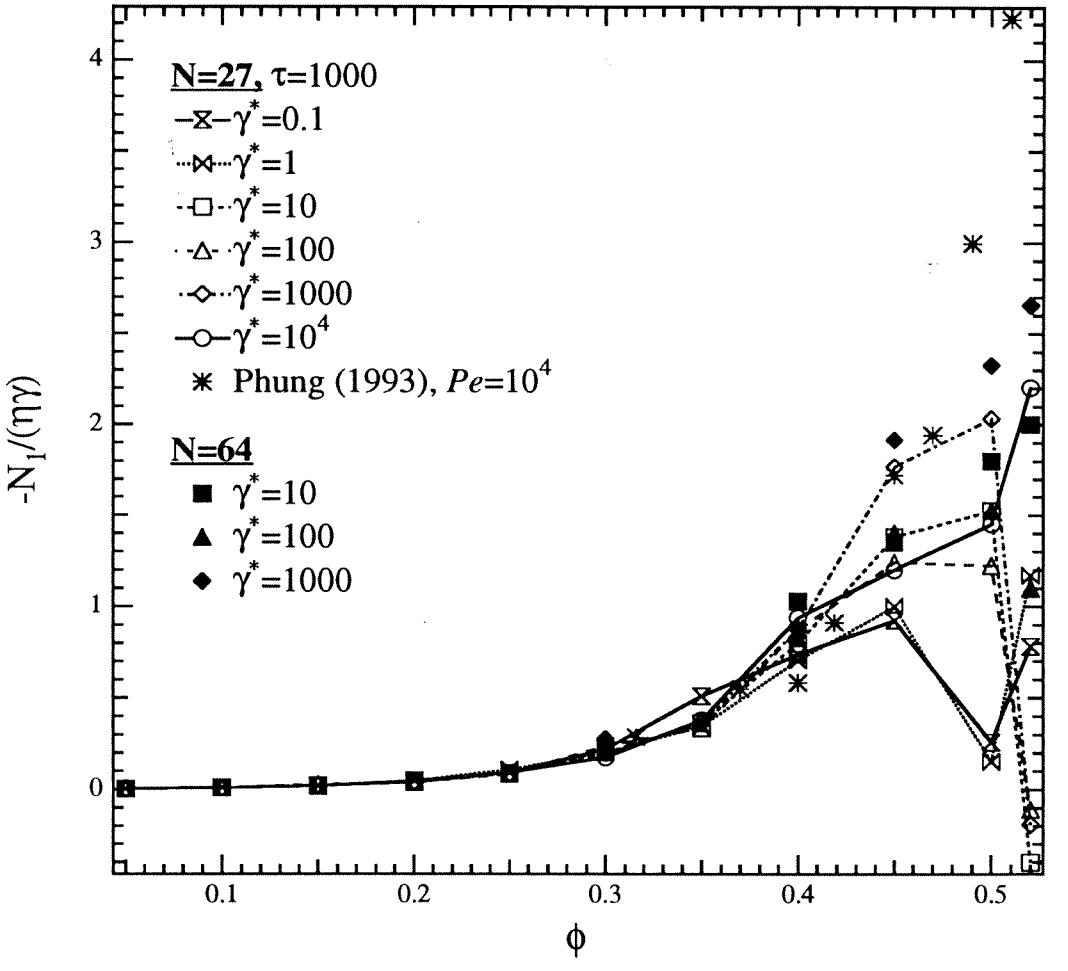

Figure 9.24: The total first normal stress difference.

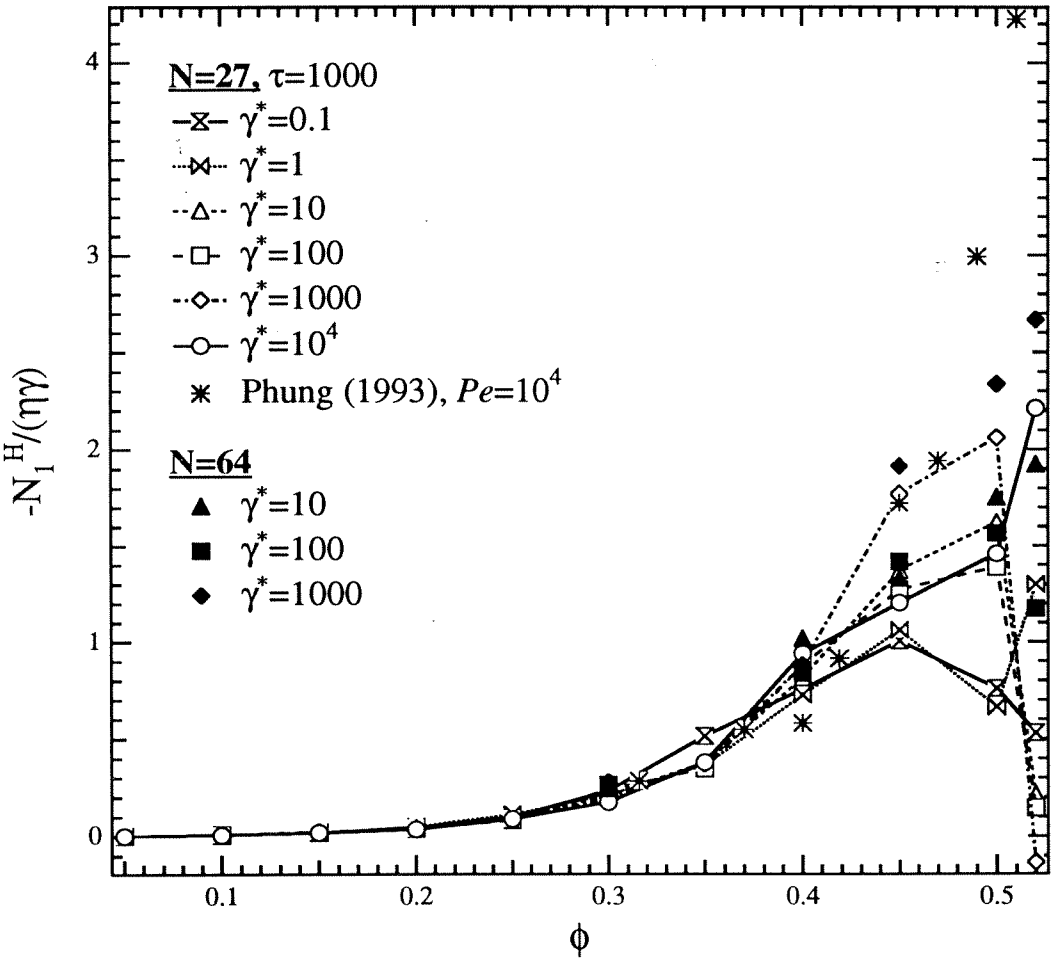

Figure 9.25: The hydrodynamic contribution to the first normal stress difference.

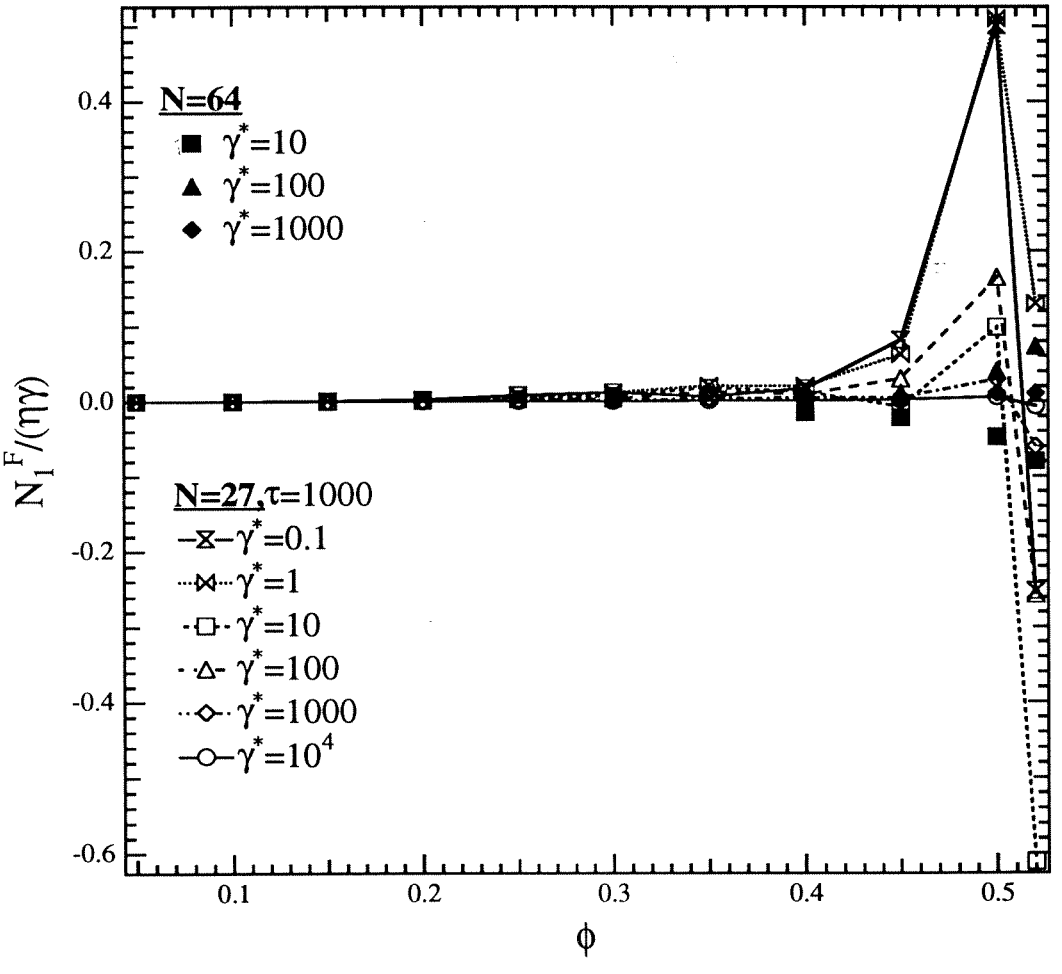

Figure 9.26: The interparticle-force contribution to the first normal stress difference.

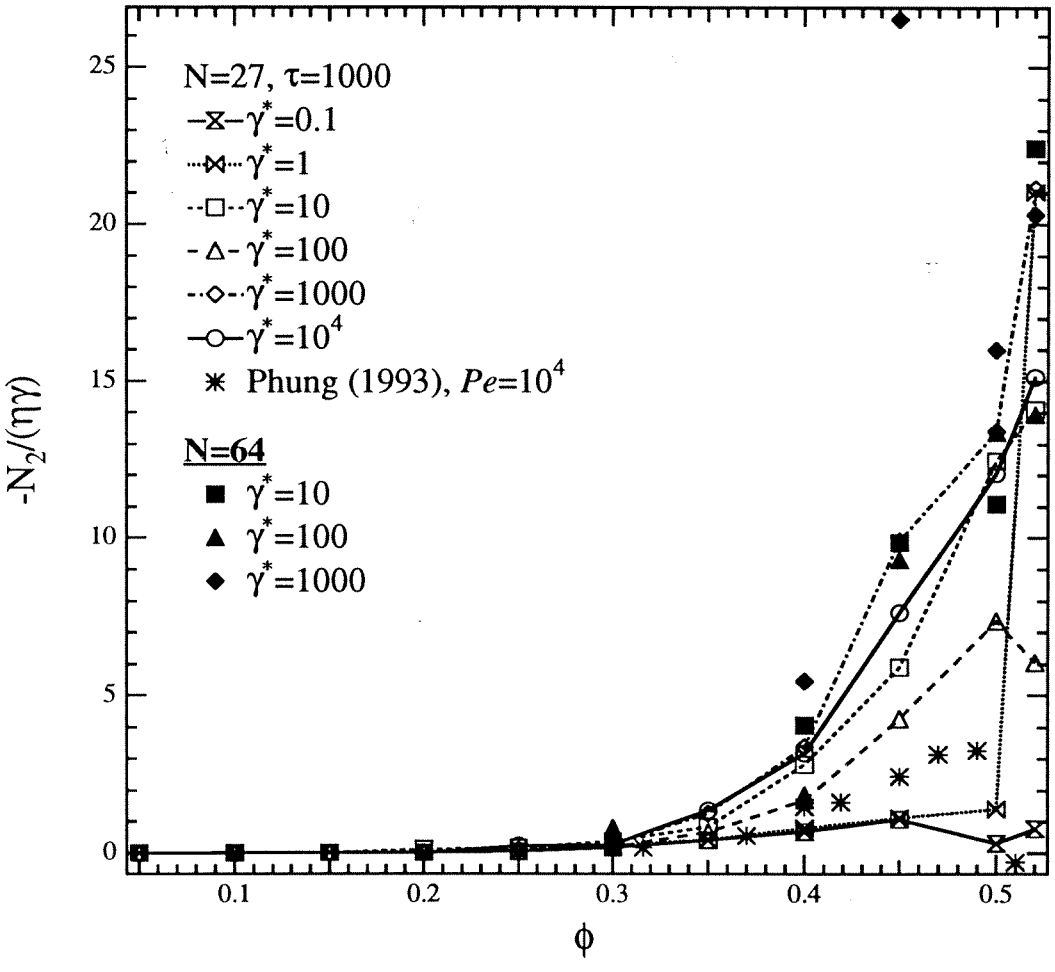

Figure 9.27: The total second normal stress difference.

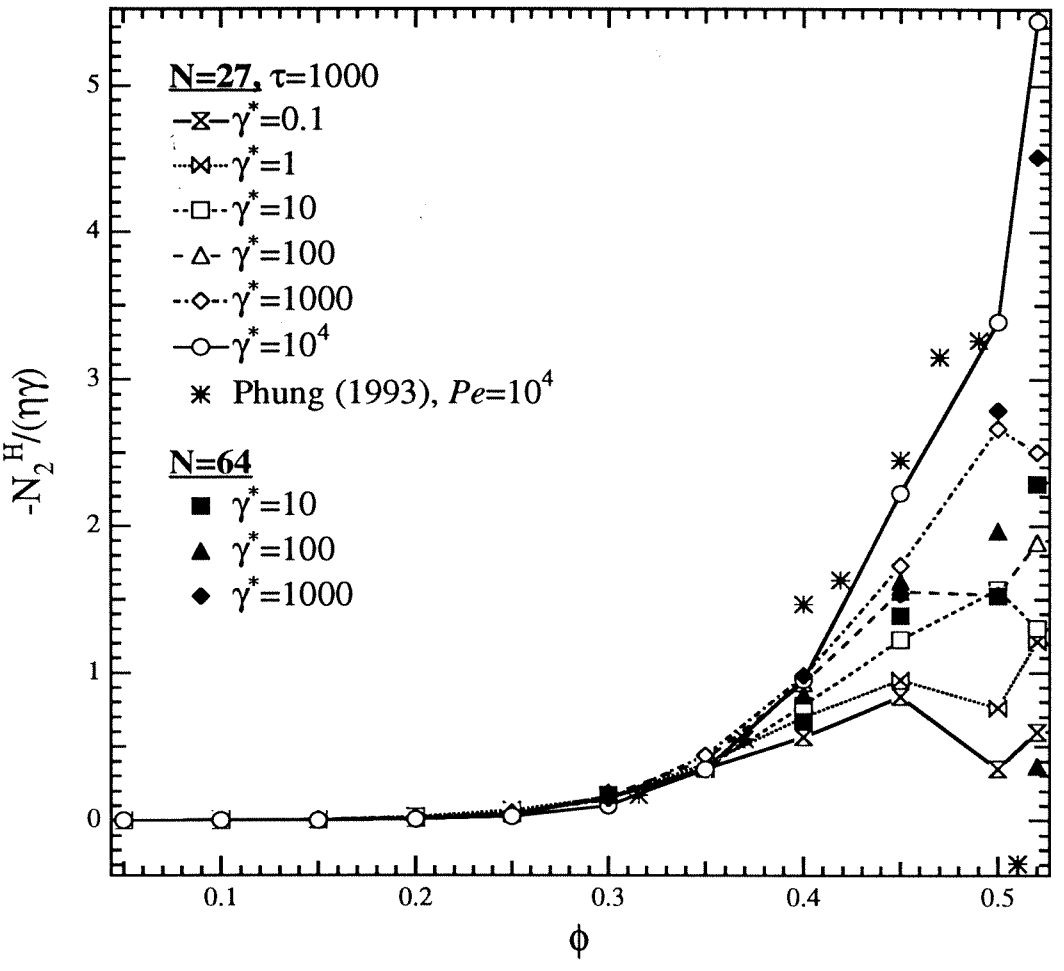

Figure 9.28: The hydrodynamic contribution to the second normal stress difference.

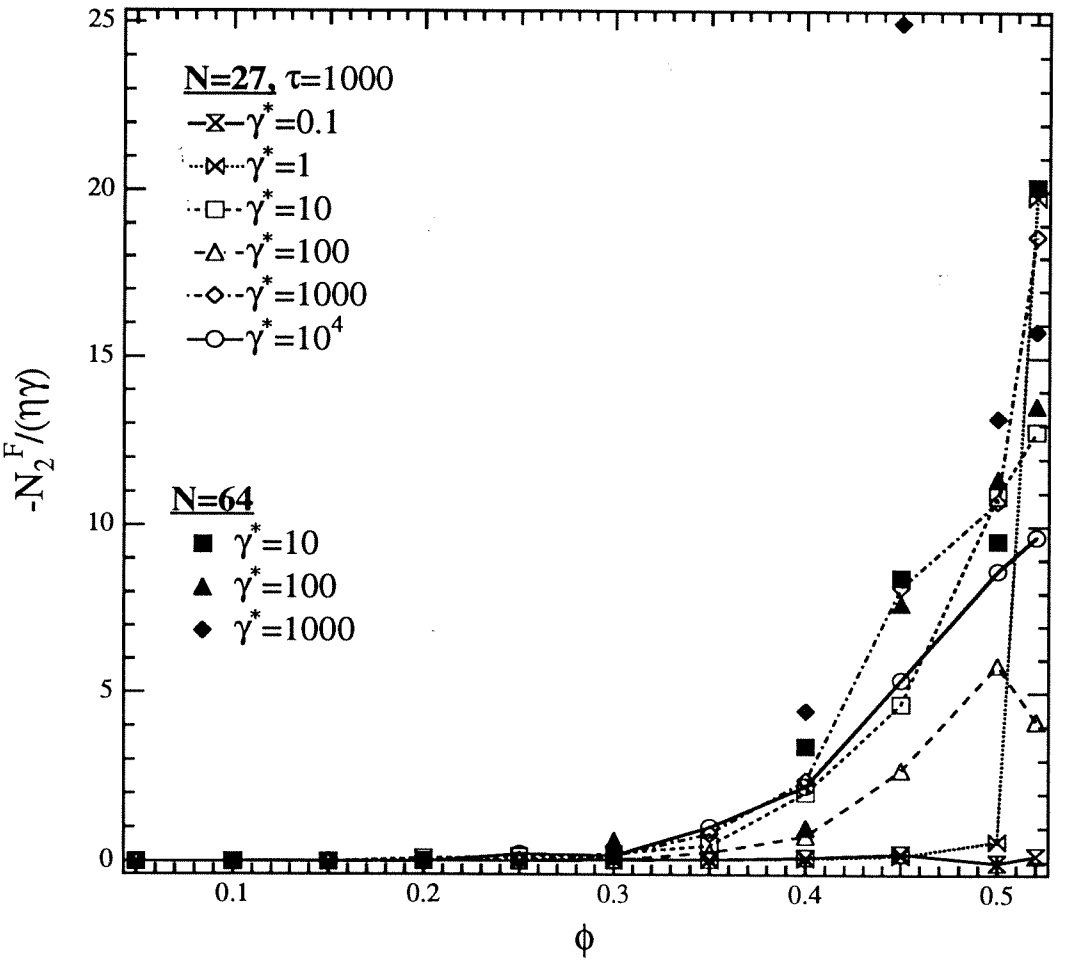

Figure 9.29: The interparticle-force contribution to the second normal stress difference.

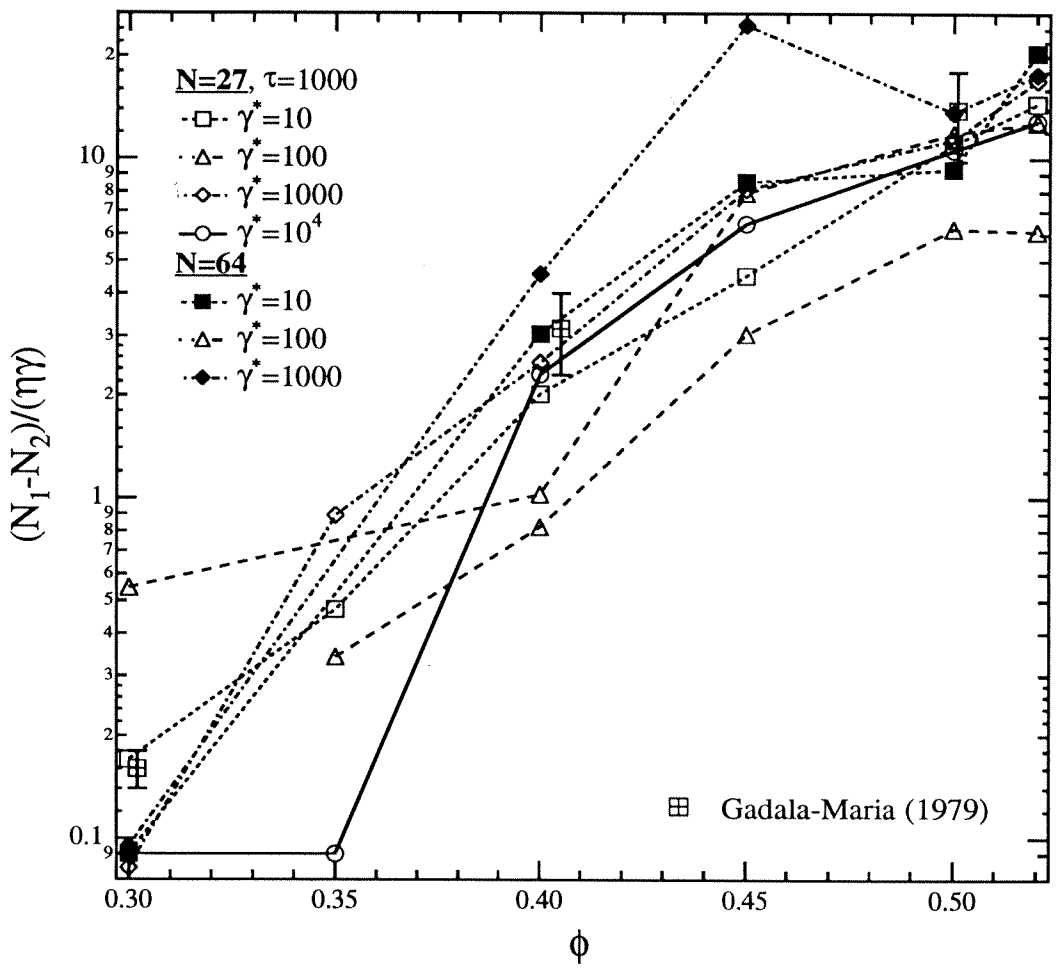

Figure 9.30: Comparison with the normal stress data (the quantity $N_1 - N_2$) in Gadala-Maria (1979). The bars on the symbols representing Gadala-Maria's data show the range of his data.

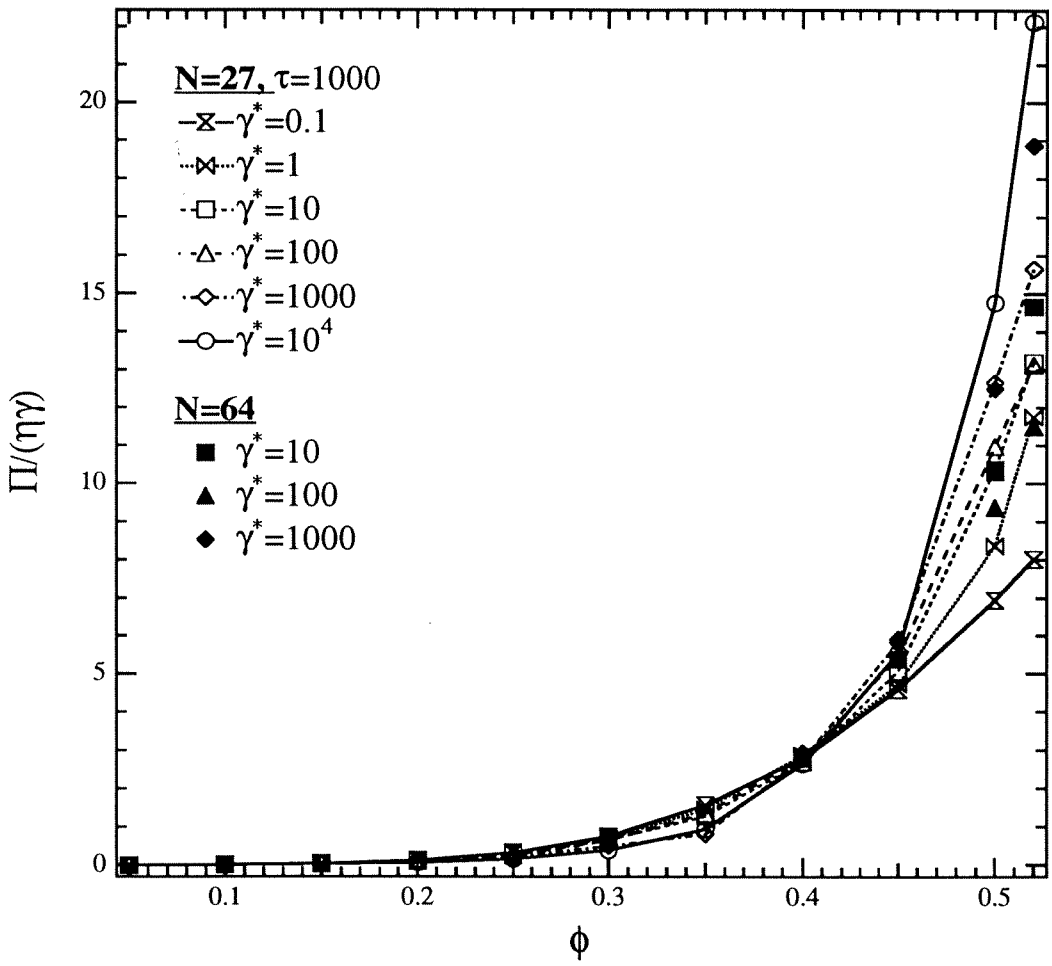

Figure 9.31: The total suspension pressure.

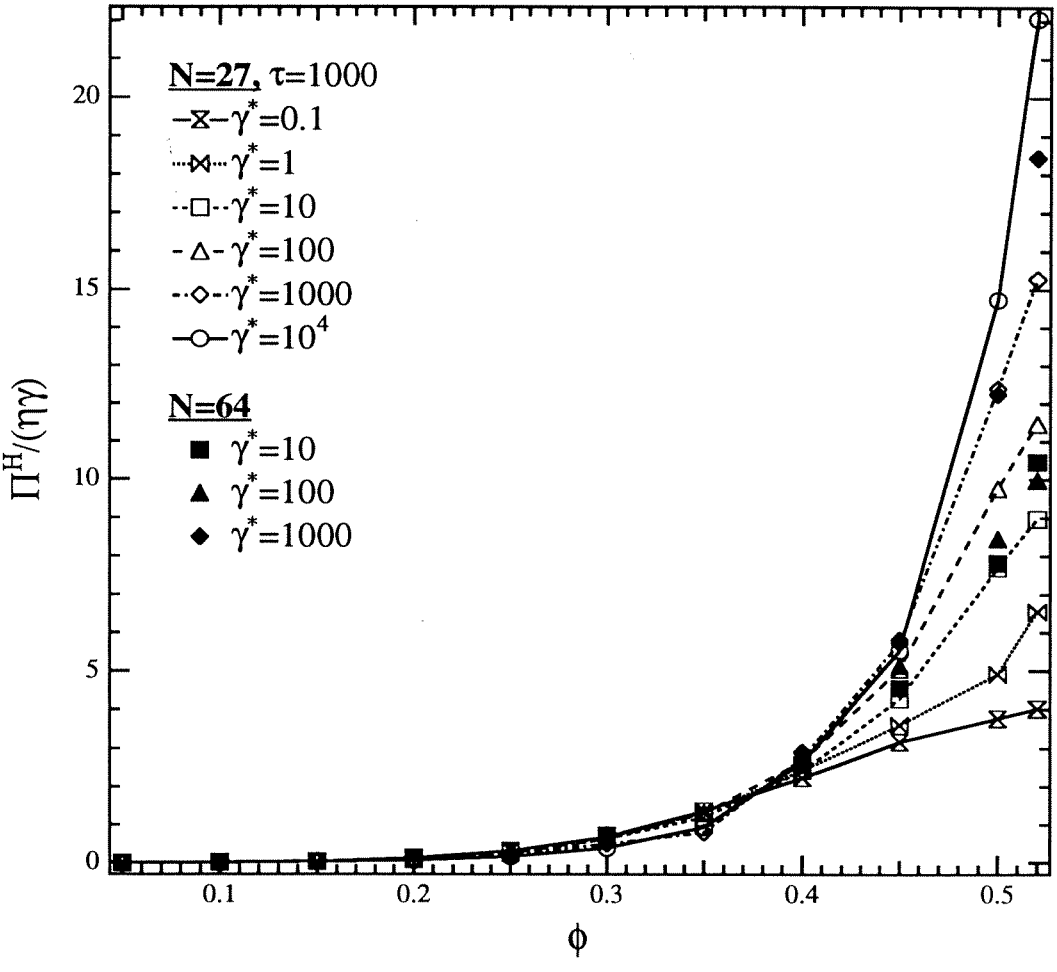

Figure 9.32: The hydrodynamic contribution to the suspension pressure.

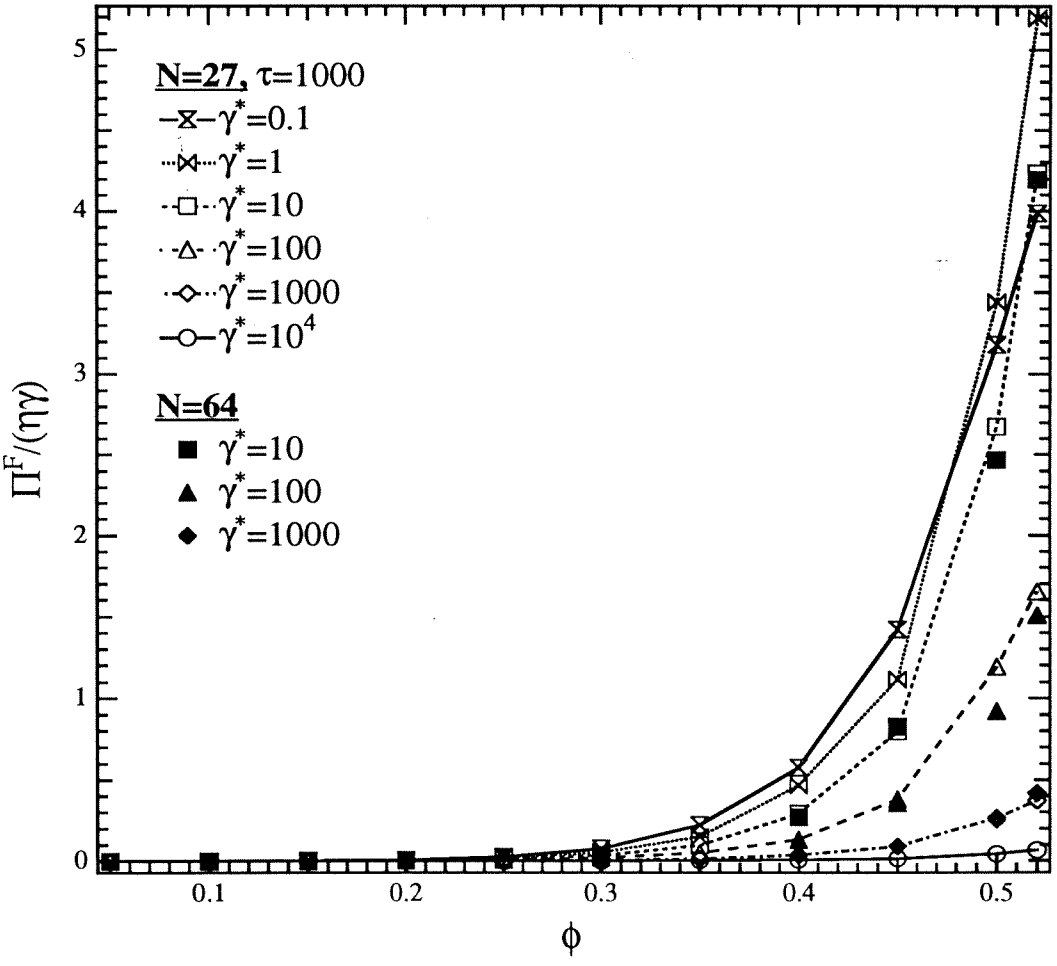

Figure 9.33: The interparticle-force contribution to the suspension pressure.

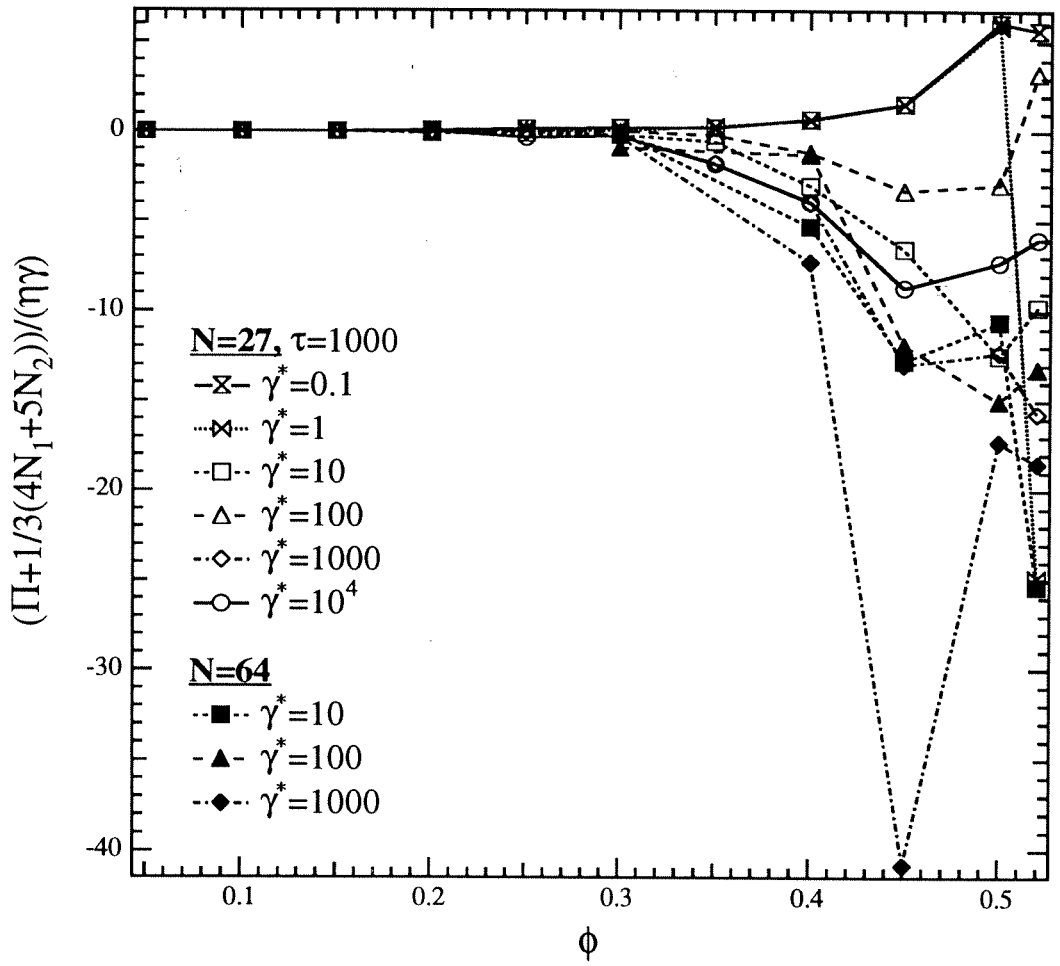

Figure 9.34: Test of the assumption that $\Pi + \frac{1}{3}(4N_1 + 5N_2) = 0$ as a possible cause of the lack of particle migration in torsional flow.

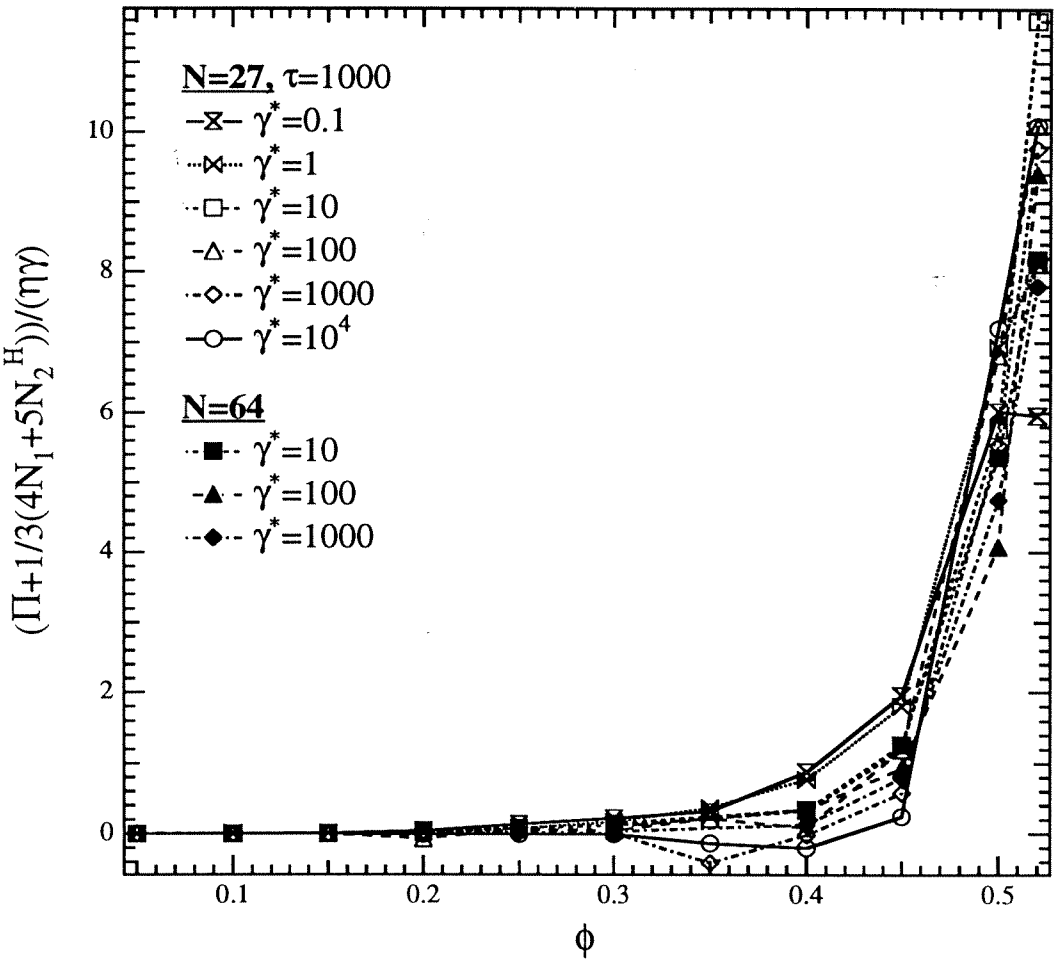

Figure 9.35: The quantity $\Pi + \frac{1}{3}(4N_1 + 5N_2^H)$ as a function of the particle phase fraction.

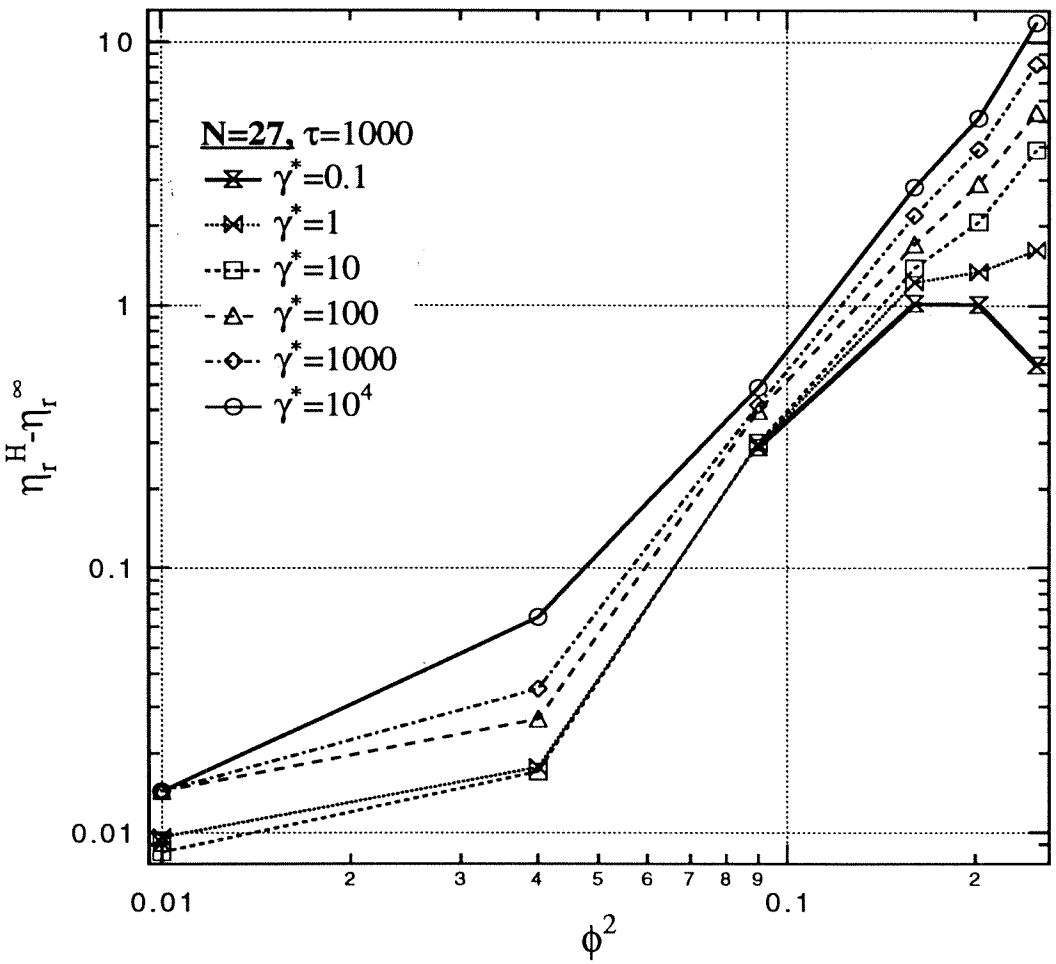

Figure 9.36: The hydrodynamic contribution to the shear viscosity (over and above the relative high-frequency dynamic viscosity $\eta_r{}^{\infty}$, as reported by Phillips *et al.* 1988) plotted against ϕ^2. At low ϕ, $(\eta_r^H - \eta_r^{\infty})$ scales as ϕ^2.

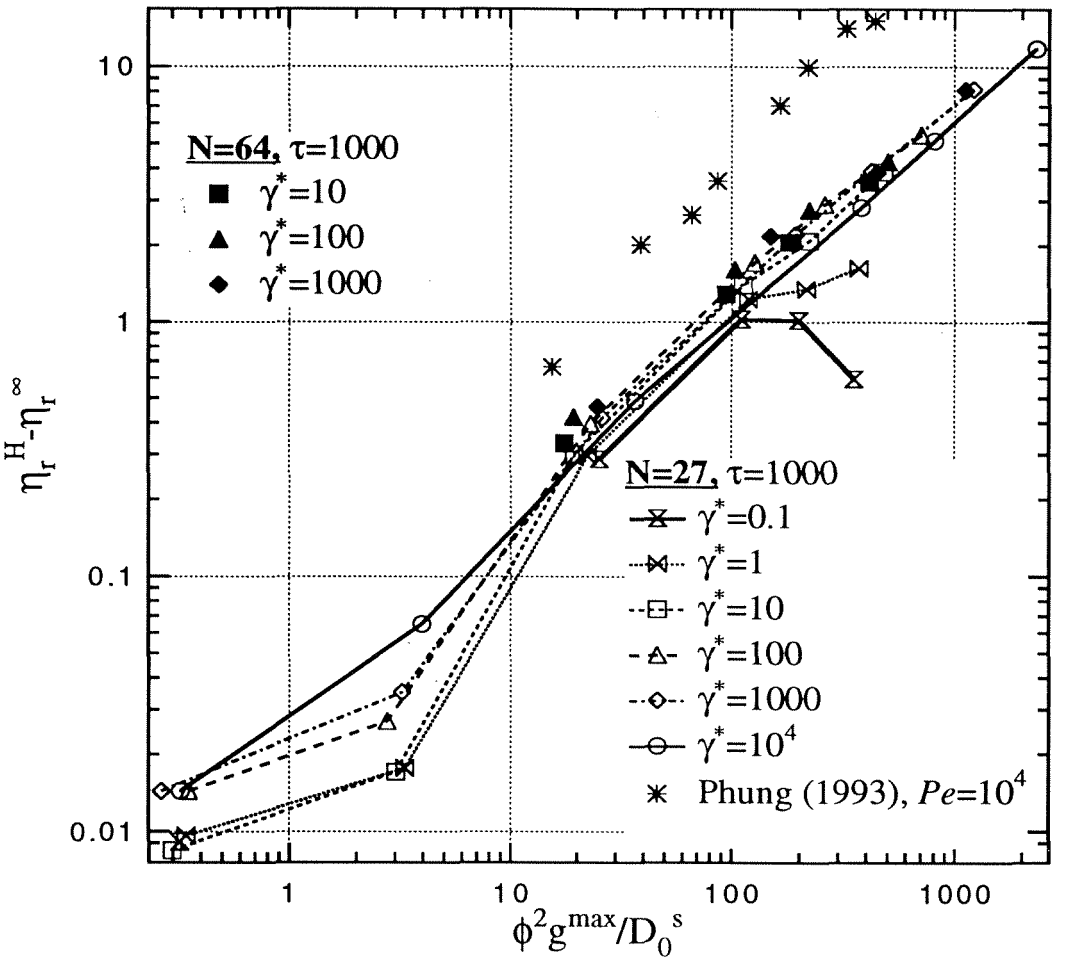

Figure 9.37: The hydrodynamic contribution to the shear viscosity (over and above the relative high-frequency dynamic viscosity $\eta_r{}^\infty$, as reported by Phillips *et al.* 1988) plotted against $\phi^2 g^\infty(2b;\phi)/\hat{D}_0^s(\phi)$. At high ϕ, $(\eta_r^H - \eta_r^\infty)$ scales with $\phi^2 g^\infty(2b;\phi)/\hat{D}_0^s(\phi)$.

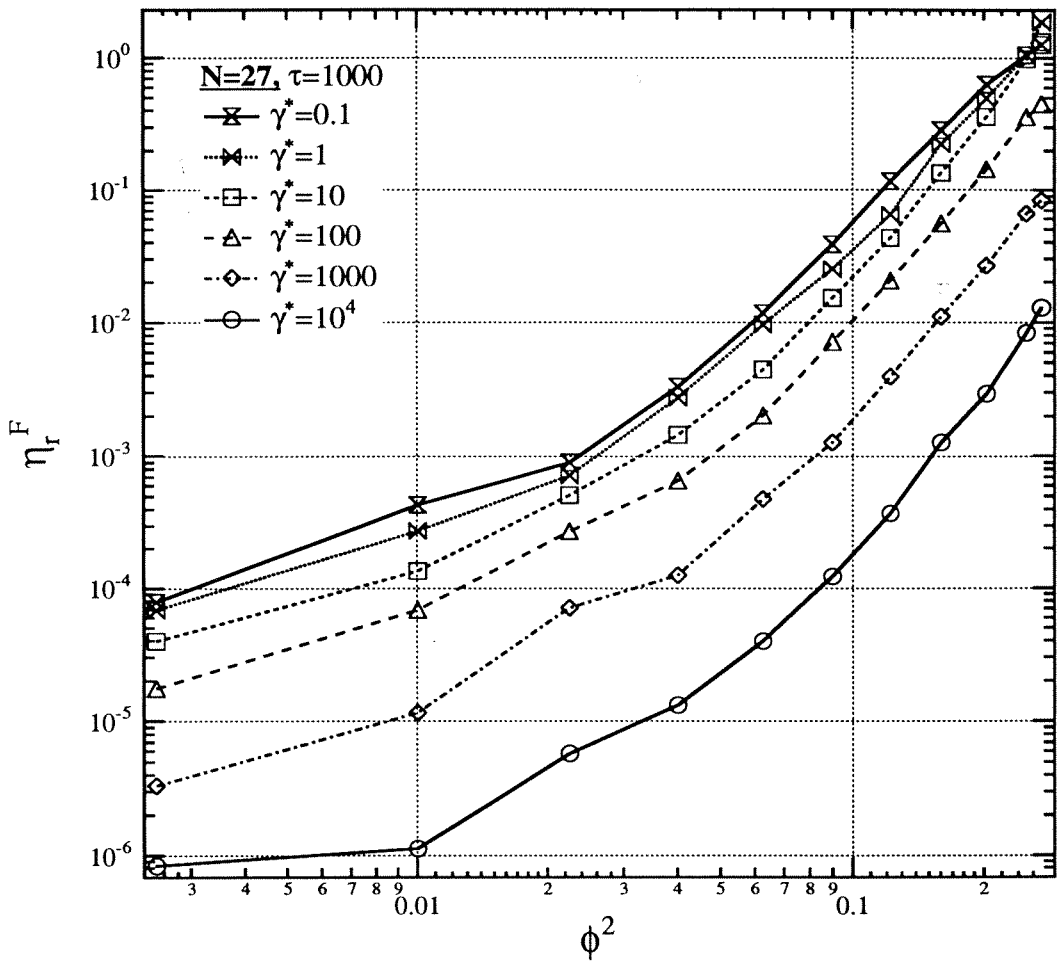

Figure 9.38: The interparticle-force contribution to the shear viscosity plotted against ϕ^2. At low ϕ, η^F scales as ϕ^2.

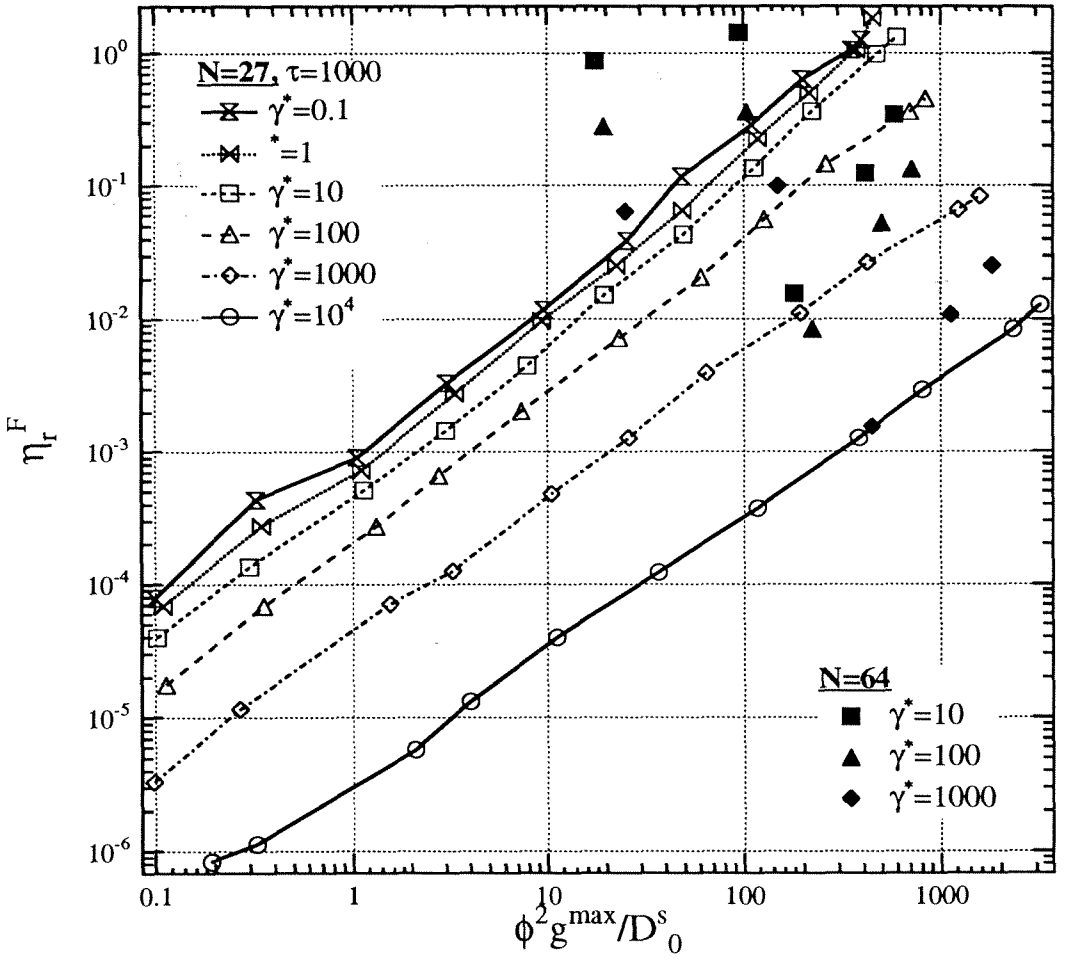

Figure 9.39: The interparticle-force contribution to the shear viscosity plotted against $\phi^2 g^{\infty}(2b;\phi)/\hat{D}_0^s(\phi)$. At high ϕ, η^F scales with $\phi^2 g^{\infty}(2b;\phi)/\hat{D}_0^s(\phi)$.

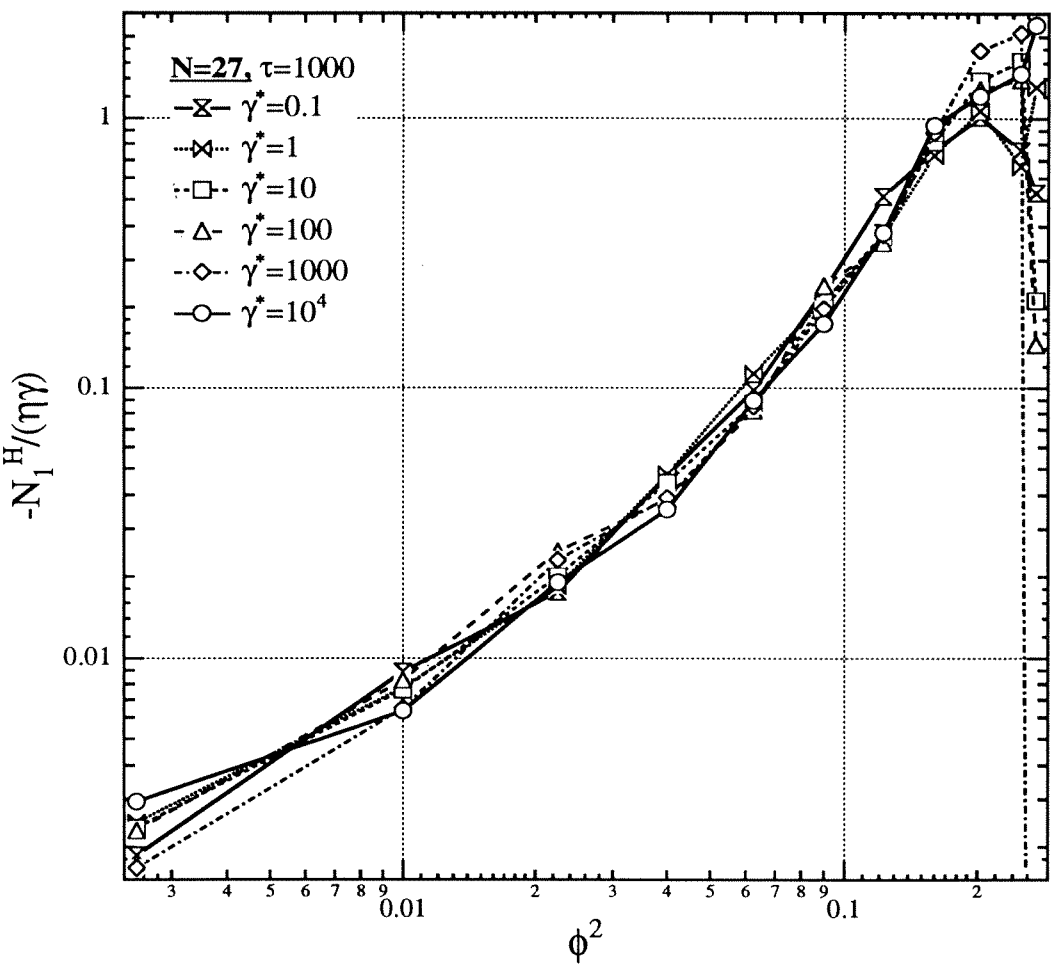

Figure 9.40: The hydrodynamic contribution to the first normal stress difference plotted against ϕ^2. At low ϕ, N_1^H scales as ϕ^2. Only the data points with negative values of N_1^H are shown.

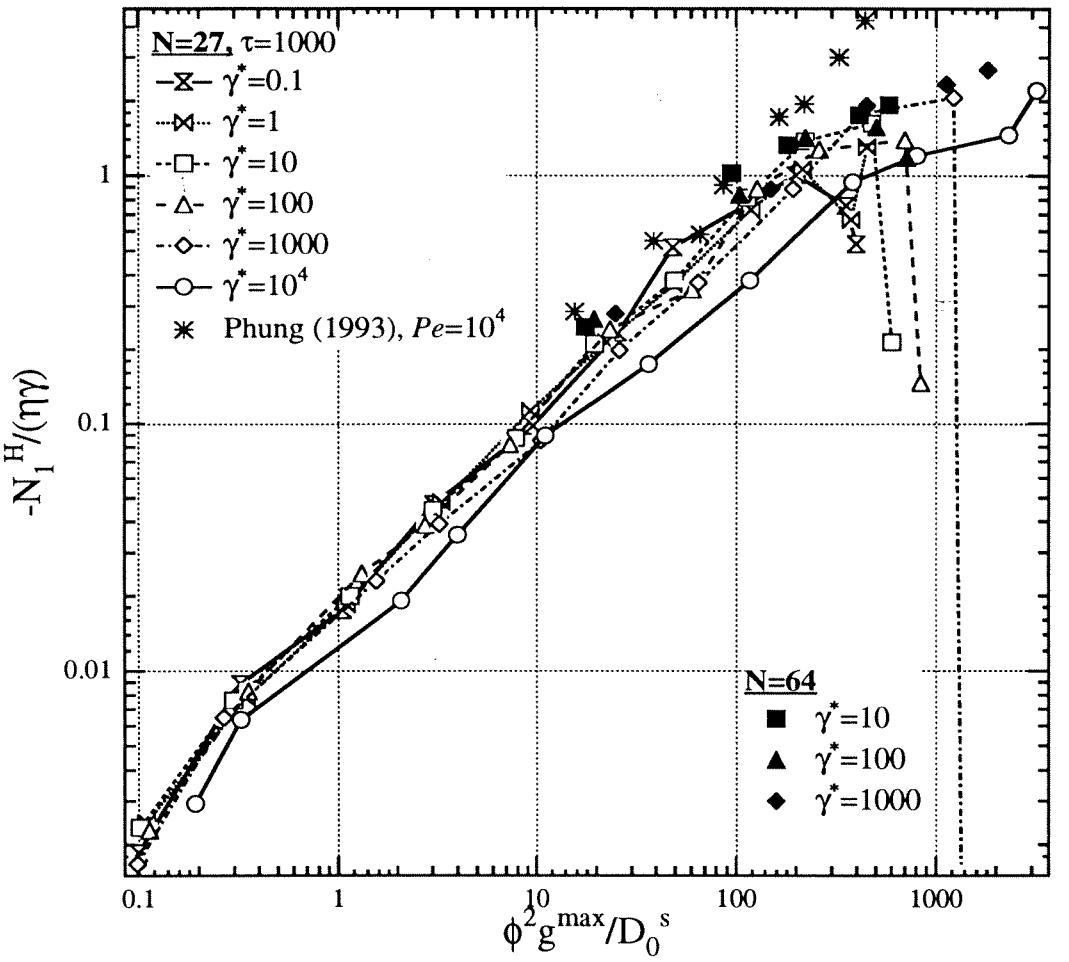

Figure 9.41: The hydrodynamic contribution to the first normal stress difference vs. $\phi^2 g^{\infty}(2b;\phi)/\hat{D}_0^s(\phi)$. At high ϕ, N_1^H scales with $\phi^2 g^{\infty}(2b;\phi)/\hat{D}_0^s(\phi)$. Only the data points with negative values of N_1^H are shown.

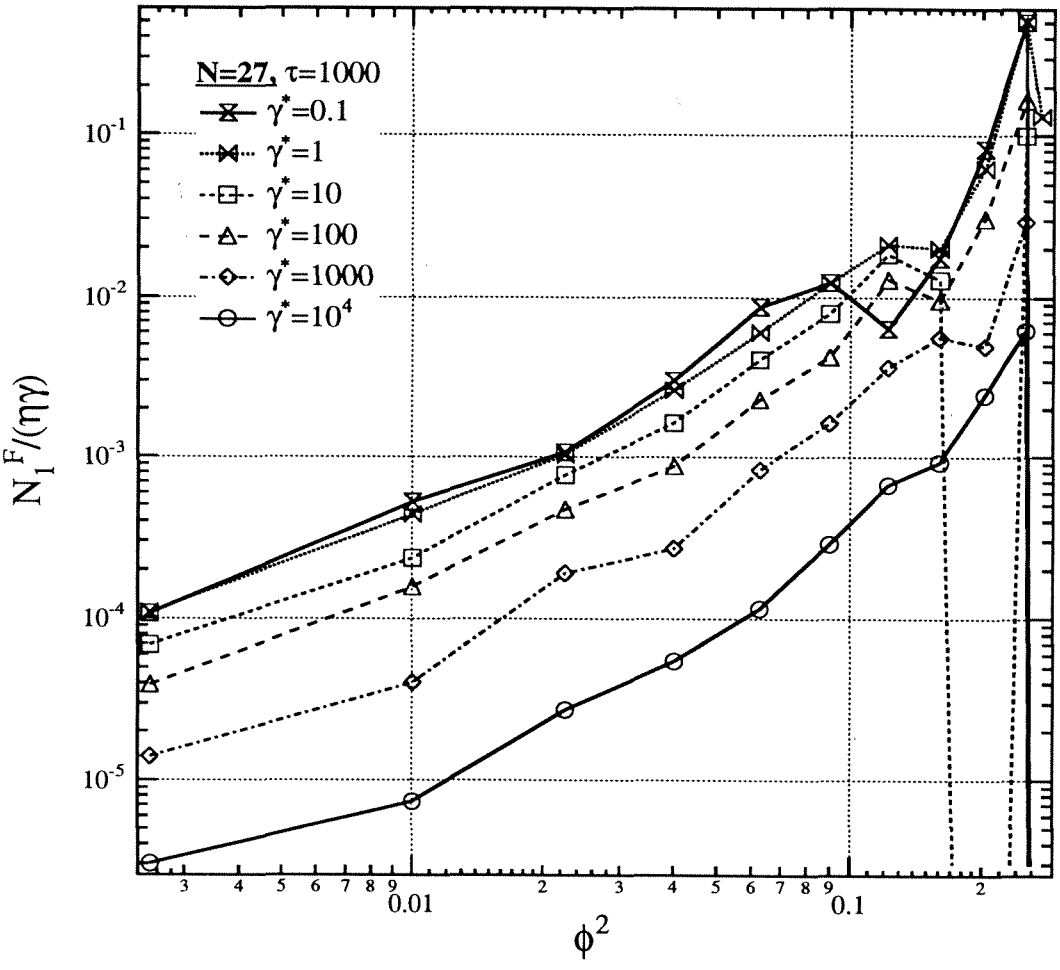

Figure 9.42: The interparticle-force contribution to the first normal stress difference plotted against ϕ^2. At low ϕ, N_1^F scales as ϕ^2. Only the data points with positive values of N_1^F are shown.

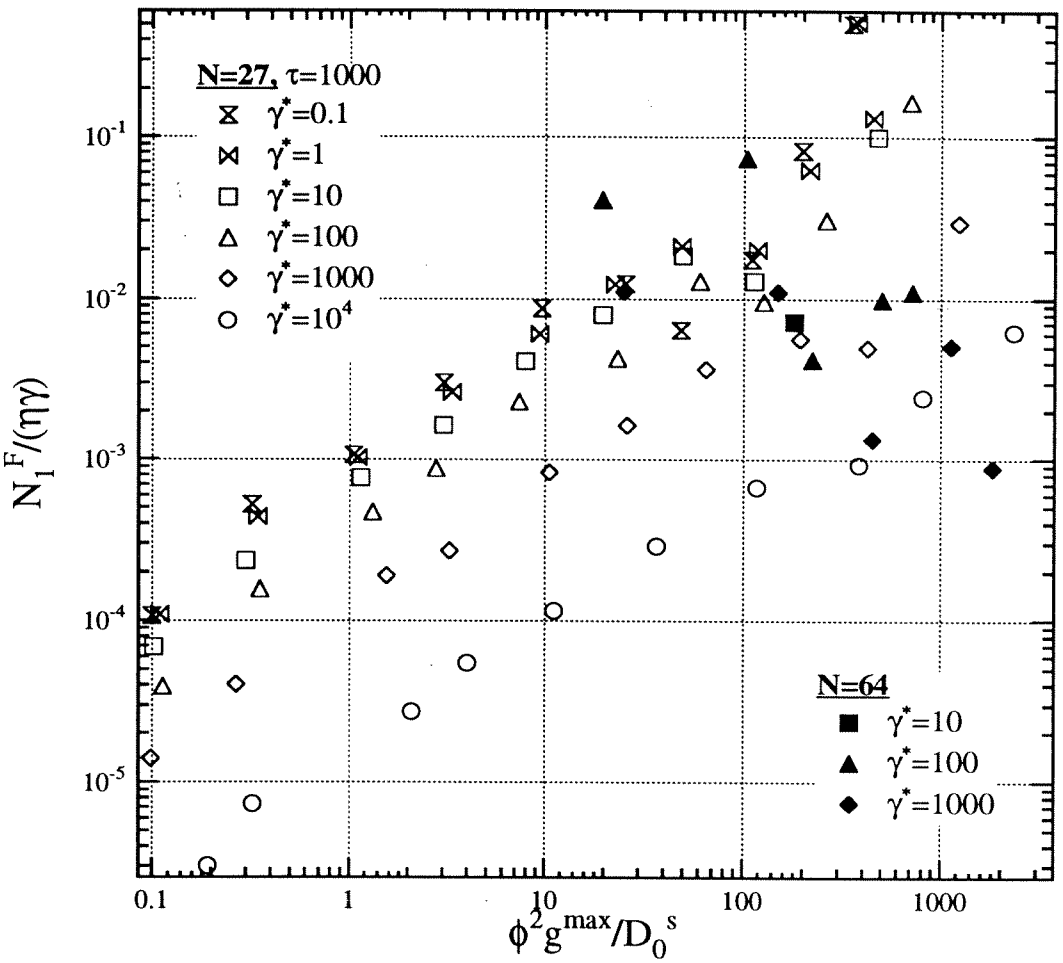

Figure 9.43: The interparticle-force contribution to the first normal stress difference plotted against $\phi^2 g^{\infty}(2b;\phi)/\hat{D}_0^s(\phi)$. Only the data points with positive values of N_1^F are shown.

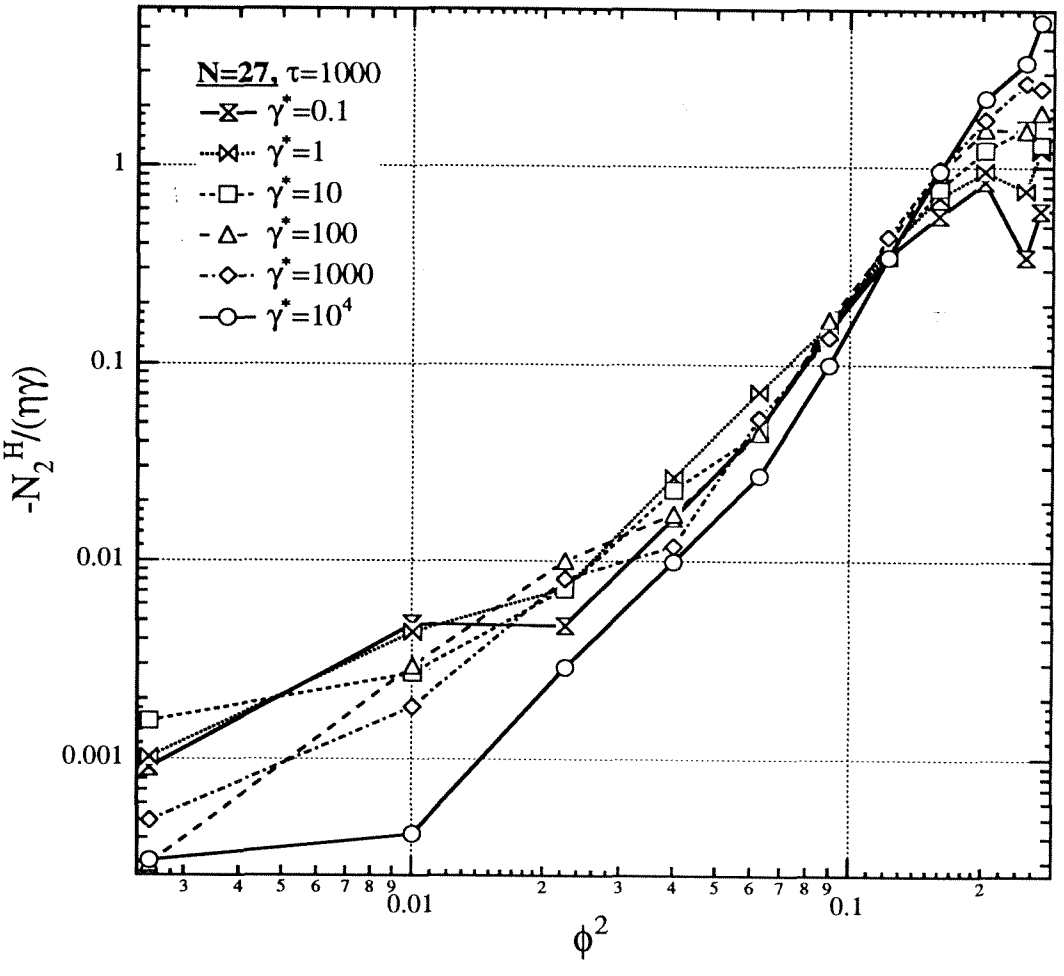

Figure 9.44: The hydrodynamic contribution to the second normal stress difference plotted against ϕ^2. At low ϕ, N_2^H scales as ϕ^2. Only the data points with negative values of N_2^H are shown.

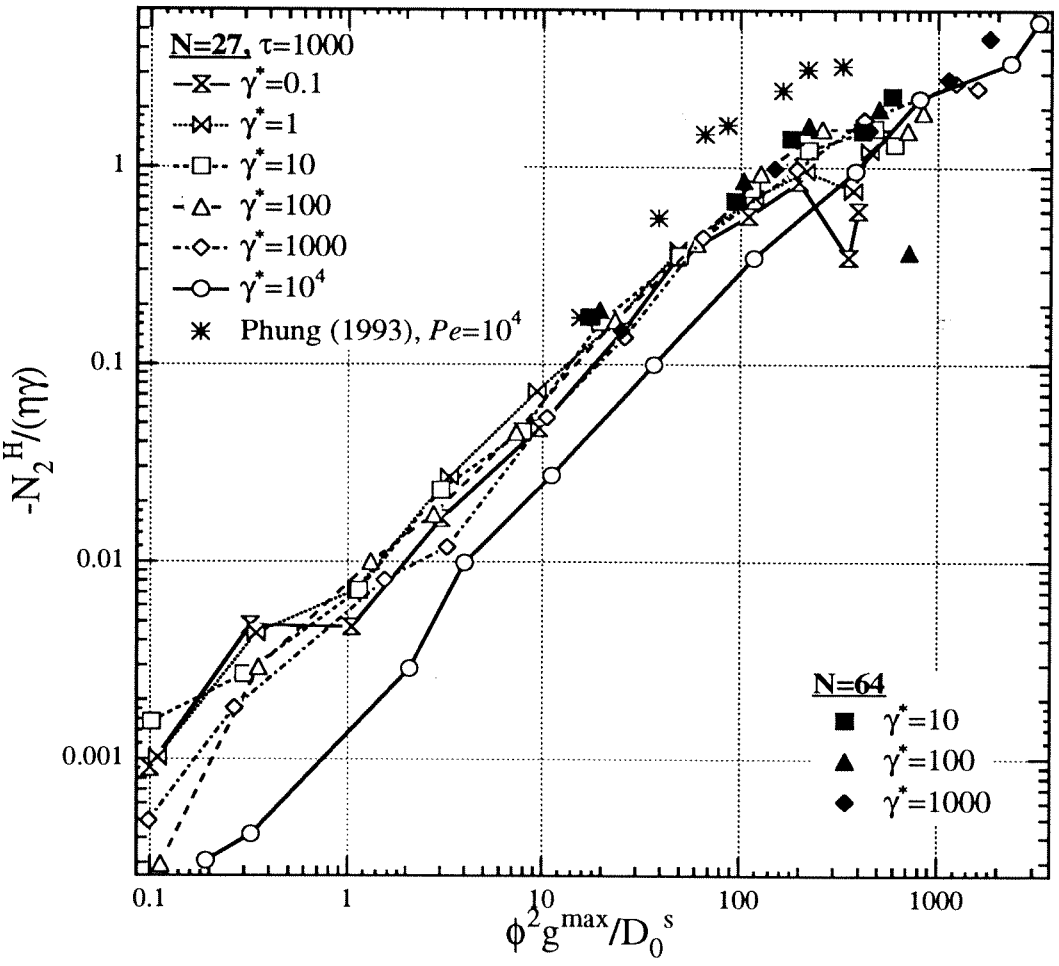

Figure 9.45: The hydrodynamic contribution to the second normal stress difference plotted against $\phi^2 g^{\infty}(2b;\phi)/\hat{D}_0^s(\phi)$. At high ϕ, N_2^H scales with $\phi^2 g^{\infty}(2b;\phi)/\hat{D}_0^s(\phi)$. Only the data points with negative values of N_2^H are shown.

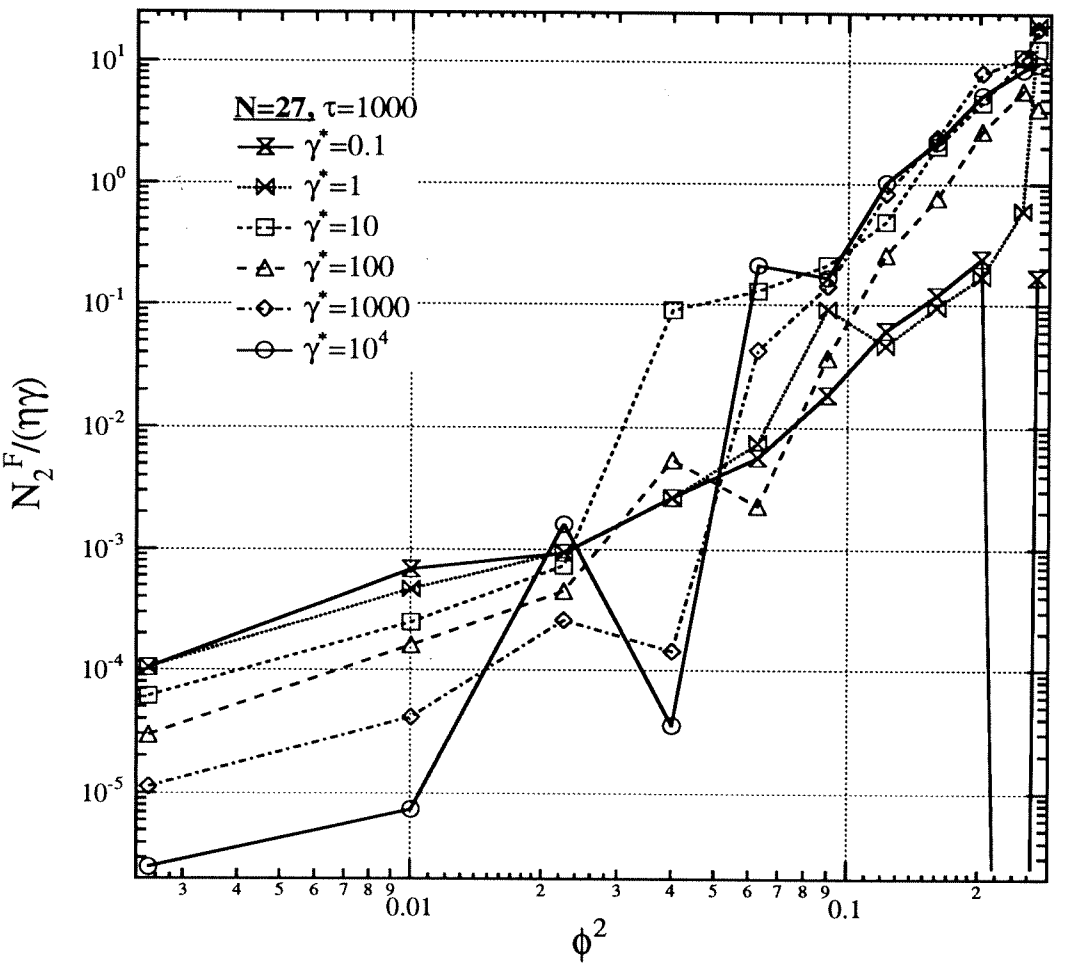

Figure 9.46: The interparticle-force contribution to the second normal stress difference plotted against ϕ^2. At low ϕ, N_2^F scales as ϕ^2. Only the data points with negative values of N_2^F are shown.

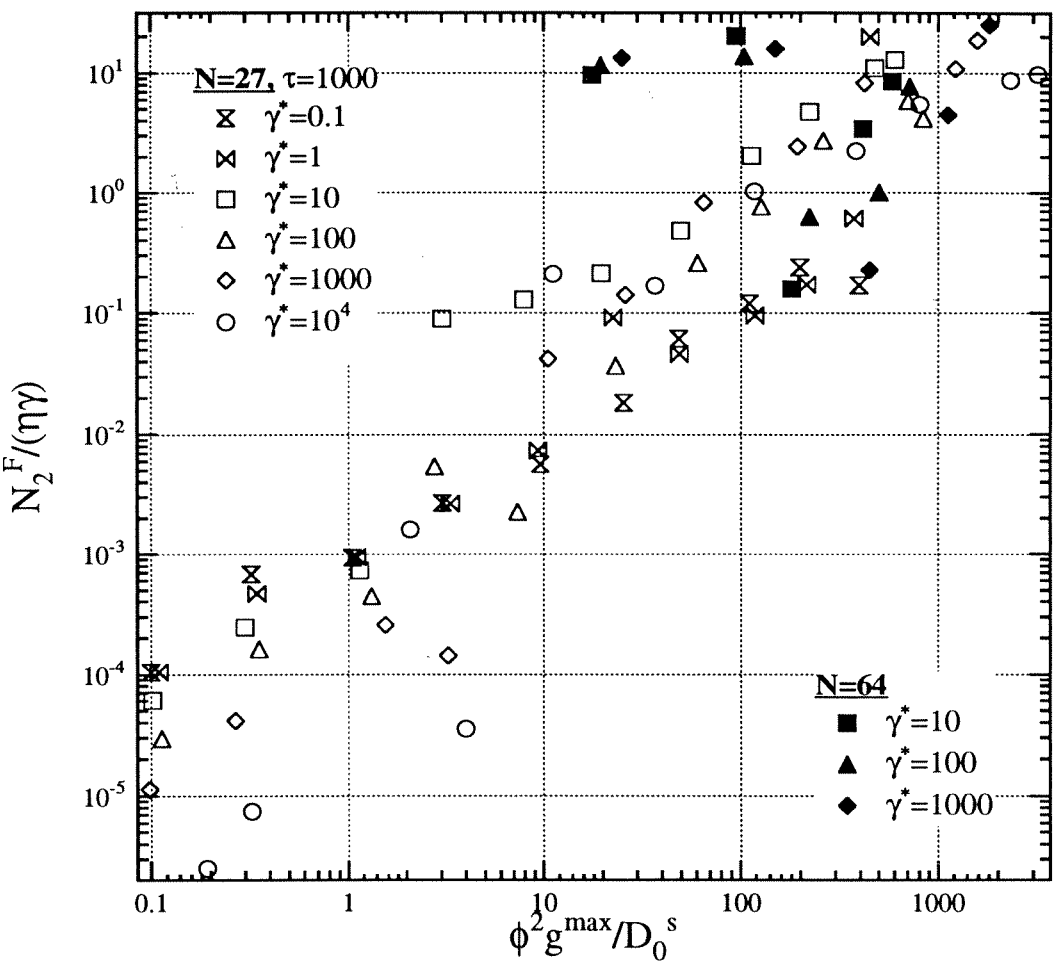

Figure 9.47: The interparticle-force contribution to the second normal stress difference plotted against $\phi^2 g^{\infty}(2b;\phi)/\hat{D}_0^s(\phi)$. Only the data points with negative values of N_1^F are shown.

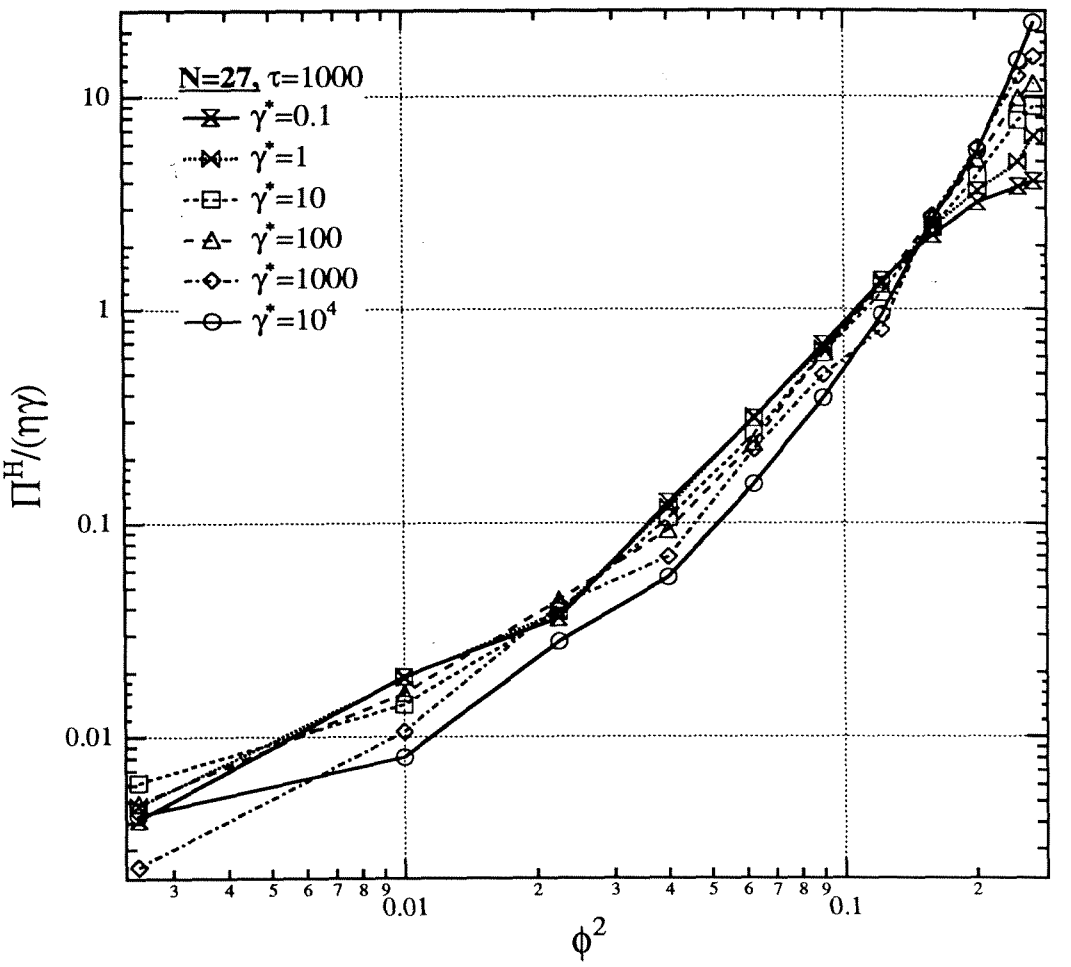

Figure 9.48: The hydrodynamic contribution to the suspension pressure plotted against ϕ^2. At low ϕ, Π^H scales as ϕ^2.

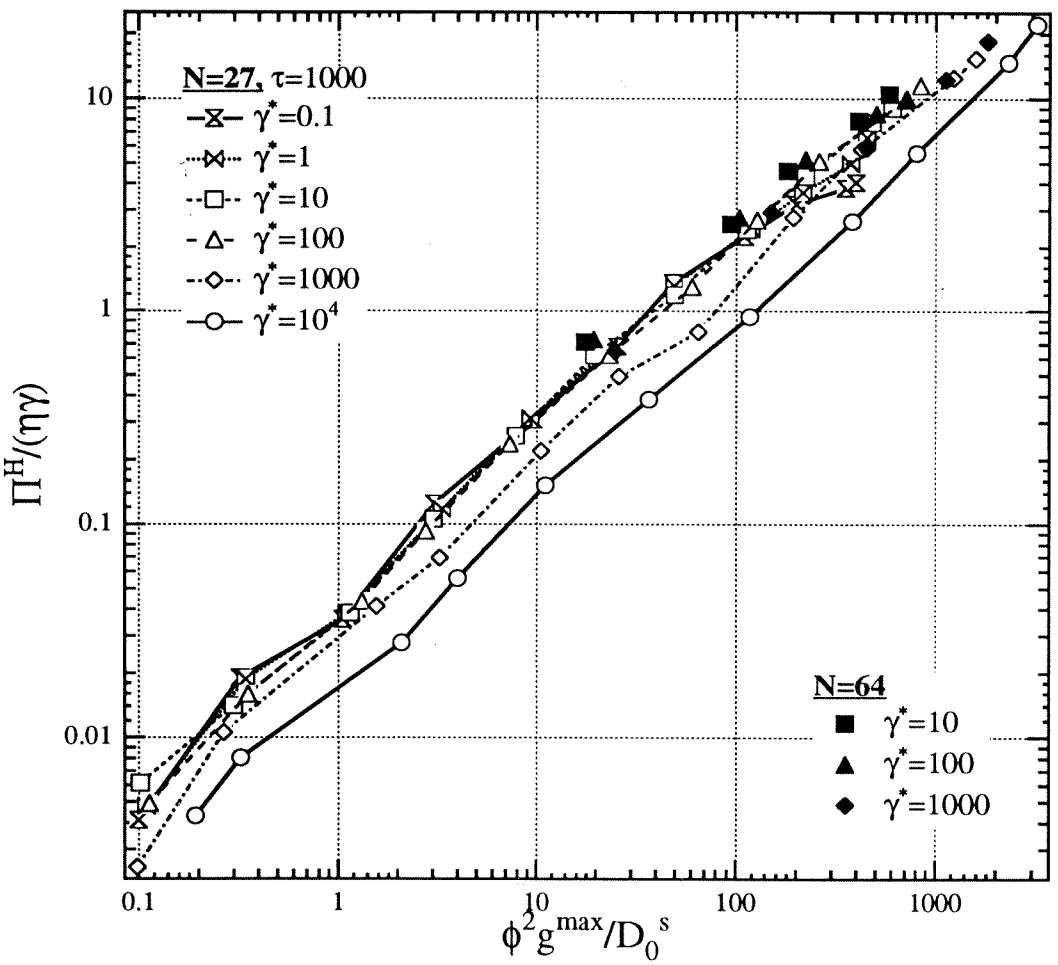

Figure 9.49: The hydrodynamic contribution to the suspension pressure plotted against $\phi^2 g^{\infty}(2b;\phi)/\hat{D}_0^s(\phi)$. At high ϕ, Π^H scales as $\phi^2 g^{\infty}(2b;\phi)/\hat{D}_0^s(\phi)$.

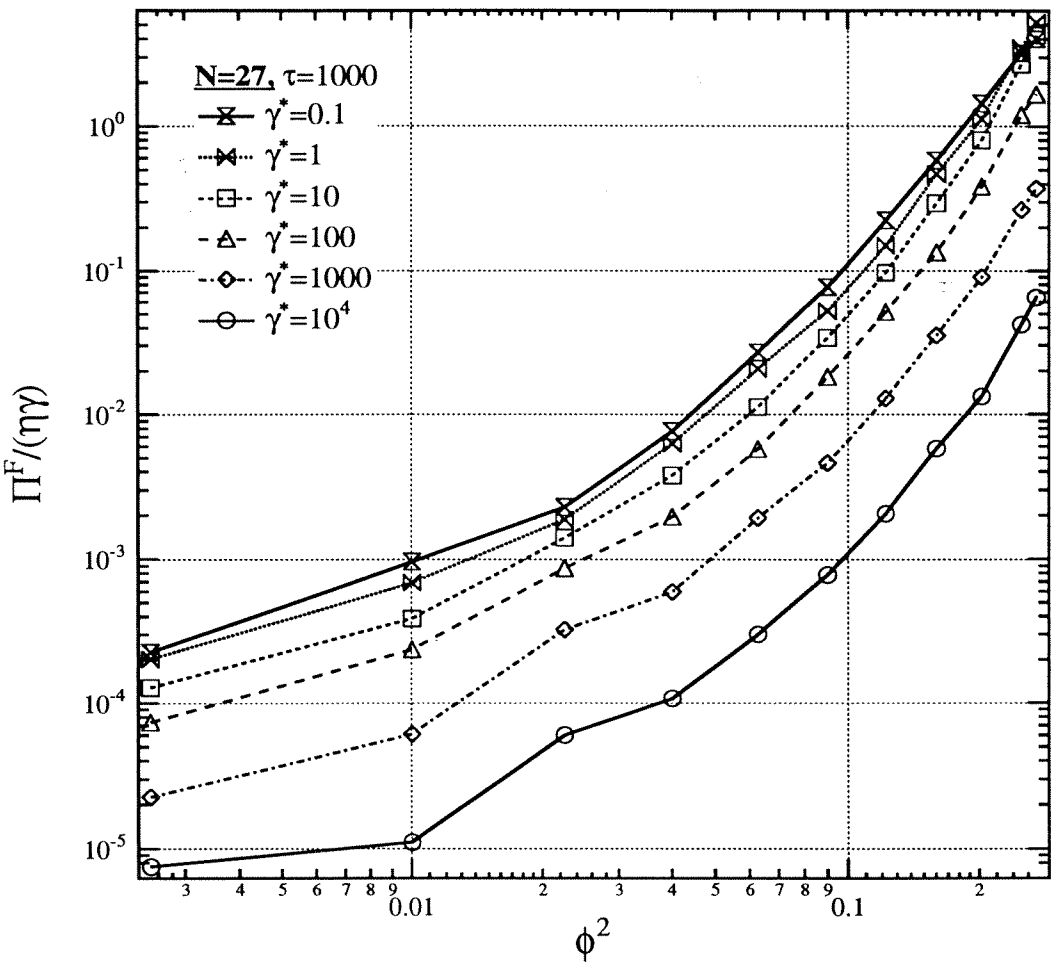

Figure 9.50: The interparticle-force contribution to the suspension pressure plotted against ϕ^2. At low ϕ, Π^F scales as ϕ^2.

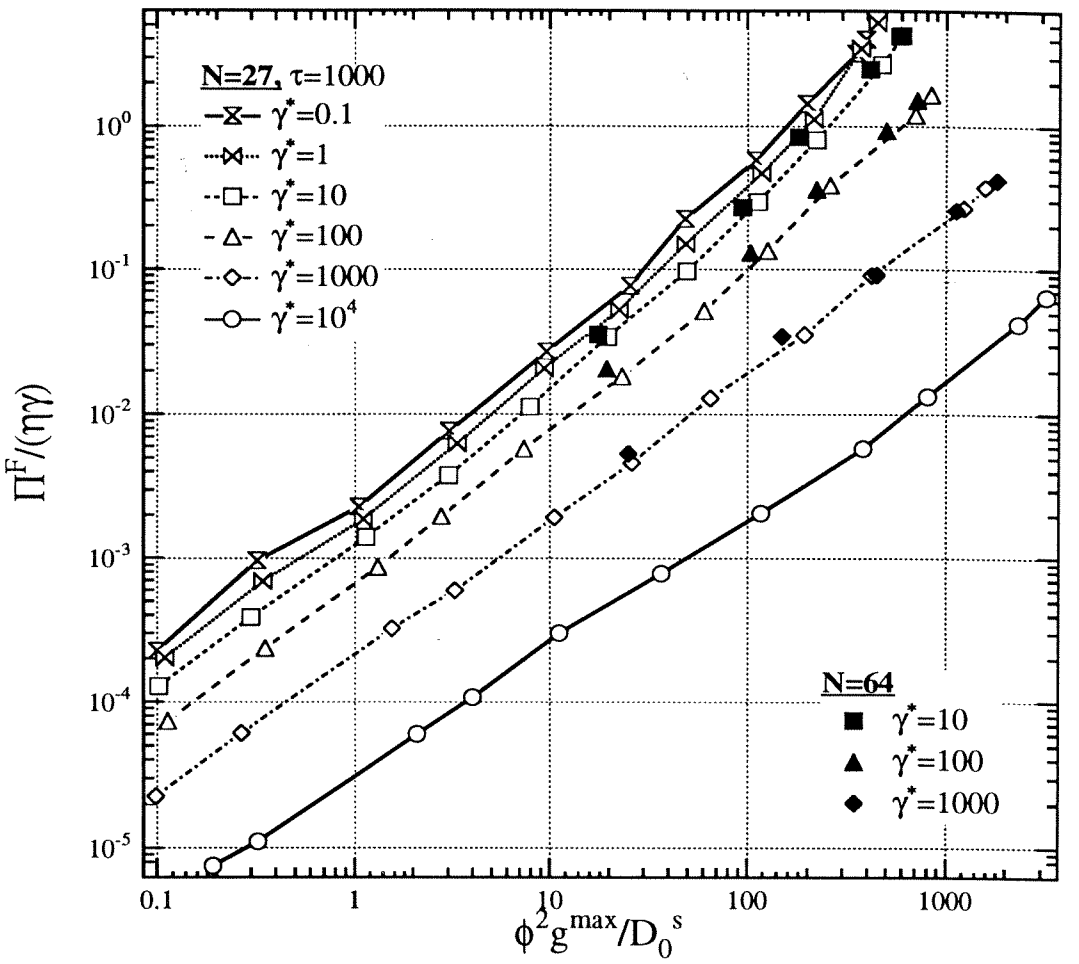

Figure 9.51: The interparticle-force contribution to the suspension pressure plotted against $\phi^2 g^\infty(2b;\phi)/\hat{D}_0^s(\phi)$. At high ϕ, Π^F scales as $\phi^2 g^\infty(2b;\phi)/\hat{D}_0^s(\phi)$.

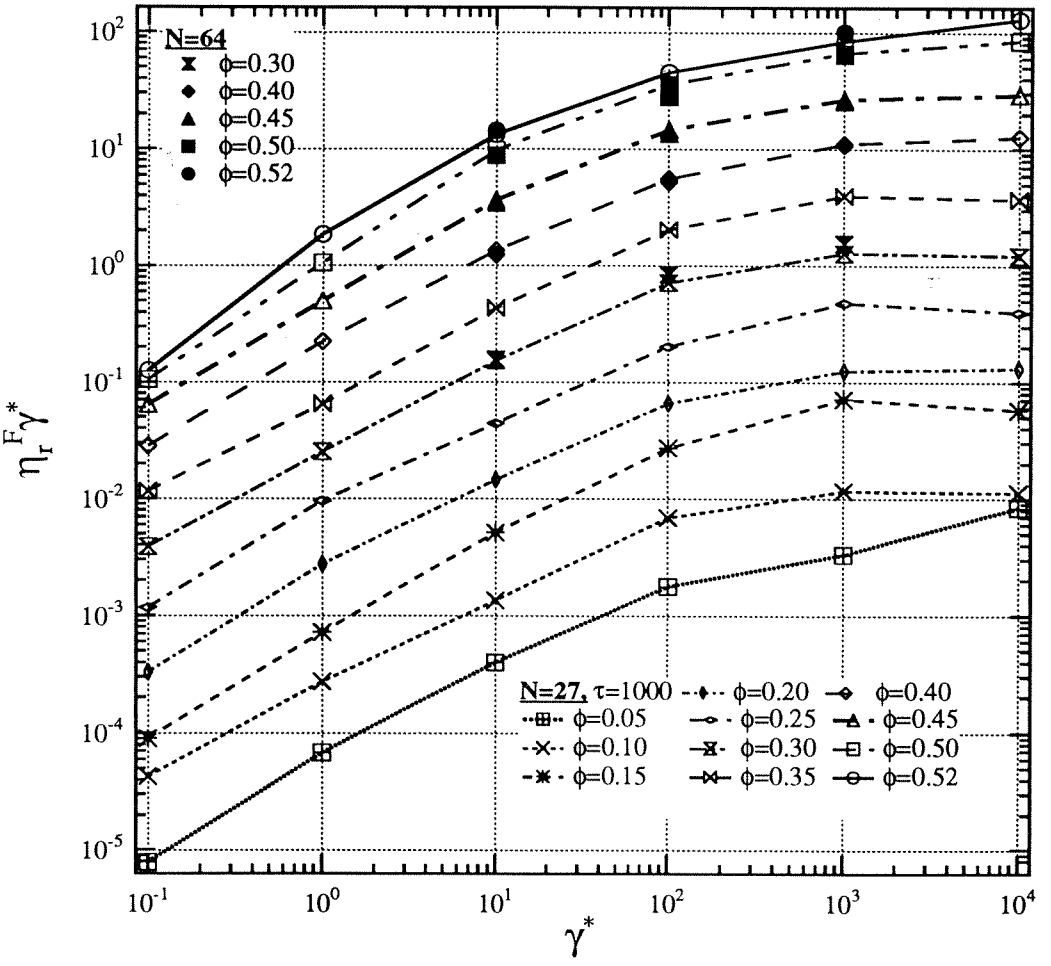

Figure 9.52: The product of the dimensionless shear rate and the interparticle-force contribution to the shear viscosity plotted against $\dot{\gamma}^*$.

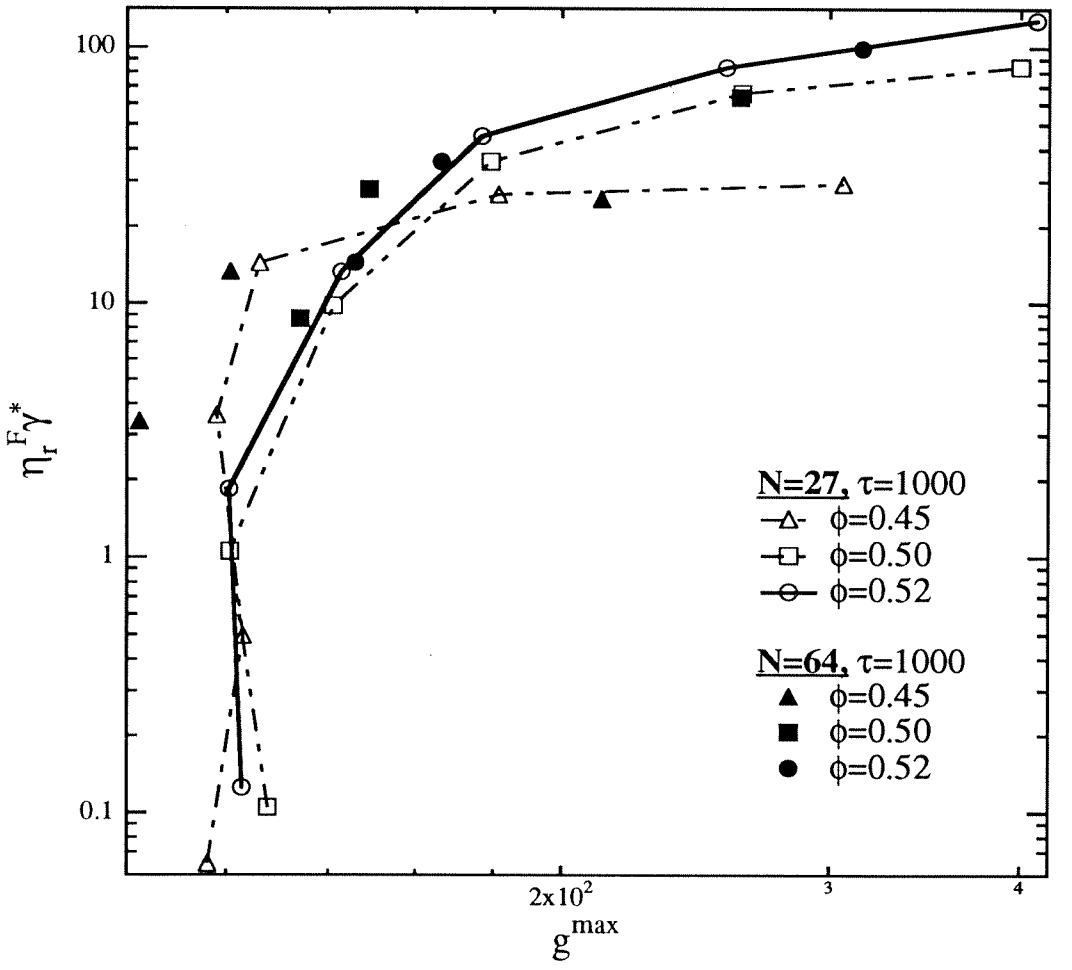

Figure 9.53: The product of the dimensionless shear rate and the interparticle-force contribution to the shear viscosity plotted against $g^{max}(r)$. At high ϕ and $\dot{\gamma}^*$, $\eta_r^F \dot{\gamma}^*$ scales as $g^{max}(r)$.

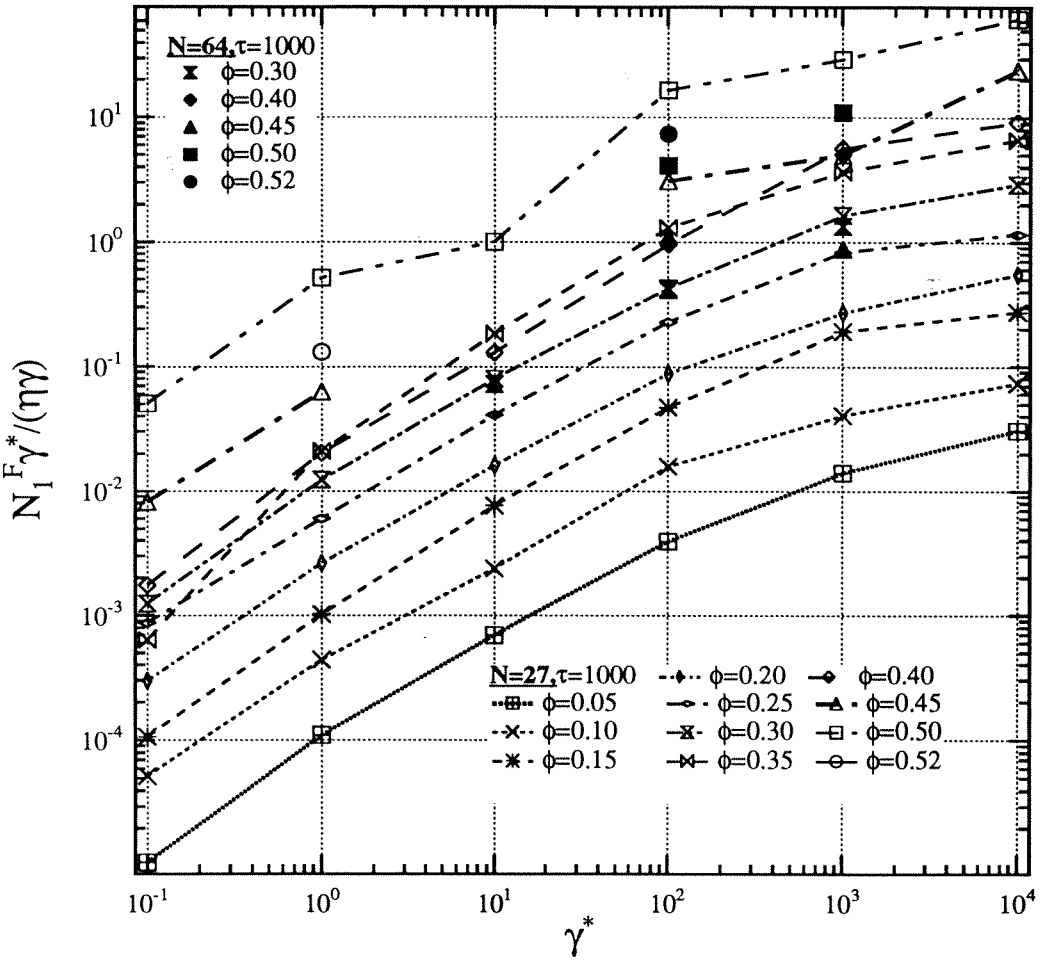

Figure 9.54: The product of the dimensionless shear rate and the interparticle-force contribution to the first normal stress difference plotted against $\dot{\gamma}^*$.

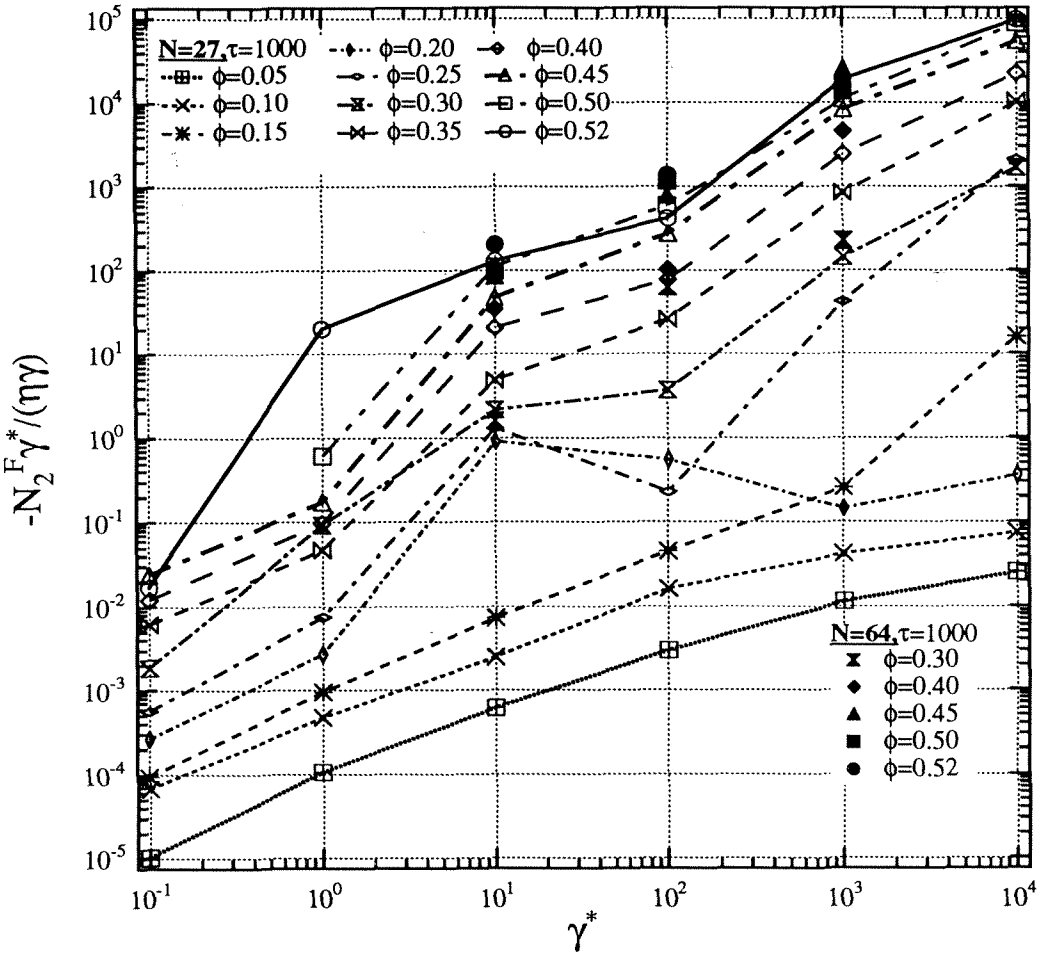

Figure 9.55: The product of the dimensionless shear rate and the interparticle-force contribution to the second normal stress difference plotted against $\dot{\gamma}^*$.

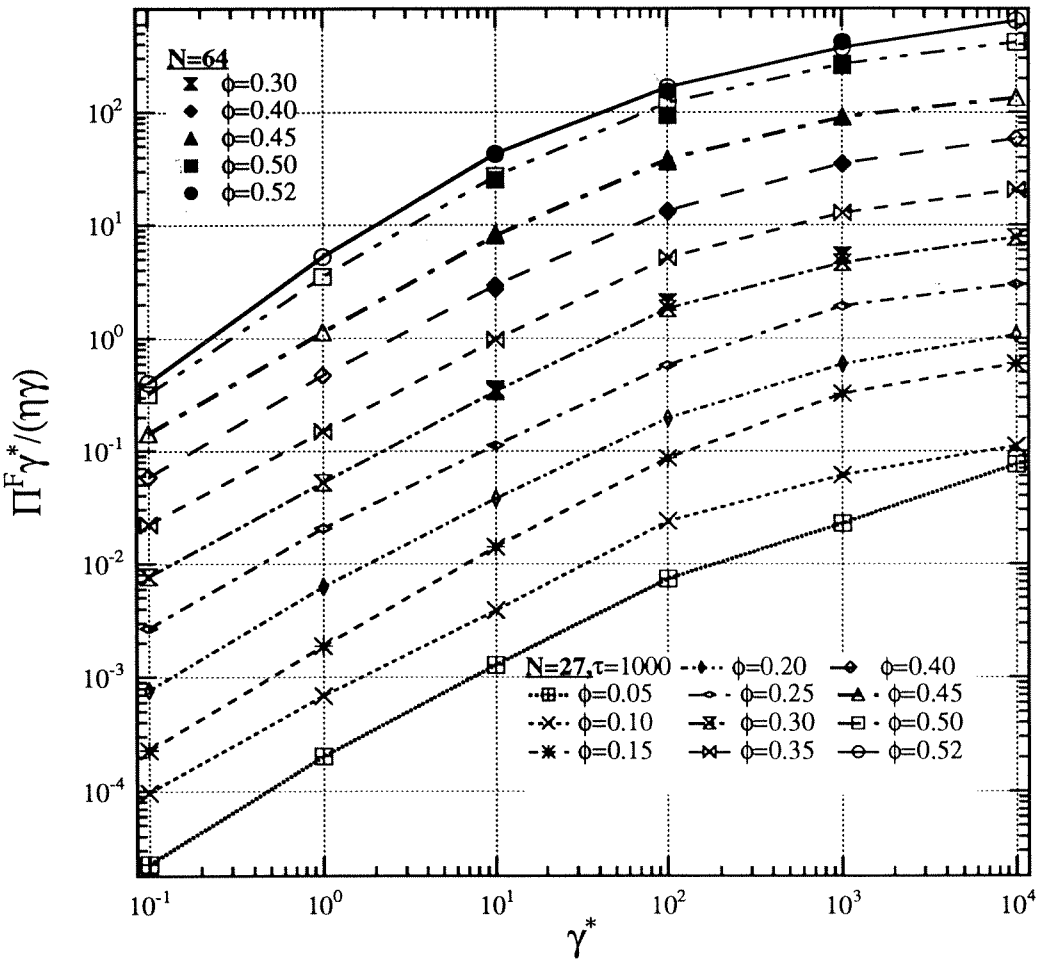

Figure 9.56: The product of the dimensionless shear rate and the interparticle-force contribution to the suspension pressure plotted against $\dot{\gamma}^*$.

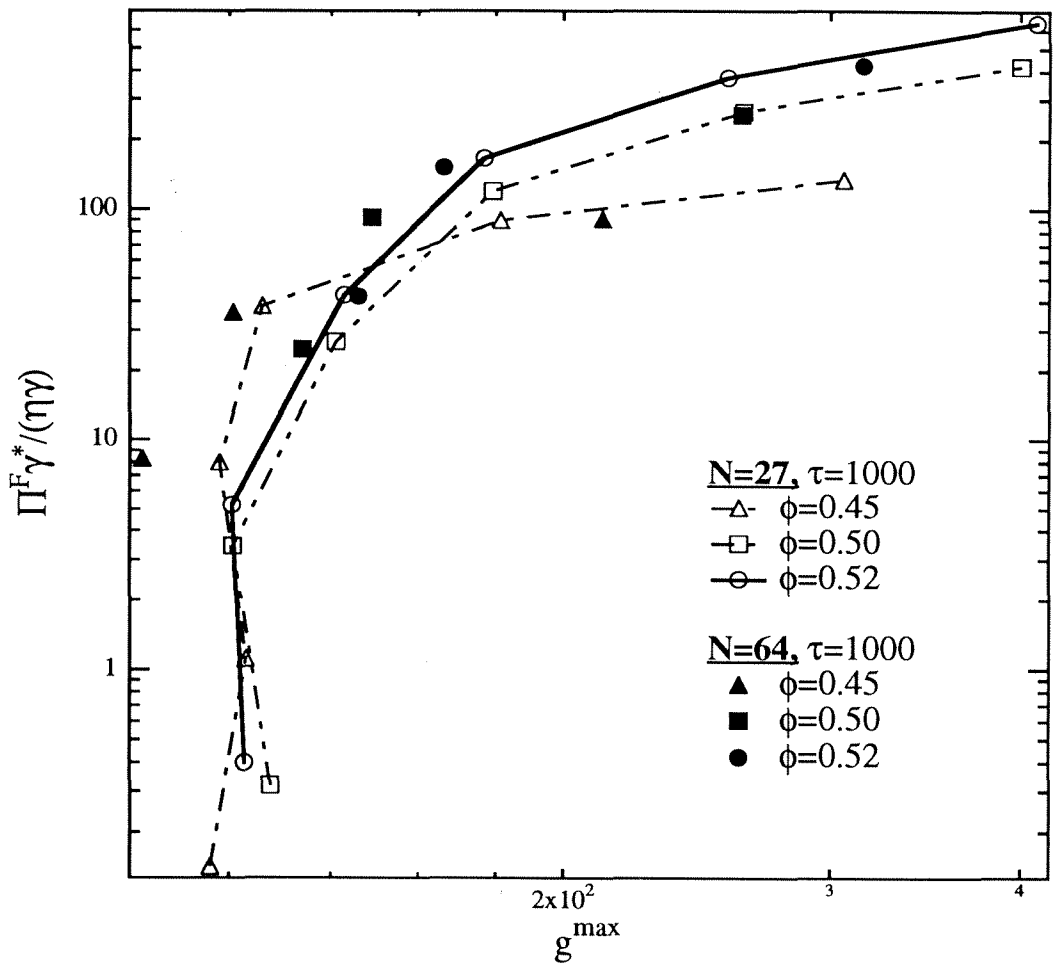

Figure 9.57: The product of the dimensionless shear rate and the interparticle-force contribution to the suspension pressure plotted against $g^{max}(r)$. At high ϕ and $\dot{\gamma}^*$, $\Pi^F\dot{\gamma}^*$ scales as $g^{max}(r)$.

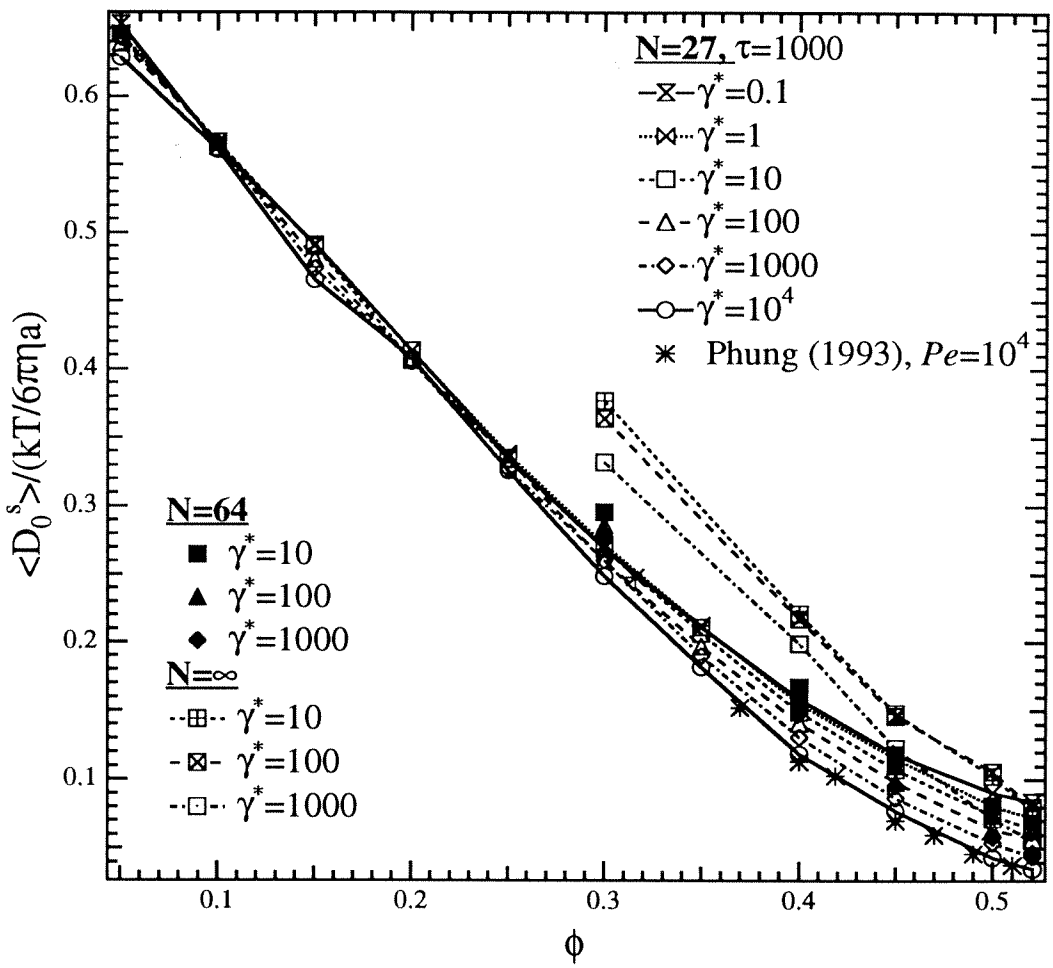

Figure 9.58: The translational short-time self-diffusivity.

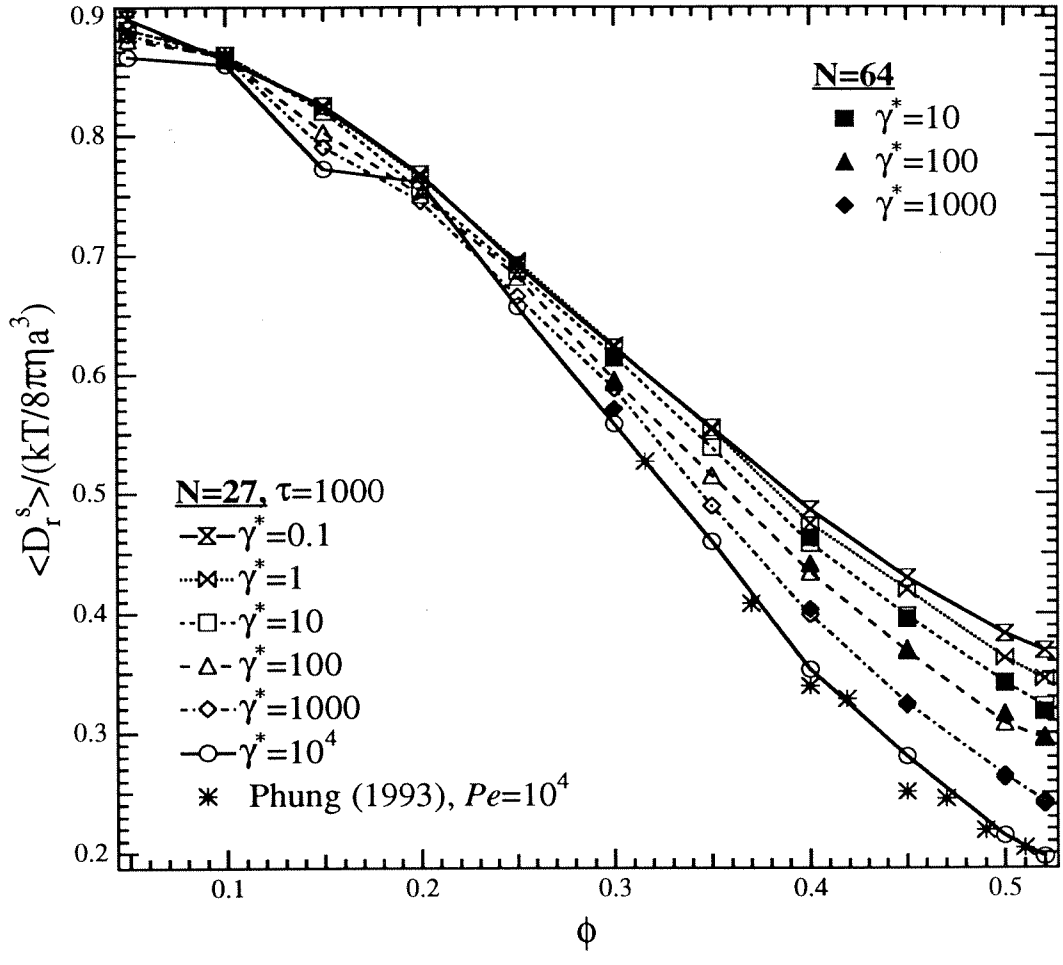

Figure 9.59: The rotational short-time self-diffusivity.

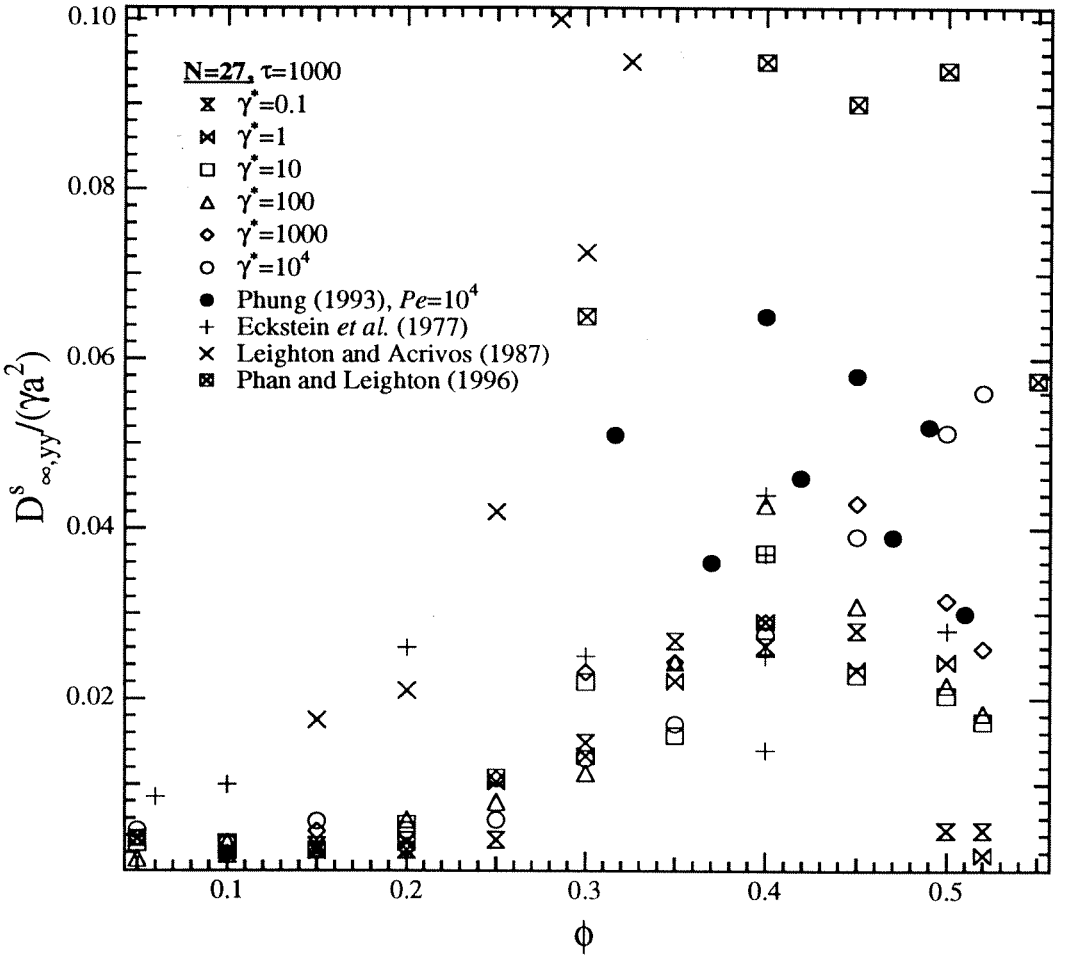

Figure 9.60: The long-time self-diffusivity in the velocity-gradient direction.

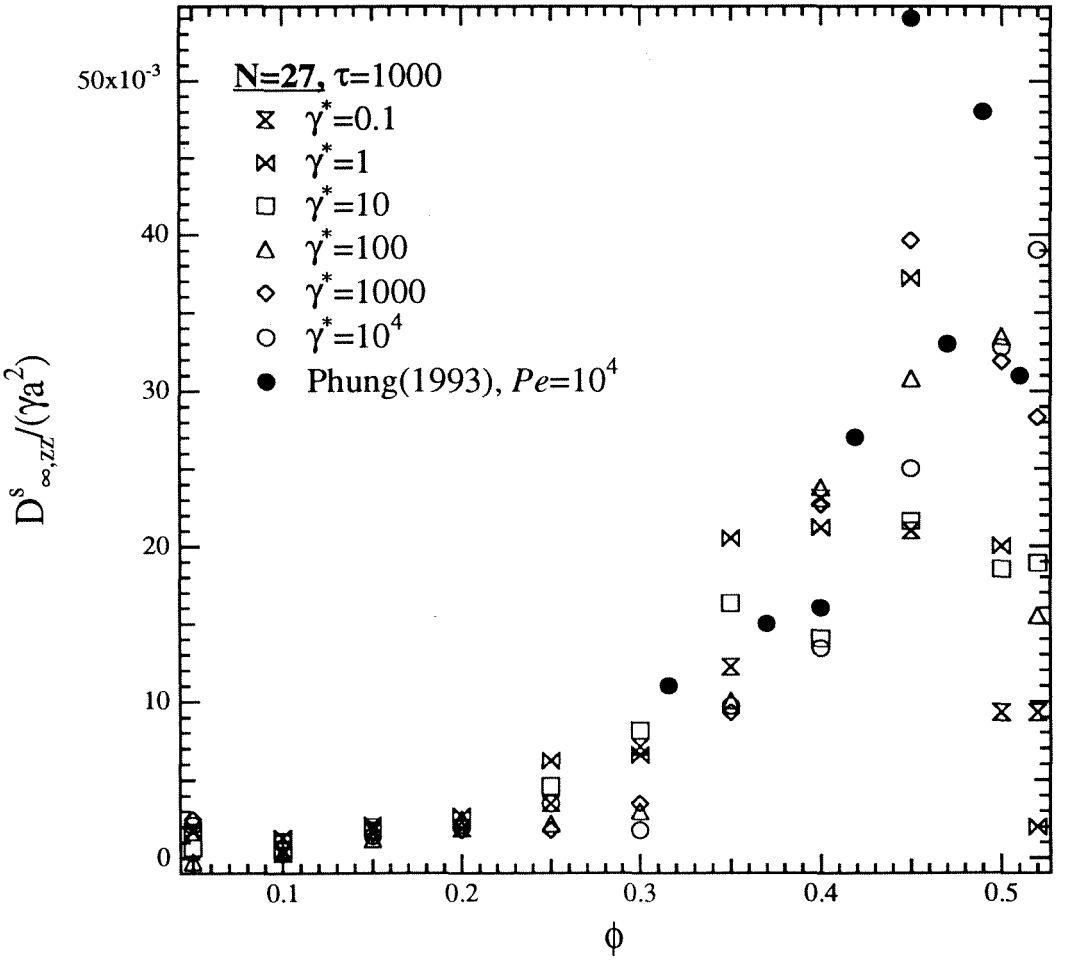

Figure 9.61: The long-time self-diffusivity in the vorticity direction.

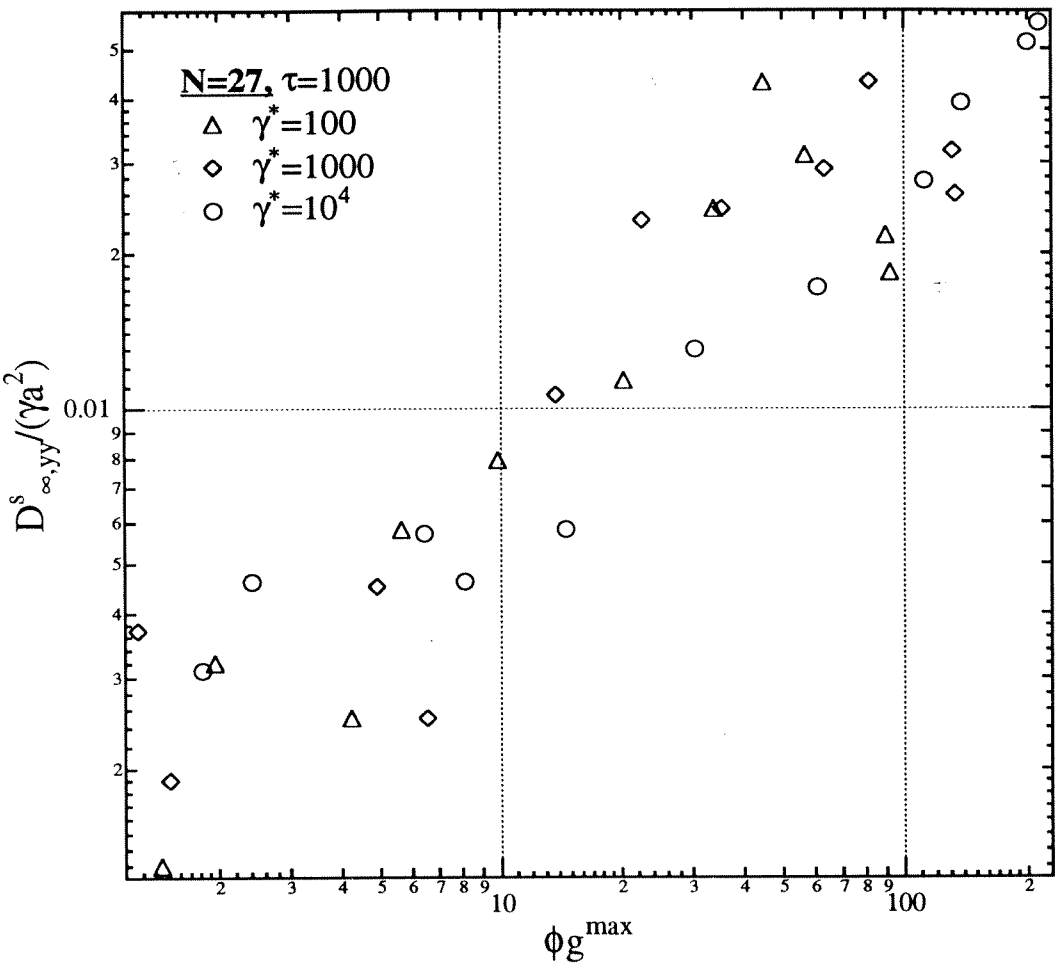

Figure 9.62: The long-time self-diffusivity in the velocity-gradient direction plotted against ϕg^{max}.

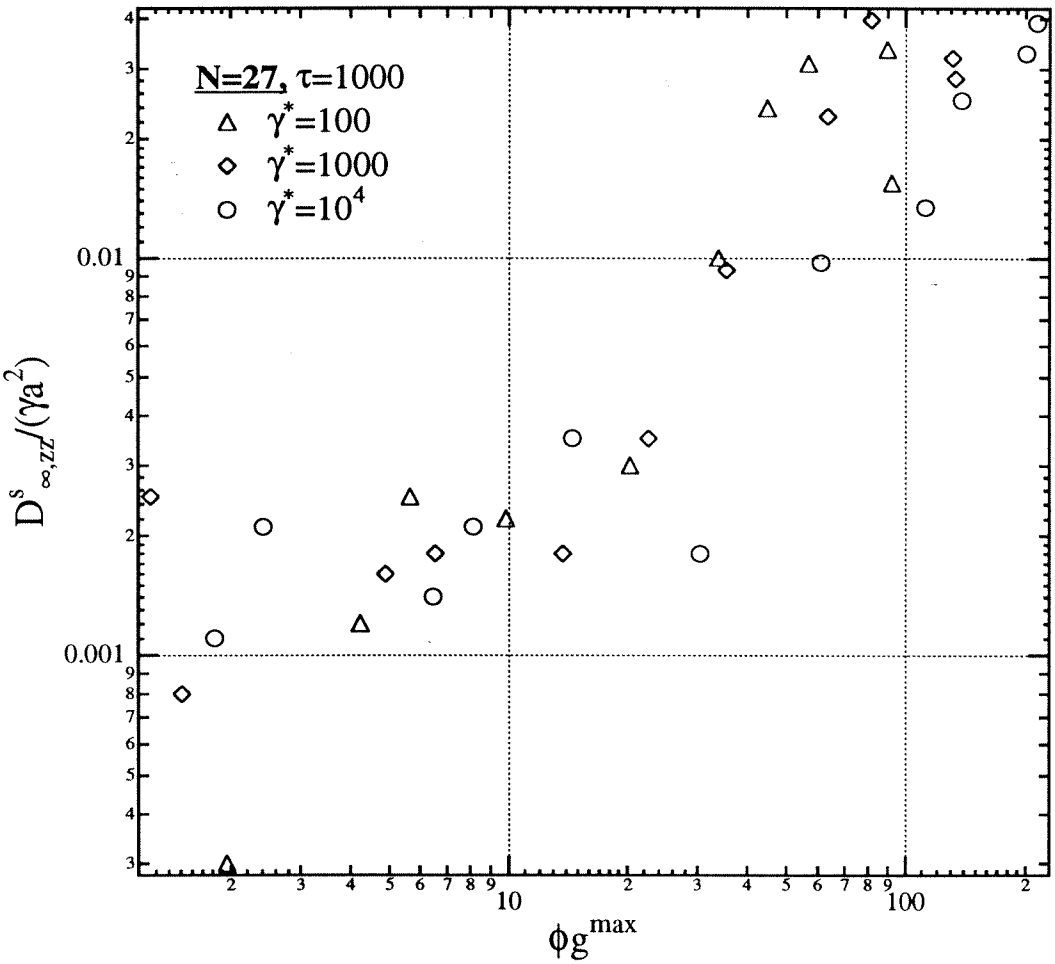

Figure 9.63: The long-time self-diffusivity in the vorticity direction plotted against ϕg^{max}.

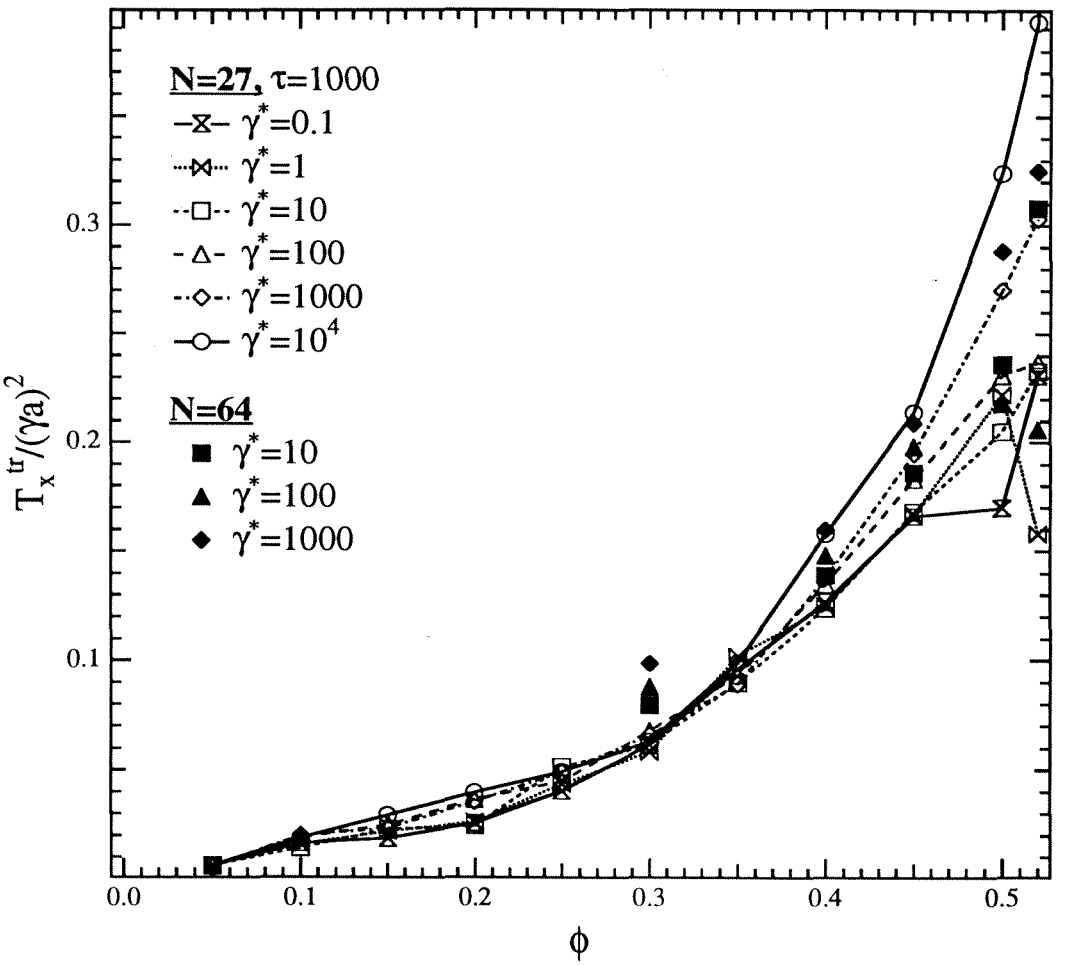

Figure 9.64: The mean square of particle translational velocity fluctuation in the flow direction.

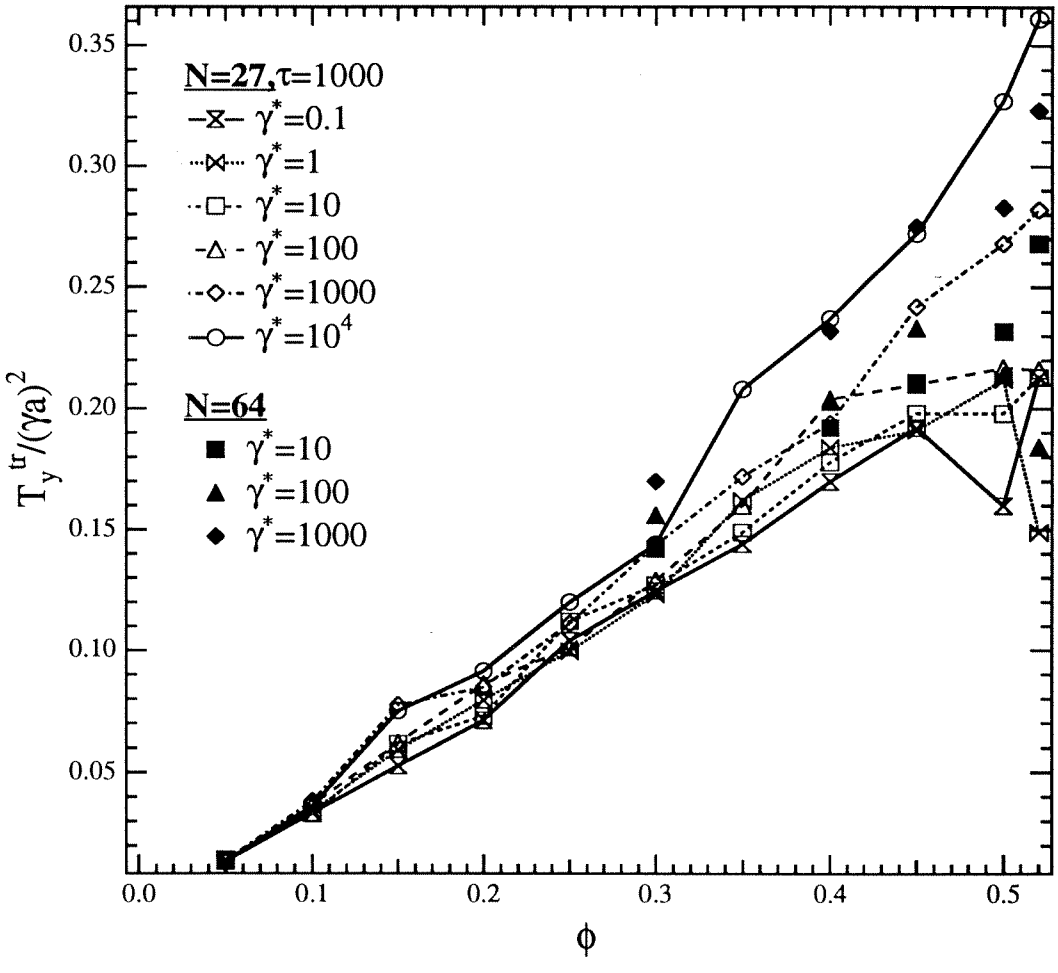

Figure 9.65: The mean square of particle translational velocity fluctuation in the velocity-gradient direction.

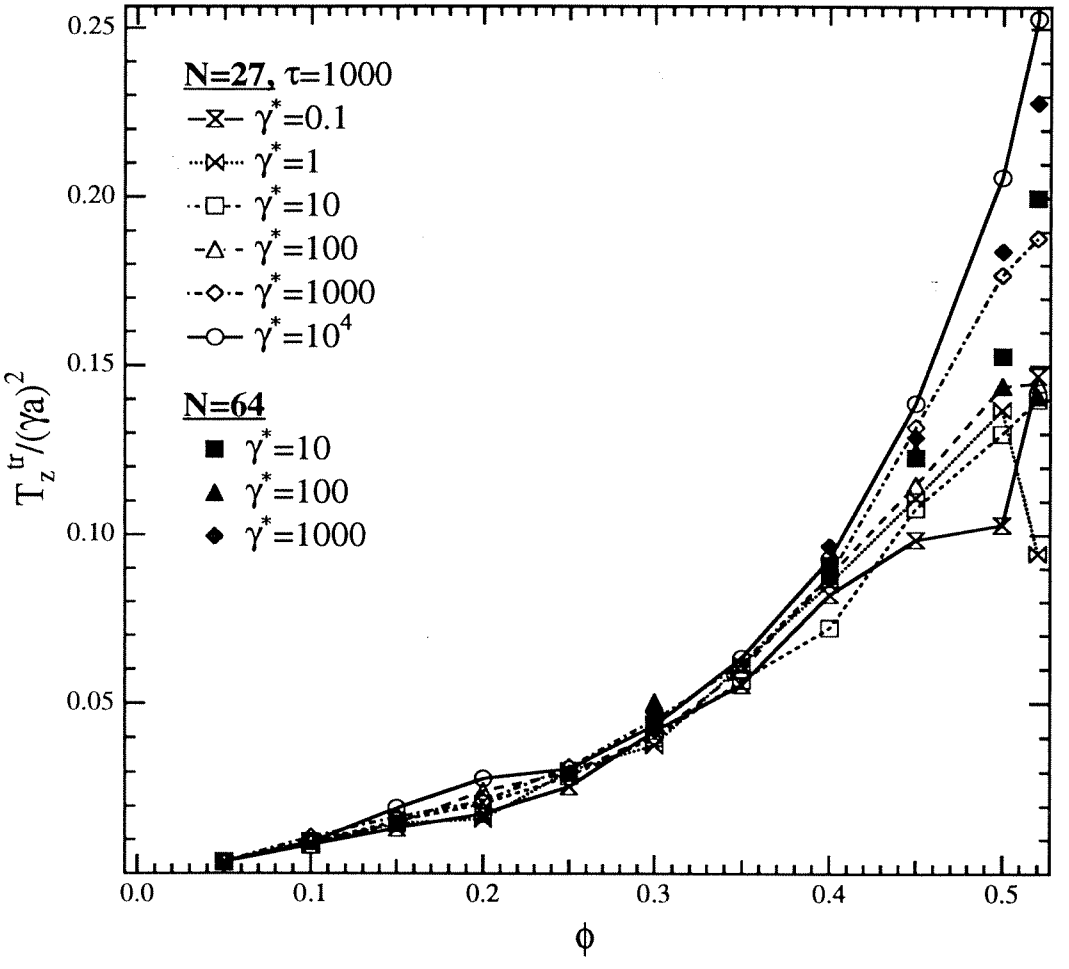

Figure 9.66: The mean square of particle translational velocity fluctuation in the vorticity direction.

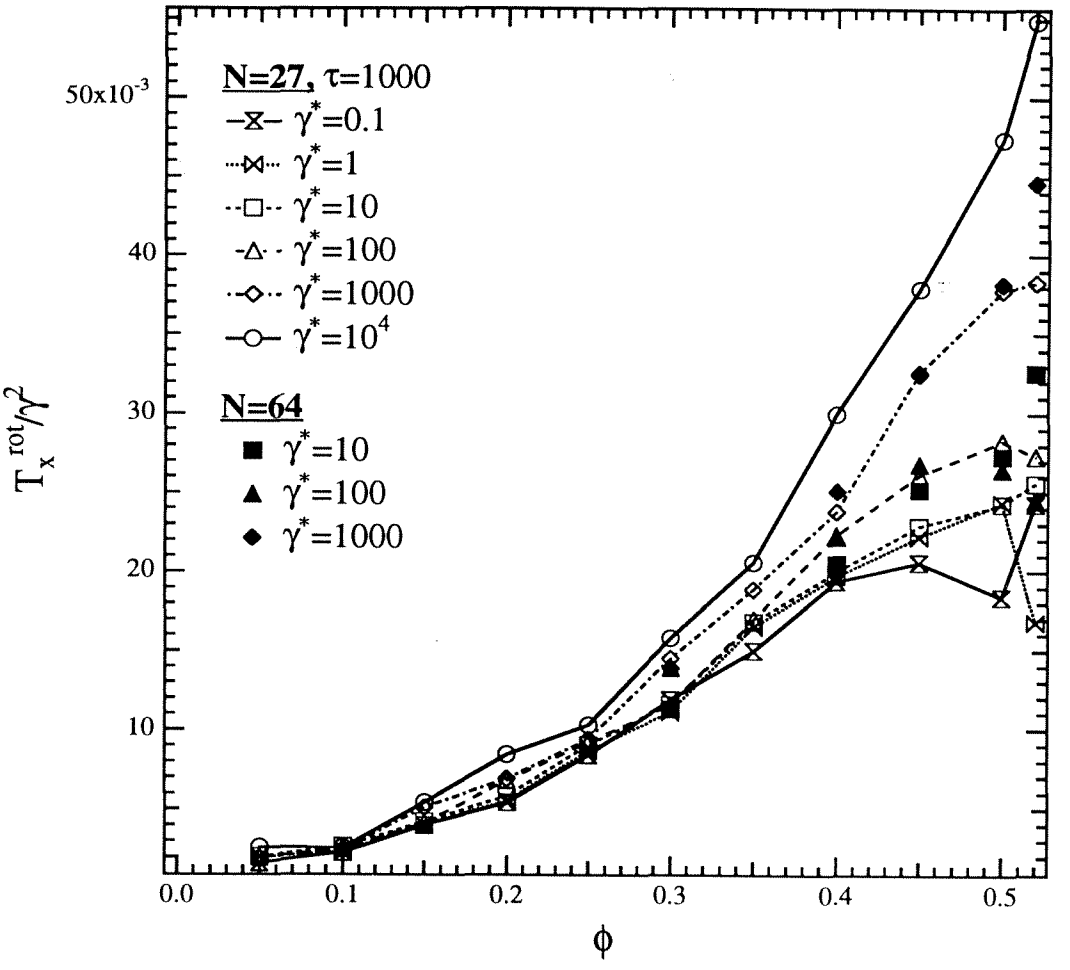

Figure 9.67: The mean square of particle rotational velocity fluctuation in the flow direction.

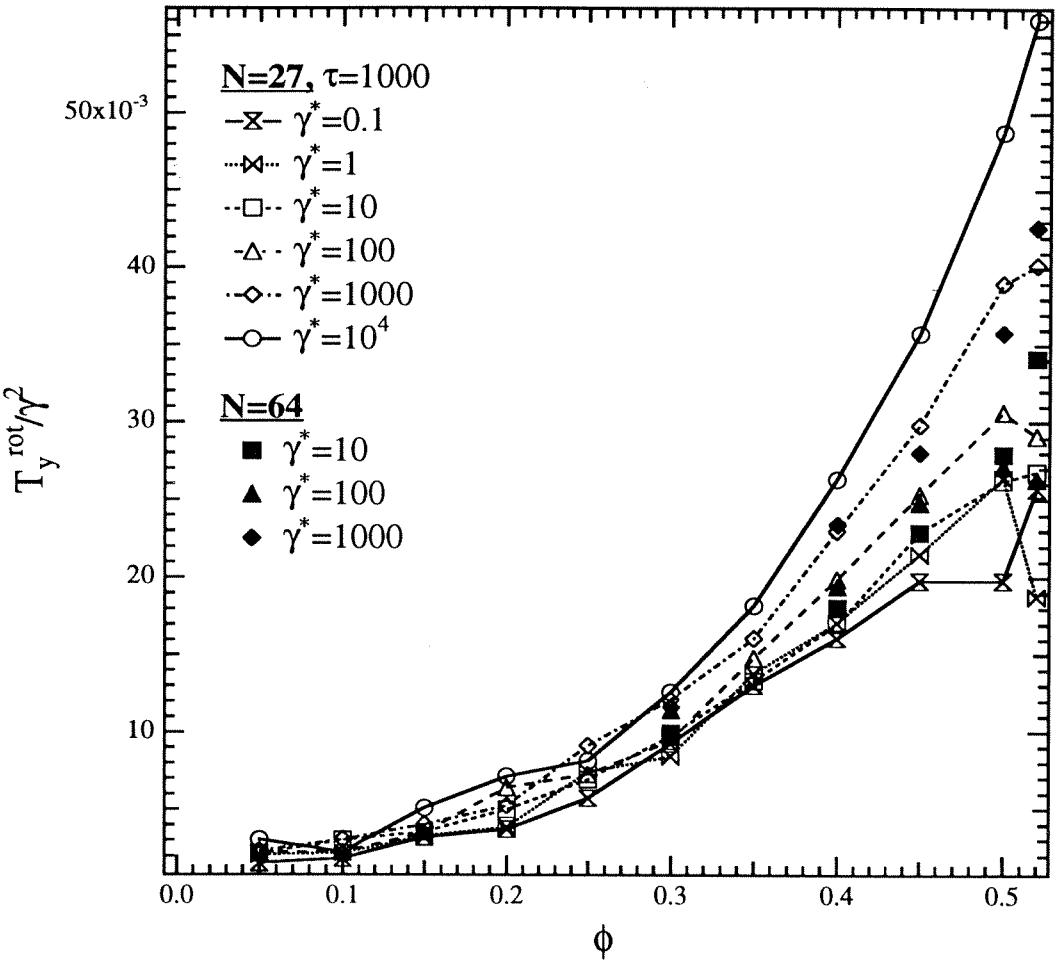

Figure 9.68: The mean square of particle rotational velocity fluctuation in the velocity-gradient direction.

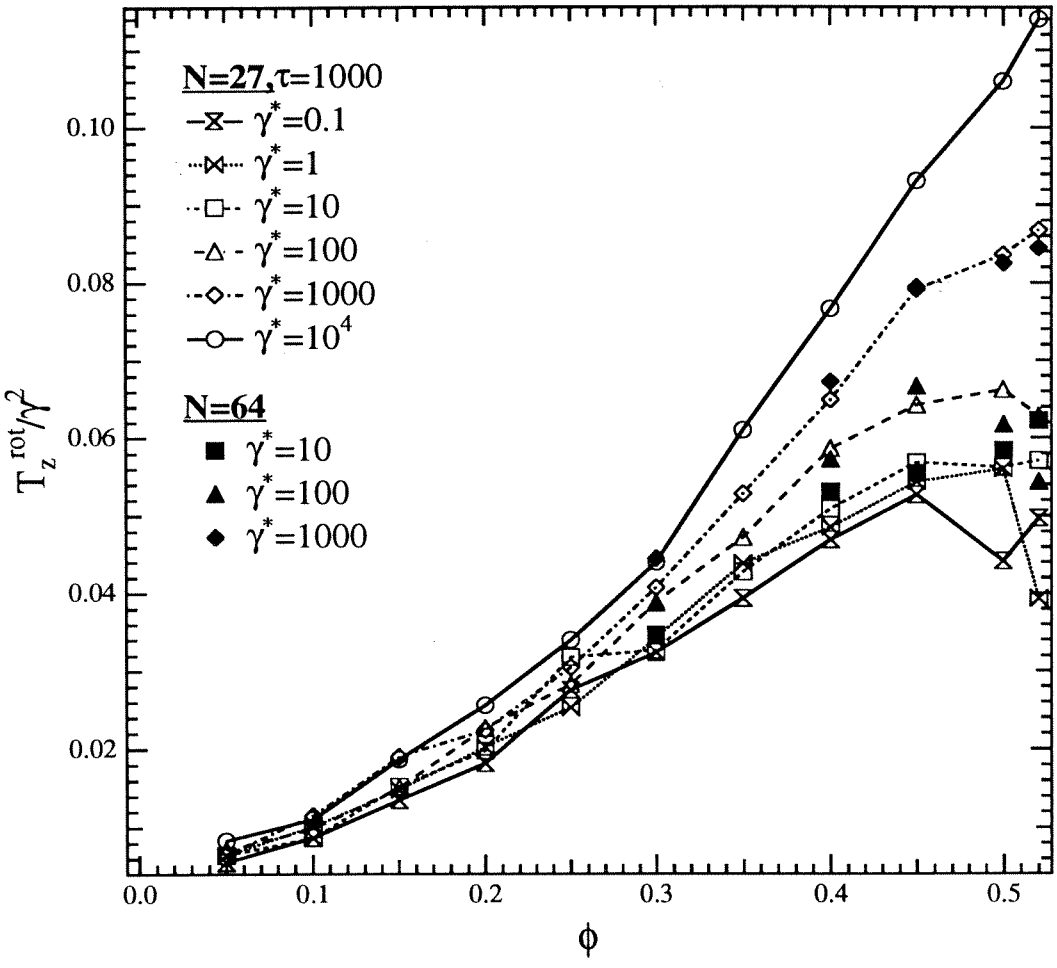

Figure 9.69: The mean square of particle rotational velocity fluctuation in the vorticity direction.

Chapter 10 Conclusions

In this work we have conducted a comprehensive study of suspensions of non-Brownian particles interacting by means of a short-range pairwise repulsive force. We have used Stokesian Dynamics to simulate the range of particle phase concentrations from very dilute ($\phi = 0.05$) to very dense ($\phi = 0.52$) over five decades in the nondimensional shear rate (from $\dot{\gamma}^* = 0.1$ to 10^4). The goal of the simulations was to clarify the nature of the connection between the suspension microstructure, as determined by the balance of the shear and interparticle forces, and the macroscopic suspension properties, such as the non-Newtonian rheology (normal stress differences and suspension pressure), hydrodynamic diffusion, and the suspension temperature defined as the mean square of the particles' velocity fluctuation.

The main conclusions of this study can be summarized as follows.

(i) Suspension microstructure. In concentrated suspensions at the lowest values of the shear rate $\dot{\gamma}^*$ (i.e. when the repulsive interparticle force dominates the suspension) the particles form strings oriented along the direction of the flow, hexagonally packed in the velocity-gradient–vorticity plane; at the same time individual particles at all times stay separated from other particles by a thin layer of the solvent. As $\dot{\gamma}^*$ increases, the ordering of particles in strings gradually disappears being replaced by noncompact clusters of particles kept together by strong lubrication forces. Additionally, at high shear rates, pairwise particle collisions display a broken fore-aft symmetry in a thin boundary layer adjacent to the particle surface.

(ii) Suspension rheology. In concentrated suspensions at high values of $\dot{\gamma}^*$ the noncompact clusters of particles result in a marked increase in the shear viscosity. Simultaneously, due to the broken fore-aft symmetry of particle pair-distribution, the normal stress differences and suspension pressure increase, in agreement with theoretical findings of Brady & Morris (1997).

(iii) Hydrodynamic diffusion. The long-time self-diffusivity of suspended particles is found dependent on the details of their microstructural arrangement. The long-time self-diffusion coefficients in the velocity-gradient and vorticity directions, $D^s_{yy,\infty}$ and $D^s_{zz,\infty}$, at the highest value of $\dot{\gamma}^* = 10^4$, monotonically increase over the entire simulated range of particle phase concentrations ϕ. As $\dot{\gamma}^*$ decreased, the particles begin to form strings and that leads to a dramatic decrease in $D^s_{yy,\infty}$ and $D^s_{zz,\infty}$ at high concentrations ϕ. In dilute suspensions little long-time self-diffusivity is found owing to the infrequency of inter-particle collisions.

(iv) Suspension temperature. In concentrated suspensions both the translational and rotational suspension temperatures are found to be the highest at the highest shear rates $\dot{\gamma}^*$. At the lowest $\dot{\gamma}^*$ the formation of strings results in a decrease in the particles' fluctuational motions; accordingly, the computed values of the temperatures are low.

References

Batchelor, G.K. and Green, J.T. 1972 The hydrodynamic interactions of two small freely-moving spheres in a linear flow field. *J. Fluid Mech.* **56**, 375.

Beenakker, C.W.J. 1986 Ewald sum of the Rotne-Prager tensor. *J. Chem. Phys.* **85**, 1581.

Bonnecaze, R. T. and Brady, J. F. 1990 A method for determining the effective conductivity of dispersions of particles. *Proc. R. Soc. Lond.* A **430**, 285.

Bossis, G. and Brady, J.F. 1984 Dynamic simulation of sheared suspensions. I. General method. *J. Chem. Phys.* **80**, 5141.

Bossis, G. and Brady, J.F. 1987 Self-diffusion of Brownian particles in concentrated suspensions under shear. *J. Chem. Phys.* **87**, 5437.

Bossis, G. and Brady, J.F. 1989 The rheology of Brownian suspensions. *J. Chem. Phys.* **91**, 1866.

Brady, J.F. and Bossis, G. 1985 The rheology of concentrated suspensions in simple shear flow by numerical simulation. *J. Fluid Mech.* **155**, 105.

Brady, J.F. and Bossis, G. 1988 Stokesian dynamics. *Ann. Rev. Fluid Mech.* **20**, 111.

Brady, J.F., Lester, J., Phillips, R., and Bossis, G. 1988 Dynamic simulation of hydrodynamically interacting suspensions. *J. Fluid Mech.* **195**, 257.

Brady, J.F. and Morris, J.F. 1997 Microstructure of strongly-sheared suspensions and its impact on rheology and diffusion. *J. Fluid Mech.* **348**, 103.

Da Cunha, F.R. and Hinch, E.J. 1996 Shear-induced dispersion in a dilute suspension of rough spheres. *J. Fluid Mech.* **309**, 211.

Davis, R.H. 1996 Hydrodynamic diffusion of suspended particles: a symposium. *J. Fluid Mech.* **310**, 325.

Durlofsky, L.J., Brady, J.F., and Bossis, G. 1987 Dynamic simulation of hydrodynamically interacting particles. *J. Fluid Mech.* **180**, 21.

Eckstein, E.C., Bailey, D.G., and Shapiro, A.H. 1977 Self-diffusion of particles in shear flow of a suspension. *J. Fluid Mech.* **79**, 191.

Gadala-Maria, F.A. 1979 *The Rheology of Concentrated Suspensions.* Ph.D. thesis, Stanford University.

Jeffrey, D.J., Morris, J.F., and Brady, J.F. 1993 The pressure moments for two spheres in a low-Reynolds-number flow. *Phys. Fluids* A **5**, 2317.

Ladyzhenskaya, O.A. 1963 *The Mathematical Theory of Viscous Incompressible Flow.* Gordon and Breach.

Leighton, D.T. and Acrivos, A. 1987 Measurement of shear-induced self-diffusion in concentrated suspensions of spheres. *J. Fluid Mech.* **177**, 109.

Nott, P.R. and Brady, J.F. 1994 Pressure-driven flow of suspensions: simulation and theory. *J. Fluid Mech.* **275**, 157.

O'Brien, R.W. 1979 A method for the calculation of the effective transport properties of interacting particles. *J. Fluid Mech.* **139**, 261.

Parsi, F. and Gadala-Maria, F. 1987 Fore- and aft-asymmetry in a concentrated suspension of solid spheres. *J. Rheol.* **31**, 725.

Pätzold, R. 1980 Die Abhängigkeit des Fließverhaltens konzertierter Kugelsuspensionen von der Strömungsform: Ein Vergleich der Viskosität in Scher- und Dehnströmungen. *Rheol. Acta* **19**, 322.

Phan, S.E. and Leighton, D.T. 1996 Measurement of the shear-induced tracer diffusivity in concentrated suspensions. To appear in *J. Fluid Mech.*

Phillips, R., Brady, J.F., and Bossis, G. 1988 Hydrodynamic transport properties of hard-sphere dispersions. I. Suspensions of freely mobile particles. *Phys. Fluids* **31**, 3462.

Phung, T.N. 1993 *Behavior of Concentrated Colloidal Suspensions by Stokesian Dynamics Simulation.* Ph.D. thesis, California Institute of Technology.

Phung, T.N., Brady, J.F., and Bossis, G. 1996 Stokesian Dynamics simulation of Brownian suspensions. *J. Fluid Mech.* **313**, 181.

Rutgers, Ir. R. 1962 Relative viscosity of suspensions of rigid spheres in Newtonian liquids. *Rheol. Acta* **2**, 202.

Van der Werff, J.C., de Kruif, C.G., Blom, C., and Mellema, J. 1989 In *Proceedings of the Fourth EPS Liquid State Conference*, Arcachon, France. M. Nijhoff, Amsterdam.